

ENHANCING THE RADIAL VELOCITY PRECISION OF
HIGH-RESOLUTION NEAR-INFRARED SPECTROGRAPHS FOR
DETECTING EXOPLANETS AROUND ULTRACOOOL DWARFS

ROBERTO VARAS GONZÁLEZ



UNIVERSIDAD
DE GRANADA

Programa de Doctorado en Física y Matemáticas

Universidad de Granada

Instituto de Astrofísica de Andalucía

Supervised by

Pedro J. Amado

and

Francisco J. Pozuelos

Submitted on April 2026 (Granada)



A thesis submitted in partial fulfillment of the requirements for the Doctoral Program in Physics and Mathematics

Roberto Varas González: *Enhancing the radial velocity precision of high-resolution near-infrared spectrographs for detecting exoplanets around ultracool dwarfs* © April 2026

This thesis was written during an ongoing genocide in Palestine.
1947–present

Esta tesis ha sido escrita durante un genocidio en curso en Palestina.
1947 – presente

POSITIONALITY STATEMENT

Tengo y he tenido siempre el apoyo de mi familia, biparental y con dos hermanos. Mi padre y mi madre siempre han trabajado, con un salario digno y una posición estable. He ido al colegio, instituto, y universidad. He realizado deporte desde pequeño, he tenido una dieta equilibrada, me he podido relacionar socialmente con gente de diferentes contextos, he viajado por el estado español y en algunas ocasiones en el extranjero. Soy un hombre-cis, blanco, joven, europeo, con familia de clase media-alta, tengo un cuerpo normativo, y he trabajado desde que terminé los estudios universitarios.

I have and always have had the support of my bi-parental family and two brothers. My mother and my father have always worked with gainful employment and stable positions. I went to school, high school, and university. I have been involved in sports from a young age, have had a well-balanced diet, have had diverse social relationships, and have traveled through Spain and even visited other countries. I am a cis-man, white, young, European, with a middle-upper social class family, I have a normative body, and I have worked since I finished university.

Granada, abril 2026

Roberto Varas González

PRÓLOGO

Hades II es un juego que salió a la venta en septiembre de 2025. Fue desarrollado durante varios años por *Supergiant Games*, como consecuencia del éxito que tuvo la primera parte, el aclamado *Hades* (2020). En el videojuego, Melinöe, hija de Hades, el dios griego del inframundo, quiere vengarse de su abuelo Cronos, el titan del tiempo, por la captura de su familia: Hades, Hera, y Zagreus. Nuestra protagonista entrena durante años en las encrucijadas, bajo la supervisión de Hecate, la diosa titánide de la brujería, la nigromancia¹, los portales y las encrucijadas. Además, para combatir a Cronos disponen del apoyo de los dioses del Olimpo, así como muchos otros personajes mitológicos.

Algunas de las aliadas más poderosas son Moros, Eris, Némesis, Hipnos, y Caronte, las hijas de Nyx, la diosa primordial de la noche. Hecate y Melinöe, junto con Artemisa (diosa de la caza), y Selene (la encarnación de la Luna) forman las hermanas argénteas, un grupo de diosas de la Luna. Todo el juego está estrechamente relacionado con el concepto de la noche y la Luna (Imagen 1), ya que otorgan poderes a nuestra heroína para que pueda lograr su cometido. Muchas otras deidades ofrecen su ayuda, como Apolo (dios del Sol), y también elementos como las cartas del Arcano, el máximo exponente de la astrología.

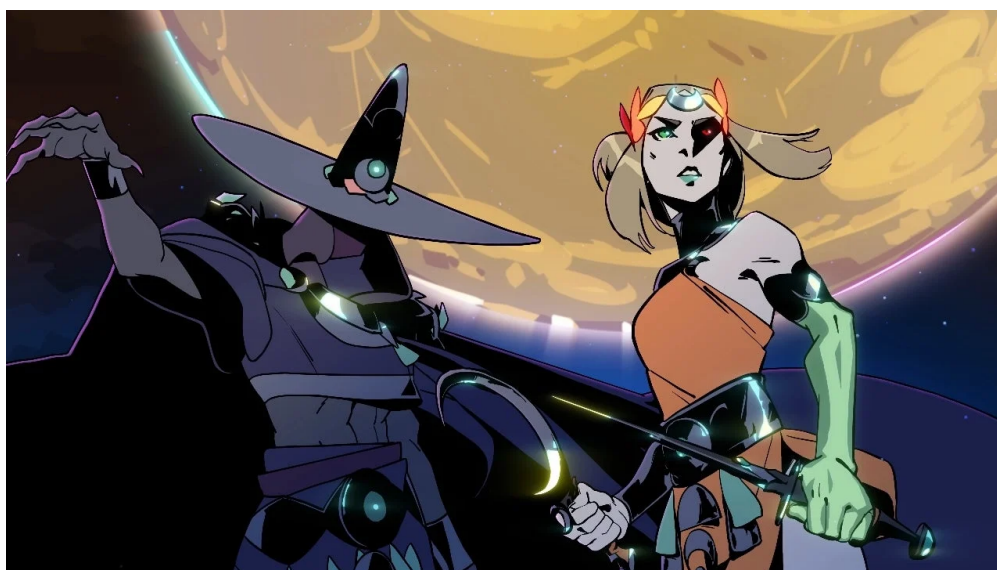


Imagen 1: Imagen del tráiler de *Hades II*. Fijate en las referencias a la noche y la Luna.

Hades II es uno de los muchos ejemplos en el imaginario colectivo que podemos encontrar que hacen referencia a la astronomía. La Luna, las estrellas, el Sol, ... Están en todas partes, siempre acompañando a la humanidad en cada etapa de la historia, y en cualquier parte del mundo. Este juego es un

¹ La nigromancia es la práctica de la adivinación mediante el contacto o invocación de los muertos, con el objetivo de conocer lo oculto o predecir eventos futuros.

ejemplo de la influencia de la mitología griega, y un claro exponente de como esto sigue formando parte de la cultura moderna, conectando así la historia occidental a través de más de tres milenios. Se trata de un fenómeno que tiene lugar en muchos otros rincones del mundo, en tiempos muy diferentes. Este es el motivo esencial por el cual podemos justificar la existencia de la astronomía como disciplina, así como la gran cantidad de recursos que se invierten para entender cómo funciona el Universo, ya que tiene un gran impacto en nuestras vivencias personales, que nos une a través del tiempo y las culturas.

Hacer un resumen de la historia de la ciencia y la filosofía que han conducido a la astronomía como la conocemos hoy en día está fuera del foco de esta tesis. Al menos la historia de la astronomía *mainstream* de occidente, liderada por hombres blancos, con recursos económicos, cis-heterosexuales, y principalmente europeos. Sin embargo, aprender y entender un poco de cómo ha evolucionado e impactado la astronomía en otras culturas puede ser mucho más útil y enriquecedor.

Existe una gran cantidad de estudios sobre la historia de la astronomía enfocados en diferentes épocas y culturas. Las dos principales disciplinas son la *arqueoastronomía* y la *etnoastronomía*. La arqueoastronomía se centra en el estudio de los restos materiales, prácticas, sabiduría tradicional, mitología, religión, y cosmología de todas las culturas antiguas relacionadas con la astronomía. Por otro lado, la etnoastronomía es el estudio de la astronomía y cosmología de las culturas indígenas y nativas contemporáneas que han sobrevivido a lo largo del tiempo².

Dos libros referentes son de Selin and Sun (2000), titulado *Astronomy Across Cultures: The History of Non-Western Astronomy*, y Boutsikas (2014), que tiene *Handbook of Archaeoastronomy and Ethnoastronomy* como título. Ambos ofrecen un análisis exhaustivo de la historia e influencia de la astronomía en culturas muy diversas alrededor de la Tierra. Aquí voy a intentar dar una pincelada sobre el contenido de estos magníficos trabajos, desarrollados por parte de muchas personas expertas, con el objetivo de llevarnos una serie de datos muy interesantes a casa, pero también para hacernos reflexionar sobre lo que sabemos de la ciencia, así como el concepto que tenemos de *cómo es* y *cómo debe ser* la ciencia.

El libro de Selin and Sun (2000) se centra en multitud de culturas y épocas, con capítulos dedicados a cada una de estas. Mi intento de extraer información interesante de este trabajo (y otros cuantos relacionados), no tiene un orden tan claro en cuanto a las culturas. He optado por ordenarlo en base a la temática (cómo afecta la astronomía a la visión religiosa, el poder, el tiempo, ...). Además, tanto el libro mencionado como mi prólogo, así como otros muchos estudios, no abordan la totalidad de las culturas y regiones del mundo (por ejemplo Asia central, o gran parte del norte de África).

El estudio del cielo ha sido sin duda uno de los primeros inicios de la ciencia, ya que las personas necesitaba observarlo y entenderlo para comprender cómo funcionaba el mundo a su alrededor. Mirar al cielo y analizar los cambios de los astros a lo largo del tiempo permitía mantener una noción del tiempo más

² Esta información la he obtenido de www.jesterbear.com/Aradia/astronomy.html.

“objetiva”. Por ejemplo, los calendarios de muchísimas culturas están basados en eventos astronómicos. El movimiento de los astros también ha sido fundamental en la navegación (tanto terrestre como marítima) y el diseño de mapas. Mirar al cielo ha servido como guía para la recogida y planta de las cosechas desde hace milenios. La observación de la bóveda celeste incluso ha tenido un fuerte impacto en la determinación de gobiernos, liderazgos, y comunidades, así como en la explicación de diferentes eventos y sucesos históricos. Tampoco podemos obviar el gran impacto de la astronomía en la vida espiritual de casi todas las culturas que conocemos.

Pero, ¿cómo estudian la arqueo- y la etnoastronomía las actividades relacionadas con la astronomía a través del tiempo y las culturas? En algunos casos, como el antiguo Egipto, Mesopotamia, la cultura hebrea o la maya, existe mucha documentación al respecto. En otros casos, hay que interpretar restos, huesos, tumbas, o megalitos, incluso confiar en la información de exploradores y colonizadores europeos. En este último caso, la información se ha distorsionado debido a los prejuicios europeos de lo que estaban viendo, e incluso mucha documentación fue destruida. En cualquier caso, en muchos casos hay que confiar en las interpretaciones y suposiciones que pueden hacerse de los restos de los que disponemos, incluso extrapolando en base a culturas o sociedades contemporáneas o mejor documentadas. El perfil de las personas que investigan estas áreas es muy variada, desde astrónomas, hasta lingüistas, así como historiadoras. Pero, sobre todo, perfiles y grupos interdisciplinarios.

Bien es cierto que el estudio del cielo, nocturno y diurno, ha sido una actividad común alrededor de nuestro planeta y del tiempo, pero el interés que hemos mostrado por estos estudios, documentación, estructuras, ... No ha sido equitativo. Tenemos el gran ejemplo de Stonehenge en Europa, con cientos de escritos al respecto y ampliamente conocida por la población, pero existe mucha (mucha mucha) menos literatura e investigación acerca de otras regiones del mundo. Se podría decir que es un problema de datos e información, al fin y al cabo, la historia no es lo que ha pasado, pero lo que ha sido constatado y transmitido a través del tiempo³.

Sin embargo, esta no es la barrera más grande, puesto que existe una mucho mayor: nuestra percepción única de cómo debe hacerse la ciencia, incluso nuestra propia definición de lo que es la ciencia. Esto ha restringido enormemente nuestra habilidad para entender (y querer comprender) otras astronomías o formas de hacer ciencia, excluyendo a la mayor parte del conocimiento que proviene de fuera de la investigación académica.

Si una cosa queda clara después de leer sobre estos temas, es la gran influencia que tienen las culturas en cómo se desarrollan las actividades científicas y astronómicas. Por ejemplo, en occidente nos definimos como racionales y materialistas, por lo que consideramos que cosas como el tiempo y el espacio son objetivamente medibles. Sin embargo, en otras culturas, como las personas Aborígenes de Australia, la distancia depende del tiempo que se tarda en llegar de un punto a otro, que a su vez depende de las cosas que te puedas encontrar

³ Esta idea o frase es originalmente de David Malouf, en su columna *The Sydney Morning Herald*, del 23 de noviembre de 1998, pág. 17.

o puedan pasar en el camino. Después de todo, tiempo y espacio no parecen ser tan objetivos. Basta con pensar cómo una misma situación, lugar, o tiempo, no es igual para todas las personas, sino que depende de las circunstancias que nos atraviesan (así como las que nos han atravesado).

Siguiendo con el concepto del tiempo, el calendario es algo que, en prácticamente todas las culturas conocidas, ha estado fuertemente ligado a la astronomía. Un calendario, al fin y al cabo, trata de reunir el orden y secuencia, así como el ciclo y ritmo que tienen los sucesos del universo que podemos percibir. Los calendarios pueden ser lunares, solares, o luni-solares, y en muchas ocasiones coexistían varios de ellos. La duración y división de un calendario puede variar mucho entre culturas. Por ejemplo, en Mesoamérica, el calendario solar tenía 365 días, y se combinaba con un calendario lunar de 260 días y el ciclo de Venus de 584 días. Algunos de los calendarios tenían un enfoque puramente religioso y ceremonial, mientras que otros eran puramente seculares (no religiosos). También hay registros acerca de como algunos *años nuevos* empezaban con la aparición de las Pléyades, o la primera visión tenue de la luna creciente. Algunos calendarios se dividían en dos estaciones sin el concepto de meses. Otros estaban muy cerca del concepto del calendario Gregoriano.

Pero no solo en cuanto al tiempo y al espacio, también en otras actividades influye el cielo. Como decía, tanto por tierra como por mar, el cielo ha sido un elemento crítico para poder guiarse adecuadamente. Por ejemplo, las culturas de la Polinesia y árabe desarrollaron sistemas muy sofisticados para poder guiarse en mar abierto. También existen excepciones, donde los sistemas de navegación y guía eran completamente ajenos al cielo.

De igual forma, las estaciones o los tiempos adecuados para las cosechas y la caza han sido marcados por los cambios que se observan en el cielo: las constelaciones, la posición del Sol y la Luna, o la duración de los días y noches, por ejemplo. Es el caso de los !Kung de África, o Bosquimanos, que se separaban en grupos más pequeños con la llegada de la época de lluvias, marcada por la aparición de Canopus y Capella.

Una de las mayores influencias de la astronomía ha sido en los mitos y la religión. Algunos ejemplos son:

- En la mitología hawaiana, el dios Kāne⁴, que significa *al hombre*, es el padre de las criaturas vivas, un símbolo de vida y naturaleza. Aunque los mitos alrededor de esta figura han sido diversos, debido a la migración de diferentes zonas de la Polinesia, coinciden en muchos puntos. Pō es el caos primordial, donde los dioses originalmente habitaban. En determinado momento, Kāne se desligó de Pō gracias a su fuerza de voluntad. Como consecuencia, Lono (dios de las lluvias, mar, agricultura, y productividad) y Kū (dios de la guerra, el poder, y el amanecer) también se liberaron de Pō. Es en este momento cuando Kāne creó la luz, alejando así la oscuridad, mientras que Lono y Kū crearon el sonido y la sustancia, respectivamente. Los tres dioses primordiales, que siempre han existido, crearon entonces al resto de dioses menores. Acto seguido, Kāne creó el Sol, la Luna, y

⁴ Fuente: <https://sobreleyendas.com>.

las estrellas. Es entonces cuando Lono creó al hombre a base de arcilla, con ayuda de Kāne y Kū, a imagen de Kāne, y a la mujer a partir de sus costillas.

- En el antiguo Egipto, Nut⁵ es una de las diosas primordiales y una de las más importantes de Heliópolis, el lugar donde nacieron los dioses. Es la diosa del cielo, y está fuertemente asociada con la resurrección y el renacimiento. Además, es la madre de Osiris, Isis, Seth, y Neftis, por lo que es conocida como *la que dio luz a los dioses*. Una de sus representaciones es en forma de niña, con los brazos extendidos hacia arriba sujetando un ganso, que hace alusión a la constelación del Cisne. Sin embargo, la representación más habitual es con cuerpo, piernas y brazos extendidos, sobre un fondo estrellado. Estos representan los cuatro puntos cardinales o los cuatro pilares del cielo. De hecho, uno de los mitos más importantes de Nut cuenta como el cielo fue creado a partir del propio cuerpo de la diosa. Entre su iconografía también se encuentra la imagen de Nut cerca de Mesjetiu (la Osa Mayor), la cual representa la pierna que perdió Seth (dios de las fuerzas incontrolables de la naturaleza e hijo de Nut), que es custodiada por los dioses en el firmamento.
- El mito de origen del imperio Inca cuenta que Inti, el Sol mismo, envió a dos de sus hijos, Manco Capac y Mama Ocllo, al mundo terrenal. Su principal cometido era el de llevar el orden y la civilización a la humanidad. Ambos emergieron entonces del lago Titicaca, y emprendieron su camino hacia el norte. Después de caminar lo que se conoce como el *Primer Camino Inca*, encontraron el lugar donde fundarían Cusco. Es entonces cuando Manco Capac, hijo del propio Sol, se convirtió en el primer líder del imperio Inca⁶.
- La astronomía navajo o *diné*⁷ es radicalmente distinta a la académica occidental, puesto que se basa en una cosmovisión en la que el Universo se considera holístico y ordenado, con una red que interrelaciona todos los elementos, que existen dentro de un *todo*, y están en constante flujo. El componente espiritual es esencial en la astronomía *diné*, y eventos como los eclipses son momentos sagrados. A diferencia de lo que hacemos normalmente en occidente durante un eclipse, los sabios navajos instan a su comunidad a entrar en el hogar, ya que el eclipse es un momento en el que Sol y Luna interaccionan. Es un momento de contemplación y silencio, e incluso se relatan enseñanzas tradicionales de cómo se originaron el Sol y la Luna, que se formaron a partir de trozos perfectos de un mineral de turquesa y una concha blanca, respectivamente.
- El Jyotisha⁸ (literalmente ciencia de la luz) es un concepto que surgió para unir la religión o mundo espiritual con la astronomía, y una de las

5 Fuente: www.arsgravis.com.

6 Fuente: <https://americanindian.si.edu>.

7 Fuente: www.exploratorium.edu.

8 Fuente: www.wisdomlib.org.

seis vedangas fundamentales del hinduismo, diseñadas para la correcta interpretación, recitación, y aplicación ritual de los textos védicos. El desarrollo de la astronomía o astrología (indistinguibles en este contexto) del Jyotisha era bastante matemático y abstracto, con influencia de otras culturas como la Grecia antigua. La astronomía y matemática india tienen una fuerte herencia del Jyotisha, con una relación muy estrecha con lo espiritual.

- La astronomía aborigen australiana⁹ es considerada una de las más antiguas, si no la primera, con más de 65000 años, que además sigue existiendo a día de hoy. La astronomía ha tenido una gran influencia en la navegación, los calendarios, la predicción del tiempo, así como ser fundamental en el mundo espiritual. En la astronomía indígena, las constelaciones están formadas por varias estrellas o por estrellas (o planetas) individuales, que representan figuras ancestrales o animales. Por ejemplo, la estrella que conocemos como Arturo, es denominada Marpeankurrk, una figura que representa la llegada de la estación de las hormigas de la madera. Existe otro tipo de constelaciones completamente diferentes a las nuestras, lo que serían las constelaciones oscuras. Son las regiones oscuras de la Vía Láctea, que a día de hoy sabemos que es acumulación de gas y polvo. Entre ellas está *Gugurmin in Wiradjuri* (el emú oscuro), que se asocia con la mejor época para la recolecta de comida.
- China, Korea¹⁰, y Japón son también países con una larga historia astronómica, que consta desde la prehistoria. Sin embargo, muchos de los restos y legado de la astronomía del este asiático han sido destruidos debido a las diferentes guerras e invasiones. En Korea, el cinturón de Orión se conoce como las estrellas de los trillizos o Samtaeseong¹¹, siendo el número tres fuente de buenos augurios. La leyenda de Samtaeseong narra el origen de esta constelación. Hace mucho tiempo, en el Lago del Dragón Negro (en los humedales de Heung Yongdam), vivían unos trillizos desde la muerte de su padre. Sus caminos se separaron durante diez años, en los que buscaron mentorazgo, y volvieron con un gran desarrollo de sus habilidades. Poco después, sintieron la violenta batalla entre dos dragones negros (macho y hembra), que generó fuertes vientos y lluvias sin precedentes. El macho siguió a la hembra, que ascendió hasta el límite del cielo y engulló el Sol. Es entonces cuando los trillizos se enfrentaron a los dragones negros, consiguiendo recuperar el Sol, y devolviendo así la luz al mundo. Sin embargo, uno de los dragones consiguió escapar. Es por ello que los trillizos ascendieron al cielo, para custodiar el Sol de cualquier ataque, formando así Samtaeseong.

La influencia de la astronomía ha sido tan grande que en muchas civilizaciones, especialmente la Inca y China, ha existido una relación muy estrecha

⁹ Fuentes: www.aboriginalastronomy.com.au y www.space.gov.au.

¹⁰ Fuente: www.kasolym.org.

¹¹ Fuente: <https://folkency.nfm.go.kr>.

entre el Cielo¹² y la Tierra, la cual ha sido utilizada para legitimar el poder y gobierno. Por ejemplo, cuanto mayor fuera su conocimiento y predicción sobre eventos astronómicos, como eclipses o cometas, más grande era su poder terrenal. La línea que separaba lo religioso y lo secular era difusa. Similar a la situación actual, quién poseía la ciencia y tecnología más poderosa tenía también el mayor estatus y poder.

Existen muchas evidencias sobre culturas que diseñaban y construían edificios y templos para alinearlos con el solsticio de invierno y/o verano, y que la luz incidiera de una forma muy particular en ese determinado momento. Esto demostraba un gran conocimiento astronómico, que como hemos visto, era sinónimo de poder. Es el caso de culturas como la egipcia, polinesia, inca, nativa norteamericana, o musulmana. En la cultura polinesia es especialmente intrigante, puesto que existen pocas evidencias escritas que expliquen por qué tenían un número tan elevado de monumentos religiosos y de navegación con orientaciones relacionadas con eventos astronómicos muy particulares.

La astronomía se ha realizado de forma muy diferente en las distintas culturas. Por ejemplo, muchas de ellas lo han hecho con el ojo, sin ningún tipo de instrumentación sofisticada. El antiguo Egipto se caracterizaba por una astronomía observacional muy sofisticada, con una base matemática casi inexistente. Por otro lado, las culturas musulmana, india, y china desarrollaron técnicas astronómicas verdaderamente complejas. Muchos de los instrumentos y las matemáticas que utilizamos hoy en día derivan de estas civilizaciones. De hecho, la mayoría de los nombres de astros que tenemos a día de hoy son herencia de la cultura árabe.

El progreso de la astronomía occidental, más observacional, matemática, racional, y “objetiva”, ha ido ocultando otras visiones y versiones de la astronomía. Toda la astronomía que no ha tenido un enfoque idéntico a la occidental ha sido completamente borrada y marginada, ridiculizada incluso. Sin embargo, son simplemente formas diferentes de relacionarse con el espacio. Mientras que en las culturas que he mencionado (y las que no) utilizan/utilizaban el cielo en su día a día, les acompañaba en las cosechas y viajes, o en los momentos más importantes de su vida, la astronomía occidental se relaciona con el espacio de una manera más distante, poniendo entre el investigador y su objeto de estudio una capa de ecuaciones y conocimientos que lo alejan del cosmos. Cabe plantearnos si esto es lo ideal o si, quizás, podemos aprender de otras culturas para dar un toque más humano e inclusivo a nuestro trabajo. Con este prólogo, espero dar pie a caminar en esa dirección.

Aprovecho esta mención a nuestro trabajo y la reflexión sobre la concepción que tenemos de hacer ciencia, para seguir desgranando los entresijos y mecanismos del mundo académico. Particularmente introducir los conceptos del *conocimiento situado*, la *parcialidad*, y la *intersubjetividad u objetividad dinámica* (ver los trabajos de Collins, 1986; Keller, 1991; Haraway, 1995), que derivan del marco teórico de las epistemologías feministas (Harding, 1996; García Dauder and Ruiz Trejo, 2021). Estas últimas no pueden desligarse de las aportaciones

¹² En este caso, *Cielo* con mayúscula hace referencia al concepto del más allá, lo que sería *heaven* en inglés.

de las perspectivas negras y decoloniales (Collins, 1986; Miñoso, 2017), que han dado lugar a otras miradas y aproximaciones a la ciencia.

Estas perspectivas pretenden desmontar el marco occidental que instruye a sus científicos ajenos a toda emoción y con una completa “objetividad”. Esto ha marginalizado otras perspectivas, como las provenientes de comunidades indígenas, categorizadas como ausentes de razón científica (Miñoso, 2017). Básicamente, se dualiza y separan en extremos opuestos el conocimiento científico y las emociones, quedando estas últimas completamente fuera del ideal de la academia.

Sobra decir que las emociones nos atraviesan en cada momento de nuestras vidas, y que esto tendrá un impacto en las investigaciones que realizamos. Estas emociones a su vez están atravesadas por el género, la clase social, la raza, la edad, o la orientación sexual, entre otros. Cada vez existen más estudios que intentan evaluar el impacto de las emociones en los resultados académicos. No obstante, son escasos aquellos que consideran el impacto emocional que tiene una investigación en aquella persona que la realiza. Eran Hubbard, Backett-Milburn, and Kemmer (2001) quienes hacían esta reflexión: se han destinado ingentes esfuerzos y aproximaciones para evitar que nuestros sentimientos contaminen los datos, pero ¿podemos asegurar que nuestros datos no afecten nuestros sentimientos? Es decir, no solo nuestra subjetividad puede afectar a la investigación, sino que también pueden afectarnos los procesos a quienes nos involucramos en su desarrollo.

Resulta extremadamente complicado sostener la idea de que la investigación es objetiva puesto que está indudablemente atravesada por los contextos socio-políticos en multitud de sentidos. Por ejemplo, el aumento de la relevancia y reconocimiento de las mujeres en la academia y de estudios sobre temáticas de género ha ido en paralelo con las luchas y progreso en materia de derecho, de la política. Sin embargo, existe una fuerte resistencia a combinar los términos *ciencia* y *política* en una misma conversación.

La mayoría de acciones institucionales en las últimas décadas han sido enfocadas en la paridad de género. De hecho, se celebra el avance hacia la paridad, medida como el porcentaje de mujeres frente al de hombres en un cierto ámbito. Este parámetro es escaso, cuanto menos, si pretende reflejar un verdadero avance en la desaparición de los sesgos y violencias estructurales que existen, por ejemplo, en la academia. Basta con hacer uso de los datos y estudios que apuntan a que aquellos campos con mayoría de mujeres son menos citados y respetados que aquellos dominados por hombres. Existe, de hecho, lo que se conoce como la *paradoja de la paridad*: el esfuerzo destinado hacia la paridad no resulta en una equidad real. Esto es verdaderamente preocupante, ya que la paridad sin la correspondiente equidad acaba devaluando el trabajo que pretende recompensar (Sugimoto and Larivière, 2023).

No sorprende que esto no es exclusivo de las mujeres. Existe un privilegio de elección en la producción de conocimiento científico, donde la investigación sobre un tema en particular está influenciada por la raza y el género de quien la realiza (Kozłowski et al., 2022). Existen también evidencias de desigualdades estructurales en colaboraciones internacionales (Miao et al., 2024). Aquellas

personas investigadoras que pertenecen a países científicamente “*más avanzados*” tienden a ocupar roles dominantes, mientras que aquellas de países “*menos desarrollados*” son relegadas a roles de apoyo. Además, los países con menor capacidad científica son más propensos a participar en colaboraciones internacionales que se desvían de su ciencia local. Todos estos factores tienden a mantener el sistema jerárquico y perjudicar adicionalmente a las personas con menores recursos.

El envío de propuestas y artículos científicos a revistas está ampliamente dominado por hombres (Teele and Thelen, 2017). Esta brecha aumenta la dificultad de éxito científico de las mujeres. No solo esto, además, los trabajos liderados por mujeres son menos citados que los liderados por hombres (Dion, Sumner, and Mitchell, 2018; Mitchell, Lange, and Brus, 2013). Existen varias teorías que intentan explicar esta brecha, como la *aversión al riesgo* (risk aversion; Djupe, Smith, and Sokhey, 2019), la *brecha de percepción* (perception gap; Brown et al., 2020), y el sesgo de género de un tema de investigación (Key and Sumner, 2019). Este último viene a decir que aquellos temas de investigación que son tratados de forma desproporcionada por mujeres se pueden considerar de nicho y por tanto inadecuados para ciertas revistas de alto impacto. Lo que es innegable, es la existencia de sesgos en las revistas, las cuales tienden a seleccionar menos aquellos temas relacionados con la mujer.

No solo esto, sino que existe una evidente correlación entre artículos liderados por mujeres y la probabilidad de incluir el género y/o el sexo como variable del estudio. La medicina es un claro ejemplo de este fenómeno. Nielsen et al. (2017) estudiaron más de 1.5 millones de artículos del campo, y encontraron una fuerte correlación entre la autoría de mujeres y los estudios con una perspectiva consciente de los factores del género y sexo. Esto no hace otra cosa que demostrar los claros beneficios de involucrar a las mujeres en los estudios de investigación médica, así como evidenciar una brecha, que no es exclusiva del campo de la medicina.

El reparto de la financiación es también un gran fuente de desigualdades en la academia. Larregue and Nielsen (2023) estudiaron las intersecciones entre la disciplina, la temática, y la metodología de aplicantes a financiación con su género. Los resultados muestran como las mujeres reciben un 20% menos de financiación. Observaron que tiende a financiarse más los estudios cuantitativos, los cuales están principalmente dominados por hombres.

Por otro lado, Wong and Rubin (2024) exploran la devaluación de ciertos campos o temas científicos, especialmente aquellos dominados por mujeres y otros grupos minorizados. Esto es resultado de múltiples factores, como las dinámicas en las colaboraciones, el hecho de que gente con menor prestigio recibe un menor crédito por su trabajo, o que las personas tienden a favorecer a otras de su mismo grupo de identidad social. Esto es algo que no nos es ajeno, pues está estrechamente relacionado con cómo entendemos la historia de la ciencia y por cómo intentamos promover la investigación científica diversa.

Me resulta imposible no centrarme también en uno de los temas más actuales del momento, la inteligencia artificial (IA)¹³. No pretendo cubrir todas las cuestiones éticas del uso de la IA, ni si quiera todas aquellas relacionadas con la academia, que, sin duda, son muchas. Pero sí creo que la reflexión de cuánto, cómo, y con qué objetivo utilizamos la IA es imprescindible para poder hacerlo desde una perspectiva justa, sostenible, y equitativa.

Es especialmente habitual en la ciencia escuchar que el progreso es lo más importante, muchas veces sin ningún tipo de reflexión crítica de qué puede suponer ese progreso y a costa de qué, o de quién puede quedarse fuera o atrás como resultado. Además, estos avances en la ciencia y la tecnología son impuestos a la fuerza a los trabajadores y usuarios. Actualmente, podemos encontrar un *bot* que nos ayude en cualquier página web, y cada vez más productos incluyen de una forma u otra la IA. Por ello, son múltiples los llamamientos que hay para evitar la adopción de la IA en la academia de una forma no crítica. Sin embargo, no debemos caer en el *critical washing*: animar al uso de la IA “estando al corriente de los problemas” (Guest et al., 2025)¹⁴. No es suficiente criticar y reflexionar sobre los problemas éticos asociados al uso de la IA, sino que debemos actuar en consecuencia (Suarez Estrada et al., 2025).

Como decía, las cuestiones éticas de la IA son numerosas, y entre ellas podemos encontrar los sesgos, habituales y recurrentes en los humanos, empezando por mí. Durante años se ha hecho énfasis en ser conscientes de estos con el objetivo de evitarlos, pero ¿Y si estos sesgos los estuviéramos metiendo en una caja negra, a la que, por ejemplo, llamaremos IA? ¿Qué pasaría entonces? ¿Seríamos capaces de hacer consciente a la IA o ser conscientes por nuestra parte de estos sesgos?

No son pocos los estudios que han decidido explorar qué ocurre en estos casos. Kotek, Dockum, and Sun (2023) analizaron cuatro modelos extensos de lenguaje (LLMs), demostrando que estos expresaban asunciones sesgadas sobre la ocupación de hombres y mujeres. De hecho, estos modelos son de tres a seis veces más propensos a escoger una ocupación estereotípica en base al género de una persona. Además, esta selección está más alineada con la percepción de la población que con los datos reales, y llegan a amplificar estos sesgos más allá de la realidad. Los LLMs tienden a ignorar las ambigüedades en las estructuras de las oraciones el 95 % de las ocasiones, mientras que si se les pide explícitamente, entonces reconocen dicha ambigüedad. No solo esto, sino que incluso justifican sus preferencias incorrectas ocultando los verdaderos motivos, los sesgos. Lo que ocurre es, simple y llanamente, que la IA tiende a reproducir los sesgos y prejuicios con los que son entrenados y los que poseemos las personas usuarias, amplificándolos en muchas ocasiones.

Estos sesgos reproducidos y no criticados ni percibidos por la IA son preocupantes. Lo son especialmente si tenemos en cuenta que muchas decisiones

13 Existen diferentes tipos de IA, y en general se cuestiona el uso de la IA generativa, como ChatGPT o Gemini, que utilizan grandes conjuntos de datos para crear contenido “nuevo”. Aquí hablaré de la IA en genérico, aunque me centre esencialmente en las IA generativas.

14 Os animo a entrar en detalles y leer este artículo, puesto que hace reflexiones mucho más profundas respecto a estos temas, sobra decir que con un criterio y rigor mucho mayores que los míos.

como contratación, aceptación de propuestas, financiación, supervisiones e investigaciones, entre otras, están empezando a integrar la IA como parte del proceso. An et al. (2025) estudian los posibles sesgos raciales y de género de las IA más populares (ChatGPT, Gemini, Claude, y Llama) en los procesos de selección de personas candidatas a entrar en un puesto de trabajo. Los modelos de lenguaje evaluaban mejor a las candidatas mujeres (tanto blancas como negras) con similar experiencia laboral, formación, y habilidades, mientras que daban calificaciones más bajas a los hombres negros con competencias similares. Tanto este como muchos otros estudios advierten de la peligrosidad de los sesgos, puesto que estos modelos de lenguaje muchas veces funcionan como una caja negra, y podemos desconocer los motivos que están influyendo en la toma de la decisión. Por esto mismo, instan a definir estrategias claras sobre estos sesgos, para así poder caracterizarlos y tenerlos en cuenta durante esta toma de decisiones.

Debemos tener en cuenta también cómo se desarrollan estos modelos de lenguaje o software de IA, y por parte de quién. Por un lado, es muy habitual escuchar el término de IA abierta (del término *open* en inglés), utilizado erróneamente muchas veces, puesto que deriva del concepto de ciencia abierta u *open-source*. Desde luego, las empresas que desarrollan estos modelos de lenguaje proclaman que son beneficiosas para la innovación y la democracia, mientras que la otra parte del debate se centra en los riesgos de seguridad asociados. Además, el que estos software sean gratuitos u *open-source* no elimina la concentración de poder de la IA, como bien apuntan Widder, Whittaker, and West (2024).

Si bien es cierto que podríamos seguir desgranando todos los dilemas éticos y problemáticas asociados con la inteligencia artificial, creo que han quedado claras algunas de las mayores preocupaciones que existen en el mundo de la academia respecto a su uso sin una perspectiva crítica. De esta forma, nace el concepto de *alfabetización crítica de la IA* o CAIL¹⁵, por sus siglas en inglés. Se trata de un marco que abarca los conocimientos necesarios para poder tener esta perspectiva crítica hacia la IA, que nos permiten distinguir entre exageraciones sesgadas y sin fundamento de la verdad empírica del conocimiento científico. Se nos ha hecho creer¹⁶ que la IA es inevitable, pero también sabemos que esta es incapaz de producir trabajos académicos reales de calidad, a pesar de todas las afirmaciones que la industria quiere imponer. Es nuestra responsabilidad como parte de la academia y las universidades revertir este pensamiento acrítico, puesto que lleva a un claro deterioro de la investigación, que llega incluso a escaparse de nuestro control y conocimiento. Después de todo, nuestro papel es fomentar un pensamiento crítico, no seguir las tendencias de la industria sin cuestionarlas.

Es muy probable que al leer esto haya quién se pregunte por qué una persona debe hablar o reflexionar acerca de estos temas en su tesis doctoral en astrofísica.

15 Os animo a echar un vistazo a esta web, con muchísimas reflexiones al respecto y la literatura asociada: <https://olivia.science/ai>.

16 Esto es algo recurrente con la tecnología, especialmente en las últimas décadas, que se nos ha ido imponiendo paulatinamente; mientras que el estudio y cuestionamiento de sus efectos y usos está llegando después.

El debate sobre la relación que deben (o que no deben) tener la ciencia y la política tiene una larga historia. Por un lado, se argumenta que las instituciones y la propia ciencia deben mantenerse al margen de la política, o al menos intentar que esta sea neutra y objetiva, mientras que el otro lado argumenta que esta separación radical que se propone es innecesaria e incluso imposible. De hecho, este último grupo tiende a pensar que la presencia de la política en la ciencia, y viceversa, es inevitable. Por ello, en este prólogo he querido situar cual es mi contexto particular, desde el cual escribo, investigo, y vivo, así cómo defiende Marilyn Strathern (1992, pág. 10)¹⁷:

“Importa qué ideas usamos para pensar otras ideas.”

Lo que me lleva de nuevo a hablar de conocimiento situado, y como no es riguroso sostener que la ciencia es objetiva y debe (o puede) estar aislada, más bien al contrario, está completamente atravesada por el contexto socio-político. Instituciones como el consejo científico de Reino Unido definen la ciencia como “la búsqueda y aplicación del conocimiento y el saber del mundo social y natural siguiendo una metodología sistemática basada en la evidencia”, y la Asociación Americana para el Avance de la Ciencia (AAAS en inglés, que además publica la revista *Science*), define la responsabilidad científica como “el deber de dirigir y aplicar la ciencia con integridad, por el interés de la humanidad, con espíritu de responsabilidad hacia el medio ambiente y el respeto a los derechos humanos”. De esta forma, queda clara la interrelación entre ciencia y política. Y ahora es más importante que nunca, cuando en los últimos años, las propias instituciones políticas han puesto en duda el conocimiento científico, o incluso han llevado una batalla en contra de la propia ciencia¹⁸.

Creo firmemente que la ciencia no es ajena a la política, y que decir lo contrario es evadir cualquier responsabilidad que podamos tener, tanto individual como colectiva, de actuar en consecuencia a nuestro entorno. Las personas que estamos en la academia estamos más que familiarizadas con la relación institucional de nuestro centro con ayuntamientos, ministerios, y gobiernos. O cómo ciertas temáticas reciben más financiación que otras, y ¿qué es esto sino política? Pero es más: ¿por qué tanto miedo al término “política”? Sin duda tiene una connotación negativa para una gran parte de la comunidad. ¿Por qué hacer lo que está en nuestra mano por intentar apoyar causas sociales que creemos justas es algo negativo? ¿Por qué ir en contra de aquellas personas que creen en estas causas y actúan en consecuencia? No debemos olvidar que somos personas, no solo investigamos. Vivimos en un mundo que nos atraviesa de muchas formas, y negar esto es negar nuestra humanidad.

17 Esta cita, traducida, proviene del libro de Haraway (2019), aunque originalmente es de Strathern (1992).

18 El trabajo de Fuentes (2024) ha sido una gran fuente de inspiración en esta última parte.

AGRADECIMIENTOS

Quiero dedicar unas palabras para agradecer a quienes me han ayudado y apoyado en esta etapa de mi vida, que empezó en noviembre de 2021 y durante la cual he trabajado en esta tesis, pero también hecho muchas más cosas.

A mi madre y mi padre, que son las personas que más tiempo llevan apoyándome en mi vida, desde que nací para ser exactos. Quiero agradecer el privilegio que he tenido de criarme en una familia biparental, y con trabajos dignos que nos ha permitido a mi y a mis dos hermanos, David y Jorge, poder tener una buena infancia. En la que reímos, disfrutamos, y sufrimos un poquito supongo, porque es difícil que esto no pase en algún momento. Tanto mis hermanos como mi padre y mi madre me han apoyado en todas las épocas de la vida y facetas educativas, desde el colegio, pasando por el instituto, la universidad, y ahora mi vida laboral. Siempre he tenido un hogar al que regresar y donde se me ha recibido con los brazos abiertos, un privilegio que no todo el mundo tiene y que me ha permitido estar aquí hoy. Así que gracias mamá, gracias papa, gracias Jorge, y gracias David. Os quiero mucho.

También gracias al resto de mi familia. Gracias Txetxu y Ana, Ander y June; Félix y Paula; Tere, Omar, Nora, y Mariam; Pili, Manu, Silvia, Marta, y Marina. Gracias a mis abuelas Pilar y Aurora, gracias a mi abuelo, José Luis. Gracias por apoyarme, acogerme e interesaros por mi.

A mis directores, Fran y Pedro, agradeceré todo el trabajo que hemos hecho estos años. Habiendo dirigido mi tesis, han tenido un gran impacto en mi formación como investigador, pero también han tenido que dedicar mucho tiempo a leer borradores de artículos y tesis, hecho mucha burocracia de la universidad o para los viajes, me han ayudado con los contactos y a tomar las decisiones que han hecho falta para sacar adelante esta tesis. Así que muchas gracias por todo el apoyo.

Muchas gracias a la gente del grupo, que me han ayudado y han resuelto tantas dudas. Especial mención a Dani, Luis, Alberto y Marina, con quienes he discutido incesablemente sobre estrellas y exoplanetas, pero sobre todo códigos, viajes, y burocracia. Y Muchas gracias a Pedro F. y Giuseppe. La ayuda durante que me habéis ofrecido durante esta segunda parte de mi tesis ha sido fundamental. Gracias por tanto tiempo y paciencia. Agradecer todo el trabajo y apoyo, incluso me atrevería a decir mentoría, de David Y Rocío. También al resto de integrantes de los cafés: María, Fran (x2), Javi, Carmen, Mabel, Miguelan, ...

Y gracias a tanta gente del IAA con la que he compartido comidas, congresos, seminarios, juergas, charlas de los quesos, y tantas otras actividades. Gracias Sergio, Ana, Mendi, Marianna, Oier, Luis, Miguel, Belén, Marta, Ixaka, Julio, Teresa, Clara, Valentín, Borja, Florín, Mendi, Celia, Julio, María, Pablo, Sara, Pol, ... vaya grupillo más chulo.

Gracias Belu. No puedo escribir, y menos en pocas palabras, el apoyo que me has proporcionado durante tantos años. En los momentos más difíciles siempre me has ayudado, y siempre he sabido que podía contar con ello. Gracias por los ánimos y apoyo incondicional en cada una de las fases y etapas por las que he pasado. No solo en lo educacional y profesional, sino en todos los ámbitos, ni yo (mi yo actual) ni esta tesis hubieran sido posibles sin ti. Gracias a ti, y a toda tu familia por tanto apoyo y cariño.

David y Nico... nenes, ¿qué deciros? Son tantos años que cuesta. Que por mucho que nos separe media península, ahí estamos. Pues eso, hemos compartido muchísimas cosas; horas y horas al *SpeedRunners*, deportes de todo tipo, pipas y paseos, viajesitos por muchos lados, parques de atracciones, esquí y snow, bolos, y bueno, lo que nos queda. . . Que nos hemos visto crecer, nos hemos visto en las mejores y en las peores, y aun así, aquí estamos, riendo, enfadándonos, debatiendo, y compartiendo cachitos de nuestra vida. Que esto poco se valora muchas veces, así que un millón de gracias. Porque nunca estaremos justamente aquí, nunca tocaremos exactamente dos veces en un mismo sitio, nunca seremos objetivos (porque tal cosa no existe), pero siempre estaremos ahí. Os quiero.

Cómo no dar las gracias a Quique y Antonio. El azar nos unió de forma peculiar, como supongo que siempre pasa, y lo agradezco enormemente. Lo hemos pasado de bien. . . hemos reído a carcajadas, y seguiremos haciéndolo. Paseamos, comemos, roleamos, compartimos todo lo que se puede compartir, pero sobre todo nos cuidamos. Gracias por todos esos momentos y por todo el apoyo y cariño, os quiero mucho, mis niñas.

Agradecer también a Cantabria por, a pesar de fabricar pocas personas, hacer una tan perfecta como Elvira. Y gracias a ti por la inmensa paciencia, especialmente los últimos meses, donde el cariño ha sido fundamental para soportarme, frente a tantos nervios e incertidumbre como esta etapa nos brinda. Gracias por la comprensión, las risas, las lecturas, los bocatas, las escobas, y sobre todo sobre todo, gracias por las tortillas. Y qué tortillas... te haces de querer. Mucho. Mucho mucho. Y cómo no, darte las gracias por toda la ayuda para construir el prólogo, que no sería lo que es sin toda la info que me has ido pasando, y las reflexiones que me has planetado.

A quien ha sido mi compañera y referente del activismo durante tantos años, gracias. Gracias Marta, por enseñarme tanto, escucharme tanto, y contarme tanto. Gracias por los paseos, por plantar arbolitos, por las actividades de voluntariado, por enseñarme Países Bajos, gracias por seguir en mi vida y sacar huequitos para vernos y compartir. Porque me encanta compartir contigo mi vida, y espero que así siga siendo. Te quiero.

En los últimos meses estaba yo descansando en las mesas de atrás, mientras alguien cantaba en el karaoke, imagino. Y un poco de repente, apareces entre la multitud, me coges de la mano, y me invitas a bailar *rata de dos patas*. Seguramente no seas consciente de lo contento que esto me hizo. Ana, gracias por la inmensa comprensión. Gracias por entenderme tan bien, por hacer tan fácil hablar y abrirse, y gracias por hacerlo tú también. Gracias por dejar tus trazos indefinidamente en mi piel, y por bailar incesantes horas. Espero haber

podido apoyarte y hacerte sentir comprendide un poquito, como has hecho tú, especialmente en estas etapas tan turbulentas que hemos compartido. Espero que sigamos compartiendo nuestra vida muchos más años. Y es que, te quiero. Mucho.

Gracias a Ixaka y Livia por compartir piso conmigo. Por limpiar tan espectacularmente bien el baño, la cocina, y el salón. Gracias Ixaka por estos años de convivencia que siempre me han hecho sentir Granada como un hogar. Gracias Livia por decidirte a compartir estos meses en casa, donde hemos visto como te convertías en Dr. Daniel, por compartir conmigo *Heated Rivalry*, y por todas las discusiones y debates tan enriquecedores, muchos de ellos incluidos en el prólogo. Gracias por los *catanes*, las pelis, las pizzas, los huevos *kidner* y todas las risas y cariño del hogar. Os quiero tanto. . .

Y qué decir sobre la pequeña familia que he tenido en Granada... aunque nos haya unido el trabajo, se ha convertido en mucho más. Si algo bueno me ha traído la tesis y la astrofísica son ustedes.

Marta, cuánto he aprendido gracias a ti. Eternas conversaciones con café, cerveza, o vino. Siempre hemos encontrado momentos para hablar sobre activismo, para compartir experiencias y pensamientos, con los que he aprendido tanto. Anda que no hemos viajado, bailado, y reído. Gracias por estar ahí, por la comprensión y cariño, t'estimo molt.

Mendi, Mendi, Mendi, ... Compi de master, compi de doctorado, y compi de vida. Muchas horas que hemos pasado en la montaña y en el roco, y muchas más que espero que pasen. Siento que el cariño que te tengo es muy especial, y siempre me encanta volver a verte después de unos días o semanas sin hacerlo. Gracias por compartir tanto conmigo, por poner siempre la oreja para escucharme y por aconsejarme y apoyarme. Te quiero mucho.

Muchas gracias Belén, por apoyarme y dejarme que te apoye, por confiar en mí y hacerme sentir tan agusto. De verdad que espero que hayas sentido el cariño y comprensión durante estos meses ¿años? complicados, al menos una parte de lo que tú me has hecho sentir. Te haces querer mucho, y me haces reír como poca gente.

Mi compi de escalada que ahora está a unas cuantas horas de diferencia, Marianna. Gracias por las risas, la compañía, y las aventuras. Hemos compartido mucho monte y mucha roca, pero sobre todo mucho amor. Estoy deseando verte este año en Italia, y compartir momentos inolvidables, como el verano pasado en I Dolomiti. Gracias por todo el apoyo y cariño.

Pablo Antonio, aka Pol. ¿O María? Es que cuando les miro, veo la cara de la otra, no puedo evitarlo. Mi amigo más soñador e imaginativo, que vivís la vida de una forma ejemplar. Sos más argentino que el mate, y aunque intentás hacerte madrileño, por suerte, seguís siendo Pol. Que se te echá de menos por Granada, pero se agradece que cuando venís por acá, nos tomemos algo juntas. Te quiero mucho, Pol. Y. . . ¡Viva Perón, carajo!

Ixaka. . . Nire laguna, hainbeste urteetan pisukide, momentu ahaztezinak, amaierara iristen bada ere espero dut beti gurekin egongo direnak. Nola barre egin dugu e. . . Askotan salbatu nauzu, janaria lanera ekartzen didazu ahazten zaidanean, galletak nirekin partekatzen dituzu nahi dudanean, edo pintxo

bat edo tostada bat jan duzu nik gehien behar izan dudanean. Eskerrik asko nirekin hainbeste une partekatzeagatik, eta espero dut denbora luzez horretan jarraitzea.

Gracias Carmen, por todas las horas dedicadas a jugar y hablar del Hades (uno y dos, obvio), por los paseos, las risas, y las conversaciones tan chulas. Gracias por el intercambio de libros, por ver Hanna Montana conmigo, maquillarme, por los viajesitos en coche a la playa y la montaña, y por aguantarme tanto momentos, que estoy seguro de que no es fácil de hacer sin ese sentido del humor que tienes. Se te quiere mogollón, y estoy deseando que me vuelvas a enseñar mi nuevo hogar: *Cabracity*.

Paloma! Que has vuelto después de un abandono terrible. . . que me quitas a mi Ixaka. . . te quiero. No por esto, obvio, pero por ser tan graciosa y cariñosa, por aceptarme como soy y compartir tanto conmigo, por cuidarme, apoyarme, y verme como soy. Gracias, gracias, y gracias. Espero poder seguir compartiendo muchos momentos contigo.

Cómo no mencionar a Manu y a Ana, que me han acogido tantas veces y tan bien, con quienes he podido pasar tan buenos momentos, en su mayoría haciendo yoga o escalando, pero también muchos más. Hemos tenido unas cuantas conversaciones sobre dinosaurios, y ahora tengo una funda perfecta para mis libros. Si el *TokyoWall* es una familia es gracias a Ana y Manu, sin duda. Además, nos hemos echado unas buenas carreras por el monte, incluso visitado Toledo. Así que muchas gracias por esto, y por lo que queda aún.

Especial mención a mi artista favorite anacran, a quién he escuchado en bucle incesantes horas mientras escribía los artículos y la tesis. Aunque todos tus temas son de diez, nada *hittea* tanto como "Under the roots".

Miguel, Marie Lou. . . ¿Qué decir de esta maravillosa gente? Gracias por acogerme y quererme como lo habéis hecho. He disfrutado como un niño de todas nuestras carreras, escapadas, escaladas, cenas, paseos, conversaciones, acampadas, y un sin fin de actividades. Gracias por apoyarme, escucharme, y cuidarme. No sé cómo expresar lo mucho que significáis, lo que significó para mi el viajar Tenerife, y lo feliz que me hace compartir tiempo y vida con ustedes. Así que lo dejaré así: os quiero. El cuánto os quiero, seguiré intentando expresarlo de muchas otras maneras.

Y cómo no agradecer a tanta gente que ha estado ahí, y que espero que sigan estando. Gracias por el apoyo, los momentos, el amor, cariño, y cuidado que me habéis dado durante tanto tiempo. Gracias Andrea, Andrea, Lucía, Julio, DJ gnomo, Julia, Guille, Gloria, Isa, Rubio, Emma, Ara, Mar, Marc, Sara, Yure, Francesca, Jesús, Gabri, Elena, Marina, Nathali, . . .

RESUMEN

Esta tesis tiene como objetivo mejorar la precisión de las velocidades radiales (RVs del inglés) obtenidas en la espectroscopía de alta resolución en el infrarrojo cercano, para la búsqueda de planetas tipo Tierra orbitando estrellas ultrafrías. El interés de esta línea de investigación es doble: por un lado, realizar observaciones con espectrógrafos de alta resolución en el infrarrojo, y por el otro, la búsqueda de planetas rocosos o tipo Tierra en estrellas de muy baja masa. Comencemos con el segundo.

Las estrellas enanas tipo M, hasta donde sabemos, pueden formar sistemas multiplanetarios con miembros similares a la Tierra de forma habitual. Debido a las bajas temperaturas de las enanas M, las órbitas donde estos planetas pueden ser potencialmente habitables están más próximas a ellas, facilitando así su detección y caracterización con métodos como los tránsitos o las RVs. Sin embargo, son objetos muy débiles, con actividad magnética, y que pueden rotar rápidamente, lo que complica la detección. Eso sí, las enanas M más frías emiten el máximo de su luz en el infrarrojo cercano.

La espectroscopía de alta resolución nos permite utilizar la técnica de RVs. Esta es complementaria a los tránsitos y ofrece información acerca de la masa del planeta (mientras que los tránsitos de su radio). CARMENES es un consorcio y un instrumento en el telescopio de 3.5 m del observatorio de Calar Alto, en Almería. Tiene dos espectrógrafos de alta resolución (80000–94600), uno en el visible (VIS: 520–960 nm) y otro en el infrarrojo (NIR: 960–1710 nm). Durante la operación de CARMENES, que empezó en 2016, se observaron ciertos problemas e inestabilidades en el sistema de enfriamiento. Por ello, se diseñaron una serie de mejoras, enmarcadas en el proyecto CARMENES-PLUS para aumentar la estabilidad térmica del espectrógrafo. Las mejoras incluían el control de la presión, así como el flujo de refrigerante de forma continua en vez de discreta, entre otras.

Las mejoras de CARMENES-PLUS han supuesto un antes y un después en el desempeño del espectrógrafo infrarrojo. La variabilidad de la temperatura se ha reducido drásticamente, tanto en el corto plazo (horas), como en el largo plazo (incluso años). Esto ha resultado en una estabilidad de las calibraciones nocturnas por debajo de 1 m s^{-1} . Con el sistema completamente mejorado, analizamos el impacto en las variaciones de las RVs dentro de cada noche, de una noche a otra, y de las observaciones de estrellas en cielo. Todos estos valores demuestran una gran mejora de la precisión intrínseca del instrumento, disminuyendo la variabilidad de las series temporales, así como las incertidumbres asociadas a la parte instrumental.

Una vez mejorado el instrumento, el objetivo es conseguir optimizar la extracción de las RVs. Las estrellas más frías tienden a tener una elevada actividad magnética, siendo frecuentemente rotadoras rápidas. Esto afecta al ensanchamiento de las líneas espectrales, complicando el cálculo de las RVs.

Por lo tanto, tenerlo en cuenta puede ayudarnos a mejorar la precisión de nuestras medidas, o incluso permitirnos descartar ciertas estrellas candidatas en campañas observacionales, ya que puede llegar a impedir la detección de posibles compañeros planetarios.

Por ello, comenzamos el desarrollo de una metodología para obtener la velocidad de rotación proyectada ($v \sin i$) de las estrellas. La mayoría de los códigos disponibles hacen un tratamiento del oscurecimiento hacia el limbo muy básico, o incluso lo ignoran. Este efecto (que implica la reducción del brillo en los bordes de la estrella) es especialmente significativo para los objetos más fríos, como los que observa CARMENES, y no considerarlo adecuadamente implica subestimar el valor de $v \sin i$.

El método que hemos desarrollado depende de dos espectros: el espectro objetivo, de la cual queremos conocer su velocidad rotación proyectada, y un espectro plantilla correspondiente con una estrella lentamente rotante con escaso o despreciable ensanchamiento de las líneas por rotación. El espectro plantilla es ensanchado artificialmente mediante convolución; la velocidad de rotación proyectada es obtenida del espectro plantilla ensanchado que ofrece el mejor ajuste. Durante el proceso de convolución, se tiene en cuenta adecuadamente el oscurecimiento hacia el limbo, y discutimos qué aproximación ofrece el mejor tratamiento para las estrellas consideradas en este trabajo.

Primero, validamos el método utilizando espectros sintéticos. Los resultados muestran que nuestro método ofrece estimaciones de $v \sin i$ altamente precisas, destacando la ventaja de tratar en detalle el oscurecimiento hacia el limbo. En particular, consideramos la dependencia en temperatura y longitud de onda de este efecto. Posteriormente, implementamos el método en `serval` y lo aplicamos a la muestra estelar completa de CARMENES utilizando los espectros del VIS, ofreciendo un catálogo homogéneo de la $v \sin i$ de 392 estrellas enanas M. Asimismo, realizamos una comparación con los valores previamente disponibles en la literatura. La correlación general es muy buena, con valores compatibles dentro de las barras de error. Existen algunas excepciones que discutimos, y para algunos casos ofrecemos un valor actualizado de la rotación, y proporcionamos 36 valores de $v \sin i$ nuevos. Adicionalmente, extendemos el trabajo para CARMENES NIR siguiendo la misma filosofía, y comparamos con las estimaciones de $v \sin i$ obtenidas con el VIS, observando resultados muy similares. Con `serval` obtenemos la velocidad de rotación de 61 estrellas más tardías que M5.0 con espectros de CARMENES NIR. Así, probamos que la estimación de $v \sin i$ para estrellas tipo M pueden obtenerse de manera fiable con observaciones de CARMENES NIR.

El último paso de la tesis es optimizar el cálculo de las RVs utilizando los espectros de CARMENES NIR. CARMENES utiliza `serval` para el cálculo de RVs, con una combinación de los órdenes espectrales disponibles muy particular. Sin embargo, esta selección de órdenes se hizo para todas las estrellas del catálogo de CARMENES de forma conjunta. En nuestro caso, nos interesan las estrellas más frías. Por ello, hemos desarrollado un método iterativo que optimiza los órdenes espectrales utilizados para calcular las RVs con el objetivo de minimizar las incertidumbres de las medidas. Para validar el método, utiliz-

amos tres estrellas frías como referencia, y observamos que hay una reducción de hasta un 14% en los errores medios obtenidos, comparado con la forma predeterminada de *serval*.

Con CARMENES NIR optimizado al máximo para las estrellas ultrafrías, ponemos a prueba los resultados de la tesis con la estrella Teegarden. Es una estrella lentamente rotante, relativamente brillante, poco activa magnéticamente, y con tres planetas ya detectados con CARMENES. Además, tenemos cientos de observaciones disponibles con ambos espectrógrafos, VIS y NIR, de las cuales, más de cien posteriores a las mejoras de CARMENES-PLUS.

Con la serie temporal obtenida, calculamos los periodogramas para el VIS, NIR, y los índices de actividad (CRX, dLW, y H α). Además, utilizamos *kima*, para ajustar las señales Keplerianas e incluimos una componente con procesos Gaussianos (GP) para modelar señales relacionadas con la actividad estelar. Permitimos que el número de planetas varíe libremente entre 0 y 4, obteniendo al menos 50000 muestras efectivas. Para completar el análisis, construimos mapas de detección basado en el método de “inyección y recuperación” (*injection-and-recovery* en inglés). Para construir estos mapas, primero limpiamos la serie temporal de RVs eliminando los modelos planetarios y de actividad estelar que mejor ajusta los datos. Para ambos conjuntos de datos, VIS y VIS+NIR, los mapas resultantes muestran una elevada probabilidad de recuperación para los planetas conocidos del sistema de Teegarden: aproximadamente 100% para los planetas b y c, y por encima del 60% para el planeta d. Estos resultados son consistentes con el análisis de *kima*, mostrando que los datos disponibles de CARMENES son sensibles a las señales con las propiedades esperadas para los tres planetas conocidos.

Posteriormente, usamos dos conjuntos de datos de CARMENES NIR, obtenidos antes y después de las mejoras de CARMENES-PLUS, con el objetivo de evaluar el impacto de las mejoras del instrumento. Modelamos las señales planetarias y estelares en ambos conjuntos de datos; ninguna señal planetaria se detecta con elevada significancia, aunque la actividad estelar es descrita adecuadamente por el modelo de GP. Asimismo, construimos los mapas de detección diferenciales restando los mapas de detección individuales obtenidos antes y después de la mejora. Los datos posteriores a CARMENES-PLUS muestran una mejoría en la probabilidad de detección, particularmente a bajas masas y periodos orbitales cortos. Estos resultados evidencian la mejora del comportamiento del canal NIR de CARMENES en estudios de velocidades radiales en estrellas M tardías después de la mejora de CARMENES-PLUS. Además, discutimos por qué la estrella de Teegarden, a pesar de ser una referente valiosa, no es óptima para demostrar la importancia del canal NIR, debido a su relativamente elevado brillo. Como trabajo futuro, proponemos una campaña de observación intensiva con CARMENES enfocada en enanas M tardías más débiles, donde se espera que el canal NIR ofrezca una mayor ventaja.

ABSTRACT

This thesis aims to improve the precision of radial-velocity (RV) measurements obtained from high-resolution near-infrared spectroscopy for the search for Earth-like exoplanets orbiting ultracool dwarfs. The interest of this research line is twofold: on the one hand, observing with high-resolution near-infrared spectrographs, and on the other, the search for rocky planets around very-low-mass stars. Let's start with the second.

M-dwarf stars, as far as we know, can form multiplanetary systems with members very similar to Earth. Because of the low temperature of M dwarfs, the orbits where these planets might be habitable are close to the host star, facilitating detection and characterization using methods such as transits or RVs. However, M dwarfs are intrinsically faint and often magnetically active, and some of them can be fast rotators. These properties complicate the detection of planetary signals and may also affect the potential habitability of their planets. Remarkably, the coolest M dwarfs emit the maximum of their light in the near-infrared.

High-resolution spectroscopy allows us to use the RV technique. It is complementary to transits and provides information on planetary mass (whereas transits provide information on radius). CARMENES is both a consortium and an instrument at the 3.5 m telescope in Calar Alto observatory (Almería). It has two high-resolution spectrographs (80000–94600), one in the visible (VIS: 520–960 nm) and the other in the near-infrared (NIR: 960–1710 nm). During CARMENES operation, which started in 2016, some problems and instabilities were observed regarding the cooling system. Thus, a set of upgrades was designed as part of the CARMENES-PLUS project to improve the instrument's thermal stability. The upgrades included pressure control as well as continuous flow control rather than discrete, among others.

The CARMENES-PLUS upgrades, have resulted in a before-and-after improvement in the infrared spectrograph's performance. The temperature variability has been drastically diminished, both in the short term (hours) and the long term (even years). This has resulted in nightly calibration stability below 1 m s^{-1} . With the fully-upgraded system, we have analyzed the impact on the intra-night RV variability, from night to night, and the on-sky observations. All of these parameters demonstrate a significant improvement in the instrument's intrinsic precision, reducing scatter in the time series and instrument-associated uncertainties.

Once the instrument was upgraded, we aimed to optimize RV extraction. The coolest stars tend to have high magnetic activity and are frequently fast rotators, which broaden spectral lines, complicating RV computation. Thus, taking it into account can improve the precision of the measurements or even allow us to rule out stellar candidates for the observational campaigns, as it can prevent the detection of any planetary companion.

Consequently, we began developing a methodology to derive the projected rotational velocity ($v \sin i$) of stars, which we later applied to the CARMENES sample. Most available codes treat limb darkening in a very simplified way, or even neglect it altogether. This effect reduces the contribution of the stellar limb to the observed spectrum and changes the shape of the rotational broadening profile. For cool stars, such as the CARMENES targets, an inadequate treatment of limb darkening can therefore bias the inferred $v \sin i$, typically leading to underestimated values.

The method we developed relies on two spectra: the target spectrum, for which we aim to determine the projected rotational velocity, and a template spectrum corresponding to a slowly rotating star with little or negligible rotational line broadening. The template is artificially broadened over a grid of rotational velocities through convolution; the projected rotational velocity of the target is then inferred from the broadened template that provides the best fit. In this convolution process, limb darkening is properly taken into account, and we discuss which approximation provides the most suitable treatment for the stars considered in this work.

First, we validate the method using synthetic spectra. The results show that our method provides highly accurate estimates of $v \sin i$, highlighting the advantage of a detailed treatment of limb darkening. In particular, we account for the temperature and wavelength dependence of this effect and validate the method under these conditions. Subsequently, we implement the method in `serval` and applied it to the CARMENES sample using the VIS spectra, yielding a homogeneous catalog of $v \sin i$ of 392 M dwarfs. Moreover, we compare our results with those available in the literature. The correlation is very good, with most of the values compatible within the errors. We discuss some exceptions and, in some cases, provide an updated rotation value, and we propose 36 new $v \sin i$ values. Additionally, we extend the work for CARMENES NIR following the same philosophy, and we compare the results with the $v \sin i$ measurements derived with the VIS, yielding very similar results. With `serval`, we derive the $v \sin i$ of 61 stars later than M_{5.0} with CARMENES NIR spectra. Thus, we prove that the $v \sin i$ of M dwarfs can be reliably obtained with CARMENES NIR observations.

The final step of the thesis is to optimize RV extraction from the CARMENES NIR spectra. CARMENES uses the `serval` to obtain the RV time series, with a particular combination of the available spectral orders. Nevertheless, this selection of the orders was done for all CARMENES sample M dwarfs jointly. In our case, we are interested in the coolest stars of the sample. Thus, we have developed an iterative method that optimizes the orders included in the RV computation to minimize the uncertainties. To validate the method, we use three CARMENES cool dwarfs as references and observe a reduction of up to 14% in the average errors derived, compared with those obtained by running the default `serval`.

With CARMENES NIR fully optimized for ultracool dwarfs, we test the thesis results using Teegarden's star. The interest in Teegarden is due to its slow rotation, high brightness, low magnetic activity, and the fact that it hosts three

planets already detected with CARMENES, combined with observations from other instruments. Furthermore, we have thousands of observations with both spectrographs, VIS and NIR.

With the derived RV time series, we compute the periodograms for the VIS, NIR, and activity indices (dLW, CRX, and H α). Furthermore, we used *kima*, to fit the Keplerian signals and included a Gaussian-process component to model correlated stellar-activity signals. We allowed N_p to vary between 0 and 4 and obtained at least 50000 effective posterior samples. To complement the analysis, we constructed detection maps based on an injection-and-recovery approach. To build these maps, we first whitened the RV time series by subtracting the best-fitting planetary and stellar-activity models. For both the VIS and VIS+NIR datasets, the resulting maps show high recovery probabilities at the locations corresponding to the known planets in the Teegarden's star system: approximately 100% for planets b and c, and above 60% for planet d. These results are therefore consistent with the *kima* analysis, showing that the available CARMENES data are sensitive to signals with the expected properties of the three known planets.

Subsequently, we used two CARMENES NIR data sets, obtained before and after the CARMENES-PLUS upgrade, to assess the impact of the instrument improvements. We modeled the planetary and stellar signals in both data sets; no planetary signal was detected with high significance, although the stellar activity was properly described by the GP model. Likewise, we constructed differential detection maps by subtracting the individual detection maps obtained before and after the upgrade. The post-upgrade data show enhanced detection probabilities, particularly at lower planetary masses and short orbital periods. These results provide evidence for the improved performance of the CARMENES NIR channel in radial-velocity studies of late M dwarfs after the CARMENES-PLUS upgrade. We also discuss why Teegarden's star, despite being a valuable benchmark target, is not the optimal case for demonstrating the importance of the NIR channel, due to its relative brightness. As future work, we propose an intensive CARMENES monitoring program focused on fainter late M dwarfs, where the NIR channel is expected to provide a stronger advantage.

CONTENTS

1	INTRODUCTION	1
1.1	M-dwarf stars	1
1.1.1	Main-sequence stars	1
1.1.2	Low-mass stars	2
1.1.3	Defining M dwarfs	3
1.1.4	Spectral classification of M dwarfs	4
1.1.5	M dwarf masses	5
1.1.6	Radius and metallicity of M-dwarf stars	6
1.1.7	Activity	7
1.2	Exoplanets	8
1.2.1	History of exoplanets	8
1.2.2	Exoplanet detection and characterization	11
1.2.3	Planet formation models	15
1.2.4	Atmospheric studies	17
1.2.5	Habitability of exoplanets around low-mass stars	19
1.2.6	Occurrence rate of exoplanets around M dwarfs	20
1.2.7	Planets orbiting ultracool dwarfs	21
1.3	The radial-velocity technique	22
1.3.1	The theory of radial velocities	23
1.3.2	Radial-velocity extraction with <i>serval</i>	26
1.3.3	Detecting planetary signals	28
1.4	High-resolution near-infrared spectrographs	29
1.4.1	CARMENES	32
1.4.2	NIRPS: The Near-InfraRed Planet Searcher	37
2	OBJECTIVES AND METHODOLOGY	41
3	CARMENES-PLUS: IMPROVING THE NIR CHANNEL	45
3.1	Near-infrared spectrographs cooling system	45
3.1.1	CARMENES nitrogen gas preparation unit	46
3.2	CARMENES-PLUS technical upgrade	47
3.2.1	CARMENES-PLUS description	47
3.2.2	CARMENES-PLUS timeline	48
3.2.3	Cooling system monitoring	49
3.2.4	C-PLUS: NIR upgrades and new thermal stability	51
3.2.5	Thermal stability of the NIR spectrograph after C-PLUS	60
3.3	Data reduction and calibration	61
3.3.1	Data reduction	61
3.3.2	Calibration strategy and process	62
3.3.3	Selection of on-sky datasets	62
3.3.4	Nightly zero points	63
3.4	Results and discussion	63
3.4.1	Intrinsic RV precision	63
3.4.2	Nightly zero point scatter	67

3.4.3	Contributions to the stellar RV scatter	68
3.5	Summary	72
4	PROJECTED ROTATIONAL VELOCITY OF M DWARFS	75
4.1	Why should we study stellar rotation?	75
4.2	Line-broadening	76
4.3	Observations and data reduction	79
4.3.1	CARMENES spectra	79
4.3.2	Synthetic data	79
4.4	Classic convolution and grid-based $v \sin i$ fitting	80
4.4.1	Oversampling	81
4.5	Rotation kernel with limb darkening	83
4.6	Numerical integration	89
4.7	Implementation in <code>serval</code> with CARMENES spectra	90
4.8	Comparison with the literature	91
4.9	Numerical integration Vs. oversampled convolution	97
4.10	Comparison with Deep Learning	99
4.11	$v \sin i$ using near-infrared spectra	100
4.11.1	Validation with synthetic spectra	100
4.11.2	Comparison with VIS results	101
4.11.3	CARMENES NIR results	102
4.12	Data availability	105
4.13	Summary	105
5	EXOPLANETS ORBITING AROUND ULTRACOOL DWARFS	107
5.1	Scientific context	107
5.2	Ultracool dwarfs surveys	109
5.2.1	Transit photometry	109
5.2.2	Visible and near-infrared radial velocity facilities	110
5.3	Optimizing the radial velocities of CARMENES NIR	111
5.3.1	Telluric absorption correction	116
5.4	CARMENES NIR: probing Teegarden's system	117
5.4.1	What we know of Teegarden's star	117
5.4.2	RV extraction	119
5.4.3	Periodic signals	120
5.4.4	GP modeling and planetary signals	123
5.4.5	Planet detectability	127
5.4.6	CARMENES NIR before and after the upgrades	129
5.5	Summary	131
5.5.1	Lessons learned from Teegarden's system	132
5.5.2	Future work	133
6	ADDITIONAL CONTRIBUTIONS	135
6.1	<code>ravex</code> : the RAdial VELOCITY eXplorer	135
6.2	An Earth-like planet around SPECULOOS-3	136
6.3	Impact of rotation on the RV jitter in cool stars	138
6.4	TOI-7166 b: a HZ mini-Neptune around a low-mass star	139
6.5	Four planets from the radius valley to the Neptune desert	140
6.6	A lava world and a HZ sub-Neptune orbiting TOI-1752	141

6.7 Rocky worlds in the JWST Era: CARMENES follow-up	141
7 CONCLUSIONS AND FUTURE WORK	145
BIBLIOGRAPHY	151

LIST OF FIGURES

Figure 1	Imagen del tráiler de <i>Hades II</i> . Fijate en las referencias a la noche y la Luna. ix
Figure 1.1	Hertzprung-Russell (HR) diagram (credit: ESO). 2
Figure 1.2	Three different views of the observational Hertzprung–Russell diagram used to categorize M dwarfs (Henry and Jao, 2024). 4
Figure 1.3	Radial velocity time series of 51 Pegasi (Mayor and Queloz, 1995). 9
Figure 1.4	Mass vs orbital period of confirmed exoplanets from NASA Exoplanet Archive (05/02/2026). 10
Figure 1.5	The radius valley found by Fulton et al. (2017). 11
Figure 1.6	Cumulative number of exoplanets detected against year from NASA Exoplanet Archive . 12
Figure 1.7	Illustrations of four techniques for exoplanetary detection and characterization. From left to right and up to down the Doppler spectroscopy (ESO), transit (BBC), astrometry (ESA), direct imaging (NASA), and gravity lensing (NASA). 14
Figure 1.8	Sketch of planetary formation in the Solar System (Raymond and Morbidelli, 2022). 15
Figure 1.9	Probability, depth, and frequency of transits are represented as a function of stellar mass (He, Triaud, and Gillon, 2016). 22
Figure 1.10	Illustration of the orbital parameters and configuration, with the observer's direction z . 24
Figure 1.11	Sketch of the grating diffraction. Two parallel rays in phase reach the grating, with groove distance d , and incident and reflecting angles α and β , respectively (Palmer, 2020). 31
Figure 1.12	Opto-mechanical layout of the CARMENES FE. 33
Figure 1.13	Layout of the fibers connecting the FE, CU, and spectrographs of CARMENES. 34
Figure 1.14	CARMENES NIR optical layout with the identified elements. 35
Figure 1.15	Simplified layout of the CARMENES cooling system during normal operation showing the main components, escribed in Becerril et al. (2016). 36

- Figure 1.16 Temperature response of the radiation shield (black) to the binary states of the on/off valve (red), recorded on 2020-06-05. The valve opens and closes periodically, producing a saw-tooth temperature pattern characteristic of the discontinuous flow mode. 37
- Figure 1.17 Optical layout of NIRPS spectrograph (Bouchy et al., 2025). 38
- Figure 3.1 Cut view of the N₂GPU showing the different components (Lizon and Accardo, 2010). 46
- Figure 3.2 Location of key temperature sensors in the CARMENES NIR cryogenic system. The top panel shows the upper radiation shield (Ts₁₉) and the OB (Ts₁₀) sensors. In the bottom panel, sensors placed at the 1st inlet flow splitter (Ts₀₂), and at heat exchangers of the 1st (Ts₂₂) and 3rd (Ts₀₆) cooling lines of the lower radiation shield. 50
- Figure 3.3 Data history of the temperature sensors NIR-CS-Ts₁₀ and NIR-CS-Ts₁₉. The shaded region indicates the period during which the C-PLUS interventions were implemented. 50
- Figure 3.4 CAD view of the CARMENES NIR spectrograph. The vacuum vessel and radiation shield are semitransparent, so the spectrograph is visible. 51
- Figure 3.5 *Top*: Layout of the automatic vacuum system for transfer lines (AVSTL). *Bottom*: CAD layout of the N₂GPU and AVSTL. 52
- Figure 3.6 Picture of the N₂GPU inspection in May 2021. Not the tin solder at the bottom of the image. 53
- Figure 3.7 Preliminary CAD design of a new N₂GPU-Evo. 54
- Figure 3.8 Temperature variability over 3-day intervals at the heat exchanger attached to the radiation shield (NIR-CS-Ts₀₆). 55
- Figure 3.9 Images of the CAD and physical design, and the implementation, of the EGWS at the exit of the CS. 56
- Figure 3.10 *Top*: Schematic layout of the main components of the Pressure Control Unit (PCU) in the CARMENES NIR cooling system. *Bottom*: Pressure inside the fixed-dewar over a representative 7-day period. 57
- Figure 3.11 *Top*: Layout of the system in the fixed-dewar configuration. *Bottom*: Coolant temperature at the inlet flow splitter over two representative 10-day periods. 58
- Figure 3.12 *Top*: Layout of the Johnston coupling. Note the check valves highlighted in pink. *Bottom*: Photograph of the feed line's check valve (top) and the manifold's check valve with orifices (bottom). 59
- Figure 3.13 Temperature measured by the NIR-CS-Ts₁₉ sensor. 60

- Figure 3.14 Temperature variation at the radiation shield (T_{s19} ; top panel), and the OB (T_{s10} ; bottom panel) thermal fluctuation around the working conditions ($\Delta T_{s10} = T_{s10} - 138$ K). 61
- Figure 3.15 Data history of nightly FP RV calibrations of the CARMENES NIR channel. On top, the relative data (set to zero every night), and at the bottom the absolute RV measurements (cumulative from the start of the operations). 64
- Figure 3.16 RV drift of the NIR spectrograph during individual nights, derived from FP calibration spectra. The dashed lines represent the quadratic fits applied to the calibration data for each night. 65
- Figure 3.17 *Top*: Histogram of the peak-to-peak RV variation from FP calibrations. *Bottom*: Histogram of the rms_{res} after subtracting a quadratic fit. The median values are indicated on the top axis. 66
- Figure 3.18 Time series of the CARMENES NIR NZPs. Solid black circles mark NZPs included in our analysis; crosses within the grey-shaded area corresponds to the C-PLUS interventions. Red diamonds highlight $3\text{-}\sigma$ outliers; empty red circles denote nights with fewer than three RV-standard observations, and solid red dots nights without any RV measurement. 67
- Figure 3.19 Histogram of RV scatter ($m\text{rms}$) of CARMENES stellar sample. 70
- Figure 4.1 Illustration of the line-broadening due to rotational velocity. 76
- Figure 4.2 Illustration of the instrument broadening in a schematic single-line spectrum. 77
- Figure 4.3 Illustration of the fitting process for deriving the $v \sin i$ of a target star based on a set of broadened templates with different $v \sin i$. 78
- Figure 4.4 χ^2 minimization between reference and target synthetic spectra as a function of $v \sin i$ for three spectral orders, computed without limb-darkening correction. The spectra correspond to $T_{\text{eff}} = 3000$ K, with a target value of $v \sin i = 8 \text{ km s}^{-1}$ (vertical line). 81
- Figure 4.5 Top: χ^2 minimization as a function of $v \sin i$ for different oversampling factors. Bottom: residuals relative to the best-fit solution (oversampling factor = 9). The convolution kernel does not include any limb-darkening effect. The vertical line marks the target value $v \sin i = 8 \text{ km s}^{-1}$, obtained from synthetic spectra with $T_{\text{eff}} = 3000$ K. 82

- Figure 4.6 Best-fitting $v \sin i$ values as a function of wavelength for different oversampling factors, obtained without accounting for limb darkening in the convolution process. Horizontal lines correspond to the median values. The spectra correspond to $T_{\text{eff}} = 3000$ K and a target value of $v \sin i = 8 \text{ km s}^{-1}$. 83
- Figure 4.7 Normalized error of the $v \sin i$ estimation using oversampling (factor = 5), compared with not including it, as a function of the target $v \sin i$. 84
- Figure 4.8 Normalized difference between input and fitted $v \sin i$ as a function of the input $v \sin i$ for different limb-darkening laws. 85
- Figure 4.9 Rotational broadening kernel for different limb-darkening coefficients u . Circular markers correspond to the effective width of each kernel. 86
- Figure 4.10 Limb-darkening u coefficient as a function of wavelength, when fitting simultaneously with $v \sin i$. 87
- Figure 4.11 Best-fitting $v \sin i$ values as a function of wavelength, obtained with and without accounting for limb darkening during the convolution. Horizontal solid lines indicate the median values, and the shaded regions represent the standard deviations. The dashed line marks the target value $v \sin i = 8 \text{ km s}^{-1}$, for spectra with $T_{\text{eff}} = 3000$ K. 88
- Figure 4.12 Normalized difference between input and fitted $v \sin i$ as a function of input $v \sin i$ and spectra's T_{eff} , for oversampled convolution (top panel) and numerical integration (bottom panel). 89
- Figure 4.13 $v \sin i$ values obtained in this work using the oversampled convolution method compared with literature measurements. Newly determined $v \sin i$ values not previously available are shown in the shaded area at $v \sin i$ (literature) = 100 km s^{-1} . The solid line indicates the 1:1 relation, while the dashed lines correspond to a 10% deviation. Gray dashed lines and the shaded area mark the 2 km s^{-1} limit of CARMENES. 93

- Figure 4.14 Values of $v \sin i$ derived from the oversampled convolution method compared to v_{eq} . The linear $1:\frac{4}{\pi}$ relation (dashed line) represents the expected value of $\sin i$ for an isotropic distribution of inclination angles (see Appendix B of Ruh et al. 2024). The 1:1 relation with a 10% margin (solid line and shaded region) and the $1:\frac{1}{2}$ relation (dotted line) correspond to $i = 90^\circ$ and $i = 30^\circ$, respectively. The vertical gray dashed line indicates the 2 km s^{-1} threshold, and the diamond markers correspond to young candidates (Cortés-Contreras et al., 2024). 94
- Figure 4.15 Top: chunk of the CARMENES VIS co-added spectrum of J14155+046 compared to the spectrum of J03133+047, without rotational broadening and with 6.8 km s^{-1} rotational broadening (Jenkins et al., 2009). Bottom: residuals with respect to the spectrum of J14155+046. 97
- Figure 4.16 Histogram of the normalized difference between the $v \sin i$ value ($> 2 \text{ km s}^{-1}$) computed with oversampled convolution and the literature, excluding the outliers. The median is marked with a horizontal solid line. 98
- Figure 4.17 Top panel: comparison between $v \sin i$ computed with NI and OC. Dashed lines represent the 2 km s^{-1} limit, and diagonal lines mark the 1:1 relation $\pm 10\%$. Bottom panel: histogram of the normalized residuals with respect to the 1:1 relation for $v \sin i > 2 \text{ km s}^{-1}$. Median value represented by a vertical line. 98
- Figure 4.18 *Left*: Comparison of our $v \sin i$ values with the results from Passegger et al. (2020) and Mas-Buitrago et al. (2024). *Right*: The rms of the residuals between target spectrum and template rotationally broadened using both $v \sin i$ from this work and Mas-Buitrago et al. (2024). 99
- Figure 4.19 Normalized difference between input and fitted $v \sin i$ as a function of input $v \sin i$ and spectra's T_{eff} , without limb darkening (top panel) and with linear limb darkening (bottom panel), using NIR synthetic spectra. 101
- Figure 4.20 Comparison of $v \sin i$ derived from CARMENES VIS and NIR spectra for M dwarfs later than M5.0 V. Lines indicate the 1:1 relation ($\pm 10\%$) and the 2 km s^{-1} limit. 103

- Figure 5.1 Overview of the CARMENES spectral range. The spectrum covered by the VIS channel is shown in blue, and the NIR channel in red. The target shown is the A2V star 50 Cas. The stellar spectrum only exhibits a few hydrogen lines; all strong features are from Earth's atmosphere (Reiners et al., 2018). 112
- Figure 5.2 Average RV precision per NIR spectral order for three CARMENES UCDS. 115
- Figure 5.3 Average error obtained for the RV time series for each iteration, for three targets. The number inside each marker corresponds to the order excluded in that iteration. The minimum value is shown in green, and the default `serval` value in yellow. 116
- Figure 5.4 Relative RV precision ($\sigma_{rv}^{tac} / \sigma_{rv}^{nc}$) per NIR spectral order for three CARMENES UCDS when including the telluric absorption correction of the spectra. 117
- Figure 5.5 RV time series of Teegarden's star for CARMENES NIR (top) and VIS (bottom), fully corrected and optimized to obtain the highest RV precision. 120
- Figure 5.6 Generalized Lomb-Scargle periodogram of Teegarden's star for NIR (top) and VIS (middle) RV time series (see Fig. 5.5). The corresponding window function for both is shown in the bottom panel. 121
- Figure 5.7 GLS periodogram of Teegarden's star of NIR and VIS RV, dLW, H α , and CRX. The vertical lines represent the observed periodic signals, (i) at 4.92, 11.42, and 26.1 days for the Keplerians, (ii) 79 and 96 days for the rotational period, (iii) the 172 days signal, and the 1-year alias. 122
- Figure 5.8 Top: fitted planetary signals of Teegarden's b, c, and d for CARMENES VIS time series. Middle: Fitted GP for the stellar component of the RV data. Bottom: residuals after whitening the RV measurements from the stellar and planetary signals. 126
- Figure 5.9 Top: fitted planetary signals of Teegarden's b, c, and d for CARMENES VIS+NIR (blue and orange, respectively) time series. Middle: Fitted GP for the stellar component of the RV data. Bottom: residuals after whitening the RV measurements from the stellar and planetary signals. 128
- Figure 5.10 Detection maps of Teegarden using whitened VIS and VIS+NIR data. The three detected planets are plotted using star markers, with the corresponding orbital periods and projected masses. 128

Figure 5.11	Differential detection map between post- and pre-C-PLUS RV time series (i.e. detection map of pre-C-PLUS subtracted from the post-C-PLUS one). Teegarden's b, c, and d are represented by the star markers. 130
Figure 6.1	SPECULOS-3 RV time series derived from CARMENES observations. 138
Figure 6.2	Radial velocity time series of the JWST-CARMENES campaign. 142

LIST OF TABLES

Table 1.1	Approximate ranges of stellar properties for the different main-sequence spectral-types. 3
Table 1.2	Summary table with the spectral range, resolution, and RV precision for high-resolution near-infrared échelle spectrographs. 30
Table 3.1	Stellar RV jitter estimates and number of measurements for a subset of CARMENES targets. For each star (Karmn ID), we list the RV jitter and number of observations for the VIS channel, and the NIR channel before and after the C-PLUS upgrades. The table contains seven stars that have a jitter estimate for all three cases; the full list is available online. 69
Table 4.1	Derived $v \sin i$ values for all the T_{eff} and target $v \sin i$ combinations, using regular convolution without limb darkening (RCWLD) and oversampled convolution with linear limb darkening (OCLLD). 88
Table 4.2	List of stars used as template for computing $v \sin i$ depending on spectral type (Schöfer et al., 2019). 90
Table 4.3	catalog of $v \sin i$ values for 392 M-dwarf stars of the CARMENES sample using VIS spectra. ^a 92
Table 4.4	Targets with unreliable $v \sin i$ values. 96
Table 4.5	Derived $v \sin i$ values for all the T_{eff} and target $v \sin i$ combinations, using VIS, NIR, and VIS+NIR spectra, using oversampled convolution with linear limb darkening. 102
Table 4.6	Derived $v \sin i$ values for CARMENES stars later than M5.0 with VIS and NIR data. Colors denote discrepancies between the datasets estimations. 104
Table 5.1	List of UCDS in CARMENES sample. 113
Table 5.2	Correspondence between échelle orders and CARMENES half-orders, with the corresponding wavelength range, and the strength of the tellurics. 114

Table 5.3	Stellar and planetary (b, c, and d) parameters of Teegarden's star system. 118
Table 5.4	Priors in <i>kima</i> for the GP models. 124
Table 5.5	Posteriors of the GP after running <i>kima</i> with the priors in Table 5.4. 125
Table 5.6	Planetary parameters derived by <i>kima</i> for Teegarden's system, for the three CARMENES datasets. 125
Table 5.7	Posteriors of the GP after running <i>kima</i> for CARMENES NIR pre- and post-C-PLUS. 130
Table 6.1	Parameters of the SPECULOOS-3 system from Gillon et al. (2024). 136
Table 6.2	CARMENES observations and the S/N in the VIS (order 82) and NIR (order 50) channels. 137
Table 6.3	Stellar and planetary parameters of TOI-7166 system (Barkaoui et al., 2025). 139
Table 6.4	Stellar and planetary parameters for the selected targets of the JWST rocky worlds large program of CARMENES. 143

ACRONYMS

AO: Adaptative Optics
APER0: A PipelinE to Reduce Observations
AVSTL: Automatic Vacuum System for Transfer Lines
BD: Brown Dwarf
CAD: Computer-Aided Design
CAHA: Centro Astronómico Hispano en Andalucía
carmencita: CARMEN(ES) Cool dwarf Information and daTa Archive
CARMENES: Calar Alto high-Resolution search for M dwarfs with Exoearths using Nearinfrared and optical Échelle Spectrographs
CCF: Cross-Correlation Function
CFC: Continuous-Flow Cryostat
CMF: Core-Mass Fraction
C-PLUS: CARMENES-PLUS
CRIRES+: Cryogenic high-resolution InfraRed Echelle Spectrograph
CRX: CRomatic IndeX
CS: Cooling System
CU: Calibration Unit
dLW: differential Line Width
DNS: Diffusive Nested Sampling
DRS: Data Reduction System
EGWS: Exhaust Gas Warm-up System
ESO: European Southern Observatory
ESPRESSO: Echelle SPectrograph for Rocky Exoplanets and Stable Spectroscopic Observations
FA: F-number Adaptation
FAP: False-Alarm Probability

FE: Front End
FP: Fabry-Pérot
FS: Feasibility Study
FWHM: Full Width at Half Maximum
GCM: Global Circulation Model
GLS: Generalized Lomb-Scargle
GP: Gaussian Process
GTO: Guaranteed Time Observations
HARPS: High Accuracy Radial velocity Planet Searcher
HCL: Hollow Cathode Lamps
HD: Henry Draper catalogue
HPF: Habitable-zone Planet Finder
HR: Hertzsprung-Russell
HST: Hubble Space Telescope
HZ: Habitable Zone
IMF: Initial Mass Function
JWST: James Webb Space Telescope
KPF: Keck Planet Finder
LBL: Line-By-Line
LN₂: Liquid N₂
MAROON-X: M-dwarf Advanced Radial velocity Observer Of Neighboring exoplanets
MLR: Mass-Luminosity Relation
N₂GPU: Nitrogen (N₂) Gas Preparation Unit
NI: Numerical Integration
NIR: Near-InfraRed
NIRPS: Near Infra Red Planet Searcher
NZP: Nightly Zero Point
OB: Optical Bench
OC: Oversampled Convolution
OCLLD: Oversampled Convolution with Linear Limb Darkening
PCA: Principal Component Analysis
PCU: Pressure Control Unit
ravex: RADial VELOCITY eXplorer
RCWLD: Regular Convolution Without Limb Darkening
rms: root-mean-square
RV: Radial Velocity
serval: SpEctrum RADial VELOCITY AnaLyser
S/N: Signal-to-Noise ratio
SPECULOOS: Search for habitable Planets EClipsing ULtra-cOOl Stars
SPIROU: SPectropolarimetre InFRaROUge
SpT: Spectral Type
SNO and SSO: SPECULOOS Northern and Southern Observatory
tac: telluric absorption corrected
TESS: Transiting Exoplanet Survey Satellite
TOI: TESS Objects of Interest
TRAPPIST: Transiting Planets and Planetesimals Small Telescope
Ts: Temperature Sensor
UCD: UltraCool Dwarf
UV: UltraViolet
VIS: VISible
WMF: Water-Mass Fraction

INTRODUCTION

1.1 M-DWARF STARS

1.1.1 *Main-sequence stars*

Stars can be considered the main component of the Universe. The light we perceive comes from one source, the Sun, and most of the radiation we can detect with telescopes is also produced by stars. They are also responsible for the formation of heavy elements and host exoplanetary systems; ultimately, it is within these systems that planets can harbor life, at least in one case.

But, what exactly is a *star*? The traditional definition is an object that will, is, or has produced energy through hydrogen fusion in its core. This is any object with a mass over the hydrogen-burning limit of ~ 0.075 solar masses (M_{\odot} ; Oswalt and Barstow, 2013). A brown dwarf, for example, is too small to fuse hydrogen, but can undergo other burning phases, such as deuterium, which produces small amounts of energy. Their mass ranges from 0.012 to $0.075 M_{\odot}$.

For both, stars and brown dwarfs, the (basic) formation model is the same, as the physics should not differ much from one object to the other, especially for low-mass stars and substellar objects. As first proposed by Emanuel Swedenborg in 1734, as the *Nebula Hypothesis*, a star is formed from a rotating cloud of gas that collapses under gravity, with the future star in the center and a disk around it (where planets can be formed). The model was expanded later in the eighteenth century by Immanuel Kant and Pierre-Simon Laplace. Surprisingly, the basic idea of the nebula hypothesis is still the basis of our understanding of star formation. Currently, this process can be divided into several phases, which do not necessarily happen one after the other. These are:

- *Molecular cloud formation.* A large cloud of gas forms within the interstellar medium. The high density allows the cloud to cool, and molecular hydrogen forms.
- *Pre-stellar core formation.* The molecular cloud is fragmented in self-gravitating condensations (*clumps*) and, on smaller scales, *cores*, the birth place of stars.
- *Embedded star formation.* Pre-stellar cores collapse forming protostars, often as multi-stellar systems, that are surrounded by a disk of gas.
- *Pre-main-sequence stars.* Most of the mass in the core is accreted onto the star(s), and the disk might be in the process of planet formation and rapidly disappears. Eventually, the star(s) will reach the main sequence.

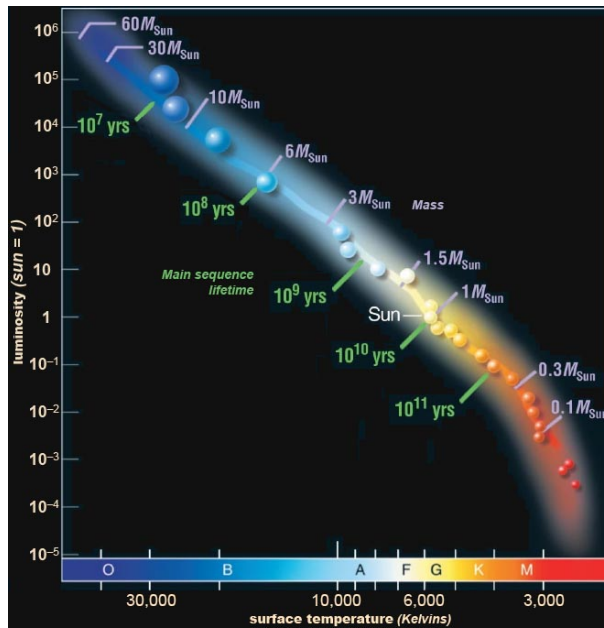


Figure 1.1: Hertzsprung-Russell (HR) diagram (credit: ESO).

- *Star clusters.* In the same molecular cloud, many stars are formed, resulting in frequent encounters between stars, which can destroy young multi-stellar systems, disrupting planet-forming disks.
- *The end of star formation.* Once one or more massive stars form, the UV radiation fields, stellar winds, and eventual supernovae, expel any gas that has not already formed stars, preventing more star formation.

One of the most typical representations of stars is the so-called Hertzsprung-Russell (HR) diagram from 1912, which represents the surface temperature against the luminosity of stars (Fig. 1.1). Here is when the concept of the main sequence emerges, because most of the stars fall on the diagonal of the diagram. The main source of energy for main-sequence stars is the burning of hydrogen, which produces helium. The more massive stars are bigger, hotter, more luminous, and have shorter life spans.

Main-sequence stars are divided into seven classes or spectral types (SpT) depending on their spectral features, the classical OBAFGKM. Table 1.1 shows the basic properties of stars and the ranges for the different spectral types. It also happens that the bigger and hotter stars are less frequent, at least in our galaxy. The most common ones are M-dwarf stars, lying at the bottom right of the HR diagram.

1.1.2 Low-mass stars

Our naked eye can see stars up to V magnitude of 6.5 in a very clear and dark night, where we can see thousands of stars in the sky. Nevertheless, the stars we can see are not representative, because none of them are M-dwarf stars due to their intrinsic faintness. The brightest one is Lacaille 9352, with a V magnitude

Table 1.1: Approximate ranges of stellar properties for the different main-sequence spectral-types.

SpT	T_{eff} [K]	Mass [M_{\odot}]	Radius [R_{\odot}]	Luminosity [L_{\odot}]
O	≥ 33000	≥ 16	≥ 6.6	≥ 30000
B	10000–33000	2.1–16	1.8–6.6	25–30000
A	7300–10000	1.4–2.1	1.4–1.8	5–25
F	6000–7300	1.04–1.4	1.15–1.4	1.5–5
G	5300–6000	0.8–1.04	0.96–1.15	0.6–1.5
K	3900–5300	0.45–0.8	0.7–0.96	0.08–0.6
M	2300–3900	0.075–0.45	≤ 0.7	≤ 0.08

of 7.34 and M2 V spectral type. This is actually a paradox, because M dwarfs are the most common stars in our Solar neighborhood, and probably in the entire Milky Way and other galaxies (Henry et al., 2006; Henry et al., 2018). Despite M dwarfs being the lightest stars, they outweigh the rest of the stars due to the large number of them.

M dwarfs also have the largest life span; so large that in the almost 14 billion years of the Universe, no single one of them has evolved in any meaningful way, as they are just at the very beginning of their stay in the main sequence. Multi-stellar systems are the most typical configuration for stars, but are significantly less frequent for M dwarfs. More than 80% of OBA-type stars and around half of solar-type stars are in multi-stellar systems, but only 10–30% for very low-mass stars and brown dwarfs (Cifuentes et al., 2025).

If something characterizes the M dwarfs as a family, is their wide variety compared with the rest of the spectral types. The changes in temperature, size, and mass are unlike any other group, and the physics of their interiors drastically change among low-mass stars. They can be divided into three types; (i) most massive M dwarfs (0.4–0.6 M_{\odot}) are partially convective and partially radiative, similar to K dwarfs; (ii) around 0.3–0.4 solar masses falls the transition to fully convective interiors, shifting in structure unlike any other type of the main sequence (Jao et al., 2018); and (iii) stars with less than 0.3 M_{\odot} are fully convective, and are characterized for the presence of molecules in the atmosphere, such as TiO or VO. The substellar regime starts at 0.075 solar masses.

1.1.3 Defining M dwarfs

The variety among M dwarfs is so big that the hottest ones are identical to K dwarfs, whereas the coolest go even beyond the M stellar type, down to L2.5. The knowledge about M dwarfs has grown significantly over time, to the point where new sub-classes were needed. L and M dwarfs are separated by the decrease in strength of TiO and VO bands, while metallic hydride and neutral alkali metal lines start appearing (Kirkpatrick et al., 1999).

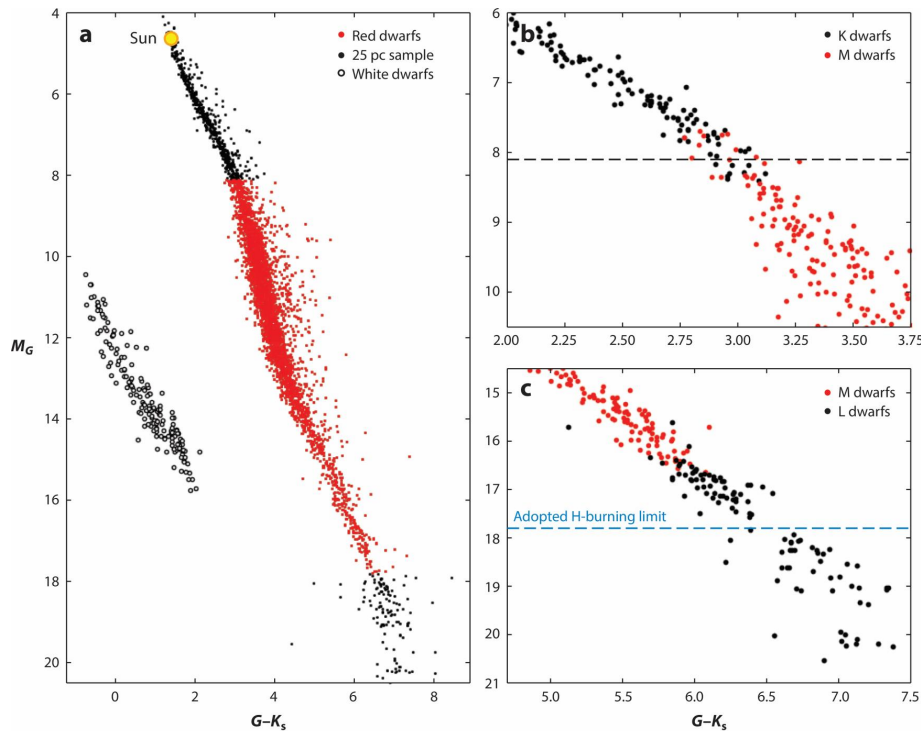


Figure 1.2: Three different views of the observational Hertzsprung–Russell diagram used to categorize M dwarfs (Henry and Jao, 2024).

The definition of spectral types has always been based on spectral features, but high-quality spectra are not always available to properly categorize them. The HR diagram can help classify stars, define the boundary between M and K dwarfs, and draw the substellar limit. Henry and Jao (2024) set the limit between K and M dwarfs at $M_G = 8.1^1$. On the other hand, the substellar limit has been examined in many articles. Dieterich (2014) explores the hydrogen burning limit using two intrinsic characteristics of low-mass stars and brown dwarfs. Whereas removing mass from a star shrinks its radius because nuclear fusion rates in its core decrease, doing it in brown dwarfs would increase the radius because electron degeneracy pressure weakens. This leads to an inflection point in radius between the two populations. Dieterich (2014) found it at $\approx 0.086 R/R_\odot$, $\log L/L_\odot \approx -3.9$, and $T_{\text{eff}} \approx 2075$ K, which leads to a lowest-mass star with spectral type L2.5 V. Dupuy and Liu (2017) suggested a lower hydrogen-burning limit. In the HR diagram (see Fig. 1.2), Henry and Jao (2024) found the substellar limit at $M_G = 17.8$, whereas Gaia Collaboration et al. (2021) did at 17.6, drawing a similar picture.

1.1.4 Spectral classification of M dwarfs

The M spectral type was first introduced by Williamina Fleming and a team of women (the Harvard Computers²), when they classified stars of the Henry

¹ M_G is Gaia's (Gaia Collaboration et al., 2016b) absolute magnitude.

² To learn more about this group, see <https://platestacks.cfa.harvard.edu/women-at-hco>.

Draper's catalog. Then, it was included in the Harvard classification system by Annie Jump Cannon (Cannon and Pickering, 1918), and divided into *a*, *b*, and *c* depending on the TiO band strength. The subtypes from M₀ to M₁₀ were introduced for the first time in 1922, at the International Astronomical Union (IAU) meeting, also based on the TiO band. The current half-types of M dwarfs were later proposed by Joy (1947).

One of the main issues with Joy's classification was the lack of standard stars. In the following years, efforts were made to identify standard stars for M dwarf classification, which was especially difficult for the latter spectral types. It is worth highlighting the extension to 6800 Å, adding more atomic and molecular lines (e.g., TiO bands, VO at 5736 Å, and CaOH at 5530 Å). Her classification covered up to M₆ because cooler stars have their spectral energy distribution peak in the near-infrared (NIR), with minimal flux in the bluer part of the visible (VIS). Kirkpatrick, Henry, and McCarthy (1991) extended until M₉ with broader spectra, covering until 9000 Å.

The principal differences between K and M dwarfs are (i) stronger TiO and (ii) weaker CaH and MgH bands for M dwarfs; (c) H α in emission for M dwarfs, as opposed to K dwarfs; (d) and for M₅ and cooler, VO absorption features start to appear.

The Sloan Digital Sky Survey (SDSS) extensive dataset of M dwarf spectra was a turning point for low-mass stars spectral classification, as many groups took advantage of it to (i) establish template spectra (Bochanski et al., 2007), (ii) develop spectral classifying pipelines (Covey et al., 2007), and (iii) building catalogs (West et al., 2011; Alonso-Floriano et al., 2015; Liu et al., 2019).

Gaia (Gaia Collaboration et al., 2016b) allows for deriving precise absolute magnitudes due to its high-quality parallaxes and photometry, which favors the use of M_G rather than classical spectral types. Nevertheless, having high-resolution spectra is very useful for deriving other spectral parameters, such as the projected rotational velocity ($v \sin i$), metallicities ([M/H]), youth (H α), and especially for exoplanetary studies, both for atmospheric characterization (see Sect. 1.2.4), and radial-velocity (RV) surveys (see Sect. 1.3).

There is a group of cool M stars less luminous and with lower metallicities compared to the main-sequence M dwarfs, the *subdwarfs*, denoted as *sdM*, *esdM*, and *usdM* (Kuiper, 1939; Gizis and Reid, 1997; Lépine, Rich, and Shara, 2007). The MgH, CaH, AlH, and FeH bands (among others) are used to classify subdwarfs.

1.1.5 *M dwarf masses*

The most important parameter of a main-sequence star is its mass, because it determines the amount of energy and its structure. Other properties that define a star are its composition, rotation, and magnetic field, which change as it ages. For M dwarfs, the mass becomes even more important because they have not changed meaningfully throughout their lives. The mass of an M dwarf will determine its observables, such as temperature, luminosity, or absolute magnitude. Nonetheless, determining the mass of an M dwarf is challenging.

The two most typical techniques are the orbital mapping of binary systems (Serenelli et al., 2021), which is very demanding, and asteroseismology (Aerts, 2021). The latter is not useful for M dwarf studies, because no oscillations have been detected on these cool objects.

The probability distribution that describes the relative number of stars formed in a given mass range during a single star-formation event is called the initial mass function (IMF). For M dwarfs, because their evolution since the beginning of the Universe is not significant, the current mass function is basically the IMF. Addressing the IMF helps us to understand the M dwarf population in the Milky Way. It is not surprising that the search for the IMF of M dwarfs has been complicated and conflicting. Scalo (1986), Reid (1987), and Bochanski et al. (2010) found the peak of the IMF around $0.2\text{--}0.3 M_{\odot}$, whereas Mazzitelli and Dantona (1986), Henry (1991), and Winters et al. (2019) concluded that is at $0.1 M_{\odot}$. The IMF is intrinsically related to the luminosity function (LF) through the mass-luminosity relation (MLR).

Many efforts have been put into establishing an MLR for M dwarfs. The first attempt was done by Henry and McCarthy (1993). Many studies have expanded the MLR, mainly in V and K filters, in the past three decades (Henry et al., 1999; Delfosse et al., 2000; Benedict et al., 2016; Dupuy and Liu, 2017), allowing for the estimation of M dwarf masses with a few percent margin on average, although individual star masses are still challenging. In the Gaia era, together with high-resolution imaging, more precise MLRs in different filters (such as V , I , and K) can be obtained, leading to more accurate exoplanet mass estimations.

1.1.6 *Radius and metallicity of M-dwarf stars*

With the apparition of the transit method for detecting exoplanets, it has become crucial to compute the precise radius of host stars. The most direct method is to measure the size of stars in eclipsing binaries. This technique is especially challenging in M dwarfs, due to the lower number of these systems compared to hotter stars (Winters et al., 2019), as well as the harder modeling of spots and limb darkening. Another direct method is interferometry, which was first used to measure Betelgeuse's radius by Michelson and Pease (1921). Empirical relations between luminosity and radius have also been tried (Morrell and Naylor, 2019) to estimate M dwarfs radii, but have been proven to be less precise than for hotter stars.

Metallicity is a fundamental stellar parameter that helps to (i) understand the diversity among nearby M dwarfs (Hejazi, Lépine, and Nordlander, 2022); (ii) characterize its relation to other stellar properties, such as mass and radius (Boyajian et al., 2012; Mann et al., 2019); (iii) assess its impact on planet formation (Fischer and Valenti, 2005; Newton et al., 2019); and (iv) explore its correlation with Galactic kinematics (Medan and Lépine, 2023).

Metallicities are typically derived by comparing spectra with a grid of model atmospheres. The leading atmospheric models for generating M dwarf synthetic spectra are PHOENIX/BT-Sett1, ATLAS, and MARCS (Hauschildt et al., 1999; Castelli and Kurucz, 2003; Gustafsson et al., 2008; Allard, 2014). The stellar

parameters, such as the metallicity, are derived by comparing the synthetic and real spectra using χ^2 minimization (Gizis and Reid, 1997) or software, such as M00G (Snedden, 1973) and Spectroscopy Made Easy (Valenti and Piskunov, 1996). The abundances are usually obtained using high- or low-resolution with VIS or NIR spectra (Woolf and Wallerstein, 2005; Rojas-Ayala et al., 2012). Machine learning techniques are increasingly used to estimate metallicities Lindgren and Heiter (2017) and Passegger et al. (2022). Most studies point to a near-solar metallicity in most M dwarfs.

1.1.7 Activity

Activity is a fundamental parameter of a star and is closely related to many other properties, such as the rotation and magnetic field. It also depends on age, and has (typically) a (quasi) periodic cycle. M dwarfs are intrinsically active; however, their activity is not always straightforward to detect, and in some extreme cases, their observational signatures may fall below the detection limits of current instruments. The study of activity on M dwarfs has now spanned a century (Luyten, 1926), and the concept of active M stars has evolved in many ways. For instance, in the second edition of the *General Catalog of Variable Stars* (1958), the first mention of flares appears as a noticeable short-duration increment in brightness in optical wavelength in M3-M6 stars.

Active-flare M dwarfs are identified by changes in brightness during photometric campaigns or by H α features in spectroscopic observations. The use of H α to define an M dwarf as more or less active has drawn some controversy because the derived H α equivalent widths differ among studies (West et al., 2008; Newton et al., 2017; Jeffers et al., 2018). Furthermore, M dwarfs defined as inactive in these studies show noticeable activity in other wavelengths, as the UV (Youngblood et al., 2017).

The understanding we have about the physics that drives activity in stars comes mainly from solar dynamo processes. Flares are generally attributed to the rapid release of energy through magnetic field reconnection (Benz and Güdel, 2010; Basri, 2021). Stellar magnetic activity exhibits features across many wavelengths, from radio to X-ray, and can be detected and characterized via photometry or spectroscopy.

The fraction of active M dwarfs is significantly higher compared with other spectral types. There are two main reasons: the rotational braking times of M dwarfs are considerably larger (Delfosse et al., 1998; Barnes, 2003; Delorme et al., 2011), and for the same rotational period, M dwarfs exhibit higher activity levels. M dwarf activity is characterized by strong chromospheric and corona emissions that depend on spectral type (Reiners and Basri, 2010; Reiners, Joshi, and Goldman, 2012; Astudillo-Defru et al., 2017; Mignon et al., 2023), and the activity emission is strongly correlated with their rotational period (Wright et al., 2011; Astudillo-Defru et al., 2017; Wright et al., 2018; Ruh et al., 2024).

The long-term variations of activity are not well characterized for M dwarfs, as they are for FGK stars. Many different properties have been observed, such as long-term stable spots (Bonfils et al., 2007; Robertson et al., 2020), or long-

term chromospheric variability (Gomes da Silva et al., 2011; Gomes da Silva et al., 2012). Activity cycles have been found for slow and fast rotators, and for partially and fully convective stars (Buccino et al., 2010; Mignon et al., 2023).

Stellar activity is critical in many research topics; for example, in RV observations, activity imprints on precision as an excess scatter in the RV time series (Ruh et al., 2024), and activity-related signals can dominate the periodicities found in the time series (Faria et al., 2022; Cortés-Zuleta et al., 2023). It is also important in exoplanetary studies, either because it can hide planetary signals, but also plays a key role in the planet's life and evolution, as it can blow away any atmosphere the planet could have formed at the beginning of its life, making it completely uninhabitable (Buccino, Lemarchand, and Mauas, 2007; von Bloh et al., 2007; Vidotto et al., 2015; Attia et al., 2021).

Planetary studies using the RV technique are specially sensitive to spot and plage contrast caused by stellar activity (Saar and Brandenburg, 1999; Meunier, Desort, and Lagrange, 2010; Dumusque, Boisse, and Santos, 2014). Processes such as the meridional circulation (Makarov, 2010; Meunier and Lagrange, 2020), and granulation/supergranulation (Dumusque et al., 2011; Meunier et al., 2015; Meunier and Lagrange, 2019; Meunier, Lagrange, and Borgniet, 2020) lead to long-term variability. Nevertheless, small-scale flows are smaller in M than in FGK stars (Allende Prieto et al., 2013; Beek et al., 2013a; Beek et al., 2013b; Tremblay et al., 2013; Meunier et al., 2017; Meunier, Mignon, and Lagrange, 2017).

1.2 EXOPLANETS

1.2.1 *History of exoplanets*

The search for stellar companions originated in the 18th century with the first catalogs of visual double stars; hence, the modern detection and analysis was originated by the study of stellar kinematics. In 1844, Friedrich Wilhelm Bessel first claimed that Sirius had an unseen companion. Alvan G. Clark (1862) confirmed the existence of Sirius B, which became the first of such detection. Almost a century later, in 1938, Van de Kamp, an astrometric expert, began a program to search for stellar companions. At first, he began looking for binary systems, but later switched to the hunt for exoplanets. In 1963, he claimed that Barnard's star had a companion with 1.6 Jupiter masses, based on astrometric data. Nevertheless, the community was very cautious at the time, because two planetary candidates were refuted in 1943, 70 Ophiuchi (Reuyl and Holmberg, 1943) and 61 Cygnus (Strand, 1943). The controversy surrounding Van de Kamp's claim lasted for decades. In 1973, John L. Hershey found an almost identical pattern in GJ 793 data as that of van de Kamp (1969). This could be due to two identical planets orbiting both stars or some trend in the data, but Van de Kamp did not give up. The most sophisticated instruments and observatories have allowed Basant et al. (2025) to confirm four planetary companions hosted by Barnard's star, almost 90 years after first Van de Kamp's claim.

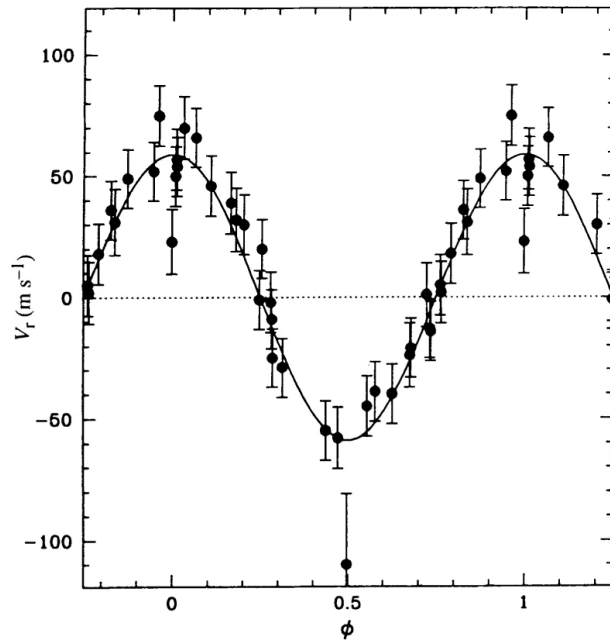


Figure 1.3: Radial velocity time series of 51 Pegasi (Mayor and Queloz, 1995).

The first detection on an exoplanet had to wait until 1992, when Wolszczan and Frail (1992) published the discovery of two planetary-mass bodies. They claimed it based on the anomalies found in the timing of the radio pulses of PSR1257+12, a millisecond pulsar. Although this is not considered the start of exoplanetology, because at the moment, it was not contemplated that planet formation could occur in the extreme environment of a neutron star. The race for discovering a new Earth orbiting another star started with the detection of a *hot Jupiter* around 51 Pegasi (Mayor and Queloz, 1995). This detection was possible thanks to the ELODIE (Baranne et al., 1996) spectrograph at the Haute-Provence Observatory and the RV technique (see Fig. 1.3). The RV method is based on identifying periodicities in the measurement of spectral line Doppler shifts over time. 51 Pegasi b is a Jupiter-sized planet with an orbital period of 4.2 days which, at the time of its discovery, challenged existing theories of planet formation based on the Solar System. This discovery ultimately contributed to the awarding of the 2019 Nobel Prize in Physics.

The technological advances of the following years led to an exponential increase in the detection of exoplanets. At first, most of the detected planets were indeed giant, but soon enough, smaller planets began to appear, as did multiplanetary systems with up to 8 companions (Butler et al., 1999; Rivera et al., 2005; Lovis et al., 2011; Anglada-Escudé et al., 2016). As telescopes have become larger and instruments more sensitive, it has become possible to characterize increasingly smaller exoplanets and a wider variety of host stars. The first surveys focused on FGK stars, but more recent ones (since the 2010s) are also focusing on M dwarfs. The increasing number of exoplanets detected also increases the variety we find, from tiny rocky planets to hot-gas giants with tens of Jupiter masses, going through lava worlds, super-Earths, sub-Neptunes, and more.

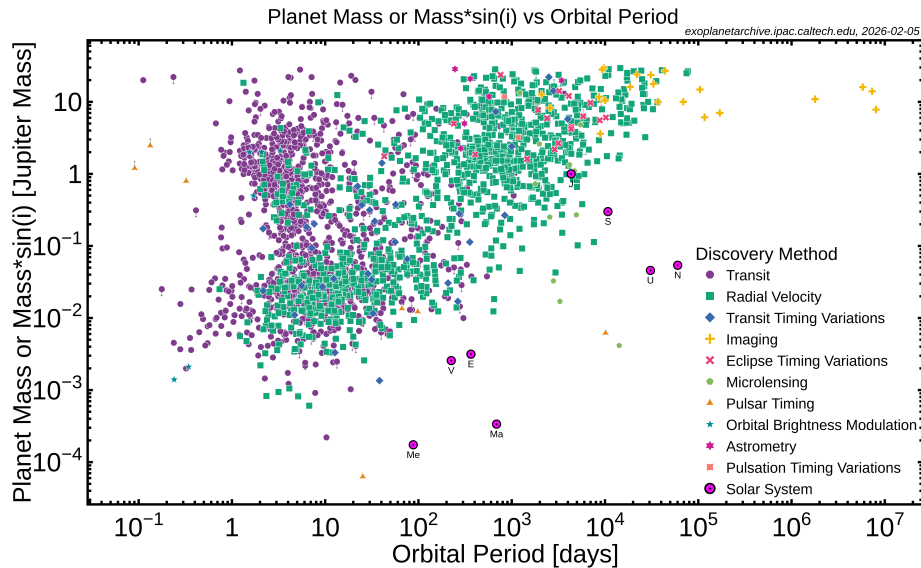


Figure 1.4: Mass vs orbital period of confirmed exoplanets from [NASA Exoplanet Archive](https://exoplanetarchive.ipac.caltech.edu/) (05/02/2026).

As of February 5, 2026, 6100 exoplanets³ have been confirmed, with a huge variety that goes beyond that of our Solar System. The current picture of exoplanets is summarized in Fig. 1.4, where the planet's (projected) mass is compared to its orbital period. Depending on the technique (see Sect. 1.2.2) used to detect (and characterize) each exoplanet, different properties can be measured. For example, using RVs, the absolute mass of a planet can not be obtained, but rather its projected mass to the angle of sight ($M_P \sin i$). Comparing the Solar System planets to the whole picture suggests that our neighboring worlds are indeed rare throughout the rest of the Galaxy. Nevertheless, the limitations of the current instrumentation are what (possibly) is giving us this impression. Many biases may be present in current surveys and samples. For example, bigger and close-in planets are easier to detect.

There are several ways to classify exoplanets based on the chosen planetary parameter. Depending on the classification, we can find hot Jupiters, lava worlds, rocky planets, sub- and super-Neptunes, super-Earths, puffy planets, ocean worlds, etc. One of the most common ways to analyze exoplanets is by their radius, because it is one of the most basic properties and is derived from transit detections (the most successful method in terms of the number of detections). Fulton et al. (2017) studied the distribution of exoplanet radii and, to their surprise, found that it was not unimodal but rather bimodal. There was a significant drop in the detection of objects between the so-called super-Earths and sub-Neptunes, which is now well known and widely studied: the *radius valley* (see Fig. 1.5). Owen and Wu (2017) showed that this bimodality matched the predictions of the photoevaporative mass-loss hypothesis. Even so, the extent to which photoevaporation alone explains the observed valley remains under discussion, and this topic continues to be actively investigated.

³ <https://exoplanetarchive.ipac.caltech.edu/>.

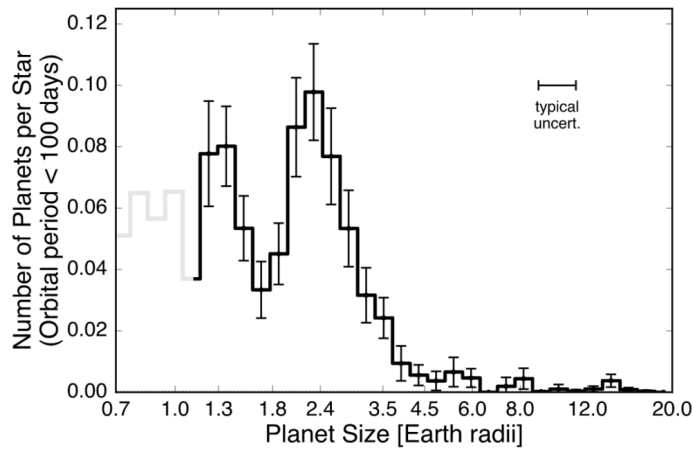


Figure 1.5: The radius valley found by Fulton et al. (2017).

1.2.2 Exoplanet detection and characterization

The first detection of an exoplanet was made using the RV method, but in the thirty years of exoplanetology, many more techniques have been developed, each with different advantages and limitations. Fig. 1.6 shows the cumulative number of planets detected each year, differentiating the technique used for the discovery.

- *Doppler spectroscopy*: The radial-velocity method pioneered exoplanet detection, and is now the second most productive technique after the transit method. About one-fifth of the confirmed exoplanets have been discovered by this technique. The larger the mass and the shorter the orbital period of the planet, the better it is for RV detectability. It is based on comparing spectroscopic observations to identify Doppler shifts in spectral lines (see the illustration in the top-left of Fig. 1.7). Periodicities in the measurements can be related to planetary companions, although other non-Keplerian mechanisms, such as stellar activity, can mimic these signals. Using RVs, one can determine the orbital period, eccentricity, and projected mass of the planet.
- *Transits*: More than 70% of confirmed exoplanets have been discovered by the transit method. If a star has a companion (star, brown dwarf, or planet) and we see this system from a privileged angle, an eclipse event (or transit) will occur. By monitoring the flux emitted by the host star, we might detect a drop in the light curve due to this companion (see illustration in top-right of Fig. 1.7). We can also derive the planet's orbital period and radius, the orbital inclination, and the long half-axis of the orbit. Nevertheless, the probability of a transit is small, unlike RV, which does not need a specific system configuration.
- *Gravity microlensing*: Gravity lensing refers to the alignment of a *lens* celestial body and a background light source with respect to the observer,

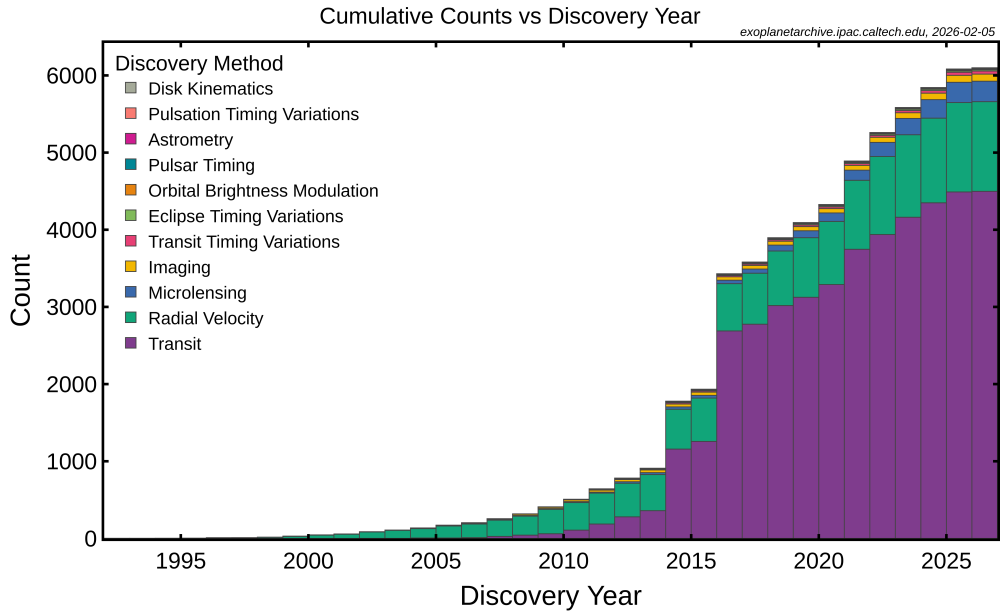


Figure 1.6: Cumulative number of exoplanets detected against year from NASA Exoplanet Archive.

producing a similar effect as the light-gathering effect of a lens (see bottom illustration in Fig. 1.7). Thus, if the lenticular body is a star with a planetary companion, the planet will also be a lens of the background light. It can be used to detect Earth-like planets, but it is a transitory phenomenon.

- *Astrometry*: Astrometry has been one of the most used and powerful techniques in astronomy. It consist on a photometric monitory of a target, such a star, so we can measure its movement on sky (see illustration in middle-left of Fig. 1.7). The motion observed can be due to many factors, one of which is the gravitational pull of a companion, such as an exoplanet. Using astrometry, we can derive the planet's mass, the system's orbital inclination, and the orbital period (Liu and Zhao, 2005).
- *Direct imaging*: Using adaptive optics or coronagraph direct imaging, one can block the light coming from a star. If it has planetary companions large enough and in a large orbit, a direct image of the planet can be taken using the reflecting light from the star on the planet (see illustration in middle-right of Fig. 1.7). Using time series, one can characterize the system, like Chauvin et al. (2004) or Lagrange et al. (2009). This is a direct technique, unlike the RV, transit, or astrometry methods. In general, only loose constraints can be given on the planet's mass, derived from the star's age and the planet's temperature.

A more detailed explanation of these methods can be found in the work from Dai et al. (2021). Although these are the main methods used to detect and characterize exoplanets, there are many more, such as *transit timing variations*, *eclipse timing variations*, *pulsar timing*, *orbital brightness modulation*, or *pulsation timing*

variation. Combining several of the methods allows us to properly characterize a planetary system. For example, using transit and RV measurements, we can derive the planet's true mass and radius, and thus its density, which can inform modeling of its interior and atmosphere.

There are a large number and variety of space missions, observatories, and surveys dedicated to the detection and characterization of exoplanets using different methods. Worth mentioning space-based missions and observatories are (i) the Kepler mission, a turning point in the search of exoplanets providing thousands of new detections from 2009 to 2018 (Borucki et al., 2010). (ii) TESS⁴ (Transiting Exoplanet Survey Satellite), launched by NASA in 2018 that performs an all-sky survey searching for exoplanets around the closest and brightest stars to the Sun, which delivered remarkable results (Ricker et al., 2015); and (iii) the JWST (James Webb Space Telescope) launched in 2021, which has changed the atmospheric characterization of exoplanets (Kempton and Knutson, 2024). Many other examples are HST (Hubble Space Telescope; Anderson et al., 1994), Gaia (Gaia Collaboration et al., 2016b), CHEOPS (CHaracterising ExOPlanet Satellite; Benz et al., 2021), or the future missions of PLATO (PLANetary Transits and Oscillations of stars; Rauer et al., 2025), ARIEL (Atmospheric Remote-sensing Infrared Exoplanet Large-survey; Pascale et al., 2018), and HWO (Habitable Worlds Observatory Domagal-Goldman, Crooke, and Dressing, 2023).

There is also a large number of ground-based observatories, starting with ELODIE that make the first dedicated spectrometer for very accurate RV measurements. HARPS[High Accuracy Radial velocity Planet Searcher;]] (Pepe et al., 2000) is, like ELODIE, a RV planet hunter that started observing in 2002. Recently, NIRPS (Near Infra Red Planet Searcher; Bouchy, Wildi, and González Hernández, 2022) joined HARPS in the NIR with excellent results. CARMENES⁵ (Quirrenbach et al., 2014), at the Calar Alto Observatory, searches for Earth-like planets around M-dwarf stars since 2016 with the RV technique both in the VIS and the NIR. First TRAPPIST (Transiting Planets and Planetesimals Small Telescope; Gillon et al., 2011) and now SPECULOOS (Search for habitable Planets Eclipsing ULtra-coOL Stars; Jehin et al., 2018; Sebastian et al., 2021) look for transiting Earth-like companions around ultracool dwarfs, with big contributions such as the multiplanetary system TRAPPIST-1 (Gillon et al., 2017a), the detection of SPECULOOS-2 b, a temperate super-Earth (Delrez et al., 2022), and the discovery of SPECULOOS-3 b (Gillon et al., 2024). And many other instruments, such as MAROON-X (M-dwarf Advanced Radial velocity Observer Of Neighboring exoplanets; Seifahrt et al., 2018), ESPRESSO (Echelle SPectrograph for Rocky Exoplanets and Stable Spectroscopic Observations; Pepe et al., 2021), KPF (Keck Planet Finder; Gibson et al., 2024), SPIRou (SPectropolarimètre InfraROUge; Artigau et al., 2014), CRIRES+ (Cryogenic high-resolution InfraRed Echelle Spectrograph; Dorn et al., 2023), etc. The future also looks very bright with the upcoming Extremely Large Telescope

⁴ <https://tess.mit.edu/toi-releases/>.

⁵ Calar Alto high-Resolution search for M dwarfs with Exoearths using Nearinfrared and optical Échelle Spectrographs.

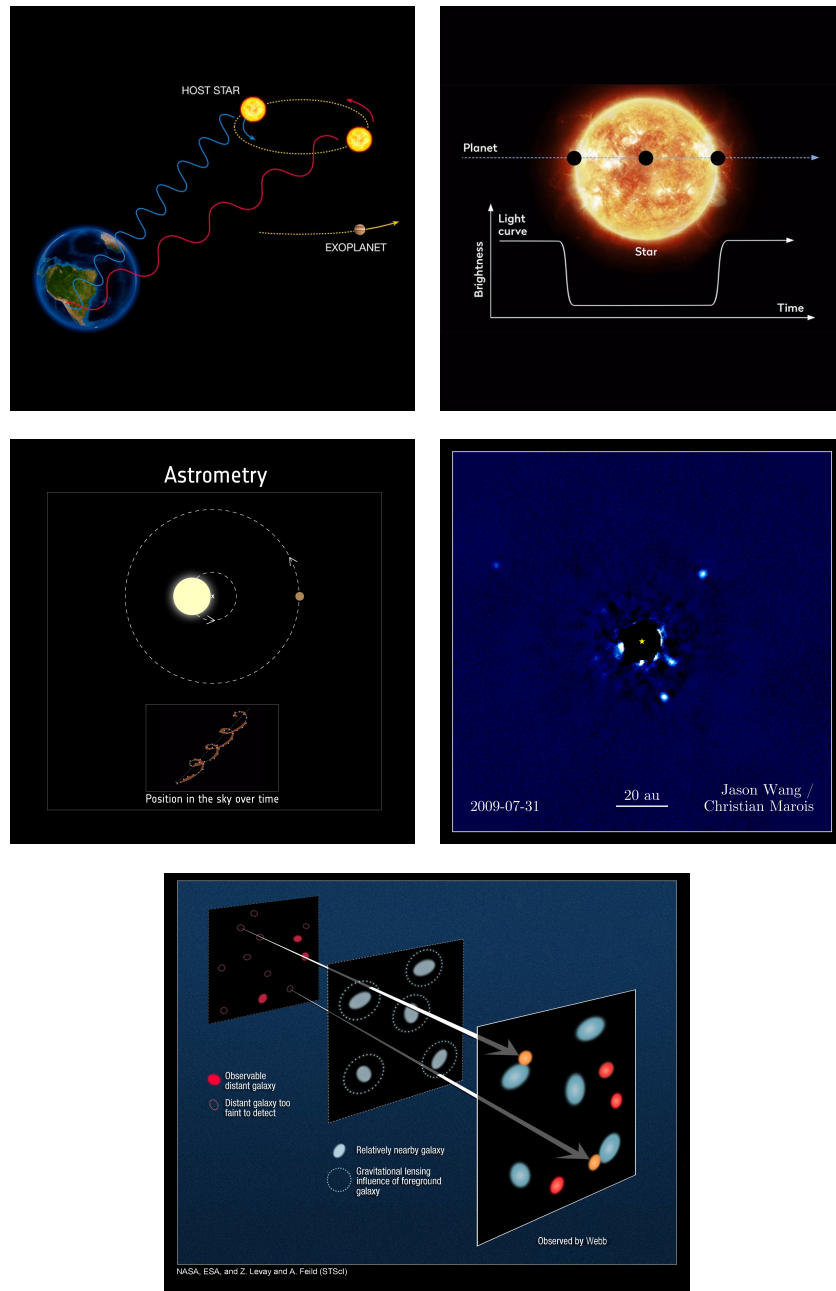


Figure 1.7: Illustrations of four techniques for exoplanetary detection and characterization. From left to right and up to down the Doppler spectroscopy (ESO), transit (BBC), astrometry (ESA), direct imaging (NASA), and gravity lensing (NASA).

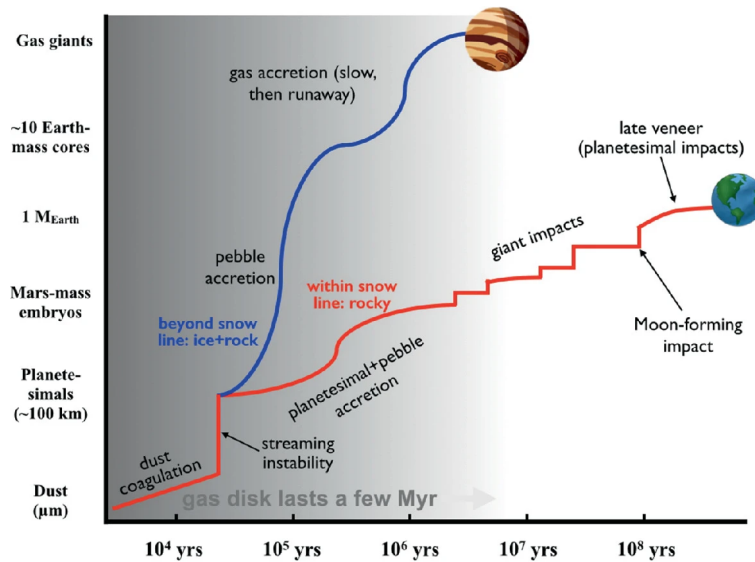


Figure 1.8: Sketch of planetary formation in the Solar System (Raymond and Morbidelli, 2022).

(ELT; Padovani and Cirasuolo, 2023) from the European Southern Observatory (ESO), equipped with instruments such as ANDES (ArmazoNes high Dispersion Echelle Spectrograph; Marconi et al., 2024).

1.2.3 Planet formation models

Classical models of planet formation propose that planetary systems form in protoplanetary disks of gas and dust around young stars, as a natural outcome of the star formation process (Safronov, 1972). Fig. 1.8 shows a sketch of the timeline of planetary formation in the Solar System. Planetary formation can be divided into the following phases (Armitage, 2020; Raymond and Morbidelli, 2022).

From dust to planetesimals

At the beginning, dust is strongly coupled with gas, which produces an aerodynamic drag on the dust (Whipple, 1972; Weidenschilling, 1977). This produces a significant variation in the relative velocity between dust particles and the gas. The gravity of the host star and the gas drag dominate the dynamics of dust particles in the perpendicular direction to the medium plane of the disk. Consequently, dust settles toward the disk mid-plane on a timescale inversely proportional to particle size. Without taking into account the growth of the particles during this process, a typical $1\ \mu\text{m}$ particle settles down on the plane in 10^5 years in a Sun-like star 1 au disk. The growth of the particles significantly reduces the timescale by about two orders of magnitude. Further effects, such as the disk turbulence, must be taken into account for a refined theory of this process.

Once the dust settles onto the disk mid-plane, the particles, coupled to the gas, move at sub-Keplerian velocities and drift toward the disk center. The particles collide due to their differential velocity. When they reach a few-meter size, the orbital decay time becomes smaller than the collision time (a few hundred years), so bigger particles can not be explained with a simple coagulation model (Takeuchi and Lin, 2002). Thus, we need an alternative mechanism that allows to create bigger structures, not based solely on accretion, and needs to be quick enough to form planetesimals (order of kilometers) before they are pulled to the central object.

Whipple (1972) proposed that particles move towards pressure maxima, gathering huge solid groups. The *streaming instability* model (Youdin and Goodman, 2005) proposes the formation of pebbles from these groups. The mechanism is based on a turbulent disk with gravitational instabilities arising from an increase in the surface density of solids due to local accumulation of individually coupled particles in the gas. In a high-density region, particle groups will approach the Keplerian speed, halting the inward decay and initiating planetesimals (Johnson et al., 2007).

From planetesimals to protoplanets

In the classical models, protoplanets grow from an already formed population of planetesimals. The first stage corresponds to orderly growth, in which larger pebbles experience slower relative growth than smaller ones, while their radii increase linearly with time (Safronov and Zvjagina, 1969; Nakagawa, Hayashi, and Nakazawa, 1983). Once one of the pebbles is big enough, gravity starts to dominate the growth, in proportion to the escape velocity and inversely proportional to the relative velocity between the largest pebble and the surrounding planetesimals. As it grows, the escape velocity increases, whereas the relative velocity decreases due to the dynamic drag.

Under these conditions, the runaway growth phase begins (Kokubo and Ida, 1996), in which larger bodies grow exponentially faster than smaller ones. First, the relative velocity between the growing pebble and the planetesimals increases mass-independently. At some point, it starts to depend on mass, and the larger objects grow more slowly than the smaller ones; the growth is linear. The high-velocity planetesimals begin to fragment, enhancing the growth of larger pebbles. Each protoplanet accretes planetesimals within its gravitational sphere of influence until a maximum mass is reached (Hasegawa and Nakazawa, 1990). This new regime lasts for about 10^6 years (Ormel and Klahr, 2010).

From protoplanets to terrestrial planets

During the gas phase, as protoplanets accrete material, the gas will also grow, forming an atmosphere in hydrostatic equilibrium. After the gas is dissipated, some perturbations will occur due to collisions when growing zones superpose. This leads to fragmentation, ejection, and impact of the protoplanets. This will

happen until they reach stable orbits with enough separation between them. The giant-impact phase can last for over 10^8 years until terrestrial planets form.

Giant planets can also form if the gas and dust density is high enough (Perri and Cameron, 1974; Mizuno, 1980; Pollack et al., 1996). If the solid nucleus has a mass equal to that of the accreted gas, the gas collapses gravitationally, leading to a runaway gas accretion that lasts about 10^5 years until the gas giant is formed. For low-mass stars such as M dwarfs, the observed protoplanetary disks are not massive enough for giant planets to form (Ward-Duong et al., 2018), although some of them have been detected (Bryant et al., 2025).

The *pebble accretion* model suggests that in an early stage, protoplanets and planetesimals coexist with particles strongly coupled to the gas, and under certain circumstances, the planetary growth might be essentially dominated by pebble accretion (Ormel and Klahr, 2010; Lambrechts and Johansen, 2012; Rubie et al., 2015; Johansen and Lambrechts, 2017). Pebble accretion leads to a growing process in which both gas and gravity play important roles. It is characterized by the settling of gas in the gravity potential of the massive object, which is mass-dependent. There is a critical mass that determines whether the growth is dominated by the object's gravity or by the Hill radius, which ends when the isolation mass is reached (Adams and Batygin, 2022). The pebbles being pulled towards the star greatly affect the growth rate, which is more efficient beyond the ice line, where pebbles are larger and harder to fragment. This would explain the formation of gas giants in the outer Solar System, and smaller rocky planets in the inner part (Lambrechts et al., 2019). Although migration processes might play a significant role in the formation of close-in gas giants in other stellar systems, additional explanations are needed to better describe planet formation.

1.2.4 Atmospheric studies

A planet's atmosphere is a fundamental planetary property and one of the most informative probes of its physical and chemical state. Its composition, pressure-temperature structure, clouds, and dynamics provide key insights into planetary formation and evolution, present-day climate, and, in some cases, potential habitability. In exoplanet science, atmospheric properties can be constrained through spectroscopy, most commonly in transmission and emission, as well as through phase-curve observations and, for some systems, direct imaging. At the same time, atmospheric modeling, building on our understanding of Solar System planets, is essential for interpreting these observations and connecting the measured spectra with the underlying physical and chemical processes. Atmospheric studies, therefore, bring together theory and observations, and play a central role in our broader understanding of exoplanets.

In order to characterize the atmosphere of an exoplanet, it will ideally be transiting⁶. The techniques for observing and characterizing the atmospheres

⁶ It is not mandatory that the planet is transiting; we can also use reflected light to study the atmospheres. Nevertheless, we focus on transiting planets because they offer special opportunities to measure atmospheric properties.

use the system's orbital geometry to extract the planetary signal from the combined light of the planet and the host star.

The first detection of an atmosphere outside the Solar System was in 2002 (Charbonneau et al., 2002), in HD 209458b (a hot Jupiter), the only transiting planet known at the time. They observed an excess of absorption at 589.3 nm during the transit, the sodium resonance doublet, using data from the HST. It is also possible to study the atmosphere in emission during a secondary eclipse (Deming et al., 2005; Charbonneau et al., 2005).

Over the past two decades, more than 100 exoplanetary atmospheres have been claimed, with detections of several dozen atomic and molecular species, as well as clouds and hazes (Burrows et al., 2014; Madhusudhan et al., 2016; Deming and Seager, 2017; Madhusudhan, 2019). Although many of these detections have high statistical significance, some are questioned by the community and remain open for discussion, with many revisits to some interesting systems, especially as instrumentation evolves; a clear example is the JWST era (Kempton and Knutson, 2024). In particular, ground-based and space-based surveys such as WASP (Wide Angle Search for Planets; Butters et al., 2010), SPECULOOS, Kepler, and TESS, have played a crucial role in identifying transiting planets around suitable host stars, thereby providing prime targets for atmospheric follow-up with facilities such as JWST.

One of the most powerful techniques for characterizing exoplanet atmospheres is high-resolution spectroscopy, from facilities such as CARMENES, ESPRESSO, CRIRES+, GIANO, and MAROON-X. With high-resolution spectra of transit and dayside geometries, both in the optical and infrared, we can identify atmospheric elements and discuss different chemical compositions and dynamical patterns (Seidel et al., 2020; Snellen, 2025; Peláez-Torres et al., 2026). The sensitivity to Doppler and shape shifts of spectral lines of high-resolution spectroscopy allows to access to circulation in the atmospheres (Snellen et al., 2010; Miller-Ricci Kempton and Rauscher, 2012; Flowers et al., 2019), and is been used for detection of single species (Charbonneau et al., 2002; Snellen et al., 2008; Snellen et al., 2010; Brogi et al., 2012; Birkby et al., 2013; de Kok et al., 2013; Lockwood et al., 2014; Casasayas-Barris et al., 2021; Stangret et al., 2022) and multiple molecules in the same atmosphere (Hawker et al., 2018; Giacobbe et al., 2021; Sánchez-López et al., 2022). This methodology has ultimately led to the development of Bayesian retrievals (Brogi et al., 2017; Gibson et al., 2020; Cont et al., 2022; Blain, Sánchez-López, and Mollière, 2024).

Using retrieval and Bayesian statistics, we can place constraints on relevant parameters, such as atmospheric elemental abundances, temperature structure, winds, and the planet's rotational velocity. Their implementation has yielded robust statistical significance for detecting molecular signatures in close-orbiting gas giants observed via transmission and emission spectroscopy (Lesjak et al., 2023; Cont et al., 2024; Nortmann et al., 2025). Low-resolution retrievals (e.g. JWST, Madhusudhan and Seager, 2009; Madhusudhan et al., 2014; Evans et al., 2016; Pinhas et al., 2018; Wakeford et al., 2018; Chachan et al., 2019; Chubb et al., 2020) and photometric observations (e.g. TESS, Cont et al., 2024; Cont et al., 2025) can be combined with high-resolution studies in order to provide

tighter constraints on the retrieved parameters (Brogi et al., 2017; Boucher et al., 2023; Smith et al., 2024). High-resolution analysis allows us to distinguish the core and wings of spectral lines, which makes this technique ideal to attempt detections in hazy exo-atmospheres where only line cores may appear above the continua (Pino et al., 2018b; Pino et al., 2018a; Sánchez-López et al., 2020).

There is also a huge effort on atmospheric studies from a modeling perspective. This field was first developed and excelled in the Solar System using global circulation models (GCMs), from one- to three-dimensional approaches. The development of GCMs for Earth science applications, like the Coupled Model Intercomparison Project (CMIP, Eyring et al., 2016), led to the application to other planets in the Solar System, such as Mars (Forget, Hourdin, and Talagrand, 1998), Venus (Lebonnois et al., 2010), and Titan (Lora et al., 2019), and has eventually been applied to exoplanets (Flowers et al., 2019; Steinrueck et al., 2019; Deibert et al., 2019). GCMs can model three-dimensional atmospheres, including equatorial jets and varying temperature profiles across latitude, longitude, and altitude.

1.2.5 Habitability of exoplanets around low-mass stars

The habitable zone (HZ) is defined as the region around a star (or a multi-stellar system) where a terrestrial planet could retain liquid water (Kasting, Whitmire, and Reynolds, 1993). This definition assumes that the most important greenhouse gases are CO₂ and H₂O, so the carbon-silicate cycle acts as a thermostat to regulate the temperature as it does on Earth (Watson, Donahue, and Walker, 1981; Walker, Hays, and Kasting, 1981; Kasting, 1988). The HZ properties (distance and width) will depend on the stellar luminosity. As the luminosity varies with the stellar age, so does the HZ. This strongly depends on the star's spectral type, due to differences in age evolution and luminosity, but also on other factors, such as activity. Depending on the chosen atmospheric model for the planet, the derived HZ properties will vary (Selsis et al., 2007; Kopparapu et al., 2013; Ramirez and Kaltenegger, 2014).

The scientific community has made significant efforts to search for exoplanets, especially Earth-like exoplanets orbiting M dwarfs. There are several reasons for the big interest:

- M dwarfs are less massive, detecting smaller exoplanets around them is easier. The main techniques used to detect and characterize exoplanets are RV and transit (see Sect. 1.2.2), and both benefit from smaller hosts (Fig. 1.9). The amplitude of RV signals is bigger for a same-mass planet hosted by an M dwarf. The depth of transits is also deeper for a same-size exoplanet. It is true that the probability of transit for M dwarfs is smaller than for bigger stars due to their smaller size.
- The HZ of M dwarfs is closer to the star due to their lower temperature. This links to the previous point: because planets in the HZ of M dwarfs are closer to their host stars, they are easier to detect both via RV and transit.

- Low-mass stars also have larger life-spans, making it easier and more probable for life to develop. They are also the most common type of stars in the Milky Way.
- Smaller and cooler stars also result in stronger atmospheric features in transmission spectroscopy, which makes the study of planetary atmospheres more accessible for planets around M dwarfs (Trifonov et al., 2021; Kuzuhara et al., 2024).

Nevertheless, there has been controversy around the potential habitability of worlds orbiting these stars. The main mechanisms that can prevent these exoplanets from harboring life are (i) the tidal locking that can create a hot and a cold side; (ii) the intense flux variability in wavelengths such as X-ray, UV and VIS; and (iii) the effect on flares on the atmosphere, that can even erase them completely (Heath et al., 1999; Lingam and Loeb, 2017), like the study by Crossfield et al. (2022) show. Nonetheless, Tarter et al. (2007) concluded that these effects might not be as worrying as initially was conceived for habitability around M dwarfs.

1.2.6 Occurrence rate of exoplanets around M dwarfs

The study of occurrence rates of exoplanets around M dwarfs is very valuable for understanding the impact of mass, temperature, and stellar environments (activity, disk, ...) on planet formation and evolution. With these analyses, we can understand whether low-mass planets are more frequent around specific subtypes of M dwarfs. The Kepler mission (Borucki et al., 2010) was a turning point in exoplanetary detection, although it primarily targeted G-type stars. Thus, planets orbiting M dwarfs were highly underrepresented (Hardegree-Ullman et al., 2019). Still, the occurrence rate of small planets near their host stars was found to be higher for low-mass stars, especially for early- to mid-M stars (Howard et al., 2012). However, the occurrence rate of exoplanets around late M-dwarf stars is unknown due to their faintness and the lack of dedicated missions or projects focused on them. The statistics of low-mass planets also help test planet formation theories that aim to reproduce the population of exoplanets (Ida and Lin, 2004; Bitsch, Lambrechts, and Johansen, 2015; Miguel et al., 2020; Izidoro, Bitsch, and Dasgupta, 2021; Schlecker et al., 2021a; Schlecker et al., 2021b; Mishra et al., 2021).

Sabotta et al. (2021) compute a preliminary occurrence rate of the CARMENES⁷ GTO (Guaranteed Time Observations) M dwarf sample using 71 targets. The percentage of giant planets increases towards longer periods and is lower than or equal to that found for G stars. Their results for intermediate-mass planets are similar, with an increasing frequency to long periods, in contrast to previous works (Bonfils et al., 2013). In line with the results obtained in the Kepler survey, the abundance of low-mass planets around M dwarfs is at least twice that of G stars (Mayor et al., 2011), with more than one low-mass planet per star. Contrary

⁷ For a detailed description of CARMENES see Sect. 1.4.1.

to the Kepler results, they found that the occurrence rate of short-period orbits is at least equal to, if not greater than, that of longer-period orbits.

Using a much more extensive sample, Ribas et al. (2023) expanded the work from Sabotta et al. (2021). The sample consisted of 238 targets, after filtering from the 362 targets in the CARMENES GTO sample according to specific requirements. For the occurrence rate computation, they account for possible biases, such as the survey's higher sensitivity to stars with planets, because targets with interesting signals are prioritized. They found (i) an excess of giant planets compared with the theoretical predictions, that do not predict any to be formed around stars with masses below $0.5M_{\odot}$; (ii) whereas models predict a bimodal distribution in $M_p \sin i$, they found a power-law distribution; (iii) short-period planets (below 10 days) are significantly less frequent for stars with $M > 0.4M_{\odot}$ compare to the synthetic population; (iv) a high number of low-mass planets (over 1 planet per star in orbits from 1 to 100 days); and (v) an overabundance of short-period planets around low-mass stars compared with more massive stars. The sensitivity of CARMENES is found to be around 15%, and approximately 18% of the stars in their sample host at least one exoplanet, which points to the scenario in which each M dwarf has at least one planetary companion. These occurrence rates are consistent with previous works from HARPS (Bonfils et al., 2013) and HADES (HARPS-n red Dwarf Exoplanet Survey; Pinamonti et al., 2022) surveys, although with a significantly larger sample.

Regarding the lower end of masses, Kaminski et al. (2025), extended the analysis for CARMENES M5.5 and cooler stars ($M \leq 0.16M_{\odot}$). With 15 of these targets, they showed that late spectral types tend to host more small exoplanets in shorter orbits. They found at least twice as many planets on shorter orbits as the occurrence rates found by Ribas et al. (2023). They made an exhaustive analysis to avoid detection biases, and compared their results with planet formation models, observing shorter periods and smaller minimum masses than predicted by standard core accretion (Burn et al., 2021).

1.2.7 Planets orbiting ultracool dwarfs

Thousands of planets have been discovered, with several hundred around M dwarfs. As previously discussed, the variety of low-mass stars is unlike any other spectral type. The stars at the bottom of the main sequence are especially interesting and are called ultracool dwarfs (UCDs), objects later than M6-M7 that extend down to the substellar regime, including brown dwarfs. Only four planetary systems have been detected hosted by UCDs, TRAPPIST-1 (Gillon et al., 2017b), SPECULOOS-2 (Delrez et al., 2022) and -3 (Gillon et al., 2024), and Teegarden's star (Zechmeister et al., 2019; Dreizler et al., 2024).

The interest in these objects, especially for exoplanet detection and characterization, stems from their small, cool, and faint nature. Although at first sight this complicates their observability, RV signals have greater amplitude, their HZ is closer to the host star, and transits are deeper, more frequent, and more likely to occur compared to GFK-type stars. A classical representation of the

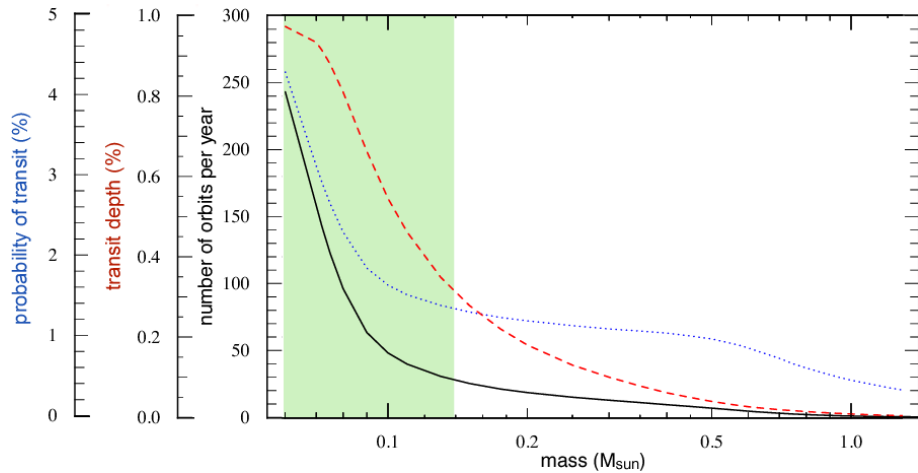


Figure 1.9: Probability, depth, and frequency of transits are represented as a function of stellar mass (He, Triaud, and Gillon, 2016).

transit studies around UCDs is shown in Fig. 1.9, where the probability, depth, and frequency of transits are represented as a function of stellar mass (He, Triaud, and Gillon, 2016). All these characteristics significantly improve for stellar masses below $0.15 M_{\odot}$. Furthermore, for both transits and occultations, the signal-to-noise ratio (S/N) will be higher for UCDs than for early- and mid-type M dwarfs for a given light curve (Pont, Zucker, and Queloz, 2006).

Analysis of spectral features, both in transmission and emission, is also enhanced for late M dwarfs, compared to early- and mid-type stars, as the S/N obtained increases (Wunderlich et al., 2019). Earth-like planets around UCDs are expected to have atmospheres rich in CH_4 and H_2O . The cooler the star, the more the spectra will be shifted to the NIR, leading to an enhancement in the abundances of H_2O , NO_2 , and CH_4 , and a decrease in the production of O_3 , because of weaker UV emission (Rugheimer et al., 2015). Earth-like planets with lower O_3 levels are expected not to have a temperature inversion, unlike Earth, and higher CH_4 concentrations heat the middle atmosphere by up to 60 K. These spectral features are expected to be accessible to JWST.

1.3 THE RADIAL-VELOCITY TECHNIQUE

This section introduces the physical basis of the RV technique, the extraction of RVs with `serval` (SpEctrum Radial Velocity AnaLyser), and the statistical tools used to identify planetary signals. This section provides an overview of the RV technique, focusing on its physical foundations, practical implementation, and modern developments. We describe the principles behind Doppler spectroscopy, the extraction of precise RV measurements using state-of-the-art tools such as `serval`, and the statistical methods employed to identify and validate planetary signals. Particular attention is given to recent advances in mitigating stellar activity and improving detection sensitivity, which are especially relevant for the study of low-mass and ultracool dwarfs.

1.3.1 The theory of radial velocities

It was Newton in 1687 who first introduced a theoretical framework for gravity. If we apply the equations in a two-body system (e.g., a host star and a planet), we can find a point of equilibrium, the barycenter of the system, around which both bodies orbit. If we can measure the movement of the star (though the induced RV by the planet), we can derive some properties, such as the orbital period and the projected mass of the planet in the line of sight.

To measure this movement (i.e. the RV), we use the Doppler effect. Regarding electromagnetic waves, the movement of a light source will produce a shift in its spectrum for an observer. This reddening follows specific equations, derived by Einstein (1905):

$$\lambda = \lambda_0 \sqrt{\frac{1 - v_r/c}{1 + v_r/c}}, \quad (1.1)$$

where λ is the observed wavelength, λ_0 the original wavelength, v_r the RV of the star, and c the speed of light in vacuum. Defining the spectrum shifts as $\Delta\lambda = \lambda_0 - \lambda$, the equation can be re-write as:

$$\frac{\Delta\lambda}{\lambda} = \frac{v_r}{c}, \quad (1.2)$$

which corresponds to the classical approximation of the Doppler effect, valid in the limit $v_r \ll c$. Therefore, the spectral shift is directly proportional to the RV of the star, and will be negative (redder) for a star moving away, and positive (bluer) if it is moving towards the observer. In practice, this shift is derived in high-resolution spectroscopy by measuring the movement of narrow spectral lines relative to their reference wavelengths.

Using the equations of orbital mechanics, we can derive some properties of the system once the RVs are measured. Assuming a two-dimensional reference framework, with the system's origin at the barycenter, and the x-axis positive towards the periapsis, we can write the Cartesian coordinates of the moving star as:

$$x = r \cos \nu, \quad y = r \sin \nu, \quad z = 0, \quad (1.3)$$

where r is the distance of the star to the barycenter, with a general expression for an ellipse:

$$r = a \frac{1 - e^2}{1 + e \cos \nu}, \quad (1.4)$$

being e the orbit's eccentricity and ν the true anomaly, that is related to the eccentric anomaly (E) by:

$$\tan \frac{\nu}{2} = \left(\frac{1 + e}{1 - e} \right)^{1/2} \tan \frac{E}{2}. \quad (1.5)$$

For a circular orbit, where $e = 0$, both true and eccentric anomalies would be equal; thus E accounts for the non-circularity of the orbit. Going to Kepler's equation of movement:

$$M = E - e \sin E, \quad (1.6)$$

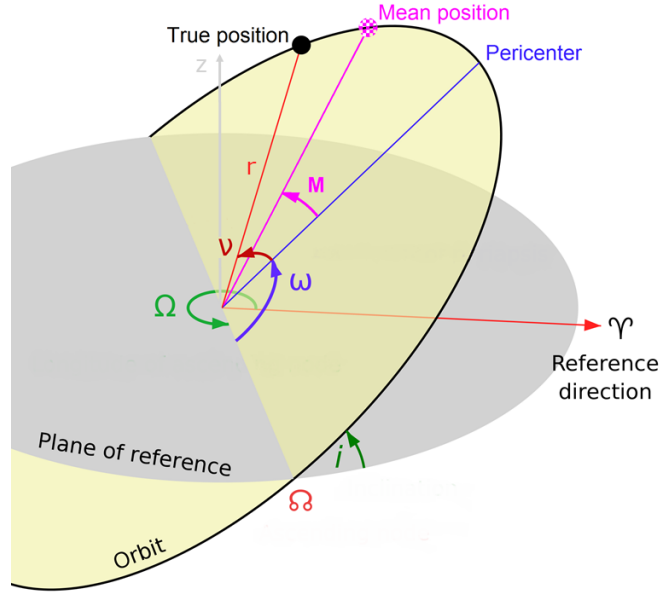


Figure 1.10: Illustration of the orbital parameters and configuration, with the observer's direction z .

where M is the mean anomaly, which does not represent a physical angle, but rather a parameter describing the position of the orbiting body as a phase since the last periastron passage (t_p), resulting in:

$$M = \frac{2\pi}{P}(t - t_p), \quad (1.7)$$

with the orbital period P , and a time t . Assuming a known t_0 , the corresponding $M_0 = M(t_0)$, and $\Delta t = t - t_p$:

$$M = \frac{2\pi}{P}\Delta t + M_0, \quad (1.8)$$

allowing to write ν as a function of e , P , and Δt .

If we define a more realistic three-dimensional framework (see Fig. 1.10⁸), we will have the Cartesian coordinates rewritten as:

$$\begin{aligned} x &= r [\cos \Omega \cos(\nu + \omega) - \sin \Omega \sin(\nu + \omega) \cos i], \\ y &= r [\sin \Omega \cos(\nu + \omega) - \cos \Omega \sin(\nu + \omega) \cos i], \\ z &= r \sin(\nu + \omega) \sin i, \end{aligned} \quad (1.9)$$

where i is the orbital inclination, Ω the longitude of the ascending node, and ω the argument of the periastron.

In this case, the RV of the star is obtained by deriving z as a function of time, where only ν is time-dependent. Thus, using Kepler's Second Law:

$$\frac{d\nu}{dt} = \frac{2\pi}{P} a^2 \sqrt{1 - e^2}, \quad (1.10)$$

⁸ By Tfrooo - Own work, CC BY-SA 4.0.

where a is the semi-major axis of the orbit, and the star's RV can be written as:

$$v_r = \gamma + K [\cos(v + \omega) + e \cos \omega] , \quad (1.11)$$

where γ is the systemic velocity, and K the semi-amplitude of the RV signal with respect to the observer, defined as:

$$K = \frac{2\pi}{P} \frac{a_* \sin i}{\sqrt{1 - e^2}} , \quad (1.12)$$

where a_* is the star's semi-major axis with respect to the system's barycenter.

In this way, measuring the Doppler effect, we can derive the planet's orbital period P and the semi-amplitude K . For a circular orbit, the RV time series will be a pure sinusoidal with amplitude K and period P , but for non-circular orbits, the modeling of $v_r(t)$ will also give the system's eccentricity.

Now, Kepler's Third Law can be written as:

$$\frac{P^2}{a^3} = \frac{4\pi^2}{G(M_* + M_p)} , \quad (1.13)$$

where M refers to the mass of the star ($*$) and the planet (p), and using the relations $a = a_* + a_p$ and $M_* a_* = M_p a_p$, K can be written as:

$$K_*^3 = \frac{2\pi G}{P(1 - e^2)^{3/2}} \left[\frac{M_p^3 \sin^3 i}{(M_* + M_p)^2} \right] , \quad (1.14)$$

where the term in brackets is known as the mass function, and G is Newton's gravitational constant. Assuming that the star's mass M_* is known and that $M_p \ll M_*$, the minimum mass of the planet $M_p \sin i$ can be expressed as:

$$M_p \sin i = \left(\frac{P}{2\pi G} \right)^{1/3} K M_*^{2/3} \sqrt{1 - e^2} . \quad (1.15)$$

From Eq. 1.13 and the semi-major axis-mass relation, the semi-major axis of the orbit of the planet can be written as:

$$a_p = \left(\frac{G}{4\pi^2} \right)^{1/3} M_*^{1/3} P^{2/3} . \quad (1.16)$$

The RV method allows us to establish a lower limit to the planet's mass if the orbital inclination i is unknown. Multi-technique observations of a planetary system are crucial for properly constraining the planet's parameters. From astrometry and transits, the inclination can be measured, but it is not always possible, because astrometry usually gives better results for massive objects in wide orbits, and RV observed systems are not always (rare indeed) transiting. Nonetheless, statistics tell us that systems with $i \approx 0^\circ$ are unusual. Assuming a uniform distribution for $i = 60^\circ - 90^\circ$, masses will be typically less than 15% larger than the minimum mass.

The RV amplitude of a planetary signal depends on the mass of the star and the planet, as well as the orbital period of the companion. For example, the

Earth induces a 10 cm s^{-1} amplitude on the Sun (Latham, 2011). Nevertheless, an exoplanet with one Earth mass in the HZ of an M dwarf will induce a much larger RV signal. This is a result of (i) the low temperature of M dwarfs, thus, the HZ is closer (Kopparapu et al., 2013), and (ii) the mass of the star is also significantly smaller than the Sun. For example, if the Earth was hosted by an M dwarf with a mass of $0.1M_{\odot}$ and orbiting around its HZ, the RV amplitude would be $\sim 2 \text{ m s}^{-1}$ (Omiya et al., 2014).

1.3.2 Radial-velocity extraction with *serval*

In Exoplanetology, RV time series are used to detect a Keplerian signal. For this, we obtain a specific number of spectra and compute the relative Doppler shifts (i.e., the RVs), so we can obtain the variations of the RVs with time, and look for periodic signals (see Sect. 1.3.3). The number of data points required for a detection will depend on the S/N of the spectra, the RV uncertainties, and the amplitude and period of the planetary signal. For giant planets orbiting close to a bright host, we will need a few spectra, whereas for small planets orbiting a faint star, some hundred observations are typically needed.

There is a significant variety of pipelines developed for extracting RVs from high-resolution spectra. We can divide them based on the model reference spectra, the number of model parameters, and the statistics used to select the RVs. There are algorithms based on the cross-correlation with binary masks (Queloz, 1995; Pepe et al., 2002), others on the least-squares fit with co-added templates (Anglada-Escudé and Butler, 2012; Astudillo-Defru et al., 2015), also the least-squares fitting with modeling of line spread functions (Butler et al., 1996; Endl, Kürster, and Els, 2000), Gaussian processes (GPs) (Czekala et al., 2017), and line-by-line approaches (Artigau et al., 2022). Here, I will focus on the *serval*⁹ pipeline (Zechmeister et al., 2018), which is based on least-squares fitting and template matching.

The *serval* pipeline was developed for CARMENES as the standard algorithm for RV extraction. It has also been adapted for other instruments such as HARPS. To properly weight the errors, forward modeling is applied. The spectral template used for the RV computation is constructed from real observations, thereby leveraging the RV information inherent in the stellar spectra (Anglada-Escudé and Butler, 2012).

The general concept is (i) using the highest S/N spectrum, the rest of the spectra are shifted; (ii) then, a high S/N template $F(\lambda)$ is constructed by co-adding the spectra; and (iii) the individual RV shifts v_n of each observation n are computed. Multiplicative background polynomials $p(\lambda)$ are obtained during the last step to account for flux variations. The forward model for the observed flux can be expressed as:

$$f(\lambda) = p(\lambda)F(\lambda'), \quad (1.17)$$

⁹ <https://github.com/mzechmeister/serval>.

where the last term is the Doppler-shifted template, and λ' is defined as:

$$\lambda'(\lambda, v) = \lambda \frac{1 + z_B}{1 + v/c}, \quad (1.18)$$

where z_B is the total redshift due to barycentric motion of the observer.

The stellar template is constructed directly from observations by combining all available spectra of a given target into a high S/N reference spectrum. Because individual exposures are taken at different barycentric velocities and may also include intrinsic stellar RV shifts, the spectra are sampled at slightly different wavelength points. Therefore, `serval` avoids a simple interpolation onto a common grid and instead performs the co-adding through a weighted regression using cubic B-splines. In this approach, the template is represented as a spline function whose coefficients are fitted in a least-squares sense, naturally incorporating pixel uncertainties and allowing iterative outlier rejection.

Because we are working with spectra from échelle spectrographs (see Sect. 1.4), the measurements are done for several échelle orders. The complete equation for all orders (o), observations (n), and at each pixel (i) is given by:

$$\chi^2 = \sum_{n,i} w_{n,i} [f_{n,i} - p(\lambda_{n,i}, a)F(\lambda'(\lambda_{n,i}, v_n), b)]^2, \quad (1.19)$$

where $w_{n,i} = 1/\epsilon_{n,i}^2$ are the weights, and with the polynomial coefficients a and the coefficients b describing the template.

For obtaining the RVs, Eq. 1.19 is optimized with respect to a (linear) and v (non-linear). To solve the non-linearity, `serval` uses a direct stepping through the velocity parameter space v with $\Delta v = 100 \text{ m s}^{-1}$. At a fixed velocity v_k , the Doppler-shifted template $F_{i,k} = F(\lambda_i, v_k, b)$, is evaluated at each pixel i , and $\chi^2(v_k)$ is obtained from a linear least-square fit for a .

Then, the $\chi^2(v)$ function is explored for its global minimum, which occurs at a point where it takes a parabolic shape. Thus, a parabolic interpolation through the minimum and the two adjacent neighbors provides a refined estimate of v . The uncertainty of v can also be estimated with the $\Delta\chi^2 = \chi^2 - \chi_{min}^2 = 1$ criterion. The error can be re-escalated to account for under- or overdispersion in the fit.

Each order o is fitted separately following this approach, obtaining v_o , and then a global velocity v is computed as:

$$v = \frac{\sum \epsilon_{v_o}^{-2} v_o}{\sum \epsilon_{v_o}^{-2}}, \quad (1.20)$$

and the associated error:

$$\epsilon_v = \sqrt{\frac{1}{\sum \epsilon_{v_o}^{-2}} \frac{1}{N_o - 1} \sum \frac{(v_o - v)^2}{\epsilon_{v_o}^2}} = \frac{\text{wrms}}{\sqrt{N_o - 1}}, \quad (1.21)$$

where wrms is the weighted root mean square and N_o is the total number of échelle orders.

Additionally, `serval` provides other data products such as *chromatic RV index* (CRX), *differential line width* (dLW), *spectral line indices* (e.g., Ca II H&K, H α , and Ca II IRT), or the projected rotational velocity ($v \sin i$, Chapter 4). A full and detailed description of `serval` is given in Zechmeister et al. (2018).

1.3.3 *Detecting planetary signals*

Once precise RV measurements have been extracted from high-resolution spectra, the central task is to identify whether the resulting time series contains periodic signals compatible with planetary companions. This requires separating Keplerian signatures from stellar variability, instrumental systematics, sampling aliases, and other sources of correlated noise. Here, we summarize the main statistical and physical ingredients involved in detecting and modeling planetary signals in RV time series.

An extensive review of the statistical methods for detecting and characterizing Keplerian signals in RV time series is provided by Hara and Ford (2023), and another one by Burt, Dumusque, and Halverson (2025). A great application for these methods is the work by Figueira et al. (2025).

The analysis of RV observations is treated as three coupled problems: (i) reducing raw spectra into RV estimates and diagnostic indicators (see Sect. 1.3.2); (ii) mitigating contaminating signals (stellar activity and instrumental systematics); and (iii) modeling the planetary system.

Mitigating stellar variability

The spectrum of a star varies due to several effects, from planetary signals (i.e., RVs) to stellar variability. To properly detect and confirm a planetary companion to a star, we must distinguish Keplerian from activity-induced signals.

The measured RV is thus inherently contaminated by spurious stellar RV variations induced by surface flows and magnetic activity. In order to mitigate the effects we should (i) use integration times longer than the typical timescale of stellar oscillations (Chaplin et al., 2019); (ii) granulation and supergranulation are not easily avoided as oscillations, and usually are mitigated by averaging measurements over several days (Dumusque et al., 2011; Meunier et al., 2015); and the most impactful, the magnetic activity, with several approaches such as linear combination of activity proxies, use of GPs, tailored line selection, line-depth sensitivity, PCA-based approaches, and deep learning (Burt, Dumusque, and Halverson, 2025).

Modeling planetary systems

Precise RV measurements provide one of the most powerful techniques for detecting and characterizing exoplanets, as first demonstrated by the discovery of 51 Peg b (Mayor and Queloz, 1995). In this framework, planetary signals are modeled as the line-of-sight component of the stellar reflex motion induced by orbiting companions. For a system of N_p planets, the observed RV time series can be expressed as the superposition of Keplerian signals:

$$v(t) = \gamma + \sum_{k=1}^{N_p} v_k(t) + \dot{\gamma}t + \frac{1}{2}\ddot{\gamma}t^2, \quad (1.22)$$

where γ denotes the systemic velocity, $\dot{\gamma}$ and $\ddot{\gamma}$ account for long-term accelerations, and each $v_k(t)$ is defined by the standard Keplerian parameter set (P, K, e, ω, M_0) . The semi-amplitude K encodes the planet's minimum mass through (from Eq. 1.15):

$$K = \left(\frac{2\pi G}{P} \right)^{1/3} \frac{M_p \sin i}{(M_\star + M_p)^{2/3} \sqrt{1 - e^2}}, \quad (1.23)$$

linking the observable Doppler signal to the underlying orbital dynamics. In practice, multi-instrument datasets require additional offset terms and instrument-specific noise parameters to account for differing zero-points and systematics.

Parameter estimation and model comparison are typically carried out within a Bayesian framework (Gregory, 2005). Assuming a likelihood function that incorporates both formal measurement uncertainties and additional uncorrelated “jitter” terms, the posterior distributions for the orbital parameters are sampled using Markov Chain Monte Carlo (MCMC) or nested sampling algorithms. These approaches enable robust uncertainty quantification and principled comparison between models with different numbers of planets via Bayesian evidence or information criteria such as the BIC (Bayesian Information Criterion). Particular care must be taken into account for uneven temporal sampling, spectral window effects, and aliasing, which can generate spurious periodicities or bias inferred orbital parameters.

At the precision required to detect low-mass planets, stellar variability often dominates the error budget. Photospheric inhomogeneities, rotation, and magnetic cycles introduce correlated signals that can mimic or obscure Keplerian signatures. To mitigate these effects, correlated noise is commonly modeled using GP regression with quasi-periodic covariance kernels motivated by stellar rotation and active-region evolution (Queloz et al., 2001; Figueira et al., 2013). Joint modeling of Keplerian components and correlated stellar signals has therefore become essential for reliable planet detection in the sub- m s^{-1} regime. This statistical and dynamical framework reinforces modern RV analyses, enabling the extraction of planetary architectures from high-precision spectroscopic time series.

1.4 HIGH-RESOLUTION NEAR-INFRARED SPECTROGRAPHS

In the search for an Earth-like planet orbiting a very low-mass star, such as UCDs, there have been discrepancies about which spectral range yields the best results: optical or near-infrared. Late M-dwarf stars have significantly higher S/N at NIR rather than at VIS wavelengths, whereas their spectra are extremely rich in molecular features at the visible. Thus, it is difficult to predict the true RV precision at each part of the spectrum. Nevertheless, studies have shown that the optimal wavelength range for M dwarfs lies in the red part of the visible spectrum (Reiners et al., 2018). However, high-resolution NIR spectrographs could also provide crucial information for studies of exoplanets orbiting UCDs.

Table 1.2: Summary table with the spectral range, resolution, and RV precision for high-resolution near-infrared échelle spectrographs.

Instrument	Spectral range	Resolution	RV precision ^a
CARMENES NIR	0.96–1.71 μm	~ 80400	$< 1 \text{ m s}^{-1}$ (VAR25) ^b
NIRPS	0.95–1.8 μm	~ 100000	$< 1 \text{ m s}^{-1}$ (SUMA25)
CRIRES+	0.95–5.3 μm	~ 100000	2–3 m s^{-1} (KÖH25)
SPIRou	0.98–2.35 μm	~ 70000	1 m s^{-1}
HPF	0.81–1.28 μm	~ 53000	1.5 m s^{-1}
IRD	0.97–1.75 μm	~ 70000	1.3–1.9 m s^{-1} (KOT18)
GIANO-B	0.9–2.45 μm	~ 50000	$< 10 \text{ m s}^{-1}$ (CLA17)
iSHELL	1.1–5.3 μm	~ 75000	3–5 m s^{-1}

Notes. ^a RV precision can be measured differently, either on sky or the intrinsic precision from calibration data. The reference of the given value or a link to the web is provided. ^b VAR25 (Varas et al., 2025), SUMA25 (Suárez Mascareño et al., 2025), KÖH25 (Köhler et al., 2025), KOT18 (Kotani et al., 2018), CLA17 (Claudi et al., 2017).

There are a few examples of such complex and specific instruments, especially performing RV searches for exoplanets around M dwarfs. Notable examples include GIANO-B (Tozzi et al., 2016), Infrared Doppler instrument (IRD, Kotani et al., 2018), Habitable zone Planet Finder (HPF, Hearty et al., 2014), SPIRou (Artigau et al., 2014; Moutou et al., 2015), Near Infra Red Planet Searcher (NIRPS, Artigau et al., 2024; Bouchy et al., 2025), CRIRES+, and CARMENES NIR (Quirrenbach et al., 2014; Varas et al., 2025). Table 1.2 summarizes the spectral range and resolution of each of these instruments. To properly contextualize the importance of this thesis, I provide a detailed description of CARMENES NIR and NIRPS. The former is the center of the thesis, whereas the latter is the most recent and precise.

The RV method has been used to detect exoplanets for over three decades. Among the different spectrograph configurations that have been implemented, the fiber-fed cross-dispersed échelle spectrographs are the most successful. The RV precision has lowered at a surprising pace, breaking the 1 m s^{-1} precision fifteen years ago by HARPS (Pepe et al., 2000). Many more instruments have achieved this precision, even lower in the VIS, such as ESPRESSO, with a few tens of cm s^{-1} . Recently, this frontier in the NIR was surpassed by the NIRPS team (Artigau et al., 2024).

The calibration strategy is crucial to achieving high-precision RV measurements. The use of fibers enables simultaneous calibrations during observations using stable sources such as laser frequency combs (LFCs), Fabry-Pérot (FP) interferometers, or hollow cathode lamps (HCLs), and even combining some of them. The reference light is injected in the spectrograph so that both science and calibration light follow an almost identical optical path, ensuring a proper RV measurement.

To achieve such low precision in RV observations at NIR wavelengths, many external perturbations must be minimized. This is achieved by using a thermally

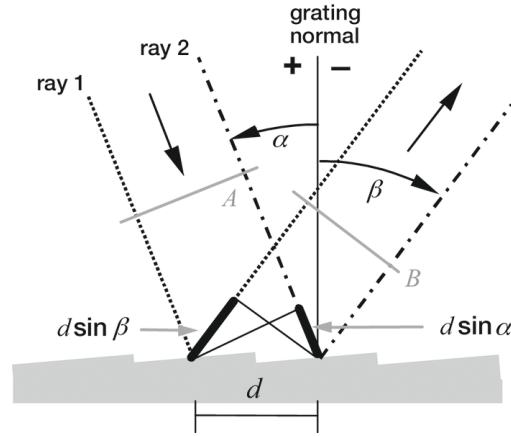


Figure 1.11: Sketch of the grating diffraction. Two parallel rays in phase reach the grating, with groove distance d , and incident and reflecting angles α and β , respectively (Palmer, 2020).

stabilized room, a vacuum vessel, and active cooling systems. An optical bench inside the isolated environment supports all the optical elements. The light is collimated and then injected into the échelle grating by the fiber. The split wavelengths go back to the collimator, redirecting the light beam towards a slit that removes stray light. Then, a second collimator directs the beam to a cross-disperser and into the detector (see Sect. 1.4.1 for details).

The key element to achieve high-resolution spectra is the échelle grating. The reflection of the rays at the different grooves of a general grating can be expressed as:

$$n\lambda = d \sin \alpha + d \sin \beta, \quad (1.24)$$

where n is the diffraction order, d the distance between grooves, and α and β the incident and reflected ray's angles, respectively (see Fig. 1.11; Palmer, 2020). The maxima of the interference pattern of the reflected rays are $n\pi$, which is superimposed on a secondary pattern that results from the interference of the rays reflected in the same groove, known as the blaze fraction. This results in a drastic decrease of the throughput of the maxima for $n \neq 0$, and for $n = 0$ there is no dispersion. This problem is usually solved by tilting the grooves to shift the blaze function to higher orders, which is known as *blazing*. The blazing angle ϕ of échelle grating is $> 45^\circ$. Instruments such as HARPS and HARPS-N are in a *quasi-Littrow configuration*, i.e., the incident and diffracted rays are almost auto-collimated ($\alpha = \beta = \phi$). This ensures high ϕ with a simple optical design. Thus, échelle gratings provide high-resolution, expressed by the angular dispersion equation as:

$$\frac{\delta\beta}{\delta\lambda} = \frac{n}{d \cos \beta} = \frac{2}{\lambda} \tan \phi, \quad (1.25)$$

that represents the increment of the angular dispersion (i.e., the resolution) with n and ϕ .

Nevertheless, high-resolution produces overlapping interference patterns from closely spaced spectral orders. That is why high-resolution spectrographs

use a cross-disperser (i.e., a prism), which allows spatially separating the échelle orders. This results in a different interference pattern and modulation of the throughput of the spectral orders maxima.

1.4.1 CARMENES

The Calar Alto high-Resolution search for M dwarfs with Exoearths using Near-infrared and optical Échelle Spectrographs (CARMENES¹⁰) is a dual-channel échelle spectrograph (VIS: 520–960 nm; NIR: 960–1710 nm) with high spectral resolution ($\mathcal{R} = 94600$ and $\mathcal{R} = 80400$, respectively), mounted on the 3.5 m telescope at the Calar Alto Observatory (CAHA) in Almería, Spain (Quirrenbach et al., 2014; Quirrenbach et al., 2018). The survey has delivered high-quality spectra and RV time series for nearly 400 nearby M dwarfs (Ribas et al., 2023) since its first light in 2016.

The light collected by the 3.5 m telescope is directed to the Cassegrain station, where the CARMENES front end (FE) is located. The FE distributes the light to the calibration unit (CU) and the spectrographs. The light is fed to both CARMENES arms via optical fibers. Each spectrograph is mounted inside a Coudé room under the telescope and isolated with a vacuum vessel and a radiation shield. The calibrations are obtained using the FP interferometer, which is calibrated at the beginning and end of each night with HCLs. The NIR channel also has a cooling system (CS) that keeps the optical bench at a constant temperature of around 140 K.

CARMENES was the first instrument to perform high-resolution spectroscopy simultaneously in both the VIS and NIR. This is especially relevant for its main scientific goal, detecting Earth-like planets around low-mass stars. When going to the lower end of the M-dwarf regime, the emitted flux starts to peak in the NIR wavelength, and the expected RV precision can surpass that of the VIS (Reiners et al., 2018)¹¹. Although in the first years of CARMENES, the NIR channel was not used independently for RV studies, it was highly successful in the study of planetary atmospheres.

CARMENES NIR

There are many subsystems defined during the design of an instrument, and such was the case of CARMENES. To understand how CARMENES NIR works, it is necessary to understand the other subsystems, especially the FE, the fibers, and the CU.

The near-infrared spectrograph system is also divided into several subsystems. The complete list includes *Focal Adapter, Slicer, Collimator, Échelle Grating, Cross-Disperser, Camera, Fold Mirror, Optical Bench, Mechanics, Electronics and Software, Vacuum System, Cooling System, Detector, Detector Cryostat, Exposure Meter, Climatic Chamber, Transport, and Contingency*. Not all these subsystems

¹⁰ <https://carmenes.caha.es>.

¹¹ This is not the only reason to use near-infrared spectroscopy for late M dwarfs, as discussed in detail in Chapter 5.

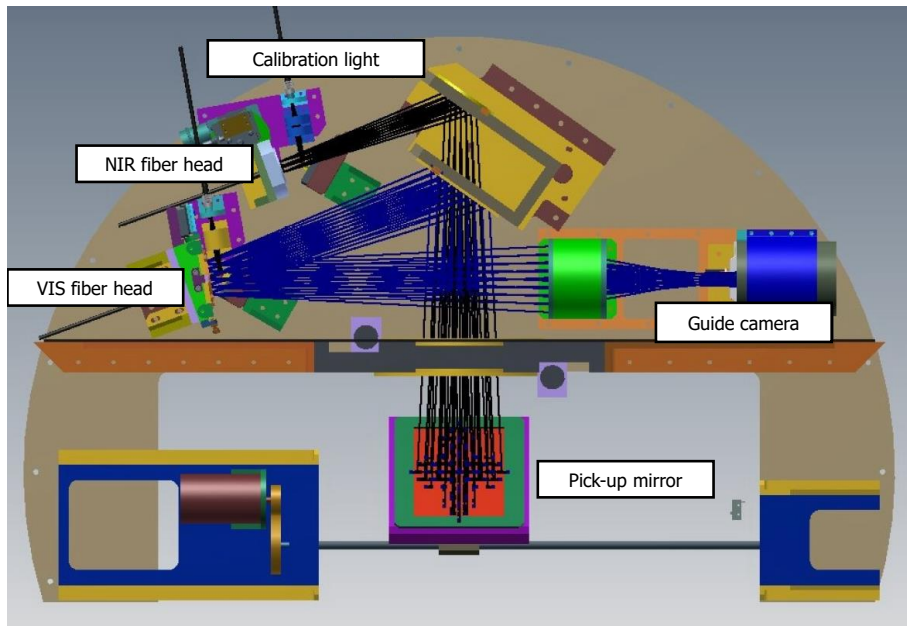


Figure 1.12: Opto-mechanical layout of the CARMENES FE.

are detailed here, but we provide a description of the most relevant ones for this thesis.

Front End and Fibers

The first element that the light encounters after the telescope is the FE. A pick-up mirror injects the light into one of the mounted instruments, the Postdam Multi-aperture Spectrophotometer (PMAS, Roth et al., 2005) or CARMENES. Following the pick-up mirror, the light beam encounters two double-prism atmospheric dispersion correctors, the dichroic beam splitter, an acquisition and guiding system, and the VIS and NIR fiber heads. Because the dichroic reflects the VIS light and transmits the NIR light, there is an additional mirror to feed the NIR fiber head. Acquisition is made easy thanks to the extraordinary pointing accuracy of the 3.5 m telescope. Guiding is performed on the wings of the target star reflected by the mirror (on-axis), on the stars in the 3 arcmin field of view (off-axis), and, on most occasions, in a hybrid mode (i.e., with both on- and off-axis, with a corresponding weight depending on the observing conditions). The FE fibers are $100\ \mu\text{m}$ in diameter, corresponding to a projected aperture of 1.5 arcsec on the sky. A layout of the CARMENES FE is provided in Fig. 1.12.

Calibration Unit

The CARMENES CU consists of two units, one for the VIS and another for the NIR. Each unit has two fibers (A1 and B1) that inject light into the spectrograph through the FE fibers A2 and B2 (see Fig. 1.13). CARMENES operates in a simultaneous-calibration mode, where fiber A2 feeds star light into the

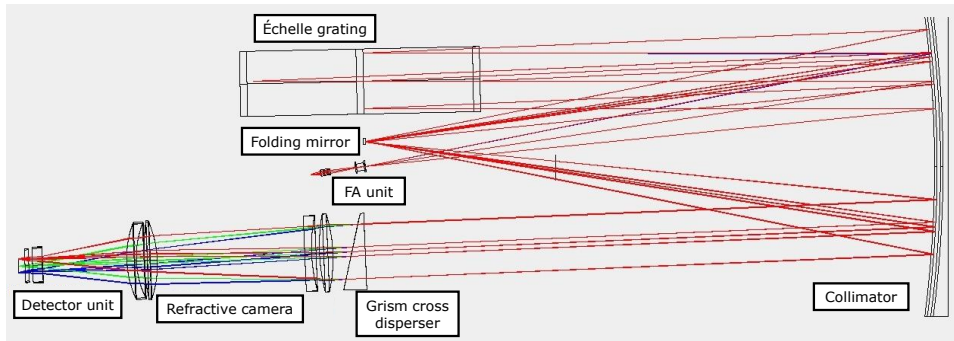


Figure 1.14: CARMENES NIR optical layout with the identified elements.

transmission grating with 80 lines/mm, with a blaze angle of 12° . The refractive camera consists of six lenses, five spherical and one aspherical, with a distance to the detector of 12 mm. The detector is a mosaic of two 2048×2048 -pixel detectors with $18 \mu\text{m}$ pixel size and is aligned with the long side in the dispersion direction. The detector has its own cryostat to maintain proper thermal conditions.

The NIR cooling system

The CARMENES NIR spectrograph requires a CS (Fig. 1.15) in order to maintain all its optical elements at cryogenic temperature (Mirabet et al., 2014; Becerril et al., 2016). Its opto-mechanics (all the optical elements and their mounts) are attached to a massive optical bench, which is surrounded by a radiation shield with a multi-layer insulation blanket. Both the optical bench and the radiation shield are enclosed in a vacuum tank, making convection heat transfer and fluctuations in the refractive index of the residual air negligible. The nitrogen gas flows through pipes that reach heat exchangers on the radiation shield, dissipating the radiative load from the vacuum tank and keeping the radiation shield at working temperature ($\sim 140 \text{ K}$).

The radiation shield passively thermalizes the optical bench via a radiation heat transfer mechanism. Heat conduction between the cold parts (the optical bench and the radiation shield) and the vacuum tank is minimized by using G-10 epoxy fiberglass and appropriate interface geometries.

A separate nitrogen gas preparation unit (N₂GPU) supplies the nitrogen gas to the radiation shield. This N₂GPU is a prototype of ESO's standard continuous flow cryostats, adapted to apply this concept to a spectrograph's CS. Although designed for high thermal stability, it did not achieve the expected performance in practice. A 350-L dewar feeds liquid nitrogen (LN₂) into the N₂GPU, which is replaced with a full, pressurized one every morning. The N₂GPU is equipped with several stages that evaporate the LN₂ and bring the gas to the working temperature using two proportional–integral–derivative control loops. It was designed to provide a highly thermally stable coolant, eliminating the need for active thermal-control heaters inside the vacuum tank and, consequently, reducing the system's dependence on their performance and the risk of failure.

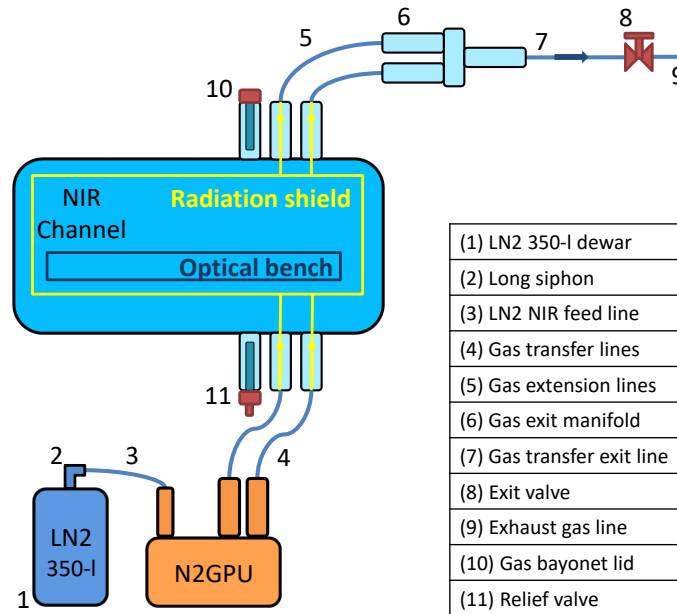


Figure 1.15: Simplified layout of the CARMENES cooling system during normal operation showing the main components, escribed in Becerril et al. (2016).

Just at the exit of the N₂GPU, the coolant is split into two independent circuits, each flowing through a vacuum-insulated gas transfer line. The coolant enters the vacuum tank through a pair of flow splitters that divide the two circuits into ten cooling lines, feeding a total of 19 heat exchangers that cool the radiation shield. The warm gas is evacuated through a single return circuit.

Originally, the thermalization was performed by a control loop with a cryogenic on/off valve installed at the exit circuit. The loop controls the valve by comparing the temperature measured by the reference sensor on the radiation shield to a predefined setpoint. The open/close states of the on/off valve kept the temperature value within a dead-band below the setpoint: when the value of the temperature sensor increased up to the limit defined by the setpoint, the on/off valve opened to cool down the radiation shield, whereas the warming phase occurred when the valve was closed, allowing the coolant to remain in the circuit.

The objective of this design and thermal stabilization strategy was to use the high thermal inertia of the metallic mass of the optical bench to dampen temperature variations from the radiation shield, ensuring that the opto-mechanics remained thermally stable.

Short-term variations in the shield introduced by the on/off valve (see Fig. 1.16) were anticipated and expected to be suppressed by the bench's damping effect. However, in practice, these fluctuations, together with additional variability caused by the underperforming N₂GPU, were not fully absorbed and were transmitted to the opto-mechanics. As a result, the RVs measured

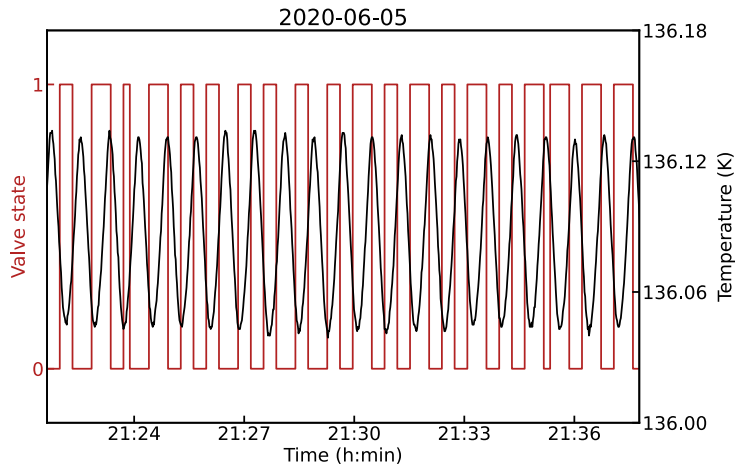


Figure 1.16: Temperature response of the radiation shield (black) to the binary states of the on/off valve (red), recorded on 2020-06-05. The valve opens and closes periodically, producing a saw-tooth temperature pattern characteristic of the discontinuous flow mode.

with the NIR channel showed a direct correlation with the thermal variability of the radiation shield, through a mechanism that remains not fully understood.

This discovery indicated that any improvement in the thermal stability of the spectrograph, and hence the intrinsic precision of its RVs, required a reduction of the thermal variability of the radiation shield and, consequently, an enhancement of the N2GPU's thermal stabilization performance.

1.4.2 NIRPS: *The Near-InfraRed Planet Searcher*

The Near-InfraRed Planet Searcher (NIRPS, Bouchy, Wildi, and González Hernández, 2022) is an instrument located at the 3.6 m telescope at La Silla Observatory (ESO) in Chile. It is the result of an international collaboration co-lead by the Observatoire du Mont-Mégantic at Université de Montréal (Canada) and the Observatoire Astronomique de l'Université de Genève (Switzerland), with many other institutions, and ESO as an associated partner. As well as CARMENES NIR, NIRPS is a high-resolution spectrograph in the YJH bands, dedicated to the search of Earth-like exoplanets orbiting low-mass stars, and can be used as the NIR arm of HARPS. The NIRPS design team drew on experience gained with HARPS, ESPRESSO, and SPIRou.

There are some similarities and some differences with the CARMENES design. It is interesting to detail them in order to understand why NIRPS is performing better than CARMENES NIR in RV studies of M dwarfs. The NIRPS results are below the 1 m s^{-1} (Suárez Mascareño et al., 2025), whereas CARMENES NIR is at few m s^{-1} . It is especially noteworthy that the NIRPS team finds a photon noise around 1 m s^{-1} (Artigau et al., 2024), while CARMENES NIR is $\sim 5 \text{ m s}^{-1}$ (Reiners et al., 2018; Varas et al., 2025).

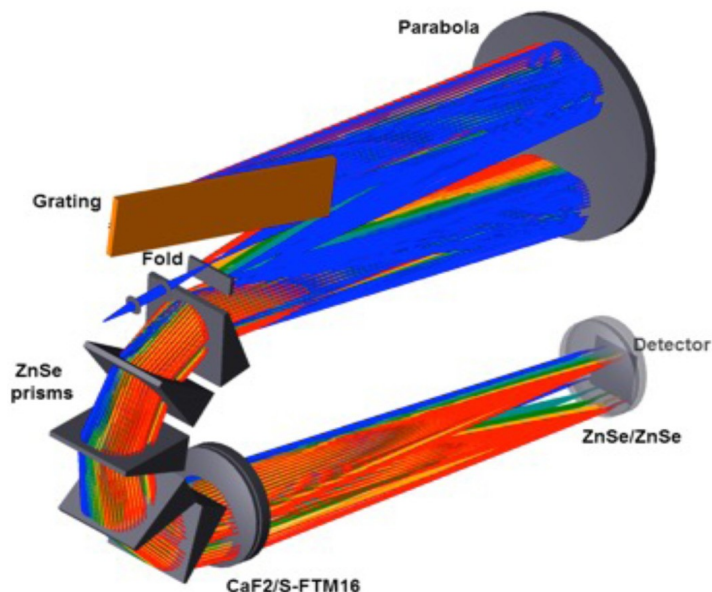


Figure 1.17: Optical layout of NIRPS spectrograph (Bouchy et al., 2025).

The FE subsystem of NIRPS collects light from the telescope at the Cassegrain focus and, using a dichroic, injects it into the fiber link. This converts the F/10.9 beam into an F/4.2 beam and injects it into the fiber. It supports a High Accuracy (HA) mode with $R \approx 84000$ and 0.4 arcsec octagonal fiber, and a High Efficiency (HE) mode with 0.9 arcsec octagonal fiber that feeds a rectangular fiber, and $R \approx 72000$. There is a simultaneous calibration, either using an FP unit or a sky light. The NIRPS spectrograph is in the Coudé room, enclosed in a cryostat, mounted inside a vacuum vessel, and the system is maintained at 75 K with a stability of 1 mK. It is also a cross-dispersed échelle spectrograph, with a similar optical layout (see Fig. 1.17) as CARMENES NIR (see Sect. 1.4.1). The detector is a hybrid CMOS HAWAII-4RG with 4096×4096 pixels. This is one of the differences with CARMENES NIR, which uses a mosaic of two 2048×2048 HAWAII-2RG detectors.

The 3.6 m telescope uses adaptive optics (AO) to improve observations, whereas the 3.5 m telescope (Calar Alto Observatory) does not have AO. The thermal stability is similar in both cooling systems¹³, as well as the vacuum conditions (see Artigau et al., 2024; Varas et al., 2025). Nevertheless, the observed night-to-night drifts in both instruments are significantly different. The typical nightly-zero points (NZPs) of CARMENES NIR are at $3\text{--}4 \text{ m s}^{-1}$ (Ribas et al., 2023; Varas et al., 2025), and at few cm s^{-1} in NIRPS (Artigau et al., 2024), with RV precision on sky around 1 m s^{-1} and 6 m s^{-1} , respectively.

In addition to the differences in the instrument design, the data reduction and calibration choices significantly affect the derived RVs. CARMENES uses *serval* (see Sect. 1.3.2), a template-matching least-squares fitting algorithm, to perform telluric masking. In recent years, efforts within the CARMENES consortium have led to a telluric absorption correction procedure (Nagel et al.,

¹³ The stability is similar since June 2022, when CARMENES NIR CS was upgraded (see Chapter 3).

2023) that uses barycentric motion to discriminate between stellar and telluric lines. On the other hand, NIRPS uses two pipelines for data reduction during cross-validation: DRS (Pepe et al., 2021) and APERO¹⁴ (Donati et al., 2020; Cook et al., 2022). APERO performs calibration and telluric correction, and provides RVs. The telluric correction strategy is particularly notable and comprises two steps. First, the TAPAS atmospheric model (Allart et al., 2022) is applied to the science data and to a set of hot star calibrators. The second step accounts for the scientific spectrum by dividing it by a stellar template, removing cross-terms between telluric absorption and stellar features. They derive the residuals of the telluric correction using hot stars, which are correlated with airmass and water absorption. Using a PCA-based approach (Artigau et al., 2014), first-order residuals are further subtracted from the stellar spectrum. The cross-correlation function (CCF) approach was rejected for RV extraction because it was found to be suboptimal for the NIR. Instead, APERO uses the line-by-line¹⁵ (LBL) algorithm (Artigau et al., 2022).

Hence, in summary, there are differences between CARMENES NIR and NIRPS. Some of them are intrinsic to the observatories (e.g., AO), others to the instrument design (e.g., working temperature and detector), and also to data reduction and observational decisions. The latter might be the most straightforward way to improve CARMENES NIR, especially for UCDs studies. Indeed, the telluric correction approach could be the most critical factor in improving the RV precision achieved with CARMENES NIR for the detection of Earth-like planets orbiting stars at the substellar limit.

¹⁴ <http://apero.exoplanets.ca>.

¹⁵ <http://lbl.exoplanets.ca>.

OBJECTIVES AND METHODOLOGY

OBJECTIVES

The astronomical community is currently investing significant effort in the detailed characterization of exoplanets located within the habitable zone. This characterization includes high-precision measurements of planetary masses and radii, as well as the study of their atmospheric properties. Among the most prominent targets is the TRAPPIST-1 system, which hosts seven transiting planets. State-of-the-art facilities, such as the JWST, have dedicated hundreds of observing hours to this system, making it one of the most extensively studied targets of the mission.

Despite these efforts, current planet formation models are unable to fully reproduce the observed properties of such systems. In particular, theoretical predictions suggest a high occurrence rate of Earth-like planets around M dwarfs, especially toward the lowest stellar masses. However, observational surveys do not yet confirm such a high abundance. This discrepancy suggests that different formation mechanisms may be at play around very low-mass stars compared to those dominating formation around more massive hosts.

The lowest-mass stars are classified as part of the ultracool dwarfs. These objects emit most of their radiation at near-infrared wavelengths, making high-resolution near-infrared spectroscopy a key tool for the detection and characterization of their planetary companions. This is the case of CARMENES, a dual-channel high-resolution spectrograph operating in both the VIS and NIR. However, during the early phase of the survey, the performance of the NIR channel was not sufficient to achieve the radial velocity precision required for the study of exoplanets hosted by low-mass stars.

The main goal of this thesis is to improve the precision of radial velocities achieved with high-resolution near-infrared spectroscopy for the detection and characterization of Earth-like planets orbiting ultracool dwarfs. This work is primarily focused on the near-infrared channel of CARMENES and is structured in two main phases: (i) a technical upgrade of the spectrograph cooling system, and (ii) the scientific exploitation of the enhanced radial velocity performance.

The technical upgrade of CARMENES NIR is part of the CARMENES-PLUS project, which aims to enhance the instrument performance after its first four years of operation. The contribution of this thesis focuses on improving the thermal stability of the NIR spectrograph. During regular operations, the instrument exhibited significant temperature variations on both short and long timescales. Because radial-velocity measurements are strongly correlated with temperature fluctuations, these interventions were designed to minimize such variability and thereby improve the achievable radial-velocity precision.

In the second phase, we address the scientific exploitation of the improved radial-velocity capabilities. In particular, we focus on the search for rocky exoplanets orbiting ultracool dwarfs, the lowest-mass stars. These objects are intrinsically faint, often magnetically active, and typically fast rotators, all of which challenge the radial velocity extraction. Furthermore, their spectral energy distribution peaks in the near-infrared, where radial velocity computation is more challenging due to fewer spectral features and telluric contamination.

This thesis aims to optimize radial velocity extraction techniques for these targets, improve achievable precision, and identify the most suitable methodologies for detecting and characterizing planetary signals. Ultimately, this work seeks to improve the detectability of Earth-like planets orbiting ultracool dwarfs through radial-velocity surveys.

METHODOLOGY

The work presented in this thesis is structured into three main lines: (i) the improvement of the cooling system of CARMENES NIR, (ii) the development of a method to derive the projected rotational velocity ($v \sin i$) of stars, particularly for the CARMENES sample, and (iii) the optimization of radial velocity extraction from CARMENES NIR data. Each of these lines follows a specific methodology, described in detail in the corresponding chapters. A summary is provided below:

- *Chapter 3.* To minimize the thermal variability of the NIR spectrograph, the CARMENES-PLUS upgrade plan was structured into a sequence of targeted interventions, each addressing specific components or limitations of the cooling system. These upgrades were implemented sequentially to achieve a fully optimized and operational system.

All interventions were carefully planned and executed in coordination with the Calar Alto staff, ensuring uninterrupted nightly operations. Each upgrade involved a cycle of design, discussion, implementation, and testing, with interventions constrained to a few hours to avoid impacting the observations.

The performance of each upgrade was evaluated by analyzing temperature and pressure sensor data within the spectrograph, as well as calibration drifts during nightly observations to assess intrinsic radial velocity stability. Finally, the impact on on-sky radial-velocity precision was quantified using empirical measurements.

- *Chapter 4.* Ultracool dwarfs are often fast rotators, which broaden spectral lines and degrade the precision and reliability of radial-velocity measurements. Accurately determining their $v \sin i$, allows this effect to be accounted for during data processing and enables the exclusion of unsuitable targets for planet searches.

Existing methods for estimating $v \sin i$ often lack an adequate treatment of limb darkening, which is particularly relevant for M dwarfs. In this work, we develop a pipeline that accounts for the limb-darkening effect. The method is based on template matching, comparing target spectra with those of slowly rotating reference stars.

The approach is first validated using synthetic spectra spanning a range of $v \sin i$ values and effective temperatures. It is then applied to the full CARMENES sample, and the results are compared with available literature values. Additionally, we compare our method with numerical integration to assess the advantages and limitations of each approach.

Subsequently, we explore the use of CARMENES NIR spectra for the estimation of the $v \sin i$ of M dwarfs. We validate the method, equivalent to the CARMENES VIS approach, using synthetic data. Then, we implement the pipeline in `serval`, and applied it to a sample of 61 M dwarfs later than M5.0 V. The results are compared with the VIS measurements.

- *Chapter 5.* Achieving high radial-velocity precision for ultracool dwarfs is essential for the detection and characterization of planetary companions, particularly in the near-infrared range. In this chapter, we explore and optimize methods for radial velocity extraction and for identifying Keplerian signals.

We adopt a spectral order-wise approach to identify the optimal subset of spectral orders for radial velocity computation from CARMENES NIR data. An iterative procedure is used to minimize the average uncertainty of the resulting radial-velocity time series. Additionally, we assess the impact of telluric correction on radial-velocity precision.

For periodic signal detection, we compute generalized Lomb-Scargle periodograms to identify periodicities in the radial-velocity data. We further implement advanced modeling techniques that jointly account for planetary signals and stellar activity using Gaussian processes. Both visible and near-infrared datasets are analyzed, and we explore their combination to enhance detection sensitivity.

Thereafter, we construct detection maps using an injection-and-retrieval approach, allowing us to quantify the probability of detecting planets as a function of their mass and orbital period, given the available data.

To conclude, we compare the results obtained using data from pre- and post-CARMENES-PLUS. We perform a similar analysis as before with both datasets, whiten the time series from any planetary signal and the stellar GP model, and build the differential detection map. This allows us to understand the improvements of the detection probability after all the upgrades carried out during the thesis.

CARMENES-PLUS: IMPROVING THE NIR CHANNEL

In this chapter, I describe the upgrades implemented in the CARMENES NIR cooling system as part of the CARMENES-PLUS (C-PLUS) project. It includes the thermal analysis to prove the thermal stability enhancement, and the improvements on the intrinsic RV precision. We also analyze the impact of these upgrades on the on-sky data. The results are available online at a GitHub repository¹. The results are based on Varas et al. (2025) work, and further extended where appropriate.

3.1 NEAR-INFRARED SPECTROGRAPHS COOLING SYSTEM

Astronomical instruments operating in the near-infrared or at longer wavelengths require cooling to reduce the environmental thermal background, which would otherwise dominate the detector signal and degrade performance. As described in Sect. 1.4, in recent years, a new generation of high-resolution spectrographs operating at NIR wavelengths has been developed specifically to deliver precise RV measurements of late-type dwarfs, key targets in the search for low-mass exoplanets.

Since the start of CARMENES operations in 2016, the instrument has primarily pursued its main science objective: the detection of low-mass planets in the habitable zones of a sample of over 300 nearby bright M-dwarf stars (Ribas et al., 2023). The VIS channel has played a key role in characterizing these planetary systems, including their host stars, through RV campaigns (Ribas et al., 2018; Trifonov et al., 2021; Suárez Mascareño et al., 2021; Luque et al., 2023). In parallel, the NIR channel enabled a breakthrough in exoplanet atmosphere studies with the detection of helium escape from hot giant planets (Nortmann et al., 2018; Allart et al., 2018). Simultaneous observations from both channels have also contributed to planetary atmosphere analyses and stellar characterization (Oshagh et al., 2020; Kossakowski et al., 2022), but only rarely to RV studies (Morales et al., 2019), and mostly in the case of massive planets.

GIANO-B and HARPS-N at the Telescopio Nazionale Galileo, located at the Roque de los Muchachos Observatory (La Palma, Spain), and NIRPS and HARPS at the ESO 3.6 m telescope at La Silla Observatory (Chile), are pairs of near-infrared and optical high-resolution spectrographs that can operate simultaneously (Pepe et al., 2000; Tozzi et al., 2016). The two telescopes have apertures similar to that of the 3.5 m Calar Alto telescope. However, both pairs of spectrographs were not originally designed to operate together, which affects their operational integration, and have a large wavelength gap between 690 nm and 950 nm, where most of the RV information content is located in M dwarfs (Reiners et al., 2018). CARMENES, having been designed specifically for planet

¹ <https://github.com/rvarasg/CARMENES-PLUS>.

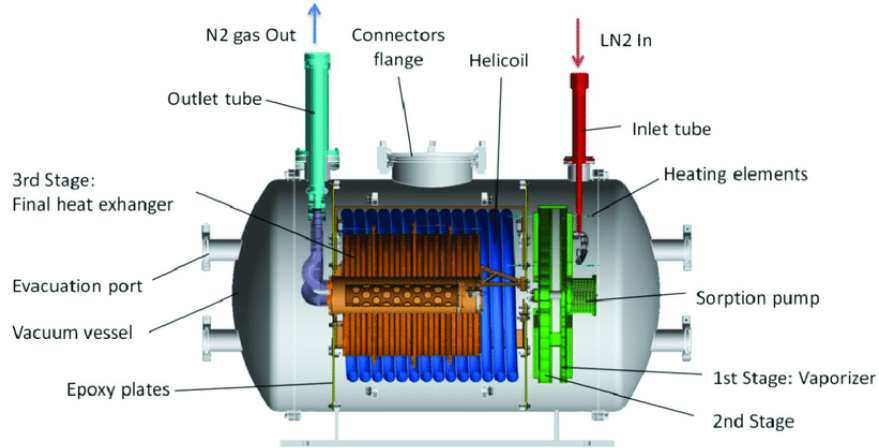


Figure 3.1: Cut view of the N₂GPU showing the different components (Lizon and Accardo, 2010).

searches around M dwarfs, does not have any major wavelength gap between 520 nm and 1710 nm, and its two channels were designed for simultaneous and integrated operation.

There are several solutions to achieve the thermal stability required by NIR instruments, from the standard solution used for detectors, which employs the liquid nitrogen continuous-flow cryostat (CFC) developed by ESO (Lizon and Accardo 2010), to the off-the-shelf solution provided by cryocoolers (Jakob and Lizon, 2010). Most of these instruments operate under full cryogenic conditions (i.e., at the temperature of liquid nitrogen, the boiling point of LN₂, 77 K), which poses technical challenges for instruments with movable parts (e.g., EMIR; Fernández Izquierdo et al. 2014). A less common solution is to evaporate the LN₂ to generate a flow of nitrogen gas at intermediate cryogenic temperatures and feed it through the instrument to cool it, as adopted for CARMENES NIR.

3.1.1 CARMENES nitrogen gas preparation unit

A critical component of the CS of CARMENES NIR is the nitrogen (N₂) gas preparation unit or N₂GPU. It was designed, integrated, and tested by ESO, based on their extensively used CFC system. This unit provides fine control over the coolant temperature and pressure within the system, thereby controlling the thermal conditions of the radiation shield and, consequently, the optical bench (OB). A layout of the N₂GPU is provided in Fig. 3.1.

The N₂GPU has a vacuum vessel that encloses the rest of the components. It has three main heaters or stages, each with a spiral-like design and several heaters with over-dimensioned power. The three heaters are in a parallel configuration, so if any of them stop working, the system can still provide heating power. The first stage is the *evaporation unit* (or vaporizer, green in Fig. 3.1), which evaporates the LN₂ and heats it up close to the working temperature.

The cross-section at the entrance of the stage is smaller than the one at the exit, so the expansion of the gas is accommodated. A sorption pump works as a cold trap, improving the vacuum level. The flow at the exit of the evaporation unit is turbulent due to the phase change. The *intermediate exchanger* (blue element in Fig. 3.1) is a long coil with a large cross-section that allows the flow to stabilize, and, if needed, the heaters can be used to provide finer temperature control. The *final heat exchanger* (orange component in Fig. 3.1) is a massive component to provide very stable temperature conditions to the gas before entering the instrument, and any potential flow instability is damped prior to the N₂GPU exit.

During the integration phase of the N₂GPU, the CARMENES team, after several tests, decided to bypass the final heat exchanger. They found LN₂ inside the stage, which perturbed and obstructed the N₂ gas flow, thereby worsening the N₂GPU performance. From that moment, only the first two stages are enabled.

3.2 CARMENES-PLUS TECHNICAL UPGRADE

3.2.1 CARMENES-PLUS description

The CARMENES consortium has been exploiting the instrument to search for exoplanets around M dwarfs since 2016, with excellent results summarized in Ribas et al. (2023), along with the GTO program data release. CARMENES is now in its second legacy project, with the prospect of a third under consideration by the CAHA (Centro Astronómico Hispano en Andalucía) staff. Due to the excellent results since the beginning of the operations, the C-PLUS project was proposed to maintain CARMENES at the forefront of technical performance by improving its intrinsic RV precision to 2 m s^{-1} over a timescale longer than five years and below 1 m s^{-1} in the short term. Bauer et al. (2020) carried out the first thorough analysis of the RV performance of the two CARMENES channels during the first years of operation. They confirmed the higher intrinsic RV scatter of the NIR channel, 3.7 m s^{-1} , compared to 1.2 m s^{-1} in the VIS, due to limitations in calibration precision and thermal stability.

C-PLUS was presented to the CAHA call for new instrumentation in May 2018 and received a positive evaluation from the scientific committee. Technical development began in mid-2020, although the implementation of upgrades was constrained by the instrument's scientific operation requirements since early 2016. The proposed plan was intended to cover most of the time between the end of the GTO CARMENES survey (mid 2020) and the first light of the new instrument for the 3.5 m telescope at Calar Alto, as part of the 2019 instrument call. Nonetheless, no instrument was selected, and C-PLUS remained as the only project approved by the observatory.

The project's main scientific goals were to detect and characterize exoplanetary systems and to characterize exoplanet atmospheres. To achieve them, two main technical goals were proposed; the primary focus of C-PLUS was to improve the behavior and performance of the NIR channel. During this initial

phase, both spectrographs continued nightly operations, while interventions on the NIR channel were carried out during daytime. The second goal was to improve the long-term RV performance of both channels by reducing instrument drift and systematics. With this aim, subsystems such as the calibration unit (including the FP etalon and the optical fiber injection arrangement), the VIS spectrograph, the coudé room conditioning, and the pipeline were also going to be revised and upgraded. The original design of CARMENES NIR is described in detail in Sect. 1.4.1.

The main issues identified in the C-PLUS Feasibility Study (FS) can be summarized as follows: (i) smooth seasonal variations in the VIS radial velocities; (ii) sharp VIS variations associated with vacuum regeneration; (iii) thermal coupling between the RVs and the VIS room and tank; (iv) high sensitivity of the VIS RVs to temperature variations in the OB; (v) a long-term decreasing drift in the NIR optical bench temperature; (vi) instabilities in the NIR associated with vacuum regeneration; (vii) a rapid thermal coupling between the radiation shield and the detector in the NIR, as well as additional instabilities induced by daily dewar changes and the temperature profile of the on-off valve; and (viii) long-term FP drifts in both VIS and NIR channels due to limitations in the FP temperature stabilization system.

The latter issue was successfully addressed by Pleiteit et al. (2024). Regarding the NIR channel, several interventions were carried out between 2020 and 2022. These are described below following the results of Varas et al. (2025), and further extended where appropriate.

3.2.2 CARMENES-PLUS timeline

The CS of CARMENES NIR intervention began in 2020, though it was affected by the COVID-19 pandemic. A quick timeline of the events is as follows:

- *March to November 2020*[♀]: Start of phase 1. Design of the different interventions of C-PLUS regarding the NIR CS.
- *November 2020*[♀]: Official kick-off meeting to start the project.
- *February 2021*: Breakdown of the N₂GPU, detected by the lack of heating power to properly evaporate the LN₂.
- *May 2021*: Inspection of the N₂GPU after some problems were detected. Some heaters were broken. Placement of new temperature sensors and regeneration of the N₂GPU sorption pump of the N₂GPU.
- *May 2021*[♂]: Replacement of the on-off valve for a proportional one, changing from discontinuous to continuous flow mode.
- *June 2021*[♀]: Implementation and verification of the automatic vacuum system for transfer lines (AVSTL).
- *September 2021*[♂]: New heaters for the N₂GPU, new temperature sensors and another N₂GPU sorption pump regeneration.

- *October 2021*[♀]: Start of phase 2. Exhaust Gas Warm-up System (EGWS) installation, including a flow meter.
- *January 2022*[♂]: Implementation and verification of the pressure control unit (PCU).
- *May 2022*[♂]: Installation and validation of the *fixed-dewar* configuration.

Two categories of interventions were defined: those considered in the C-PLUS FS (♀) and the *best-effort actions* (♂), not included in the FS but defined afterward to fulfill the FS requirements. A more detailed analysis of the most relevant events and interventions is described below.

3.2.3 Cooling system monitoring

The CARMENES CS has several sensors (Fig. 3.2; Quirrenbach et al., 2018) over different components to monitor the physical variables (e.g., pressure and temperature), both in time and position inside the system. To evaluate the impact of the upgrades, we can compare the behavior of these variables before and after C-PLUS interventions. This was already done in the work by Varas et al. (2025) through June 2024, and it is extended here until February 2026. We can define the system pre-C-PLUS from 1 November 2016 to 7 February 2021 and post-C-PLUS from 1 June 2022 to 24 February 2026, with almost two years more data than the mentioned work.

The temperature at the entrance of the first flow splitter (NIR-CS-Tso2²) monitors the temperature of the coolant entering the cooling lines. The sensor at the first heat exchanger (Tso6) shows temperature variability during thermal exchange; the one located at the midpoint of the upper radiation shield (Ts19) provides information from a location with a smooth, averaged thermal gradient, offering good insight into thermal drifts. A temperature sensor at the first heat exchanger in the first cooling line of the lower radiation shield (Ts22) is used as the setpoint reference for the control loop. The temperature of the OB (Ts10) is also monitored because it is the ultimate target for thermal stabilization. For pressure analysis, full-range vacuum gauges monitor the vacuum level of the transfer lines, and a pressure gauge (NIR-CS-S1) tracks the feeding pressure in the fixed dewar.

Temperature data from Ts10 and Ts19 since the beginning of CARMENES operations is shown in Fig. 3.3. Until the end of 2016, when the cooling system was properly tuned and stabilized, the thermal variability was significant. Similarly, during the C-PLUS interventions, the temperature variations were considerably larger (grayed out in Fig. 3.3). Note how the temperature of the OB has stabilized in the first trimester of 2024 until today. For more than half a year, the OB temperature has varied by at most ± 10 mK, indicating extreme thermal stability due to the C-PLUS upgrades described in detail below.

² All sensors will hereafter be identified in the text with the nomenclature Ts (Temperature sensor) and its corresponding number, e.g., NIR-CS-Tso2 is Tso2.

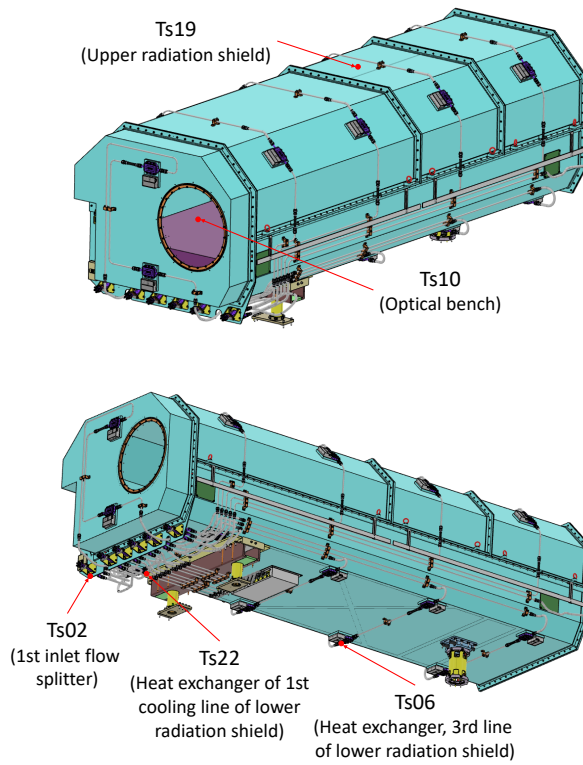


Figure 3.2: Location of key temperature sensors in the CARMENES NIR cryogenic system. The top panel shows the upper radiation shield (Ts19) and the OB (Ts10) sensors. In the bottom panel, sensors placed at the 1st inlet flow splitter (Ts02), and at heat exchangers of the 1st (Ts22) and 3rd (Ts06) cooling lines of the lower radiation shield.

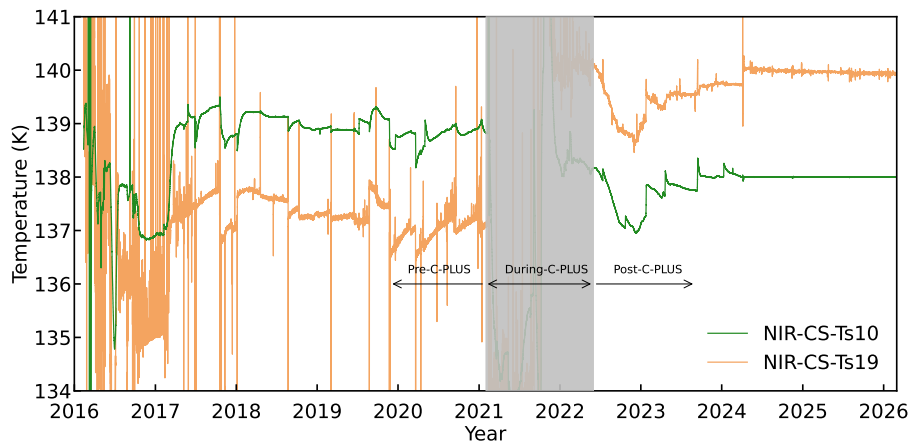


Figure 3.3: Data history of the temperature sensors NIR-CS-Ts10 and NIR-CS-Ts19. The shaded region indicates the period during which the C-PLUS interventions were implemented.

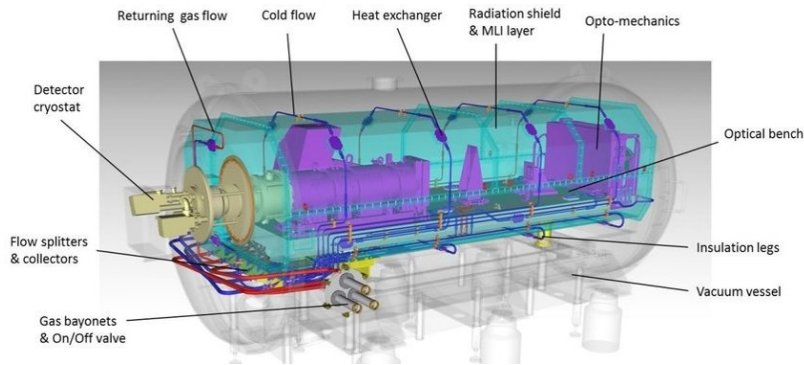


Figure 3.4: CAD view of the CARMENES NIR spectrograph. The vacuum vessel and radiation shield are semitransparent, so the spectrograph is visible.

3.2.4 C-PLUS: NIR upgrades and new thermal stability

The CAD³ of the NIR spectrograph is provided in Fig. 3.4, with the radiation shield (cyan) and vacuum vessel (gray) semitransparent, so the OB, camera, and different components of the CS are visible.

3.2.4.1 Automatic vacuum system for transfer lines (AVSTL)

The transfer lines carrying N_2 gas below 130 K are vacuum-encased to maintain low temperatures. The internal vacuum, initially preserved by a blind lid, degraded over time due to leakage and out-gassing, negatively affecting thermal performance. This degradation was exposed when frost formed on the line's ends (no vacuum gauge was available). Opening the lid for manual vacuum restoration revealed very low vacuum levels inside the line (pressure values as low as 0.1 mbar, compared to the nominal 10^{-5} mbar). These manual restorations to high-vacuum conditions resulted in significant periodic thermal perturbations in the CS.

The AVSTL (Fig. 3.5) was developed to maintain a high vacuum level, setting an upper-pressure limit requirement of 10^{-5} mbar. However, the good sealing of the AVSTL and the cold trap effect maintain the vacuum level for long periods within the range of $5.9 \cdot 10^{-7}$ to $9.1 \cdot 10^{-7}$ mbar. This upgrade minimized the radiation shield's thermal drift due to gradual vacuum degradation and eliminated the periodic thermal instabilities caused by manual vacuum regeneration every few months; thus, leading to smoother variations in coolant temperature and a higher thermal stability of the OB.

3.2.4.2 N_2 GPU intervention

In February 2021, the on-off valve controlling the CS coolant flow failed. This led to a fast overheating of the system (see Fig. 3.3). The possible malfunction was unknown, resulting in excessive heating of the N_2 GPU, exceeding the tin solder-fusing temperature. Three out of the six heaters attached to the heating

³ Computer-Aided Design.

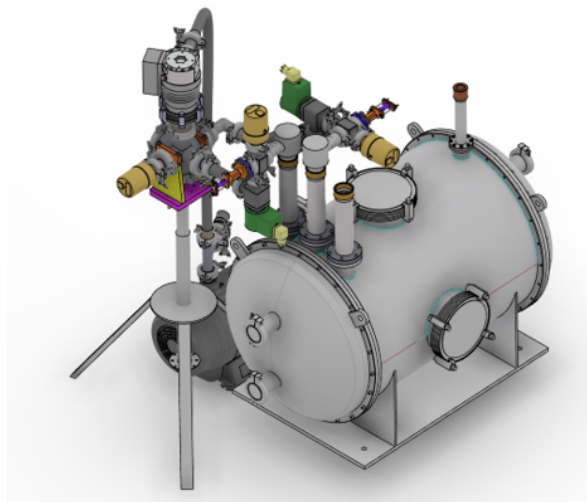
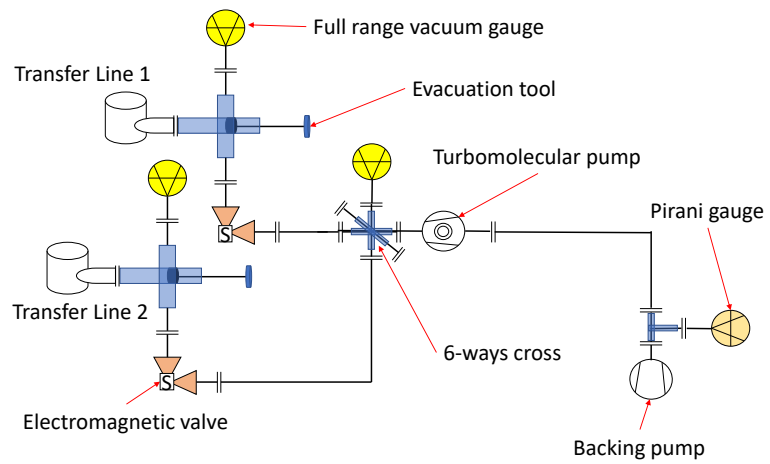


Figure 3.5: *Top*: Layout of the automatic vacuum system for transfer lines (AVSTL).
Bottom: CAD layout of the N₂GPU and AVSTL.

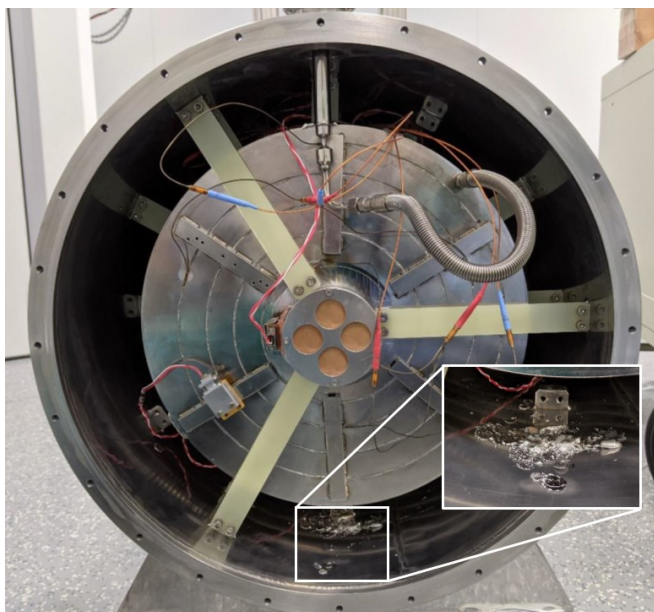


Figure 3.6: Picture of the N₂GPU inspection in May 2021. Not the tin solder at the bottom of the image.

exchangers broke (see Fig. 3.6), and the heating power was significantly affected. In September 2021, a fourth heater failed, and the power was insufficient to keep the instrument at the working temperature. All CAHA staff's efforts during those months were focused on ensuring the proper functioning of the NIR channel with the available resources and the system's status. They increased the overpressure in the LN₂, changed the controlling sensor, temporarily adopted a continuous-flow mode by integrating a cryogenic valve, and installed a larger-section pinhole to increase the flow.

Between September and October 2021, the N₂GPU power was restored after replacing the broken heaters. Several temperature sensors were installed to monitor working conditions in real time, improving the system's reaction and control capabilities. Due to the instrument's high mass and sensitivity, reaching the stationary state took a few months. The discontinuous flow mode was recovered to return to the working conditions prior to the breakdown. The recovery of the CS working conditions is noticeable in the temperature sensors (Fig. 3.3).

3.2.4.3 N₂GPU-Evo

During the CARMENES operation, it was observed that the N₂GPU, occasionally, had problems completely evaporating the LN₂. In the FS of C-PLUS, "7.3.1. Vertical Position of the N₂GPU in the FS" was included as a point, assessing the aforementioned problematic, although it has not (yet) been implemented.

Following the same line, and with the knowledge obtained from the daily experience operating CARMENES NIR (and the N₂GPU breakdown), a N₂GPU evolution unit (N₂GPU-Evo, illustrated in Fig. 3.7) was suggested as a possible improvement to add to the C-PLUS plan. In a vertical position, with similar

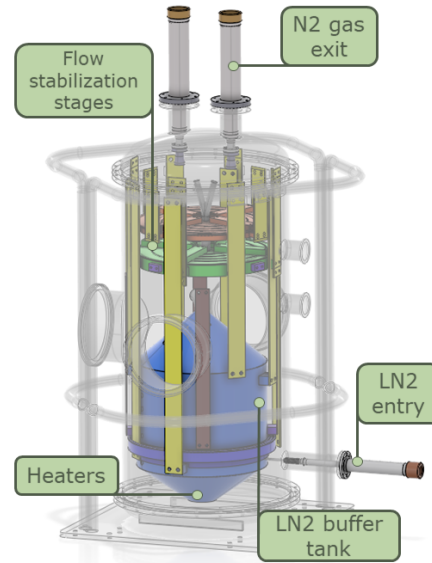


Figure 3.7: Preliminary CAD design of a new N₂GPU-Evo.

stages to the current N₂GPU, the N₂GPU-Evo aimed to address the main problems of the present unit; (i) Limited heating power, (ii) non-isolated gaseous and liquid phases of the N₂, (iii) asymmetric flow through the upper and lower radiation shield circuits, and (iv) possible presence of humidity inside the circuit. Note the vertical LN₂ buffer tank, a key element of the design to avoid L₂N in the flow stabilization stages, and as an intermediate container for the phase change.

The N₂GPU-Evo has not been further developed and is currently only a preliminary design and proposal. If, in the future, CAHA decides to have the unit as a backup or even as the main working unit, the design would advance its development status.

3.2.4.4 *Continuous flow mode*

The on/off valve used to control gas flow in a discontinuous mode causes temperature oscillations at the radiation shield, directly affecting RV measurements, as depicted in Fig. 1.16. Replacing this valve with a proportional valve changed the CS from discontinuous to continuous flow, avoiding coolant flow interruptions.

A control loop commands the proportional valve's aperture based on the Ts22 sensor's setpoint, ensuring smoother thermal conditions. The peak-to-peak variations of the temperature decreased from $\Delta T = 0.09$ K to $\Delta T = 0.002$ K. With the original on/off valve, the signal exhibited a sawtooth pattern, whereas with the new proportional valve, the variations appear as smaller, more random fluctuations around a stable set point. A typical time series over a 3-day time span is shown in Fig. 3.8.

Another important advantage of using a proportional valve to control the flow is the ability to keep the pressure gradient constant from the 350-L dewar

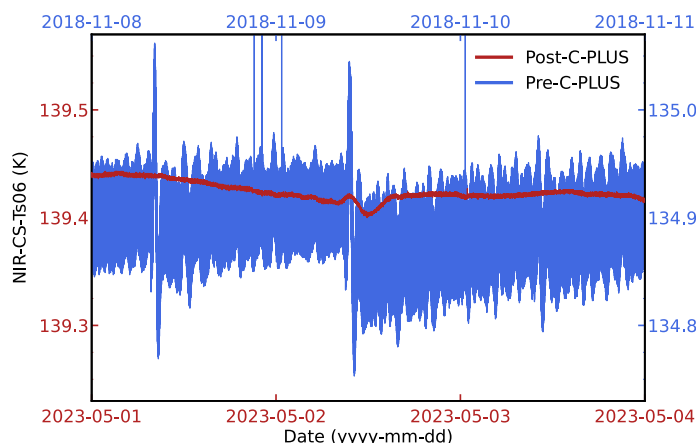


Figure 3.8: Temperature variability over 3-day intervals at the heat exchanger attached to the radiation shield (NIR-CS-Tso6).

to the exit. This is a considerable issue to take into account because the pressure in the 350-L dewar drops as the LN₂ level goes down, leading to instabilities in the CS.

Nevertheless, the proportional valve configuration exhibits greater sensitivity to pressure variability within the fixed-dewar during refills. During the refilling process, turbulence encourages evaporation, increasing pressure inside the fixed-dewar and resulting in a slight increase in flow that over-cools the system. Thus, the ability to control pressure is a key feature for counteracting these fluctuations, ensuring stable operation (see 3.2.4.6).

3.2.4.5 Exhaust Gas Warm System (EGWS)

The first CS design did not include an exit warming system, and the exhaust-gas line was not insulated. This resulted in ice forming in the exhaust line at the end of the circuit, and the ice blocks had to be removed periodically and manually. Moreover, the access to this part of the instrument is complicated because it is under the technical false floor.

The solution was an EGWS, consisting of a large heat exchanger placed downstream after the exit valve (on-off at the time). Temperature sensors and heaters are attached to the heat exchanger to warm the exhaust line above the dew point, preventing ice formation.

Fig. 3.9 illustrates the 3-D CAD design of the EGWS (top right), the physical development (bottom right), and the implementation at the exhaust line at the exit of the CS under the technical floor (left). The design included several heaters and a protective, insulated housing of the EGWS. To monitor the gas flow, a flow meter was connected at the EGWS exit.

3.2.4.6 Pressure control unit (PCU)

Inside the dewar that provides LN₂ to the N₂GPU, there is a certain amount of gas, and the pressure it generates plays a key role in the coolant flow through the system. The pressure difference between this gas compartment and the CS

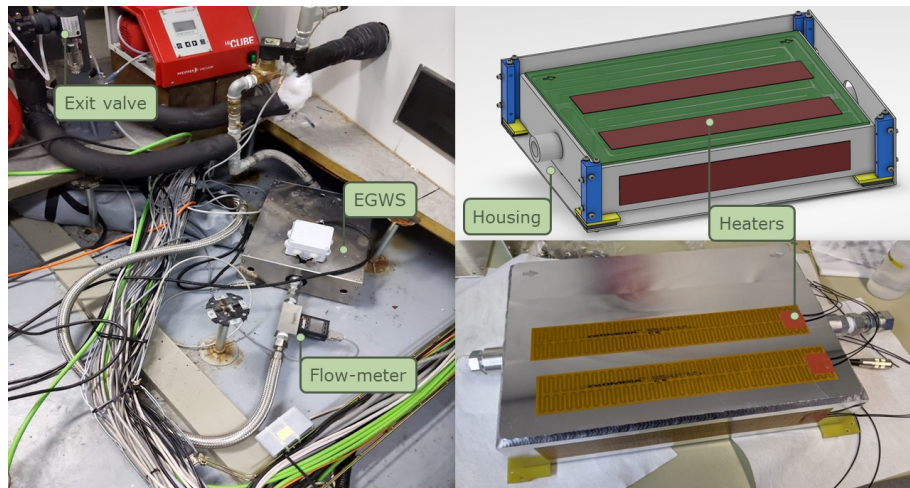


Figure 3.9: Images of the CAD and physical design, and the implementation, of the EGWS at the exit of the CS.

exit determines the flow rate. Consequently, the control of the pressure allows to control the amount of nitrogen gas fed to the CS, and as the amount of LN₂ inside the dewar lowers, so does the pressure⁴. Thus, fine control of the overpressure inside the dewar is key to maintaining constant, stable thermal conditions for the spectrograph.

The PCU (sketch in top panel of Fig. 3.10) was developed to address this problem. It uses nitrogen gas from a 150-L dewar pressurized at 0.8 bar. If the 350-L dewar's pressure drops below the lower limit, the PCU injects gas, and when the pressure exceeds the upper limit, the PCU evacuates the excess gas. These processes are controlled by two pneumatic proportional valves, with proportional-integral-derivative control for fine-tuning.

Several previous tests concluded that pressures below 0.36 bar in the 350-L dewar feeding the N₂GPU led to unstable operation, and pressures around 0.42 bar provide better results. As shown in the bottom panel of Fig. 3.10, the pressure is maintained within the peak-to-peak range of 0.421 to 0.426 bar, compared to 0.370–0.437 bar range before its implementation. This translates into less frequent instabilities, hence a higher thermal stability of the spectrograph.

3.2.4.7 Fixed-dewar configuration

The LN₂ consumption by the CARMENES CS is considerable, and the dewar is emptied in one day of operation. Consequently, the LN₂ dewar had to be replaced daily to maintain sufficient coolant for the observations. This daily replacement significantly affected the CS stability due to brief yet complete interruptions in the LN₂ flow, leading to sudden changes in thermal stability and hence RV drifts. Additionally, the LN₂ dewars used might have different working pressures, causing abrupt variations, leading to intra-day thermal

⁴ The amount of gas inside the dewar is more or less constant, and as the LN₂ is consumed, the volume of gas increases, decreasing the pressure.

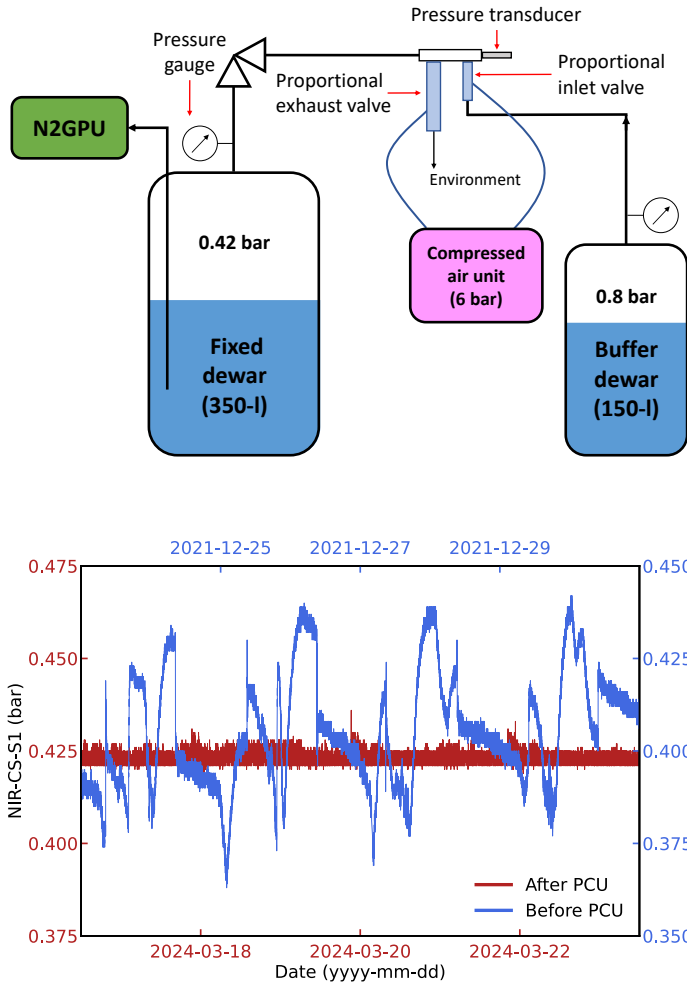


Figure 3.10: *Top*: Schematic layout of the main components of the Pressure Control Unit (PCU) in the CARMENES NIR cooling system. *Bottom*: Pressure inside the fixed-dewar over a representative 7-day period.

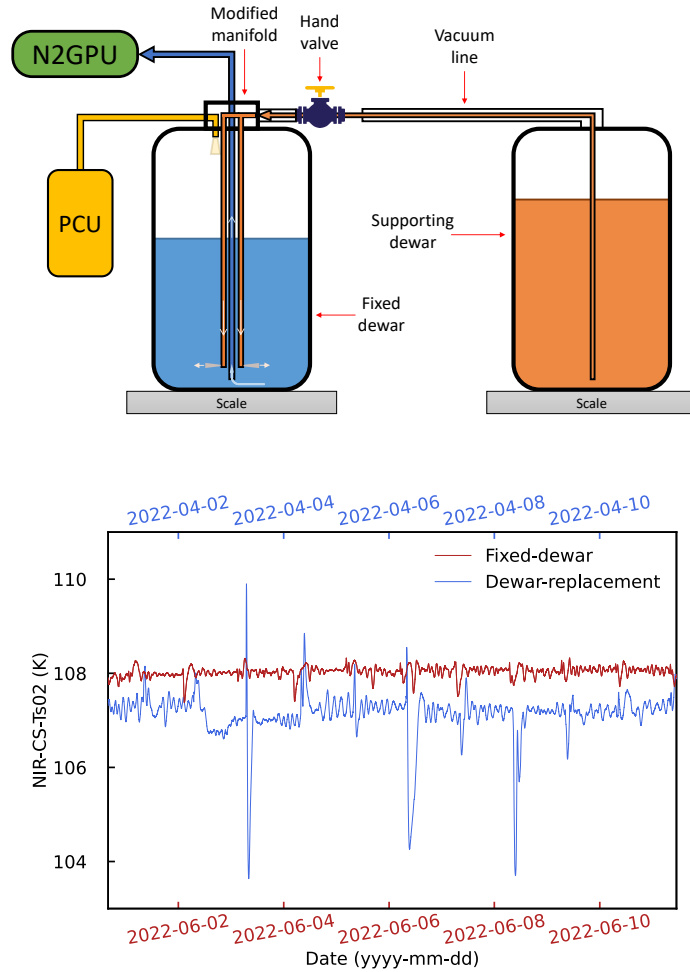


Figure 3.11: *Top*: Layout of the system in the fixed-dewar configuration. *Bottom*: Coolant temperature at the inlet flow splitter over two representative 10-day periods.

drifts. To minimize the impact of these instabilities in the observations, the dewar replacement used to be done early in the morning.

As a best-effort action during C-PLUS that tackles the impact of the LN₂ dewar replacement, a fixed-dewar configuration was proposed. This approach consist on refilling the dewar instead of replacing it, thus continually providing coolant to the N₂GPU, without any interruption. For the refilling process, a second supporting dewar with similar properties is needed, as well as a fine control over thermodynamic properties, due to the complexity of the process under cryo-vacuum conditions. In this configuration (top panel of Fig. 3.11), the flow from the supporting dewar is controlled by the pressure difference between the two dewars, with the supporting dewar maintained at 0.95 ± 0.05 bar. Furthermore, PCU plays a critical role in the process, maintaining working conditions as stable as possible to minimize the refilling effect on the OB temperature. The feed line transfers LN₂ from the supporting to the fixed-dewar at a rate of approximately 80 kg h^{-1} .

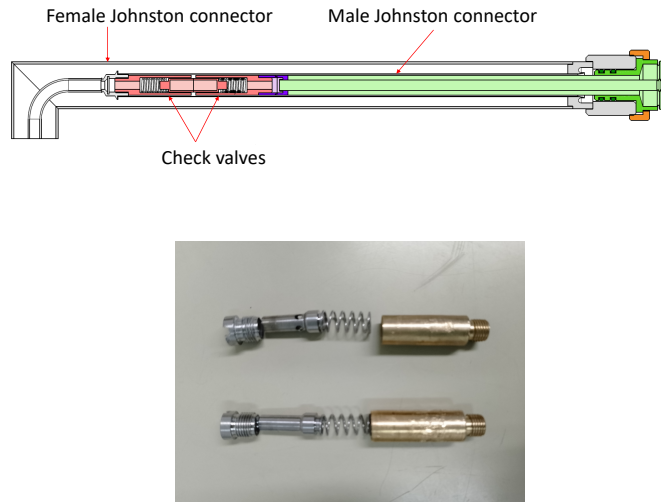


Figure 3.12: *Top*: Layout of the Johnstone coupling. Note the check valves highlighted in pink. *Bottom*: Photograph of the feed line's check valve (top) and the manifold's check valve with orifices (bottom).

A modified manifold allows the fixed dewar to be fed and refilled simultaneously through two independent circuits. The refilling circuit has two pipes to prevent narrowing and maintain a section equal to or greater than the feed line from the supporting dewar. The LN₂ is injected horizontally at the bottom of the dewar through both pipes in opposite directions, and 2 cm above the N₂GPU feeding pipe, ensuring no interaction between the processes. The LN₂ flows from the bottom of the fixed dewar to the N₂GPU through a central pipe.

The bottom panel of Fig. 3.11 compares the temperature variations at the inlet flow splitter (T_{so2}) for two periods of 10 days each. The temperature perturbation due to refills in the fixed-dewar configuration is significantly less abrupt than the previous one (dewar replacement), with temperature fluctuations reduced from ± 3 K to ± 0.4 K. To further enhance thermal stability, the interval between refills was extended from one day to two days in November 2022, as the dewar capacity was sufficient to maintain this longer interval. Hence, the perturbations caused by the refilling of LN₂ are an order of magnitude smaller in amplitude and occur at half the frequency.

3.2.4.8 Feed line's check valve removal

A feed line in vacuum conditions supplies the N₂GPU with coolant. A safety mechanism with two check valves in the Johnstone coupling (top panel of Fig. 3.12) ensures that the fixed-dewar provides LN₂ only when the feed line is connected. This type of connection is widely employed in vacuum-insulated piping systems for cryogenic fluids. One valve is located in the inner part of the dewar's manifold (female port), and the other is in the feed line's lance (male port). When the lance is plugged into the manifold, both check valves open, allowing LN₂ to flow.

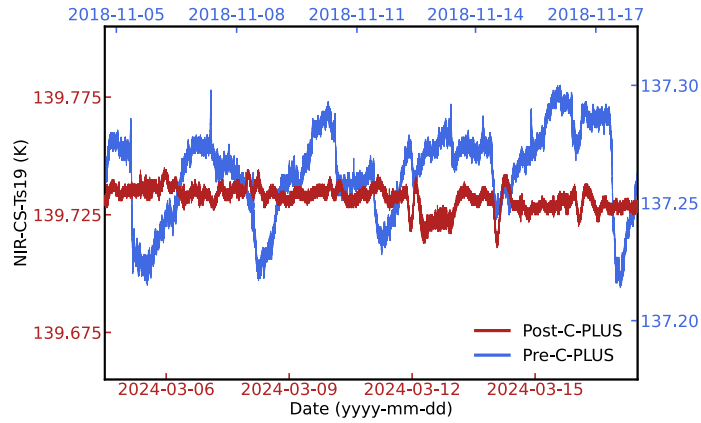


Figure 3.13: Temperature measured by the NIR-CS-Ts19 sensor.

During operation, stochastic interruptions in LN₂ flow were detected, leading to significant thermal instabilities in the system. Some tests revealed that the interruptions originated from pressure drops due to excessive narrowing of the check valve on the feed line side (male) compared to the manifold side (female; see bottom panel of Fig. 3.12). To eliminate this bottleneck, the check valve on the feed line side was removed and replaced with a fixed sleeve bushing, which is geometrically identical to the check valve but does not hinder the LN₂ circulation.

The removal of the feed line's check valve eliminated the narrowing in the circuit and the random interruptions of LN₂ flow. A side effect was a smooth thermal drift of the instrument over several months (at a rate of 0.015 K day^{-1} , within the requirements; Becerril et al. 2017) towards a new steady state. Once the new steady state was reached, the radiation shield temperature variations were considerably smoother and smaller than with the previous configurations (see Fig. 3.13).

3.2.5 Thermal stability of the NIR spectrograph after C-PLUS

The temperature at the radiation shield (the actively cooled component), exhibits two temperature variations: short-term (intra-night or over hours) and long-term (over days to weeks) (Fig. 3.13). The amplitude and frequency of the temperature variability has been significantly reduced, from daily variations over 100 mK to less than 10 mK. Additionally, big and sudden fluctuations are smaller and significantly less frequent, demonstrating the stability and robustness of the new CS configuration.

As previously seen in Fig. 3.3, the OB temperature closely follows the profile of the radiation shield. Thus, the improvement in the thermal stability of the latter translates directly into a drop in the OB temperature fluctuations. The top panel of Fig. 3.14 shows the temperature variations at the radiation shield from April 2024 until March 2026, extending the analysis of Varas et al. (2025) by almost two years. Over this period, the temperature has changed by less than $\pm 0.1 \text{ K}$ relative to the mean temperature, with typical variations during

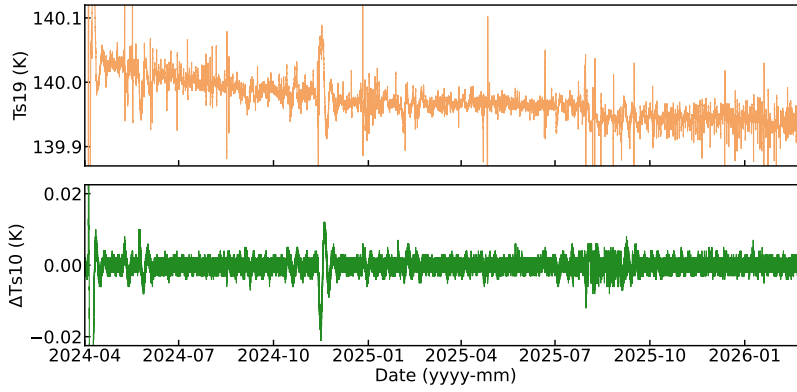


Figure 3.14: Temperature variation at the radiation shield (T_{s19} ; top panel), and the OB (T_{s10} ; bottom panel) thermal fluctuation around the working conditions ($\Delta T_{s10} = T_{s10} - 138$ K).

the operation of ± 20 mK. The OB, due to its large mass and the CS's efficient response, has been extremely stable. The bottom panel of Fig. 3.14 depicts the thermal variations with respect to the working temperature of 138 K. During this time interval, when the system has reached the steady state after the C-PLUS completion, the maximum variation of the temperature is ± 10 mK, and the typical daily fluctuations are below ± 2 mK. The impact of the C-PLUS interventions on the NIR CS has significantly improved the spectrograph's thermal stability.

3.3 DATA REDUCTION AND CALIBRATION

Demonstrated the huge impact and improvement of C-PLUS on the thermal stability of the NIR spectrograph, we can now evaluate the effect on the data quality obtained with CARMENES NIR. Our analysis is based on three types of data: (i) Fabry-Pérot calibration spectra, which allow us to quantify the intrinsic instrumental stability; (ii) spectra of RV-constant stars ($\text{rms} \leq 10 \text{ m s}^{-1}$), used to evaluate the night-to-night repeatability of the RV measurements; and (iii) on-sky stellar observations, which reveal the overall improvement in RV precision for scientific targets. These datasets provide a comprehensive picture of the improvements achieved by C-PLUS, both from an engineering and a scientific perspective.

3.3.1 Data reduction

The CARMENES spectra are reduced using the `caracal` (CARMENES Reduction And CALibration) pipeline, as detailed in Caballero et al. (2016). Starting from the raw data, `caracal` performs dark/bias correction, order tracing, flat-field relative optimal extraction, and wavelength calibration, resulting in fully reduced and wavelength-calibrated 1D spectra.

The second pipeline is `serval`, described in detail by Zechmeister et al. (2018). It creates a high signal-to-noise ratio template spectrum using the `caracal`

reduced spectra of the target star. It then computes the series of RVs via least-square fitting, telluric masking, échelle order weighting, and correcting for systematic errors. Apart from the RVs, the output also includes activity indices.

3.3.2 Calibration strategy and process

Accurate wavelength calibration and precise monitoring of instrument stability are crucial for obtaining high-precision RV measurements. Each of the two CARMENES spectrographs uses two fibers (A and B) to feed star, sky, and calibration light beams into each spectrograph. These two beams are then focused onto the detectors, providing two adjacent spectra that can be calibrated against each other (see Sect. 1.4.1).

The baseline strategy for observation involves injecting starlight into fiber A and light from a calibration source into fiber B, enabling simultaneous calibration. This setup allows continuous monitoring and correction of any instrumental drifts during observations. By calibrating the spectra against each other, wavelength shifts can be accurately tracked and corrected.

A study by Bauer, Zechmeister, and Reiners (2015) (see also Hobson et al., 2021) demonstrates that using a combination of HCLs and a FP interferometer is more effective for wavelength calibration of échelle spectrographs than using HCLs alone. The FP produces a denser grid of lines with nearly uniform intensity across the spectral range, enhancing calibration accuracy. Consequently, CARMENES adopted this technique (Schäfer et al., 2018).

At the beginning and end of each night, HCLs images are acquired to derive the wavelength solution at the detector. This solution is then used to calibrate the FP spectra, assigning wavelengths to each interferometry peak. The FP spectra are used to monitor the drift of the wavelength solution due to thermo-mechanical changes within the instrument during the night.

3.3.3 Selection of on-sky datasets

The RV time series from the 361 M dwarf stars observed by CARMENES during its GTO phase (2016-2020; Ribas et al., 2023) are publicly available⁵. CARMENES has primarily targeted early- and mid-type M dwarfs with near-solar metallicity (Marfil et al., 2021; Reiners et al., 2018; Alonso-Floriano et al., 2015).

For the analysis presented here, we used the `serval_rvc` data-product, which are RVs corrected for the instrument's drift and secular acceleration, but not for nightly zero points (NZPs; see Sect. 3.3.4). We limit our analysis to slowly rotating M dwarfs ($v \sin i \leq 2 \text{ km s}^{-1}$) with at least five spectra. These datasets can have from five to hundreds of observations, depending on how often a target has been visited (see Table 3.1). The $v \sin i$ values are sourced from Varas et al. (2026), where an upper limit of 2 km s^{-1} for $v \sin i$ is set, as values below this threshold cannot be reliably obtained (Reiners et al., 2018). These criteria reduce the stellar sample size to 174 stars for pre-C-PLUS and 38 stars for post-C-PLUS. For consistency, we used the same stellar sample for the VIS

⁵ <http://carmenes.cab.inta-csic.es/gto/jsp/dr1Public.jsp>.

channel as for the post-C-PLUS NIR sample (174 stars). This selection defines the three on-sky spectral datasets used in this work.

3.3.4 *Nightly zero points*

Despite the CARMENES spectrograph being wavelength-calibrated each afternoon and its drift monitored using the FP etalon during the night (see Sect. 3.3.2), on-sky RV measurements from a given night still share common systematic offsets, known as NZPs (Ribas et al., 2023). These offsets arise from a combination of FP drifts, degradation in the quality of the HCLs reference spectra, instrument instabilities during calibration (due to the FP and HCL not being usable simultaneously), and variations in calibration light injection caused by imperfect scrambling.

We calculate the NZPs using a sample of RV-constant stars, defined as those with a RV time series scatter of $\text{rms} \leq 10 \text{ m s}^{-1}$, following the procedure of Trifonov et al. (2018). This method involves selecting stars with minimal RV variation over time as reference points, computing the nightly offset required to align these stars RV measurements with their known values, and applying this offset to correct the RV measurements of all stars observed that night. To prevent self-biasing, a star's own RV measurements are excluded when computing the NZP. If fewer than three RV measurements of RV-constant stars were obtained on a given night, the NZP is replaced by the median of all NZP values over the survey period (Ribas et al., 2023). The computed NZP offsets are then subtracted from the `serval` RV measurements (`rvc`) to produce the final NZP-corrected RV values, ready for scientific analysis.

3.4 RESULTS AND DISCUSSION

3.4.1 *Intrinsic RV precision*

Bauer et al. (2020) studied the instrument performance of both CARMENES spectrographs analyzing calibration data. They concluded that, at that time, the VIS had, approximately, three times better intrinsic precision than the NIR, 1.2 m s^{-1} compared to 3.7 m s^{-1} , respectively.

This work was done just before the start of C-PLUS, portraying the NIR status prior to the interventions. We can set this as the baseline and compare the NIR spectrograph's performance after the upgrades, using a similar approach.

The calibration data from the FP allow for monitoring the nightly RV drift during an observing night. For this work, we consider only nights with sufficient calibration data points to realistically represent the spectrograph's behavior during the observations. Therefore, nights with calibrations only at the start and end are excluded from the analysis.

Fig. 3.15 shows the complete history of the nightly FP RV calibrations collected with CARMENES NIR. The top panel displays the relative RVs, set to zero each night, while the bottom panel shows the absolute values, accumulated since the beginning of operations. The dispersion of the points is notably

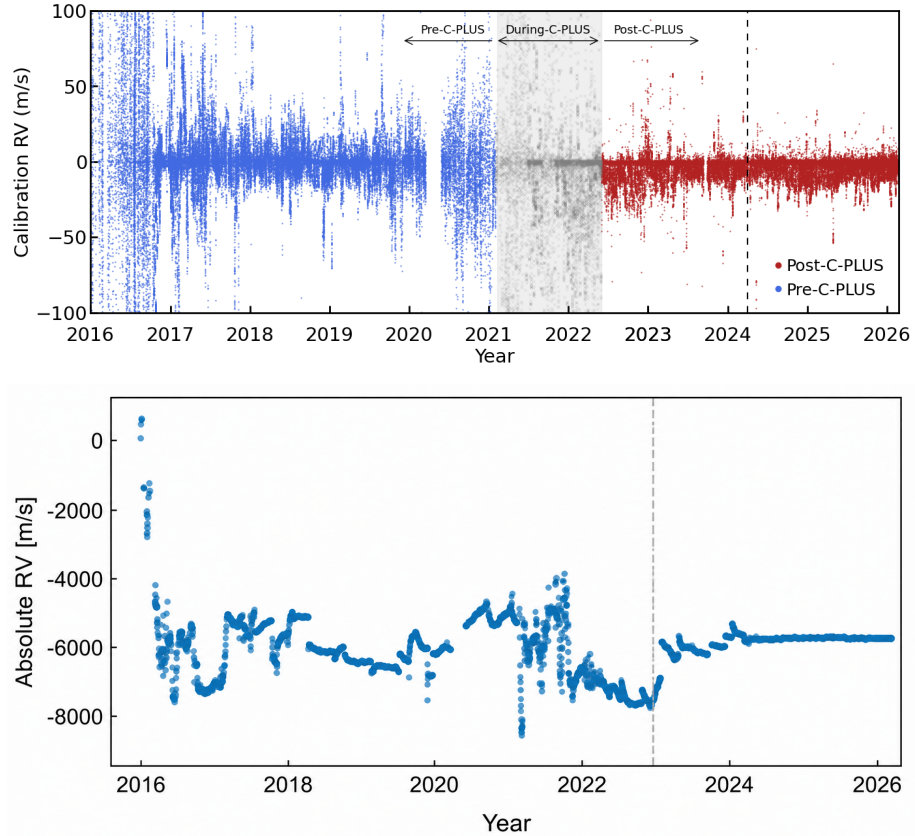


Figure 3.15: Data history of nightly FP RV calibrations of the CARMENES NIR channel. On top, the relative data (set to zero every night), and at the bottom the absolute RV measurements (cumulative from the start of the operations).

smaller after C-PLUS, and the nightly RV drifts are significantly larger during the interventions, as expected from the huge thermal variability. It is worth comparing the temperature and calibration history plots to better understand the correlation between both and the different states the NIR channel has undergone.

To quantify the RV stability, we considered two statistical properties of the nightly RV drifts, (i) the peak-to-peak amplitude and (ii) the root-mean-square of the residuals after fitting a quadratic least-squares model to the data (rms_{res}). The peak-to-peak value reflects the total RV variation induced by the instrument's drift during a single night, while the rms_{res} quantifies the scatter of the measurements around the fitted trend. Throughout this work, we adopt the rms_{res} as a measure of the intrinsic RV precision, since it represents the residual uncertainty after applying the best correction for the instrumental drift. The smoother the nightly drift and the lower its amplitude, the more precisely the FP calibration can correct the measured stellar RVs.

Fig. 3.16 illustrates the quadratic fitting for a series of three consecutive typical nights. The upper panel represents pre-C-PLUS, and the bottom panel post-C-PLUS. The amplitude and scatter of the data have decreased after C-PLUS, and the drifts are more consistent from one night to the next, exhibiting a smoother behavior.

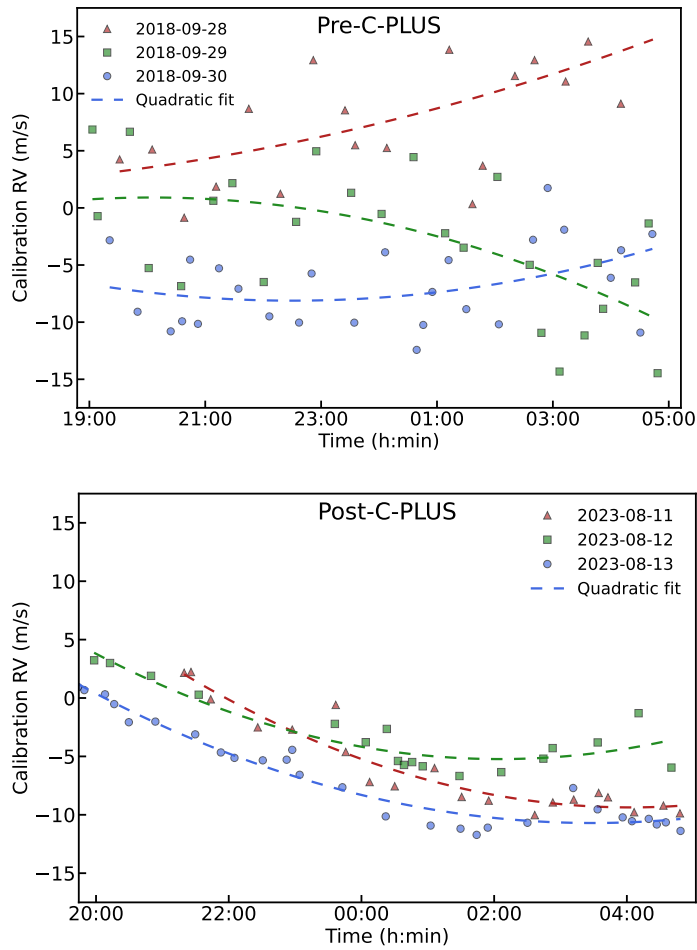


Figure 3.16: RV drift of the NIR spectrograph during individual nights, derived from FP calibration spectra. The dashed lines represent the quadratic fits applied to the calibration data for each night.

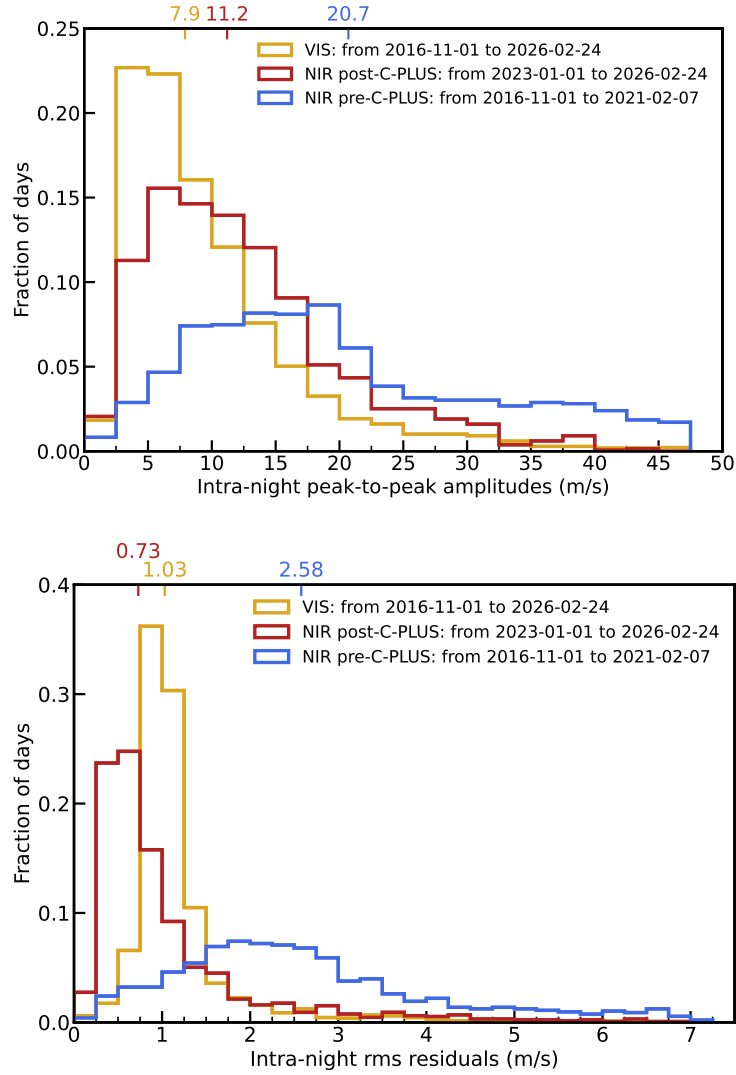


Figure 3.17: *Top*: Histogram of the peak-to-peak RV variation from FP calibrations. *Bottom*: Histogram of the rms_{res} after subtracting a quadratic fit. The median values are indicated on the top axis.

We performed a statistical analysis of both the peak-to-peak and rms_{res} values derived from the nightly RV drifts. We defined three datasets, (i) CARMENES NIR (see Sect. 3.2.3) pre- and (ii) post-C-PLUS, and (iii) CARMENES VIS (from 1 November 2016 to 24 June 2026).

The top panel of Fig. 3.17 displays the histograms of the peak-to-peak RV amplitudes. All three distributions are unimodal, indicating that the data do not exhibit significant substructures or clustering around multiple values. The pre-C-PLUS distribution spans a wide range, with a median value of 20.7 m s^{-1} . It is skewed towards higher amplitudes, suggesting that a non-negligible fraction of nights were affected by unusually large RV drifts. The variance is correspondingly high, reflecting the broad spread around the median. In contrast, the post-C-PLUS distribution shows a substantially narrower spread, with a reduced median value of approximately 11.2 m s^{-1} , indicating improved

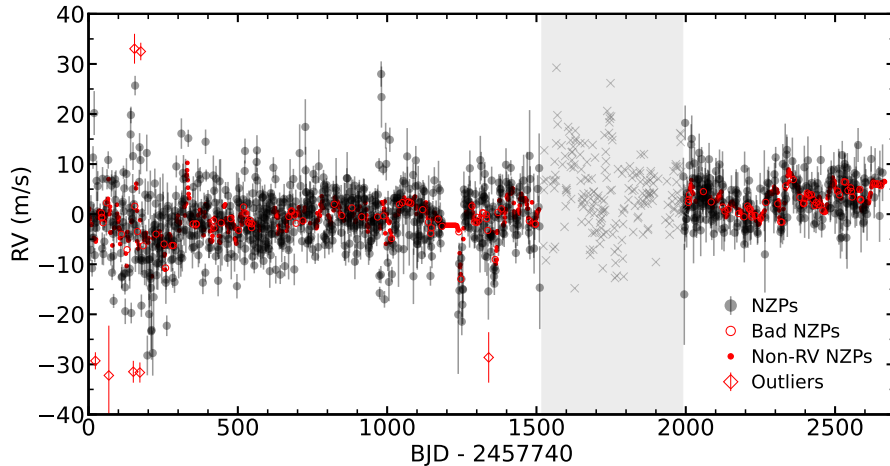


Figure 3.18: Time series of the CARMENES NIR NZPs. Solid black circles mark NZPs included in our analysis; crosses within the grey-shaded area corresponds to the C-PLUS interventions. Red diamonds highlight 3σ outliers; empty red circles denote nights with fewer than three RV-standard observations, and solid red dots nights without any RV measurement.

intra-night stability following the instrument upgrades. The VIS channel has the lowest median drift amplitude at 7.9 m s^{-1} , and its distribution is the most compact among the three.

The bottom panel of Fig. 3.17 presents the distributions of the rms_{res} values. These show a similar pattern to the peak-to-peak amplitudes, although the post-C-PLUS distribution is more sharply peaked around lower values compared to both the pre-C-PLUS and VIS datasets. The median rms_{res} values are 2.58 m s^{-1} for pre-C-PLUS, 0.73 m s^{-1} for post-C-PLUS, and 1.03 m s^{-1} for the VIS channel. Hence, the intrinsic precision improved by a factor of 3.5 as a consequence of the enhanced thermal stability.

These results confirm that the C-PLUS upgrades significantly improved the NIR spectrograph's short-term stability, bringing its performance closer to that of the VIS channel, even better in terms of rms_{res} . The more compact and symmetric post-C-PLUS histogram, centered at a lower rms_{res} , highlights the enhanced instrument stability and reduced intra-night RV scatter achieved after the upgrades.

3.4.2 Nightly zero point scatter

Fig. 3.18 presents the time series of NZPs, with the period of C-PLUS implementation and stabilization shaded in gray to distinguish the pre- and post-C-PLUS regimes. To ensure the reliability of the analysis, we exclude NZPs based on fewer than three RV-constant stars, those identified as 3σ outliers, and nights without any NZP determination due to the absence of standard stars. These exclusions are necessary, as such values are replaced by the median (see Sect. 3.3.4), which would otherwise artificially decrease the NZPs scatter.

We computed the NZPs scatter using a maximum likelihood optimization method developed by Zechmeister et al. (2018), `m1rms`⁶. It accounts for individual measurement uncertainties and allows for an additional unknown variance term, often interpreted as extra jitter or unmodeled noise. This method iteratively adjusts the unknown variance to maximize the likelihood under the assumption of normally distributed residuals.

We find a significant improvement in NZP stability after the upgrades: the scatter decreased from 6.1 m s^{-1} (pre-C-PLUS) to 3.9 m s^{-1} (post-C-PLUS), a reduction of 36%. The corresponding median NZP values are -1.2 m s^{-1} and 2.9 m s^{-1} , respectively. The rate of nights with 3σ NZP outliers also dropped from 1% pre-C-PLUS to zero post-upgrade. Notably, the average errors of the NZPs are 2.6 m s^{-1} and 3.2 m s^{-1} , with the post-C-PLUS scatter closely matching the average error, suggesting that the residual variability may be largely explained by the measurement uncertainties alone.

For comparison, the NZPs in the VIS channel exhibit even lower variability, with a scatter of 2.5 m s^{-1} , a median of 0.3 m s^{-1} , an outlier fraction of 1.6%, and an average error of 1.1 m s^{-1} .

To contextualize these results, we compare them with values reported in the literature for other high-precision spectrographs using similar NZP correction strategies. Trifonov et al. (2020) applied an equivalent approach to HARPS, finding a weighted rms (`wrms`) scatter of 1.5 m s^{-1} ; Ribas et al. (2023) reported a standard deviation of 2.3 m s^{-1} for CARMENES VIS, in close agreement with our findings. A different approach was taken by Grouffal et al. (2024), who used Gaussian Process regression informed by ancillary parameters to model systematics in SOPHIE's NZP time series. Their method, based on a small set of bright RV-constant stars, yielded an rms of 2.15 m s^{-1} .

3.4.3 Contributions to the stellar RV scatter

Following the approach by Bauer et al. (2020) to understand the factors affecting the scatter exhibited in the RV time series of CARMENES, we decompose the observed RV scatter into four main contributors; (i) the instrument's intrinsic RV precision, (ii) the scatter of the NZPs, (iii) the photon noise, and (iv) the stellar RV jitter. We then compare the quadratically combined contribution of these components with the exhibited scatter measured across the three stellar samples defined in Sect. 3.3.3.

Our approach differs from that of Bauer et al. (2020) in two important ways. They use RVs corrected for NZP offsets for their analysis, whereas we use uncorrected values, making the NZP contribution explicitly measurable in our study. Additionally, their treatment of stellar jitter assumes a representative value for M dwarfs' activity, while we derive the stellar RV jitter individually for each star in our sample using its actual time series, based on the work by Ruh et al. (2024, see also Sect. 6.3).

The contribution of the instrument to the RV scatter is characterized here by the rms_{res} of the intra-night drift, which captures short-time-scale variations.

⁶ <https://github.com/mzechmeister/python/blob/master/wstat.py>

Karmn	σ_{vis} [m s ⁻¹]	N _{obs} VIS	$\sigma_{nir-pre}$ [m s ⁻¹]	N _{obs} NIR-pre	$\sigma_{nir-post}$ [m s ⁻¹]	N _{obs} NIR-post
J17033+514	4.3 ± 0.4	65	4.3 ± 2.9	34	6.7 ± 1.1	31
J22565+165	3.3 ± 0.1	715	4.5 ± 0.5	442	2.8 ± 1.0	180
J06548+332	3.0 ± 0.1	465	3.0 ± 0.9	261	2.1 ± 1.3	122
J05033-173	4.0 ± 0.4	76	6.0 ± 1.5	46	3.4 ± 2.0	27
J02530+168	2.3 ± 0.1	301	3.2 ± 0.4	255	3.3 ± 0.8	61
J23492+024	1.5 ± 0.1	493	3.6 ± 1.0	270	3.3 ± 1.1	136
J13299+102	2.0 ± 0.1	458	4.4 ± 1.7	299	2.7 ± 1.3	89

Table 3.1: Stellar RV jitter estimates and number of measurements for a subset of CARMENES targets. For each star (Karmn ID), we list the RV jitter and number of observations for the VIS channel, and the NIR channel before and after the C-PLUS upgrades. The table contains seven stars that have a jitter estimate for all three cases; the full list is available online.

When the drift is smooth, it can be effectively corrected using simultaneous FP calibration data, making rms_{res} a good proxy for the instrument's intrinsic RV precision. It is described and discussed in Sect. 3.4.1.

As described in Sect. 3.4.2, we estimate the scatter of the NZPs with the mlrms of the time series. It is applied after removing clear outliers and poorly estimated values.

Photon noise sets a fundamental limit on RV precision due to the finite number of photons collected during an observation (Bouchy, Pepe, and Queloz, 2001). For our analysis, the photon noise is estimated by `serval`, based on the S/N of the spectra. The pipeline estimates RV uncertainty by accounting for the quality of each spectral order and the overall spectral information content, providing a robust estimate of the RV uncertainty due to photon statistics. For each star in the sample, we compute the average photon noise across all observations, and then adopt the median of all the targets as the representative value for the sample.

The stellar RV jitter refers to the excess noise in an RV time series caused by apparent Doppler shifts induced by variability in the stellar spectrum (Saar and Donahue, 1997; Saar, Butler, and Marcy, 1998). In the work of Ruh et al. (2024), the RV jitter was computed for most CARMENES VIS targets by modeling it as an additional noise term in the RV error budget. The total uncertainty for each RV measurement was treated as the quadratic sum of its internal error and the stellar jitter. A maximum-likelihood approach was used to simultaneously estimate the jitter and the mean RV, assuming normally distributed residuals. Uncertainties on the jitter were derived via non-parametric bootstrapping with 1000 resamples.

We extended this method to the NIR channel, using RVs corrected for NZPs to ensure that NZP-related variability does not bias the jitter estimate. For each star, the jitter was estimated individually, and we use the median value across the sample distribution as the representative value in our analysis.

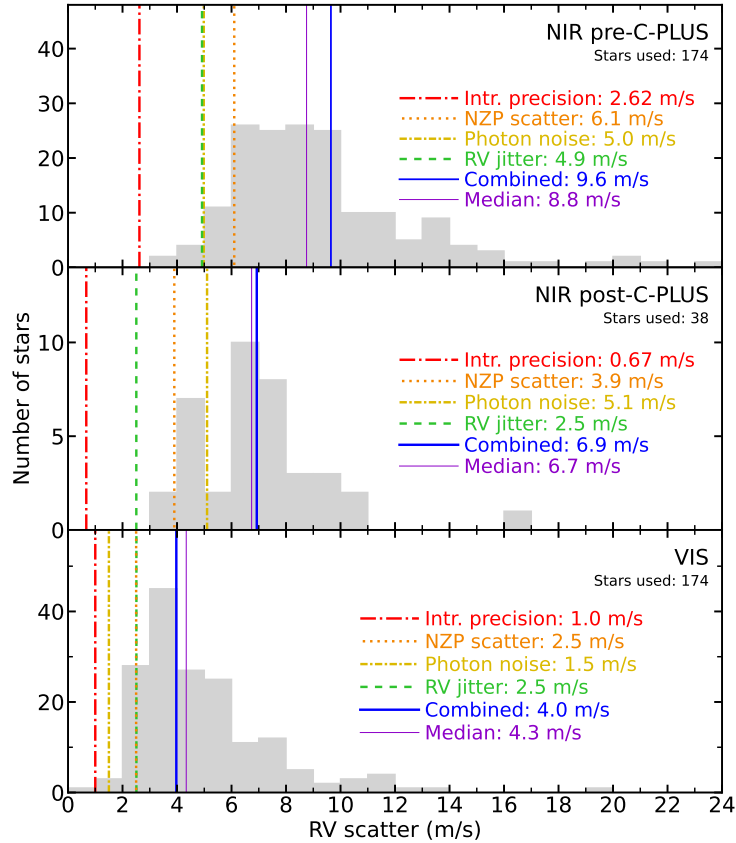


Figure 3.19: Histogram of RV scatter (m_1rms) of CARMENES stellar sample.

Looking at the individual stellar RV jitter values (see Table 3.1), we find several stars for which the estimated stellar jitter is negative. This indicates that the observed scatter in the RV time series is smaller than expected from the assigned internal uncertainties. The internal errors are primarily driven by photon noise, with additional contributions from the instrument's stability and the data reduction process. A negative stellar jitter estimate typically suggests that the internal errors were overestimated, or that the sample size is too small to reliably constrain the true external scatter. Because a star-by-star analysis is beyond the scope of this work, and the median stellar jitter is not a primary focus here, we assume that potential underestimations of the stellar jitter are balanced by conservatively estimated internal errors.

Based on the four aforementioned contributors, we compute the combined RV scatter as the sum in quadrature. The goal of this analysis is not to model the physical origin of each component in detail, but rather to evaluate their relative importance and how they compare to the observed RV scatter in each dataset. To assess the accuracy of this decomposition, we also calculate the median RV scatter of the stellar samples and compare it to the combined value.

We compute the m_1rms for the RV time series of the selected stellar samples, and present the resulting distributions in Fig. 3.19. The discrepancy between the combined RV scatter and the median scatter in pre-C-PLUS data can

likely be attributed to the significant thermo-mechanical changes in the NIR spectrograph. This might introduce additional instrument jitter, affecting all contributors and leading to an overestimation of the combined value.

A comparison of the pre- and post-C-PLUS distributions reveals a clear improvement in the combined RV scatter, decreasing from 9.6 m s^{-1} to 6.9 m s^{-1} . The pre-C-PLUS histogram exhibits a more extended right tail, indicating a greater number of stars with elevated RV variability. While the photon noise remains nearly unchanged between the two samples (5.0 m s^{-1} and 5.1 m s^{-1} , respectively), all other contributing terms show a decrease after the C-PLUS upgrades. The evolution of the intrinsic RV precision and the NZP scatter are discussed in Sect. 3.4.1 and Sect. 3.4.2, respectively.

In our analysis, the stellar RV jitter is not a directly measured physical quantity, but a derived one, estimated from the observed RV scatter and the internal error budget. It represents the excess variance beyond the formal uncertainties, but does not directly measure the intrinsic physical variability of the star. Thus, it can also reflect other effects not explicitly accounted for, such as residual instrumental instability, the size and variability of the stellar sample, the number of observations per target, or true long-term spectral variability between the two observing epochs. In the pre-C-PLUS sample, the median stellar jitter is 4.9 m s^{-1} , while in the post-C-PLUS sample it drops to 2.5 m s^{-1} . This reduction may reflect a combination of improved instrument stability, more conservative internal errors, and statistical limitations arising from smaller sample sizes. As noted earlier, jitter estimates can become negative when internal errors are overestimated, directly affecting the median value, which is particularly relevant in the post-C-PLUS dataset.

It is also worth noting that the pre-C-PLUS sample includes more targets, increasing the likelihood of including stars with higher RV jitter values. This broader sampling may bias the median upward compared to the smaller post-C-PLUS sample. However, even when we restrict the analysis to stars observed both before and after the upgrade, we still observe a lower median jitter in the post-C-PLUS data. This suggests that the observed reduction is not solely due to sample size, but likely reflects a combination of improved instrumental stability, more conservative internal error estimates, and potential changes in stellar variability between the two epochs.

For the VIS channel, the combined RV scatter is 4.3 m s^{-1} , compared to 6.9 m s^{-1} for the post-C-PLUS NIR sample. Both distributions show similarly short right tails, indicating that stars with unusually high RV variability are rare in both cases. The main difference between the VIS and NIR post-C-PLUS datasets arises from photon noise: while the intrinsic RV precision and NZP scatter are comparable, the VIS spectra contain more RV information, resulting in lower photon-limited uncertainties (Reiners et al., 2018). For the stellar jitter component, a lower value is expected in the NIR due to the reduced impact of chromatic effects at longer wavelengths (Zechmeister et al., 2018; Baroch et al., 2020; Jeffers et al., 2022). In our data, the median stellar jitter is 2.5 m s^{-1} in both VIS and post-C-PLUS NIR samples, and remains unchanged when considering only stars observed in both datasets.

Bauer et al. (2020) reported a combined RV scatter of 3.6 m s^{-1} for the VIS and 8.4 m s^{-1} for the NIR, based on data that overlaps with the pre-C-PLUS period. In their decomposition, the instrument's jitter contributions were 1.2 m s^{-1} (VIS) and 3.7 m s^{-1} (NIR), the median photon noise 1.5 m s^{-1} and 6.9 m s^{-1} , and the stellar activity component was assumed to be 3.0 m s^{-1} in both cases. These values are broadly consistent with those obtained in our analysis, and the relative contributions of each variability source show a similar pattern. Differences between the two studies likely stem from the use of different stellar samples, datasets, and RV products. In particular, Bauer et al. (2020) used RVs corrected for NZPs, whereas our analysis explicitly retains the NZP contribution. Minor discrepancies may also result from differences in how RV scatter is quantified mathematically.

3.5 SUMMARY

CARMENES is a dual-channel, high-resolution spectrograph on the 3.5 m Calar Alto telescope, with a VIS and a NIR arm. The NIR channel is cooled to $\sim 140 \text{ K}$ using a nitrogen-gas flow to ensure thermal stability. From 2016 to 2020, the VIS showed an instrument RV precision of 1.2 m s^{-1} and the NIR of 3.7 m s^{-1} (Bauer et al., 2020).

To address the limitations of the NIR channel, the C-PLUS project was launched to design and implement a series of upgrades across the instrument, with a particular focus on improving the thermal stability of the NIR CS. The goal was to enhance the intrinsic RV precision by stabilizing the instrument's CS.

In this study, we provided an overview of the NIR channel CS and described the main upgrades implemented under the C-PLUS project. The AVSTL eliminated thermal instabilities caused by vacuum losses and regeneration by maintaining the transfer line pressure below 10^{-6} mbar. Replacing the on-off valve with a proportional valve enabled continuous-flow operation. This working mode allows for a finer tuning of the thermal conditions of the OB. The EGWS facilitates instrument operation by preventing ice formation at the exit of the CS and includes a flow meter to monitor system status. The PCU ensures a stable pressure inside the feeding dewar, enabling a constant coolant flow in the system and suppressing pressure drops during operations and interventions. Finally, the fixed-dewar configuration was implemented to minimize the impact of the LN₂ refilling in the system. The LN₂ dewar was replaced daily, which had a significant impact on the thermal stability of the OB. The refilling of the feeding dewar almost neglects this process. Nevertheless, for proper implementation of this procedure, the check valve on the feed line had to be removed to clear any obstruction in the valve. The thermal stability achieved by the C-PLUS interventions is considerable, with a 2-year variability below 4 mK (peak-to-peak) at the OB.

The enhanced thermal stability is also translated into the instrument's performance. To determine this effect, we compared the intrinsic RV precision before and after C-PLUS and with the VIS channel. Using the calibration data

provided by the FP unit, we evaluated the performance of CARMENES during its operation. The histogram of nightly RV drifts for the instrument's different statuses shows a clear improvement. The peak-to-peak amplitude of the NIR has reduced from 20.7 m s^{-1} to 11.2 m s^{-1} , compare to 7.9 m s^{-1} of the VIS channel. The scatter of this nightly drift has also decreased, from 2.58 m s^{-1} to 0.73 m s^{-1} , even below the VIS with 1.03 m s^{-1} .

We also analyzed the scatter of the NZPs for the pre-C-PLUS, post-C-PLUS, and VIS datasets, using a maximum-likelihood root-mean-square method (mlrms) to quantify the variability. The scatter in the NIR NZPs decreased from 6.1 m s^{-1} to 3.9 m s^{-1} after C-PLUS, compared to 2.5 m s^{-1} for the VIS.

Additionally, we estimated the total RV scatter of slowly rotating M dwarfs ($v \sin i \leq 2 \text{ km s}^{-1}$). We decomposed the scatter exhibited by the RV time series into four main contributors: the instrument's intrinsic RV precision, the NZP scatter, the median photon noise, and the median stellar RV jitter. We estimated the photon noise from the empirical spectra using the `serval` pipeline. The stellar jitter was also computed following the work by Ruh et al. (2024) for CARMENES VIS, and computed for the NIR. The results are available online at a GitHub repository. The median RV scatter of the NIR sample has been reduced as a result, from 8.8 m s^{-1} to 6.7 m s^{-1} thanks to C-PLUS. In comparison, the VIS sample shows a lower median scatter of 4.3 m s^{-1} , primarily due to its lower photon noise (1.5 m s^{-1} in VIS and 5.1 m s^{-1} in NIR). The main drivers of the improvement in the NIR RV scatter are the enhanced intrinsic RV precision and reduced NZP variability, both achieved through the C-PLUS interventions.

These results demonstrate that the C-PLUS upgrades have significantly improved CARMENES NIR performance, both in terms of thermal and radial-velocity stability. The upgraded system now enables more reliable and precise RV measurements in the near-infrared, reinforcing the NIR arm of CARMENES as a powerful tool for exoplanet searches around low-mass stars.

PROJECTED ROTATIONAL VELOCITY OF M DWARFS

This chapter describes the oversampled convolution method we developed to estimate the projected rotational velocity of stars, later applied to CARMENES data, yielding a homogeneous catalog of almost 400 M dwarfs. The results are based on Varas et al. (2026) work, and further extended where appropriate.

4.1 WHY SHOULD WE STUDY STELLAR ROTATION?

M-dwarf stars are particularly interesting targets for spectroscopic campaigns, as discussed in Chapter 1. Characterizing their rotation provides insight into their magnetic activity, internal structure, and age (Suárez Mascareño et al., 2015; Newton et al., 2016; Díez Alonso et al., 2019; Shan et al., 2024). These constraints are essential for understanding the formation and evolution of their planetary systems.

A fundamental measure of stellar rotation is the projected rotational velocity, $v \sin i$, which represents the component of a star's equatorial rotation along the line-of-sight. It is typically inferred from the Doppler broadening of absorption lines in high-resolution spectra. Thus, CARMENES provides an excellent dataset for improving rotational velocity measurements of M dwarfs.

Determining $v \sin i$ accurately is challenging, as rotational broadening must be disentangled from other line-broadening mechanisms, such as instrument effects and stellar turbulence. Conventional approaches often approximate the rotational profile using a convolution kernel that accounts for limb darkening. However, most studies adopt a fixed linear limb-darkening coefficient (usually $u = 0.6$), independent of spectral type or wavelength (Jenkins et al., 2009; Reiners, Joshi, and Goldman, 2012; Reiners et al., 2022). As demonstrated in Varas et al. (2026), this simplification can lead to systematic biases.

Our approach introduces two key enhancements to modeling rotational broadening. First, we apply an oversampled convolution to minimize numerical artifacts. Second, we adopt order-specific limb-darkened kernels that account for wavelength- and temperature-dependent linear coefficients. For each target and spectral order, we compute average u values from stellar-atmosphere models, achieving higher fidelity across the full wavelength range. Tests based on synthetic spectra indicate that this method improves both the precision and accuracy of the results, while remaining computationally efficient.

We apply this method to 392 M dwarfs with CARMENES VIS observations, enabling direct comparison with previous studies based solely on VIS data. This application yields a homogeneous catalog¹ of $v \sin i$ measurements. In Sect. 4.11, we discuss the prospects for extending the method to CARMENES NIR data.

¹ <https://github.com/rvarasg/vsini-limb-darkening>

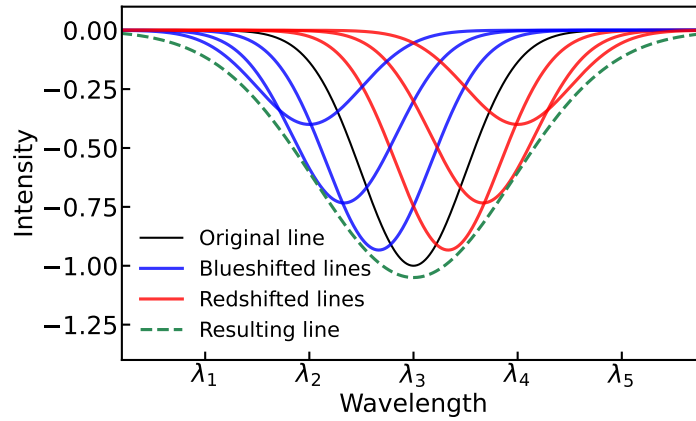


Figure 4.1: Illustration of the line-broadening due to rotational velocity.

4.2 LINE-BROADENING

Rotational broadening

The spectral lines of a rotating star are broader than those from a static one, because the light from the limbs will be Doppler shifted². Let's start with a perfectly homogeneously illuminated star, defined by only one spectral line. As it starts to rotate faster, the (one-line) spectrum of different parts of the star will be Doppler shifted. The spectrum at the edge moving away from us will be redder, whereas the edge moving toward us will be bluer, and the center will not be shifted at all. When we integrate the whole disc into a single spectrum, we will have a broader line than the same star not rotating. This is illustrated in Fig. 4.1.

Limb-darkening effect

Limb darkening has been extensively studied in astronomy, as it affects many observations, such as transits. For proper detection and characterization, modeling and correcting this effect is crucial. In spectroscopy, it has also been studied, but again for transit studies, not for deriving the projected rotational velocity of the stars.

Because the rotational broadening is most strongly shaped by the regions with the highest projected rotational velocities, the edges of the stellar disk play a key role. In the presence of limb darkening, however, these regions contribute less flux to the disk-integrated spectrum than in the uniformly illuminated case. Therefore, this effect must be considered when estimating the projected rotational velocity.

Consequently, when computing the rotational velocity of a star using its spectrum, if we do not consider the limb darkening, we will broaden the

² This is true if we work with integrated spectra in the whole disc, with no spatial resolution. If we do have spatial resolution, the spectra from the limbs will be (red or blue) shifted compare to the center of the star.

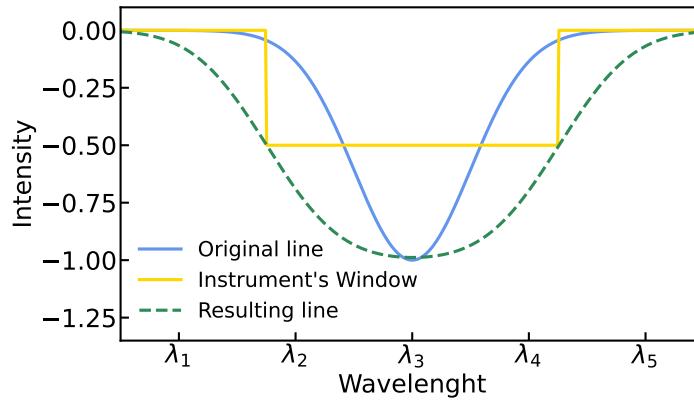


Figure 4.2: Illustration of the instrument broadening in a schematic single-line spectrum.

template spectrum with a smaller $v \sin i$ value when we try to fit it with the target one. On the other hand, if we do consider limb darkening, we will broaden the template accordingly, a bit more than before, because we know that the information about rotation is on the edges, but is hidden by the limb darkening. The conclusion is clear: if we consider limb darkening, we will derive higher $v \sin i$ values than if we neglect it.

Instrument broadening

Stellar rotation is not the only source of rotational broadening. Spectrographs such as CARMENES also produce instrument broadening of the lines. The broadening caused by a grating (see Chapter 1) is inversely proportional to the number of grooves it has. The digital recording of the light further broadens the spectrum by the point spread function.

This broadening can be empirically measured in each instrument, and we can even define a broadening profile. The resulting broadened lines will be the convolution of the original spectrum and the instrument profile, as illustrated in Fig. 4.2. Thus, each instrument has a resolution limit for rotation studies, which can be expressed as an equivalent $v \sin i$. Below this value, we can not provide reliable estimates of the stellar rotation.

Other sources of line-broadening

Spectra can also be broadened by unresolved or smeared³ Zeeman splitting, specifically lines with large Landé g -factors. Because the amount of splitting depends on the magnetic field strength, the resulting line profile may appear broadened rather than resolved into discrete components when different local field strengths contribute to the observed spectrum. This effect is especially important in strongly magnetized stars, such as white dwarfs.

³ *Smeared* refers to situations where there is a large range of magnetic field strengths or to disc-integrated spectra.

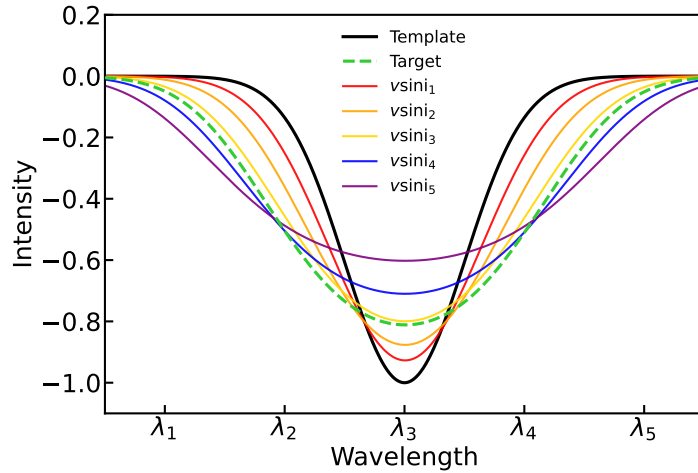


Figure 4.3: Illustration of the fitting process for deriving the $v \sin i$ of a target star based on a set of broadened templates with different $v \sin i$.

Zeeman components are plane or circularly polarized according to the direction of the magnetic field, so one should be able to recognize the Zeeman effect, even when polarization is not fully resolved. Nonetheless, for a disc-integrated spectrum, the polarization information is lost because several magnetic field directions are blended together.

Other line-broadening sources are (i) unresolved hyperfine structure in elements with a large nuclear spin (e.g., vanadium); (ii) unresolved isotopic lines in elements with several isotopes of comparable abundance (e.g., tin or chlorine), and (iii) autoionization in absorption or dielectronic recombination in emission spectroscopy for different elements (e.g., copper).

Deriving the stellar rotation

A typical approach to derive the projected rotational velocity of a star using spectroscopic data is to broaden the spectrum of a reference (i.e., slow-rotating, bright, and non-active) star with a set of $v \sin i$ values and see the best fit to the target spectrum. A schematic representation is shown in Fig. 4.3, with again, a simplified one-line spectrum (black line), broadened with five different $v \sin i$ values (color-coded lines), and a rotationally-broadened target (dashed green line).

When broadening the template spectrum, both instrument broadening and limb darkening should be taken into account. Even if we use an observational spectrum as a template, if it rotates more slowly than the spectrograph's resolution limit, the instrument's broadening will dominate over the rotation. Thus, the limb-darkening effect on the lines shape will be erased. Additionally, the spectrograph resolution will set an upper limit on the $v \sin i$ derived by this method.

4.3 OBSERVATIONS AND DATA REDUCTION

4.3.1 CARMENES spectra

The CARMENES spectra are reduced using the `caraca1` pipeline, as detailed by Caballero et al. (2016). Starting with the raw data, `caraca1` performs dark and bias correction, order tracing, flat-relative optimal extraction, and wavelength calibration, resulting in fully reduced and wavelength-calibrated 1-D spectra.

The second pipeline is `serva1`, which creates a high-signal-to-noise-ratio spectrum using the reduced spectra of the target star. It then computes the series of RVs via least-square fitting, telluric masking, échelle order weighting, and correcting for systematic effects. The output also includes activity indices. Here we present the implementation in `serva1` of the computation of the $v \sin i$ accounting for the effect of limb darkening.

4.3.2 Synthetic data

We adopted four spectra from the PHOENIX NewEra stellar atmosphere models (Hauschildt et al., 2025) and corresponding surface intensity distributions (Claret, Hauschildt, and Torres, 2025). The synthetic templates were selected among main-sequence stars with solar metallicity, covering the range $T_{\text{eff}} = 2500\text{--}4000$ K in steps of 500 K. Each template provides intensity spectra at 127 μ values, where μ is the cosine of the angle between the normal to the stellar surface and the line-of-sight, spanning the wavelength range 1000–60000 Å with a constant step of 0.05 Å. These model spectra fully cover the CARMENES wavelength range at a slightly higher sampling rate than the instrument.

We numerically integrated the stellar spectrum over a grid of 3000×3000 square cells covering the sky-projected stellar disc, following the method described by Morello et al. (2022) and Canocchi et al. (2024). Each cell is identified by the Cartesian coordinates of its center (x_j, y_j) , which are normalized to the stellar radius. The corresponding μ_j values are calculated as:

$$\mu_j = \sqrt{1 - x_j^2 - y_j^2}. \quad (4.1)$$

The “static” cell spectrum is then obtained by interpolation at μ_j from the template, here using a cubic spline, though the method is only weakly sensitive to the choice of interpolation scheme. To account for stellar rotation, we Doppler-shifted the spectrum of each cell according to its velocity along the line-of-sight,

$$v_j = (y_j \sin \bar{\lambda} - x_j \cos \bar{\lambda}) \cdot v \sin i, \quad (4.2)$$

where $\bar{\lambda}$ is a dummy parameter in this context (we set $\bar{\lambda} = 0$). In the presence of a transiting planet, $\bar{\lambda}$ traditionally denotes the sky-projected spin-orbit angle. We resampled the Doppler-shifted spectra onto the same wavelength grid as the template using linear interpolation, enabling direct summation of the cell spectra.

4.4 CLASSIC CONVOLUTION AND GRID-BASED $v \sin i$ FITTING

The rotational broadening of stellar spectra can be implemented using several approaches. The two most common ones are convolution with a rotational broadening kernel (Gray, 2005) and direct numerical integration (Carvalho and Johns-Krull, 2023). Although numerical integration provides a more general and potentially more accurate procedure, it is computationally more expensive. These methods often adopt a single linear limb-darkening coefficient (commonly $u = 0.6$), despite the fact that u depends on both stellar temperature and wavelength. In this work, we develop an oversampled convolution method that offers a fast and robust alternative while properly accounting for wavelength- and temperature-dependent limb darkening.

The following subsections describe the method and the incremental improvements, tested using synthetic spectra, that guided its development. The test setup consists of a disc-integrated reference spectrum with $v \sin i = 0 \text{ km s}^{-1}$ and a rotationally broadened target spectrum with $v \sin i$ values of 4, 8, 14, 20, 30, and 50 km s^{-1} , and effective temperatures $T_{\text{eff}} = 2500, 3000, 3500,$ and 4000 K . These values are representative of the M-dwarf sample observed by CARMENES, although the method itself does not, in principle, impose any restriction on the stellar parameters. For each case, $v \sin i$ was computed using the linear limb-darkening law with theoretical u coefficients.

The standard approach to determining $v \sin i$ involves convolving a chosen template spectrum with a rotational broadening kernel over a grid of trial $v \sin i$ values, and minimizing the residuals with respect to the target spectrum. In this work, we adopt the commonly used semi-circular kernel, which represents a rigidly rotating, uniformly emitting stellar disc:

$$\tilde{K}(\tilde{v}) = \sqrt{1 - \tilde{v}^2}, \quad (4.3)$$

where \tilde{v} is the velocity normalised to $v \sin i$. The kernel is subsequently normalized to conserve flux.

A set of broadened templates is generated by convolving the reference spectrum with the kernel over a grid of $v \sin i$ values with steps of $\Delta(v \sin i) = 0.01 \text{ km s}^{-1}$. Both the target and template spectra are cubic-interpolated onto the CARMENES wavelength grid, which has an approximately constant spectral resolution and therefore corresponds to a uniform sampling in $\ln \lambda$. Each broadened template is compared with the target spectrum, and the optimal $v \sin i$ is obtained through χ^2 minimization, defined as:

$$\chi^2(v \sin i) = \sum_i \left(\frac{f_i - f_{\text{tpl}}(\lambda_i, v \sin i)}{\sigma_i} \right)^2, \quad (4.4)$$

where f_i and $f_{\text{tpl}}(\lambda_i, v \sin i)$ are the target and the artificially broadened template fluxes, respectively, and σ_i is the target flux uncertainty. A parabola is then fitted to the χ^2 values at the minimum, and its two adjacent grid points, and the vertex is adopted as the final $v \sin i$. This procedure is applied independently to each corresponding CARMENES VIS échelle order (108–66, 562.3–934.3 nm).

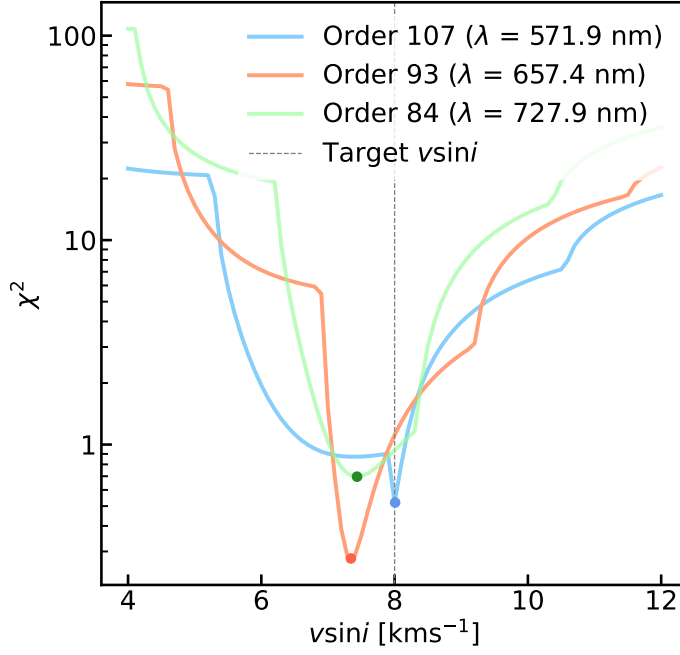


Figure 4.4: χ^2 minimization between reference and target synthetic spectra as a function of $v \sin i$ for three spectral orders, computed without limb-darkening correction. The spectra correspond to $T_{\text{eff}} = 3000$ K, with a target value of $v \sin i = 8 \text{ km s}^{-1}$ (vertical line).

The final $v \sin i$ for a given target is taken as the median of the order-by-order estimates, while the standard deviation provides the uncertainty.

Fig. 4.4 illustrates the χ^2 minimization as a function of $v \sin i$ for three spectral orders. The resulting $v \sin i$ is indicated by a circular marker. These curves exhibit kinks at different $v \sin i$ values, which biases the inferred velocity depending on their proximity to the true solution. The origin of these kinks is explained in the following subsection.

4.4.1 Oversampling

The numerical discretization of the kernel in Equation 4.3 naturally leads to small kinks when varying $v \sin i$, because the kernel is evaluated on a discrete logarithmic wavelength grid. The velocity sampling is fixed by $\Delta v = \Delta(\ln \lambda) c$, so that the theoretical kernel half-width is:

$$k_{\text{max}} = \frac{v}{\Delta v}. \quad (4.5)$$

In practice, the convolution uses the integer quantity:

$$k = \lfloor k_{\text{max}} \rfloor, \quad (4.6)$$

which is the number of grid points effectively included in the discrete kernel. The discretized rotational kernel is then computed as:

$$\tilde{K}(j) = \sqrt{1 - \left(\frac{j}{k_{\text{max}}}\right)^2}, \quad j = -k, \dots, k, \quad (4.7)$$

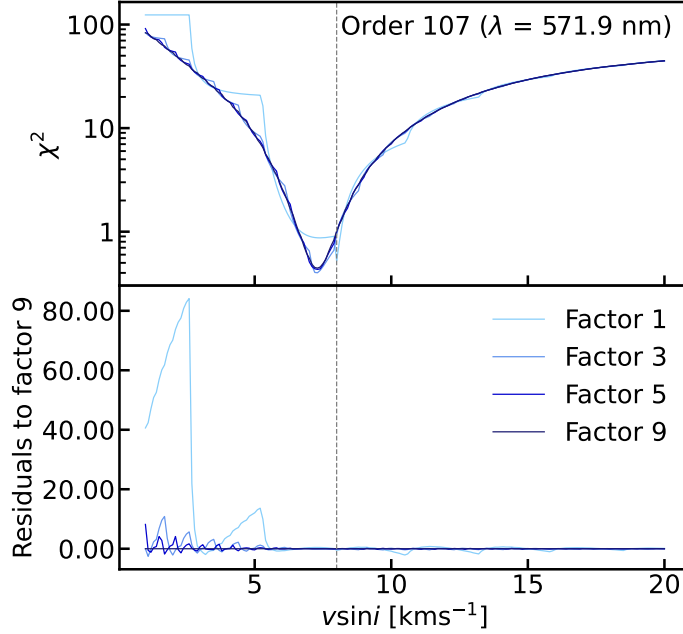


Figure 4.5: Top: χ^2 minimization as a function of $v \sin i$ for different oversampling factors. Bottom: residuals relative to the best-fit solution (oversampling factor = 9). The convolution kernel does not include any limb-darkening effect. The vertical line marks the target value $v \sin i = 8 \text{ km s}^{-1}$, obtained from synthetic spectra with $T_{\text{eff}} = 3000 \text{ K}$.

and the convolution is performed on the same logarithmic wavelength grid. Each time $v \sin i$ increases enough for k_{max} to cross an integer boundary, the kernel jumps from $k(v_0)$ to $k(v_1) = k(v_0) + 1$, producing a step-wise change that propagates into the χ^2 curve and may shift the position of the minimum.

To mitigate this effect, we oversampled the template spectrum before the convolution. It is interpolated (first-order spline) onto a finer grid, convolved with the rotational kernel for the desired $v \sin i$, and then downsampled back to the native wavelength points for the computation of residuals. This approach preserves the original sampling while smoothing the discontinuities introduced by the discrete kernel. The oversampling factor scales linearly with the wavelength grid density, hence, with a factor of N the wavelength grid contains N -times more sampling points. Note that factor = 1 means no oversampling is applied.

Fig. 4.5 illustrates how increasing the oversampling factor reduces the amplitude of the discontinuities. Fig. 4.6 shows the resulting $v \sin i$ estimates for each spectral order. Oversampling substantially improves the consistency of $v \sin i$ estimates across wavelength. Increasing the factor from 1 to 3 reduces the scatter by $\sim 50\%$. Larger factors do not yield any significant additional gain, with median values and uncertainties essentially unchanged. We therefore adopt an oversampling factor of 5 as an efficient compromise between computational cost and precision.

Oversampling has been implemented to avoid potential kinks during convolution, rotationally broadening the template spectrum and thereby reducing

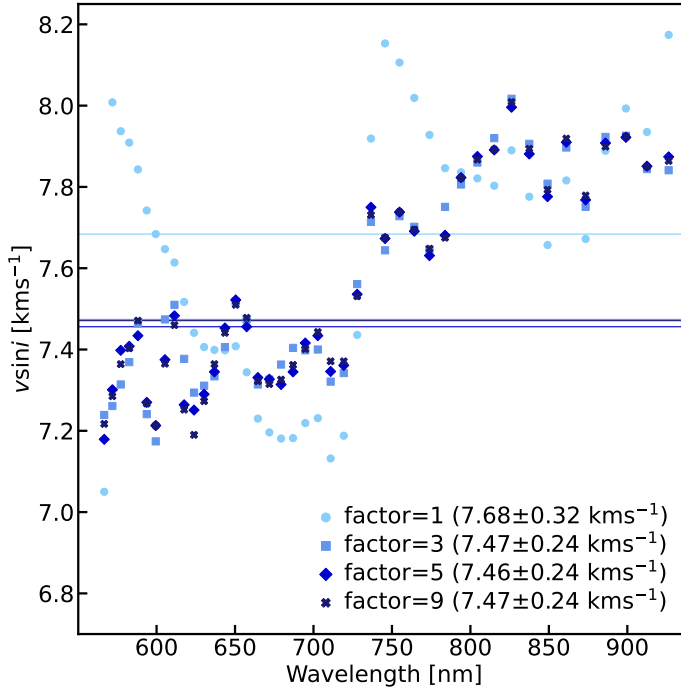


Figure 4.6: Best-fitting $v \sin i$ values as a function of wavelength for different oversampling factors, obtained without accounting for limb darkening in the convolution process. Horizontal lines correspond to the median values. The spectra correspond to $T_{\text{eff}} = 3000 \text{ K}$ and a target value of $v \sin i = 8 \text{ km s}^{-1}$.

the uncertainties obtained for the $v \sin i$ derived from the χ^2 . We explore the impact of implementing oversampling in the parameter space for both $v \sin i$ and T_{eff} .

The results are evaluated by comparing the errors (ϵ_{factor}) obtained with (factor = 5) and without (factor = 1) oversampling. Fig. 4.7 shows the relative error ($\epsilon_5/\epsilon_1 - 1$) as a function of the target $v \sin i$ for the four effective temperatures. The impact of the oversampling is significantly higher for lower $v \sin i$ values, with up to 50–70% smaller uncertainties, and almost no improvement for 30–50 km s^{-1} . This is expected from the kernel's definition, with more kinks at low-velocity values (due to the lower number of points defining the kernel), as seen in Fig. 4.5.

4.5 ROTATION KERNEL WITH LIMB DARKENING

We hypothesize that the remaining discrepancies in our analysis (offsets and trends) may be related to stellar limb darkening, which modifies the rotational broadening kernel through the non-uniform surface brightness of the stellar disc.

Following Gray (2005), the disc-integrated spectrum of a rigidly rotating, spherical star can be written as a convolution:

$$F(v) = \int_{-v \sin i}^{+v \sin i} S(v - v') \tilde{K}(v') dv', \quad (4.8)$$

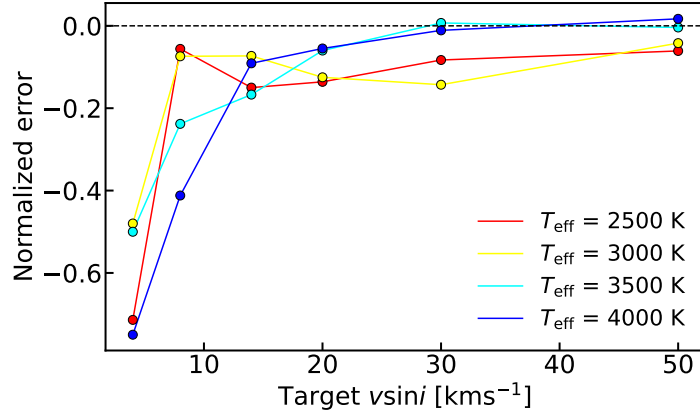


Figure 4.7: Normalized error of the $v \sin i$ estimation using oversampling (factor = 5), compared with not including it, as a function of the target $v \sin i$.

where $S(v)$ is the intrinsic, non-rotating stellar spectrum, and

$$v = c \frac{\lambda - \lambda_{\text{ref}}}{\lambda_{\text{ref}}} \quad (4.9)$$

is the Doppler velocity relative to a reference wavelength. The kernel $\tilde{K}(v')$ represents the relative contribution of all surface elements sharing the same projected line-of-sight velocity v' . Choosing the x -axis along the projected stellar equator, the line-of-sight velocity of a surface element is:

$$v'(x) = (v \sin i) x, \quad -1 \leq x \leq 1, \quad (4.10)$$

in normalized Cartesian coordinates on the projected stellar disc. Each value of v' therefore corresponds to a chord across the stellar disc perpendicular to the projected equator. The unnormalized kernel is obtained by integrating the surface intensity along these chords,

$$K(x) = \int_{-a}^a I(x, y) dy, \quad a = \sqrt{1 - x^2}. \quad (4.11)$$

We assume radial limb darkening, so that $I(x, y) = I(\mu)$ with $\mu = \sqrt{1 - x^2 - y^2}$. Most commonly used limb-darkening laws can be written as linear combinations of powers of μ :

$$I(\mu) = \sum_{\gamma} c_{\gamma} \mu^{\gamma}. \quad (4.12)$$

Replacing the above intensity profile into Equation 4.11, the kernel becomes:

$$K(x) = \sum_{\gamma} c_{\gamma} \int_{-a}^a (a^2 - y^2)^{\frac{\gamma}{2}} dy, \quad a = \sqrt{1 - x^2}. \quad (4.13)$$

Applying the substitution $y = a \cos t$:

$$K(x) = \sum_{\gamma} c_{\gamma} a^{\gamma+1} \int_0^{\pi} (\sin t)^{\gamma+1} dt, \quad a = \sqrt{1 - x^2}. \quad (4.14)$$

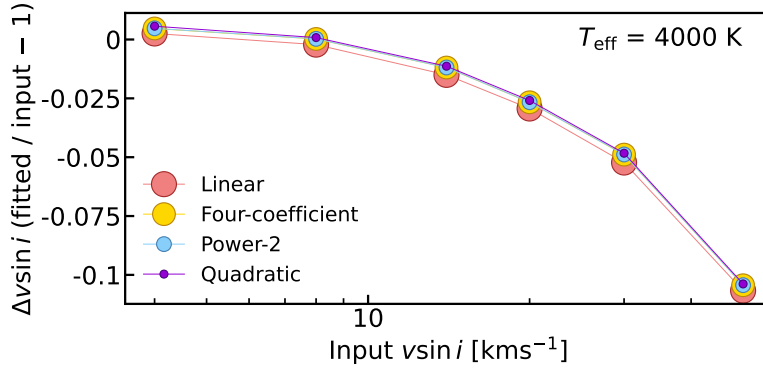


Figure 4.8: Normalized difference between input and fitted $v \sin i$ as a function of the input $v \sin i$ for different limb-darkening laws.

In the absence of limb darkening, there is only one term with $\gamma = 0$ ($c_0 = 1$), so that:

$$K_{\text{unif}}(x) = 2\sqrt{1-x^2}. \quad (4.15)$$

The linear limb-darkening law coincides with Equation 4.12 for $c_0 = 1 - u$ and $c_1 = u$. The corresponding unnormalized kernel is:

$$K_{\text{lin}}(x) = 2(1-u)\sqrt{1-x^2} + \frac{\pi}{2}u(1-x^2). \quad (4.16)$$

The kernel for the quadratic law is obtained with $c_0 = 1 - u_1 - u_2$, $c_1 = u_1 + 2u_2$, and $c_2 = -u_2$:

$$K_{\text{quad}}(x) = 2(1-u_1-u_2)\sqrt{1-x^2} + \frac{\pi}{2}(u_1+2u_2)(1-x^2) - \frac{4}{3}u_2(1-x^2)^{\frac{3}{2}}. \quad (4.17)$$

The integrals for non-integer γ exponents do not admit a closed-form analytical solution. They can, however, be expressed in terms of the Γ function:

$$\int_0^\pi (\sin t)^{\gamma+1} dt = \pi \frac{\Gamma\left(\frac{\gamma+2}{2}\right)}{\Gamma\left(\frac{\gamma+3}{2}\right)}, \quad \gamma > -2. \quad (4.18)$$

By combining Eqs. 4.13 and 4.18, the broadening kernel can be computed for other limb-darkening laws, including the square-root, power-2, and four-coefficient prescriptions.

In the context of exoplanetary transit studies, the most commonly employed laws are linear (Milne, 1921), quadratic (Kopal, 1950), square-root (Diaz-Cordoves and Gimenez, 1992), four-coefficient (Claret, 2000), and power-2 (Hestroffer, 1997). Fig. 4.8 shows the differences between the fitted $v \sin i$ values obtained as a function of the target's $v \sin i$, for 4000 K, where our approach works worst. The discrepancies among the non-linear models are minimal, remaining below 0.5% even in the most extreme cases when compared to the linear law. Thus, we selected a linear limb darkening.

The normalized kernel for a linear limb-darkening law in Equation 4.16 can be written in a discrete form as:

$$\tilde{K}(x) = \frac{2(1-u)\sqrt{1-x^2} + \frac{\pi}{2}u(1-x^2)}{\pi(1-\frac{u}{3})}, \quad (4.19)$$

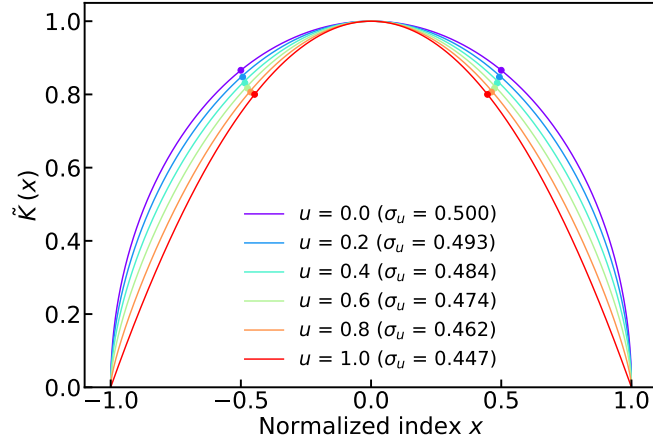


Figure 4.9: Rotational broadening kernel for different limb-darkening coefficients u . Circular markers correspond to the effective width of each kernel.

where $x = j/k_{\max}$ and u is the limb-darkening coefficient.

Fig. 4.9 shows the resulting normalized kernel in Equation 4.19 for selected values of the (linear) limb-darkening coefficient u . The kernel transitions from a semi-circular profile for $u = 0$ to an increasingly parabolic shape as $u \rightarrow 1$. We derived the effective width of each kernel, σ_u , where σ_u^2 corresponds to the kernel variance including limb darkening. The ratio σ_u/σ_0 is a measure of the underestimation of $v \sin i$ when limb darkening is neglected. For instance, $u = 0.6$ leads to an underestimation of approximately 6%. As illustrated by the narrower kernel at higher u , neglecting the limb darkening biases the recovered $v \sin i$ toward lower values.

However, because limb darkening varies with wavelength, a single coefficient cannot reproduce the stellar intensity profile accurately across all spectral orders. To account for this wavelength dependence, we determined an optimal coefficient for each spectral order. The simplest approach is to compute passband-integrated coefficients per order, following standard practice in low-resolution transit spectroscopy or photometry (Howarth, 2011). We derived these theoretical coefficients using the ExoTETHyS software (Morello et al., 2020b; Morello et al., 2020a), employing the same PHOENIX NewEra stellar templates adopted in our study.

We also investigated whether photometric limb-darkening coefficients are suboptimal for this application, as they neglect variations between continuum and spectral lines. In Varas et al. (2026) we attempted to simultaneously fit $v \sin i$ and the limb-darkening coefficient u using the oversampled convolution method, but found notable inconsistencies. The pipeline tends to assume $u \approx 1$ to compensate for discrepancies between the template and target spectra beyond the limb-darkening effect. Additionally, the derived u values were inconsistent across different target $v \sin i$ values. Because we improved the fitting process, addressing problems related to high T_{eff} and $v \sin i$, we revisited the possibility of simultaneous fitting, rather than relying on theoretical coefficients.

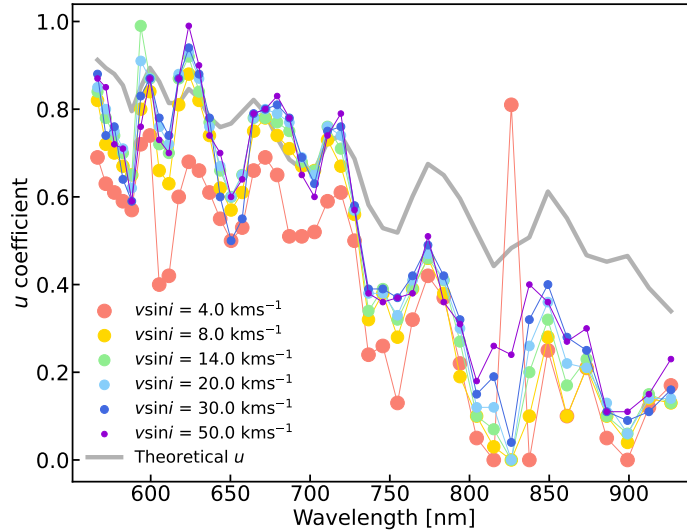


Figure 4.10: Limb-darkening u coefficient as a function of wavelength, when fitting simultaneously with $v \sin i$.

The results are more positive (see Fig. 4.10), as the trend towards $u \approx 1$ for higher T_{eff} and $v \sin i$ values disappears, and the consistency of the fit is significantly better. The only exceptions are some specific orders for target $v \sin i = 4 \text{ km s}^{-1}$. Comparing with the theoretical u coefficients, the correspondence is better for shorter wavelengths than for redder ones. Although the results are positive, the computational time is several orders of magnitude higher when fitting $v \sin i$ and u simultaneously rather than using the theoretical limb-darkening coefficients. Furthermore, the results from the one-parameter approach are sufficiently precise for our goals. Thus, we proceed with the theoretical u coefficients to model linear limb darkening.

Ultimately, including limb darkening clearly improves both accuracy and precision, reducing the mean offset and the scatter across spectral orders (Fig. 4.11). The deviation from the target is reduced by 5–10% (consistent with the decrease in the kernel’s effective width when including limb darkening), and the uncertainty is nearly halved. Top panel of Fig. 4.12 provides an overview of the derived $v \sin i$ values across the full range of T_{eff} . Because the differences between the tested limb-darkening prescriptions remain below 0.5%, the remaining discrepancies likely originate from the convolution procedure rather than from the specific choice of law. Nevertheless, including limb darkening consistently improves the precision of $v \sin i$, motivating our adoption of the linear law.

Table 4.1 presents the results obtained using regular convolution without limb darkening (RCWLD) and oversampled convolution with linear limb darkening (OCLLD) for all combinations of $v \sin i$ and T_{eff} in our spectral sample. In general, the more sophisticated approach yields values closer to the target $v \sin i$ and with smaller uncertainties (45% in median). The simplest method systematically underestimates the rotational broadening of the target spectrum and, in most cases, does not agree with the target value within 1σ .

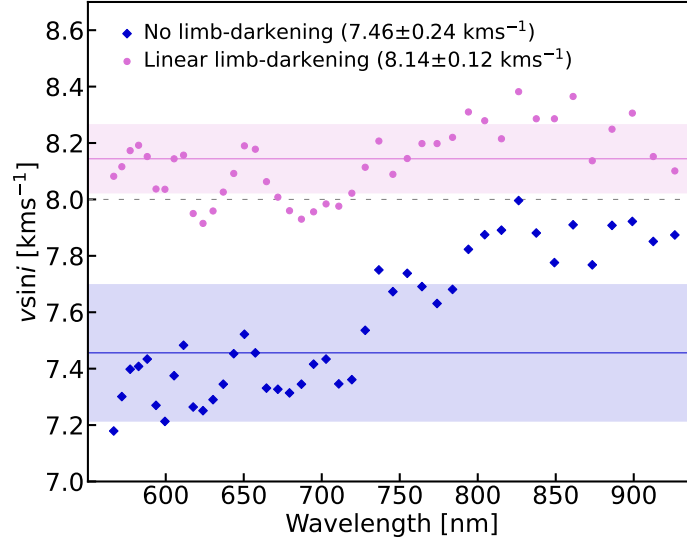


Figure 4.11: Best-fitting $v \sin i$ values as a function of wavelength, obtained with and without accounting for limb darkening during the convolution. Horizontal solid lines indicate the median values, and the shaded regions represent the standard deviations. The dashed line marks the target value $v \sin i = 8 \text{ km s}^{-1}$, for spectra with $T_{\text{eff}} = 3000 \text{ K}$.

Table 4.1: Derived $v \sin i$ values for all the T_{eff} and target $v \sin i$ combinations, using regular convolution without limb darkening (RCWLD) and oversampled convolution with linear limb darkening (OCLLD).

Target $v \sin i$ [km s^{-1}]	Method	$v \sin i$ [km s^{-1}] ($T_{\text{eff}} = 2500 \text{ K}$)	$v \sin i$ [km s^{-1}] ($T_{\text{eff}} = 3000 \text{ K}$)	$v \sin i$ [km s^{-1}] ($T_{\text{eff}} = 3500 \text{ K}$)	$v \sin i$ [km s^{-1}] ($T_{\text{eff}} = 4000 \text{ K}$)
4.0	RCWLD	3.97 ± 0.31	4.09 ± 0.25	4.20 ± 0.21	4.26 ± 0.19
	OCLLD	3.97 ± 0.06	4.11 ± 0.07	4.12 ± 0.08	4.07 ± 0.04
8.0	RCWLD	7.32 ± 0.18	7.80 ± 0.28	7.91 ± 0.24	7.80 ± 0.14
	OCLLD	7.89 ± 0.14	8.18 ± 0.13	8.18 ± 0.13	8.08 ± 0.07
14.0	RCWLD	12.67 ± 0.40	13.32 ± 0.45	13.63 ± 0.36	13.50 ± 0.18
	OCLLD	13.74 ± 0.28	14.26 ± 0.22	14.24 ± 0.22	14.06 ± 0.10
20.0	RCWLD	18.02 ± 0.55	18.90 ± 0.62	19.25 ± 0.52	19.12 ± 0.24
	OCLLD	19.64 ± 0.42	20.35 ± 0.29	20.30 ± 0.29	20.01 ± 0.14
30.0	RCWLD	27.11 ± 0.80	28.45 ± 0.83	28.82 ± 0.72	28.73 ± 0.36
	OCLLD	29.45 ± 0.65	30.42 ± 0.39	30.34 ± 0.39	29.93 ± 0.21
50.0	RCWLD	45.49 ± 1.40	47.24 ± 1.38	48.16 ± 1.04	47.65 ± 0.52
	OCLLD	48.95 ± 1.09	50.46 ± 0.65	50.17 ± 0.59	49.66 ± 0.31

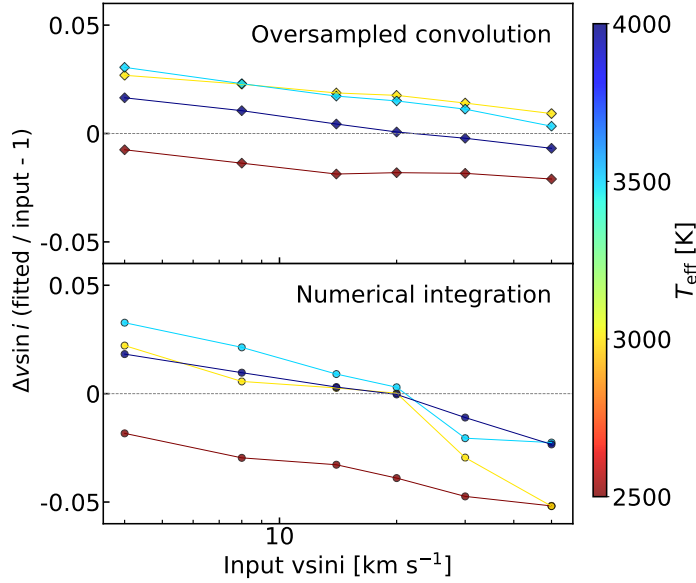


Figure 4.12: Normalized difference between input and fitted $v \sin i$ as a function of input $v \sin i$ and spectra's T_{eff} , for oversampled convolution (top panel) and numerical integration (bottom panel).

4.6 NUMERICAL INTEGRATION

Carvalho and Johns-Krull (2023) developed a method to broaden spectra due to projected rotation, incorporating linear limb darkening via direct numerical integration. We find that this approach is more accurate and precise than convolution, but at a substantially higher computational cost.

In the work by Varas et al. (2026), the results showed that at high $v \sin i$ ($\gtrsim 20 \text{ km s}^{-1}$), the fitted values increasingly deviate from the input, with the effect more pronounced at higher T_{eff} , particularly at 4000 K. Moreover, the numerical integration method was particularly more precise for hotter ($T_{\text{eff}} = 3500\text{--}4000 \text{ K}$) and faster-rotating ($v \sin i \gtrsim 30 \text{ km s}^{-1}$) M dwarfs, with up to 5–10 % better precision.

Additional work allowed us to understand that the issue originated from the numerical implementation of the oversampling convolution approach. The broadening at the edges of the spectrum at each order produced artifacts, which negatively and significantly affected the $v \sin i$ derivation. This increased the uncertainties and deviated from the absolute value obtained. We have solved this problem by suppressing the very ends of the edges when fitting the target and broadened template spectra. The OCLLD values in Table 4.1 have also been updated from Varas et al. (2026). This issue only affects the results based on the synthetic spectra, which are updated and discussed here, and not the subsequent application of the method to CARMENES VIS or NIR data.

Fig. 4.12 shows the derived normalized $v \sin i$ as a function of the input values for different T_{eff} using the oversampled convolution (updated from the previous work) on top, and numerical integration at the bottom. Both methods yield similar results, with greater consistency for oversampled convolution

Table 4.2: List of stars used as template for computing $v \sin i$ depending on spectral type (Schöfer et al., 2019).

Karmn	GJ identifier	Spectral type	T_{eff} [K]
J14257+236W	GJ 548A	Mo.0 V	3850
J18580+059	GJ 740	Mo.5 V	3800
J18051-030	GJ 701	M1.0 V	3680
J16254+543	GJ 625	M1.5 V	3600
J06103+821	GJ 226	M2.0 V	3550
J17198+417	GJ 671	M2.5 V	3450
J15194-077	GJ 581	M3.0 V	3400
J17578+046	GJ 699	M3.5 V	3250
J11477+008	GJ 447	M4.0 V	3200
J19216+208	GJ 1235	M4.5 V	3100
J03133+047	GJ 1057	M5.0 V	3050
J00067-075	GJ 1002	M5.5 V	3000
J07403-174	GJ 283B	M6.0 V	2800
J02530+168	GJ 10393	M6.5-9.0 V	2700-2450

and uncertainties 23% smaller in the median. Thus, we proceed with the convolution approach.

4.7 IMPLEMENTATION IN SERVAL WITH CARMENES SPECTRA

The `serval` pipeline was originally developed to compute RVs for exoplanet searches, but it also provides additional data products, including activity indicators and $v \sin i$. We adapted our method to operate within the `serval` framework, following a regression-based approach analogous to cross-correlation techniques (Delfosse et al., 1998; Browning et al., 2010; Jeffers et al., 2018).

Based on previous lessons, we apply an oversampled convolution (factor = 5) with a linear limb-darkening kernel, using coefficients computed for each stellar temperature and spectral order, to broaden and resample the reference spectrum. Each co-added target spectrum is compared to the corresponding template order via χ^2 minimization over a grid of $v \sin i$ values (0–150 km s⁻¹, 0.5 km s⁻¹ steps), applied independently to each spectral order. For slow rotators ($v \sin i < 4$ km s⁻¹), a finer velocity grid (0–6 km s⁻¹, 0.05 km s⁻¹ steps) is used to improve resolution near 0 km s⁻¹. The final $v \sin i$ is taken as the median of the order-by-order estimates, with the standard deviation providing the uncertainty.

Templates are chosen according to the target’s sub-spectral type (Table 4.2), following Schöfer et al. (2019), who identified the least active and slowest rotator for each subtype. For M6.5 V and later, Teegarden’s star (J02530+168) is adopted as reference. All templates are generated with `serval`, ensuring a consistent instrumental profile across all spectral orders. The numerical

integration method by Carvalho and Johns-Krull (2023) has been implemented as an alternative alongside convolution.

4.8 COMPARISON WITH THE LITERATURE

Using CARMENES VIS spectra of 392 M dwarfs, we present a catalog of projected rotational velocities that incorporates limb-darkening effects (Table 4.3). The CARMENES spectra are intrinsically broadened by the instrument, corresponding to an effective $v \sin i = 2 \text{ km s}^{-1}$ (Reiners et al., 2018). Consequently, only an upper limit of 2 km s^{-1} can be placed on stars rotating more slowly than this threshold. In Sect. 4.11 we carry out an extensive analysis using NIR spectra.

To balance accuracy and computational efficiency, we do not always use all available spectra for each target. For stars with fewer than 20 spectra, all are included; otherwise, we select 20 evenly spaced spectra. This selection follows the behavior of the underlying `serval`-inherited function. We have verified that using more than 20 spectra does not significantly improve the precision of the derived $v \sin i$.

The command-line input files used to run `serval` are provided in our GitHub repository. Template stars have projected rotational velocities below the instrumental resolution and thus have $v \sin i < 2 \text{ km s}^{-1}$ (see Table 4.2). In some cases, adjustments were necessary, for example, for certain M3.5 V stars, it is preferable to use J14310-122 as the template rather than J17578+046. For stars later than M6.0 V, only the reddest orders (orders 88–66, 688.8–934.3 nm) are used due to low signal-to-noise in the bluer orders.

Theoretical linear limb-darkening coefficients were computed for each spectral order at $T_{\text{eff}} = 2500, 3000, 3500,$ and 4000 K and assuming solar metallicity. These coefficients are available in the associated GitHub repository⁴. For intermediate temperatures, the coefficients are computed via linear interpolation in `serval`.

The stellar temperatures are obtained from Carmencita (Caballero et al., 2017), which gathers values from several works (Soto et al., 2021; Palle et al., 2020; Cifuentes et al., 2020; Marfil et al., 2021). Carmencita is the "CARMEN(ES) Cool dwarf Information and daTa Archive", and contains a large number of parameters for more than 2000 M dwarfs in the solar neighborhood brighter than $J = 11.5 \text{ mag}$.

We compare the 392 $v \sin i$ values derived in this work with literature measurements compiled in Carmencita, adopting updated values from Reiners et al. (2022) when available (see Table 4.3). The adopted $v \sin i$ is the value we found to be the most reliable among our results, using oversampled convolution (OC) and numerical integration (NI), the literature, and a cross-check with the equatorial velocity (v_{eq}). A comparison with other methods (Passegger et al., 2020; Mas-Buitrago et al., 2024) is discussed in Sect. 4.10.

Most of the derived $v \sin i$ values lie below the instrumental resolution limit of CARMENES (2 km s^{-1}), in agreement with their literature values (see Table 4.3).

⁴ <https://github.com/rvarasg/vsini-limb-darkening>

Table 4.3: catalog of $v \sin i$ values for 392 M-dwarf stars of the CARMENES sample using VIS spectra. ^a

Karmn	Name	Adopted $v \sin i$		$v \sin i$ OC		$v \sin i$ NI		$v \sin i$ literature		Ref. ^b	v_{eq} [km s ⁻¹]
		[km s ⁻¹]	[km s ⁻¹]	[km s ⁻¹]	[km s ⁻¹]	[km s ⁻¹]	[km s ⁻¹]	[km s ⁻¹]			
J00051+457	BD+44 4548	< 2	< 2	2	2	2	2	2 ± 0.2	2 ± 0.2	Rein18	1.61 ± 0.01
J00067-075	GJ 1002	< 2	< 2	2	2	2.92 ± 0.09	2.92 ± 0.09	2 ± 0.2	2 ± 0.2	Rein18	0.07 ± 0.01
J00162+198E	LP 404-062	< 2	< 2	2	2	2	2	2 ± 0.2	2 ± 0.2	Rein18	0.13 ± 0.01
J00162+198W	EZ Psc	4 ± 1.6	4 ± 1.6	21.79 ± 0.96	21.79 ± 0.96	21.82 ± 0.96	21.82 ± 0.96	4 ± 1.6	4 ± 1.6	Four18	5.04 ± 0.16
J00183+440	GX And	< 2	< 2	2	2	2	2	2 ± 0.2	2 ± 0.2	Rein18	0.45 ± 0.01
J00184+440	GQ And	< 2	< 2	2	2	2	2	2 ± 0.2	2 ± 0.2	Rein18	0.08 ± 0.01
J00286-066	GJ 1012	< 2	< 2	2	2	2	2	2 ± 0.2	2 ± 0.2	Rein18	-
J00389+306	Wolf 1056	< 2	< 2	2	2	2	2	2 ± 0.2	2 ± 0.2	Rein18	0.42 ± 0.01
J00403+612	2MASS J00402129+6112490	< 2	< 2	2	2	2	2	-	-	-	-
J00570+450	G 172-030	< 2	< 2	2	2	2	2	2 ± 0.2	2 ± 0.2	Rein18	-
J01013+613	GJ 47	< 2	< 2	2	2	2	2	2 ± 0.2	2 ± 0.2	Rein18	0.54 ± 0.01
J01019+541	G 218-020	29.25 ± 0.91	29.25 ± 0.91	29.25 ± 0.91	29.17 ± 0.90	29.17 ± 0.90	29.17 ± 0.90	30.6 ± 3.1	30.6 ± 3.1	Rein18	28.2 ± 0.26
J01025+716	Ross 318	< 2	< 2	2	2	2	2	2 ± 0.2	2 ± 0.2	Rein18	0.46 ± 0.01
J01026+623	BD+61 195	< 2	< 2	2	2	2	2	2 ± 0.2	2 ± 0.2	Rein18	1.37 ± 0.01
J01033+623	V* V388 Cas	11.83 ± 0.51	11.83 ± 0.51	11.83 ± 0.51	11.85 ± 0.51	11.85 ± 0.51	11.85 ± 0.51	10.5 ± 1.5	10.5 ± 1.5	Rein18	12.10 ± 0.10
J01048-181	GJ 1028	< 2	< 2	2	2	2	2	2 ± 0.2	2 ± 0.2	Rein18	0.05 ± 0.01
J01056+284	GJ 1029	< 2	< 2	2	2	2	2	4.1 ± 0.8	4.1 ± 0.8	Jen09	0.65 ± 0.02
J01066+192	LSPM J0106+1913	< 2	< 2	2	2	2	2	-	-	-	-
J01078+128	G 2-21	< 2	< 2	2	2	2	2	-	-	-	-
J01125-169	YZ Cet	< 2	< 2	2	2	2	2	2 ± 0.2	2 ± 0.2	Rein18	0.11 ± 0.01

Notes. ^(a) Only first 20 rows are shown as an example, the complete table is available in the GitHub repository. Listed are: star's Karmn identifier, most common or discovery name, adopted $v \sin i$, $v \sin i$ obtained using oversampled convolution (OC), numerical integration (NI), the value from the literature and reference to the work, and the equatorial rotation velocity. ^(b) Jen09: Jenkins et al. (2009), Barn14: Barnes et al. (2014), Rein18: Reiners et al. (2018).

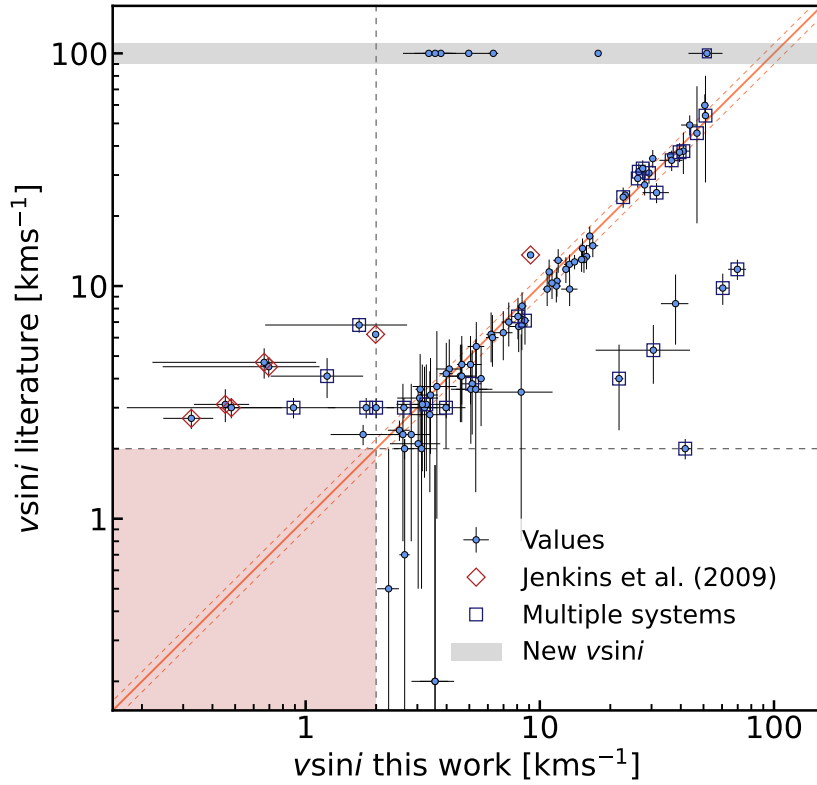


Figure 4.13: $v \sin i$ values obtained in this work using the oversampled convolution method compared with literature measurements. Newly determined $v \sin i$ values not previously available are shown in the shaded area at $v \sin i$ (literature) = 100 km s^{-1} . The solid line indicates the 1:1 relation, while the dashed lines correspond to a 10% deviation. Gray dashed lines and the shaded area mark the 2 km s^{-1} limit of CARMENES.

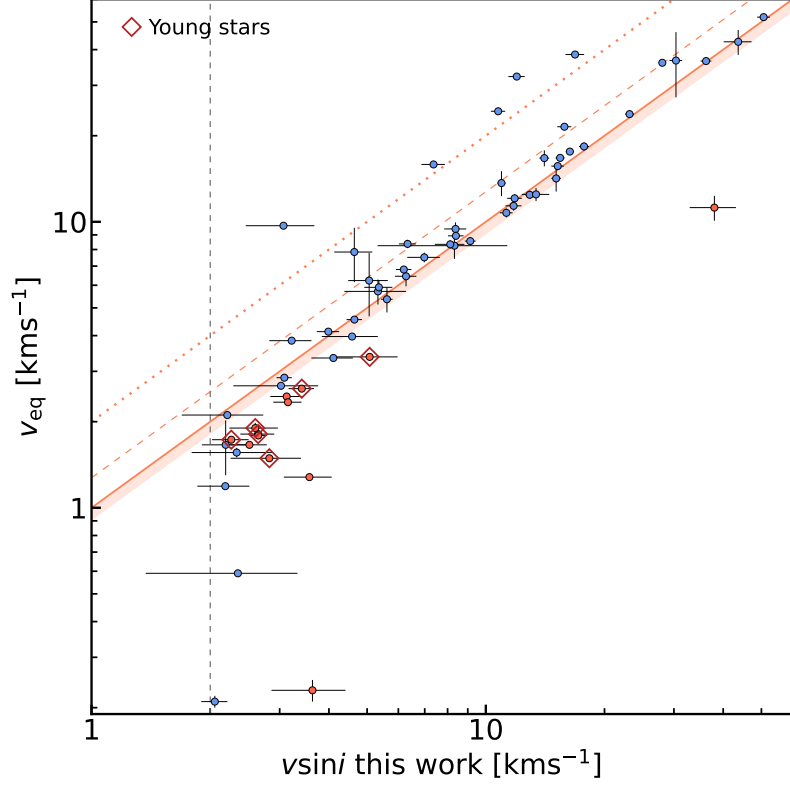


Figure 4.14: Values of $v \sin i$ derived from the oversampled convolution method compared to v_{eq} . The linear $1:\frac{4}{\pi}$ relation (dashed line) represents the expected value of $\sin i$ for an isotropic distribution of inclination angles (see Appendix B of Ruh et al. 2024). The 1:1 relation with a 10% margin (solid line and shaded region) and the $1:\frac{1}{2}$ relation (dotted line) correspond to $i = 90^\circ$ and $i = 30^\circ$, respectively. The vertical gray dashed line indicates the 2 km s^{-1} threshold, and the diamond markers correspond to young candidates (Cortés-Contreras et al., 2024).

The existing outliers can be seen in Fig. 4.13; those points deviating from the 1:1 diagonal line. Our $v \sin i$ measurements are generally in good agreement with the literature, also above 2 km s^{-1} , with a small number of outliers. The discrepancies are mainly due to either underestimated or overestimated values in previous studies, or to unresolved multiple systems affecting the observed spectra, which make the derived $v \sin i$ unreliable.

Close to the resolution limit, we find some discrepancies with values reported in the literature. Three of our targets (J01339-176, J04376+528, and J09144+526) show $v \sin i$ measurements very near the 2 km s^{-1} limit, differing from that threshold by less than 0.25 km s^{-1} . Of the remaining three objects, J05365+113 and J19346+045 exhibit $v \sin i > 2 \text{ km s}^{-1} > v_{\text{eq}}$, so only upper limits can be assigned. For J13450+176, our value agrees with that reported by Reiners et al. (2018), but not with the measurement of Reiners et al. (2022).

In Fig. 4.14, we compare our $v \sin i$ measurements from the oversampled convolution with limb darkening to the equatorial velocities v_{eq} , computed as $v_{\text{eq}} = 2\pi R_\star / P_{\text{rot}}$ for stars with available R_\star and P_{rot} . Errors in the rotational

periods were calculated following Equation 4 of Shan et al. (2024), and uncertainties in v_{eq} were propagated accordingly. Stars for which $v \sin i > v_{\text{eq}}$ are highlighted in orange and listed in Table 4.4.

We revised these outliers and identified six young candidates (J01339-176, J05366+112, J09144+526, J11026+219, J11476+002, J23548+385) as classified in Cortés-Contreras et al. (2024) based on their kinematics and activity indicators (measured from rotation, X-rays, ultraviolet, and H-alpha emission). These targets are highlighted with red diamonds in Fig. 4.14. According to this study, all of them are fast rotators for their spectral types, and all but J05366+112 present X-ray luminosities and (NUV-J) levels above the defined threshold for active stars. In addition, they exhibit significant H-alpha emission, except for J09144+526, which has a lithium measurement (Bischoff et al., 2020) instead. In particular, J11476+002 and J23548+385 are candidates for the IC2391 and UMA groups, both of which have intense magnetic fields, as measured in Reiners et al. (2022).

Among the remaining outliers, two have a doubtful youth assignment in the cited work: J04376+528 and J05365+113. Both are kinematically young (the Hyades or the galactic young disc) and have only slightly faster rotation than others. Another one (J19346+045) is a field star with a rotation period of 8.04 d (Díez Alonso et al., 2019), and evidence of chromospheric activity (NUV-J and H-alpha emission). Regarding J07361-031, it is an SB1 binary (Poveda et al., 2009) in a quadruple system. Finally, J19346+045, J08536-034, and J19169+051S present no relevant information regarding youth or activity.

We report 36 new $v \sin i$ measurements that were not previously available. In Fig. 4.13, these are represented in the gray-shaded region at $v \sin i_{\text{literature}} = 100 \text{ km s}^{-1}$. All values appear reliable except for J10182-204, a multiple system where $v \sin i$ is significantly higher than v_{eq} . Because $v_{\text{eq}} < 2 \text{ km s}^{-1}$, an upper limit of 2 km s^{-1} can be adopted for this target.

In total, 21 $v \sin i$ measurements in our sample are considered unreliable. Table 4.4 summarizes the reasons for their unreliability and provides recommended values. For most of these stars, an upper limit can be imposed based on v_{eq} , while in the remaining cases the literature $v \sin i$ is deemed more reliable and is adopted as the preferred value. Out of the 33 multiple systems in our sample identified by Cifuentes et al. (2025), 11 show discrepancies between our measurements and literature values. Seven of these are considered unreliable in our work and are listed in Table 4.4 as close.

Among the remaining systems, J01056+284, J14155+046, and J15412+759 have $v \sin i > v_{\text{eq}}$ in the literature, whereas our values are consistent, being below 2 km s^{-1} . J05532+242 lacks a measured v_{eq} , but Jeffers et al. (2018) imposed an upper limit of 3 km s^{-1} ; we adopt 2 km s^{-1} . Jenkins et al. (2009) reported a projected rotational velocity of $v \sin i = 6.8 \text{ km s}^{-1}$ for J14155+046. In our analysis, we obtained a value below 2 km s^{-1} , which corresponds to the lower limit of our method. Comparing the spectrum of J14155+046 with that of J03133+047, a reference star in our sample with $v \sin i < 2 \text{ km s}^{-1}$, we find a better match than when broadening the spectrum of J03133+047 to higher velocities, as the rms of the residuals halve (see Fig. 4.15).

Table 4.4: Targets with unreliable $v \sin i$ values.

Karmn	$v \sin i$ [km s ⁻¹]	Ref. ^a	Comments ^b
J00162+198W	< 2	Rein22	Close
J01339-176	< 2	This work	$v \sin i > v_{\text{eq}}$
J04376+528	< 2	This work	$v \sin i > v_{\text{eq}}$
J05337+019	9.8 ± 1.0	Rein18	Close
J05365+113	< 2	Rein22	$v \sin i > v_{\text{eq}}$
J05366+112	$\leq v_{\text{eq}}$	This work	$v \sin i > v_{\text{eq}}$
J05394+406	5.3 ± 0.5	Rein22	Close
J07033+346	< 2	This work	$v \sin i > v_{\text{eq}}$
J07361-031	$\leq v_{\text{eq}}$	This work	Close
J08536-034	8.4 ± 0.8	Rein22	$v \sin i > v_{\text{eq}}$
J09144+526	< 2	This work	$v \sin i > v_{\text{eq}}$
J10182-204	< 2	This work	$v \sin i > v_{\text{eq}}$
J11026+219	< 2	This work	$v \sin i > v_{\text{eq}}$
J11055+435	< 2	Rein18	$v \sin i > v_{\text{eq}}$
J11476+002	< 2	This work	$v \sin i > v_{\text{eq}}$
J16343+571	10.22 ± 1.02	Mor09	Close
J19169+051S	< 2	This work	$v \sin i > v_{\text{eq}}$
J19346+045	< 2	Rein18	$v \sin i > v_{\text{eq}}$
J20198+229	11.8 ± 1.2	Jen09	Close
J23548+385	3.6 ± 0.4	Rein18	$v \sin i > v_{\text{eq}}$
J23585+076	< 2	Rein18	Close

Notes. ^(a) Jen09: Jenkins et al. (2009), Mor09: Morales et al. (2009), Rein18: Reiners et al. (2018), Rein22: Reiners et al. (2022). ^(b) Comments indicates why they are unreliable. Close systems are identified by Cifuentes et al. (2025).

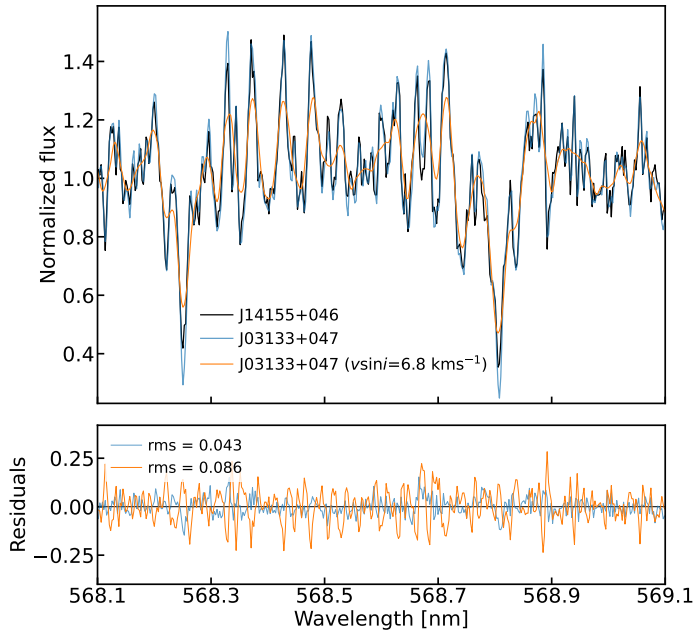


Figure 4.15: Top: chunk of the CARMENES VIS co-added spectrum of J14155+046 compared to the spectrum of J03133+047, without rotational broadening and with 6.8 km s^{-1} rotational broadening (Jenkins et al., 2009). Bottom: residuals with respect to the spectrum of J14155+046.

We identified seven $v \sin i$ measurements from Jenkins et al. (2009) that are not in agreement with our results (red diamonds in Fig. 4.13): J02022+103, J02465+164, J03090+100, J14578+566, J15100+193, J15238+174, and J20305+654. For three of these targets, the values from the cited work exceed v_{eq} , whereas our $v \sin i$ measurements are consistent. The remaining targets have $v \sin i < 2 \text{ km s}^{-1}$ in our analysis, and their spectra are better matched by a slowly rotating template than by a broadened one. We therefore recommend adopting our values as updated measurements for these stars.

Excluding outliers and considering only $v \sin i > 2 \text{ km s}^{-1}$, our measurements are systematically higher than literature values by a median of 5.7%, as illustrated in Fig. 4.16. An increase up to 10% was expected due to the inclusion of limb darkening (depending on the T_{eff} and $v \sin i$). At high rotation rates ($v \sin i \gtrsim 20 \text{ km s}^{-1}$), values may be slightly underestimated owing to intrinsic limitations of the oversampled convolution method (see Fig. 4.12). The median relative uncertainty of our $v \sin i$ values above 2 km s^{-1} is 6.8%, compared to 15.4% for the literature.

4.9 NUMERICAL INTEGRATION VS. OVERSAMPLED CONVOLUTION

The OC method is approximately 3.5 times faster than the NI approach, although the latter is expected to yield higher precision (see Sect. 4.6). Table 4.3 lists all $v \sin i$ values obtained with both methods, while Fig. 4.17 compares their results, showing excellent agreement. The histogram of the normalized residuals displays a median difference of only 0.1%, smaller than the offsets

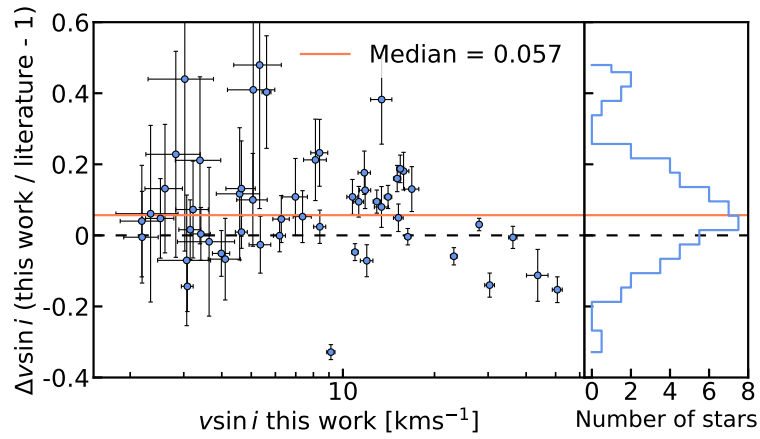


Figure 4.16: Histogram of the normalized difference between the $v \sin i$ value ($> 2 \text{ km s}^{-1}$) computed with oversampled convolution and the literature, excluding the outliers. The median is marked with a horizontal solid line.

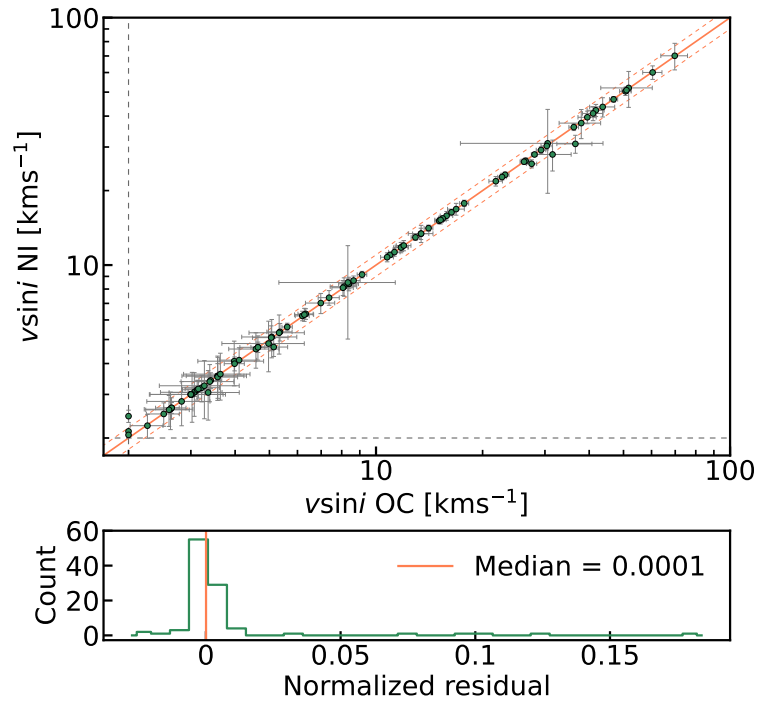


Figure 4.17: Top panel: comparison between $v \sin i$ computed with NI and OC. Dashed lines represent the 2 km s^{-1} limit, and diagonal lines mark the 1:1 relation $\pm 10\%$. Bottom panel: histogram of the normalized residuals with respect to the 1:1 relation for $v \sin i > 2 \text{ km s}^{-1}$. Median value represented by a vertical line.

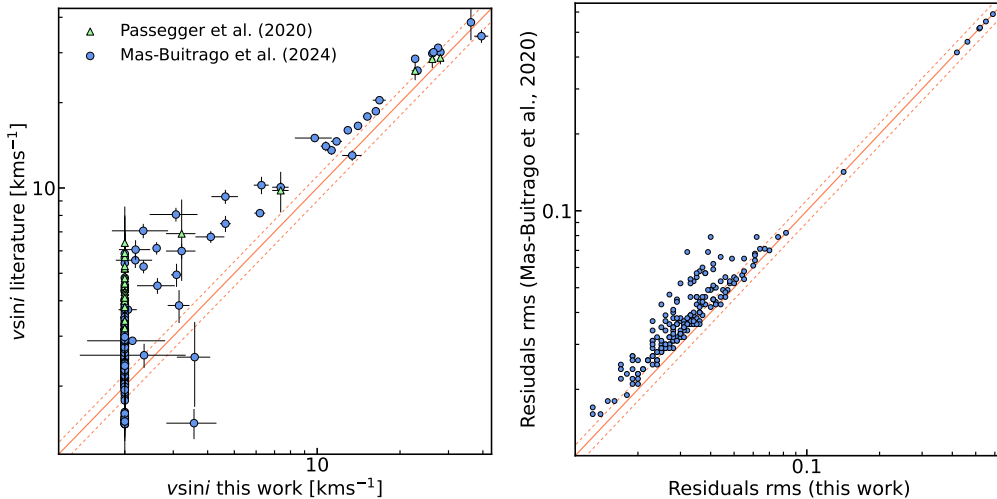


Figure 4.18: *Left*: Comparison of our $v \sin i$ values with the results from Passegger et al. (2020) and Mas-Buitrago et al. (2024). *Right*: The rms of the residuals between target spectrum and template rotationally broadened using both $v \sin i$ from this work and Mas-Buitrago et al. (2024).

predicted from synthetic data in Sect. 4.6, where differences of about 1–2% were found for slow and intermediate rotators, and up to 5–10% for the fastest rotators (see Fig. 4.12).

Overall, values below and above 2 km s^{-1} are fully consistent between methods. The substantial increase in computational time relative to the modest gain in precision does not justify using NI instead of OC, particularly for statistical studies or slow-to-moderate rotators ($v \sin i < 20 \text{ km s}^{-1}$). As discussed in Sect. 4.6, the improvement from NI becomes noticeable only for faster rotators ($30\text{--}50 \text{ km s}^{-1}$) and hotter stars ($T_{\text{eff}} = 4000 \text{ K}$). However, this effect disappears for the CARMENES sample, yielding a median error similar to that of the OC, 6.5%.

The main difference between the procedures for synthetic and CARMENES spectra is that, when using convolution, the synthetic spectra need to be resampled to the CARMENES wavelengths, changing from a constant step in λ to a constant resolution, which is mandatory for convolution to work properly. This interpolation may smooth the line peaks a bit, especially in the unbroadened template, leading to an underestimation of $v \sin i$.

4.10 COMPARISON WITH DEEP LEARNING

We also compared our catalog with the results of Passegger et al. (2020) and Mas-Buitrago et al. (2024) (see left panel in Fig. 4.18), who derived the projected rotational velocities of CARMENES targets using deep-learning methods. Their $v \sin i$ values are typically larger, particularly for slow rotators. For $v \sin i$ above 10 km s^{-1} , the differences decrease. Both studies also report systematically higher $v \sin i$ values than those derived by Reinert et al. (2018). Our results lie

between these estimates, but are closer to those of Reiners et al. (2018) and Reiners et al. (2022).

For all targets in common with Mas-Buitrago et al. (2024), we compared the stellar spectrum with the corresponding template, rotationally broadened using both sets of $v \sin i$ values (see Table 4.2). The rms of the residuals is shown in the right panel of Fig. 4.18. In general, our $v \sin i$ measurements yield smaller rms values, particularly for slow rotators. This indicates that our results reproduce the observed broadening of the spectral lines in the CARMENES VIS spectra more accurately.

4.11 $v \sin i$ USING NEAR-INFRARED SPECTRA

Varas et al. (2026) focused on computing the $v \sin i$ using CARMENES VIS data and performing the analogous computation with synthetic data for validation. We expand this work for the CARMENES NIR following the same approach. This is one of the few studies that uses NIR spectra to derive the projected rotational velocity of stars, and the most extensive one. The use of NIR spectra has several advantages, such as (i) the number of lines is smaller than in the visible, meaning that fewer lines will be blended due to the rotational broadening, (ii) the limb-darkening effect is smaller, thus, any additional error coming from the limb-darkening modeling will be smaller in the NIR compare to the VIS, (iii) for fainter stars, the S/N in the NIR tend to be similar or even higher than the VIS, favoring the use of the NIR for reliable $v \sin i$ estimations, and (iv) is an additional source to compute the $v \sin i$, allowing as to cross-check the estimations from both spectral samples. Nevertheless, there are some possible disadvantages with the NIR, such as the higher impact of the Zeeman splitting and telluric contamination at near-infrared wavelengths than in the visible.

4.11.1 *Validation with synthetic spectra*

Because we follow the same approach as for the VIS, most of the steps are similar, as well as the conclusions. Consequently, we use the oversampling convolution approach with linear limb darkening, and no reliable $v \sin i$ can be estimated below 2 km s^{-1} . We start validating the method for the NIR using synthetic spectra, computing the limb-darkening coefficients for the corresponding spectral orders, which are also available in the GitHub repository.

We computed the $v \sin i$ values for the T_{eff} and target $v \sin i$ grids, with and without limb darkening included. The normalized difference between input and fitted values as a function of the input is shown in Fig. 4.19. The results are very similar in general, with slightly smaller median uncertainty ($\sim 14\%$) when including limb darkening. Depending on the specific set of T_{eff} and $v \sin i$, one or the other is closer to recover the target value. The inclusion of limb darkening is not critical for NIR spectra, as the effect is smaller (i.e., the u coefficients are smaller) at redder wavelengths.

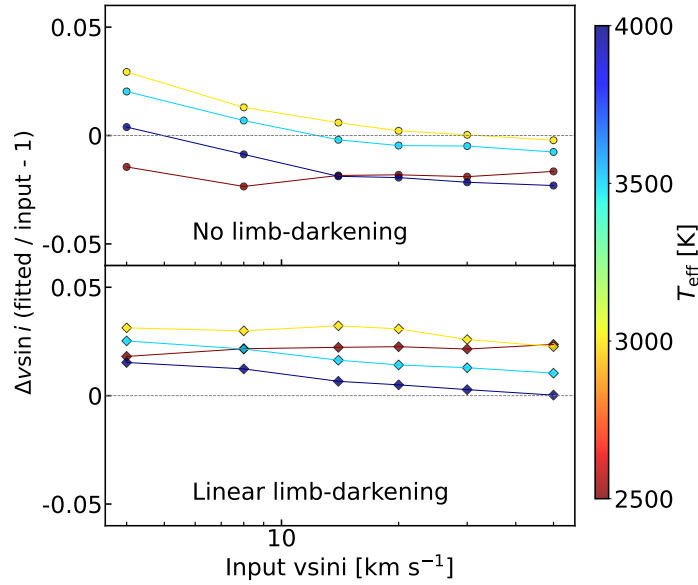


Figure 4.19: Normalized difference between input and fitted $v \sin i$ as a function of input $v \sin i$ and spectra's T_{eff} , without limb darkening (top panel) and with linear limb darkening (bottom panel), using NIR synthetic spectra.

4.11.2 Comparison with VIS results

We proceed with the method that includes linear limb darkening, as the results tend to be more homogeneous and, in principle, more realistic. The next step is to compare the values derived from NIR spectra with those from VIS data. Additionally, we combine the two datasets to compute $v \sin i$. We treated all the orders, both from VIS and NIR, similarly, and derived the $v \sin i$ in the same manner, with the median as the resulting value and the standard deviation as the associated uncertainty. The results from the three datasets are provided in Table 4.5.

The results are consistent between VIS and NIR, with comparable uncertainties and true values, although NIR estimates tend to be slightly higher (generally below 1%). The $v \sin i$ obtained from the combined datasets provides similar results, with higher uncertainties. The latter is expected because more orders are used, and the data dispersion tends to be higher from a statistical point of view. Further analysis, using weighted median and uncertainties, could improve the results, especially for the VIS+NIR dataset.

The potential advantages of the NIR over the VIS, such as the fewer line blending and the smaller limb-darkening effect, are not significant for the synthetic spectra, as both datasets provide almost identical results. The S/N in the VIS and NIR does not apply for synthetic spectra, but rather to observational data. The consistency across wavelength provides a strong argument for the method validation, further expanding the results from the VIS.

Table 4.5: Derived $v \sin i$ values for all the T_{eff} and target $v \sin i$ combinations, using VIS, NIR, and VIS+NIR spectra, using oversampled convolution with linear limb darkening.

Target $v \sin i$ [km s^{-1}]	Dataset	$v \sin i$ [km s^{-1}] ($T_{\text{eff}} = 2500 \text{ K}$)	$v \sin i$ [km s^{-1}] ($T_{\text{eff}} = 3000 \text{ K}$)	$v \sin i$ [km s^{-1}] ($T_{\text{eff}} = 3500 \text{ K}$)	$v \sin i$ [km s^{-1}] ($T_{\text{eff}} = 4000 \text{ K}$)
4.0	VIS	3.97 ± 0.06	4.11 ± 0.07	4.12 ± 0.08	4.07 ± 0.04
	NIR	4.07 ± 0.06	4.13 ± 0.05	4.10 ± 0.05	4.06 ± 0.03
	VIS+NIR	4.02 ± 0.07	4.11 ± 0.07	4.12 ± 0.07	4.06 ± 0.04
8.0	VIS	7.89 ± 0.14	8.18 ± 0.13	8.18 ± 0.13	8.08 ± 0.07
	NIR	8.17 ± 0.17	8.24 ± 0.10	8.17 ± 0.10	8.10 ± 0.06
	VIS+NIR	8.02 ± 0.20	8.20 ± 0.13	8.18 ± 0.12	8.09 ± 0.06
14.0	VIS	13.74 ± 0.28	14.26 ± 0.22	14.24 ± 0.22	14.06 ± 0.10
	NIR	14.31 ± 0.31	14.45 ± 0.17	14.23 ± 0.15	14.09 ± 0.12
	VIS+NIR	13.99 ± 0.39	14.31 ± 0.21	14.24 ± 0.20	14.08 ± 0.11
20.0	VIS	19.64 ± 0.42	20.35 ± 0.29	20.30 ± 0.29	20.01 ± 0.14
	NIR	20.45 ± 0.47	20.62 ± 0.18	20.28 ± 0.20	20.10 ± 0.20
	VIS+NIR	20.06 ± 0.59	20.43 ± 0.29	20.29 ± 0.27	20.03 ± 0.16
30.0	VIS	29.45 ± 0.65	30.42 ± 0.39	30.34 ± 0.39	29.93 ± 0.21
	NIR	30.64 ± 0.67	30.78 ± 0.25	30.39 ± 0.25	30.08 ± 0.31
	VIS+NIR	30.12 ± 0.89	30.58 ± 0.40	30.37 ± 0.36	29.98 ± 0.25
50.0	VIS	48.95 ± 1.09	50.46 ± 0.65	50.17 ± 0.59	49.66 ± 0.31
	NIR	51.18 ± 1.02	51.13 ± 0.43	50.52 ± 0.41	50.01 ± 0.50
	VIS+NIR	50.33 ± 1.45	50.80 ± 0.67	50.36 ± 0.57	49.80 ± 0.41

4.11.3 CARMENES NIR results

We also included the possibility of computing the $v \sin i$ using *serval*, as previously done for the VIS. One of the main differences between the two channels is the limb-darkening coefficients used, which are also T_{eff} -dependent, and the spectral order handling. CARMENES NIR have several orders that can not be recovered due to the high telluric contamination.

Varas et al. (2026) carried out a preliminary analysis using CARMENES NIR spectra and compared the results to the VIS. However, at that point, oversampling and limb darkening were not included, and only M6.0 V and cooler targets were considered. Here, we expand this work for a larger sample of stars, with 61 targets (compared with 16) later than M5.0 V, including oversampled convolution with linear limb darkening. The results are shown in Fig. 4.20 and Table 4.6.

From the total 61 derived $v \sin i$ values, 20 of them, roughly one third, are below the 2 km s^{-1} limit in both cases, thus, in agreement. Above the resolution limit of CARMENES, all except 8 ($\sim 13\%$) values are not in agreement within the uncertainties, marked with red diamonds in Fig. 4.20 and red-colored in Table 4.6.

J01056+284, J08413+594, J13102+477, and J14155+046 have an upper limit at 2 km s^{-1} in Varas et al. (2026), but derived values above this threshold using NIR spectra. These values are overestimated in this work, as the spectra match better with a slower rotator. J05394+406 has a significantly lower estimate from

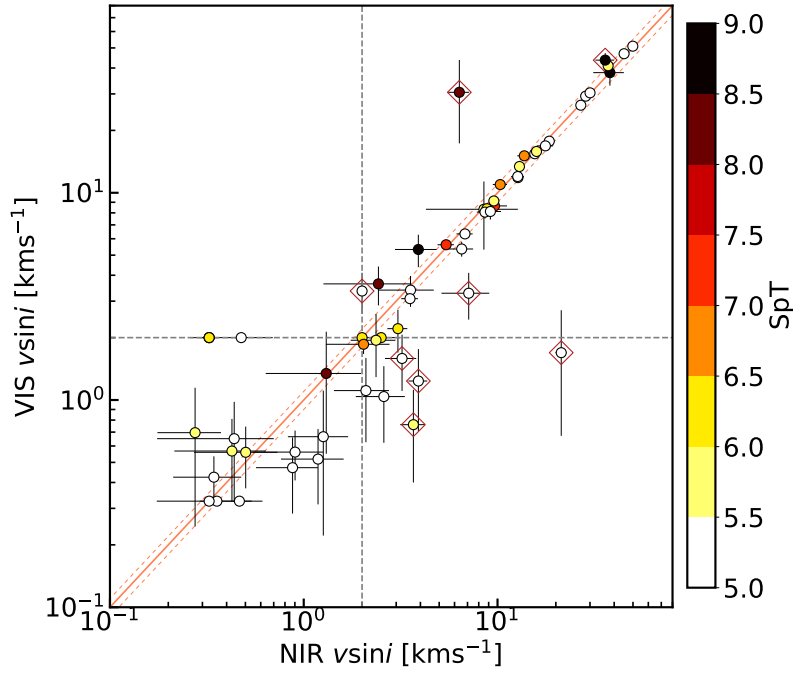


Figure 4.20: Comparison of $v \sin i$ derived from CARMENES VIS and NIR spectra for M dwarfs later than $M_{5.0} V$. Lines indicate the 1:1 relation ($\pm 10\%$) and the 2 km s^{-1} limit.

NIR data than from VIS. Previous estimations from the literature (Reiners et al., 2018) estimated a value of $5.3 \pm 1.5 \text{ km s}^{-1}$, closer to our estimation of $6.35 \pm 0.78 \text{ km s}^{-1}$, and compatible within the errors. Thus, we propose this value for the target.

J11474+667 has a value over the limit in both datasets, although it is not compatible. Computing the v_{eq} from the available estimations of the rotational period and radius, we derive a value of $1.13 \pm 0.01 \text{ km s}^{-1}$. The best estimation for this target is an upper limit of 2 km s^{-1} . J18356+329 is an active and faint M8.5 V star, which drastically reduces the S/N. The $v \sin i$ from both spectra datasets is very close to being in agreement, and is clearly a fast rotator. Because it is a late M dwarf, we trust the NIR estimation over the VIS one. The remaining target is J19573-125, with an estimation of $3.36 \pm 0.75 \text{ km s}^{-1}$ with VIS data, whereas the NIR suggests an upper limit of 2 km s^{-1} . The latter seems the most realistic scenario, as the spectrum better matches the smaller broadening.

The NIR uncertainties tend to be $\sim 20\%$ larger than the VIS ones. Nevertheless, there is still room for improvement, especially for the NIR. For example, we want to explore the reliability of each spectral order in the $v \sin i$ estimation to optimize the derived value and its associated uncertainty. It is particularly important due to the telluric contamination, which may affect more some specific orders. The potential combination of the two datasets can also improve the estimated values. Furthermore, the NIR is less sensitive to the limb-darkening coefficients and models than the VIS, which is an additional advantage. The CARMENES NIR spectra have proven to provide reliable $v \sin i$ determinations, performing as well as the VIS estimates.

Table 4.6: Derived $v \sin i$ values for CARMENES stars later than M5.0 with VIS and NIR data. Colors denote discrepancies between the datasets estimations.

Karmn	NIR $v \sin i$ [km s ⁻¹]	VIS $v \sin i$ [km s ⁻¹]	Karmn	NIR $v \sin i$ [km s ⁻¹]	VIS $v \sin i$ [km s ⁻¹]
J00067-075	0.32 ± 0.02	2.0 ± 0.1	J10584-107	3.56 ± 1.13	3.39 ± 0.58
J01019+541	28.5 ± 1.79	29.25 ± 0.91	J11055+435	8.51 ± 4.23	8.33 ± 3.01
J01033+623	12.75 ± 0.82	11.83 ± 0.51	J11474+667	7.1 ± 1.96	3.28 ± 0.83
J01048-181	0.36 ± 0.18	0.32 ± 0.03	J12189+111	15.56 ± 0.64	15.43 ± 0.41
J01056+284	3.91 ± 0.44	1.23 ± 0.53	J13102+477	3.22 ± 0.59	1.59 ± 0.48
J01550+379	1.19 ± 0.42	0.52 ± 0.21	J14155+046	21.32 ± 1.41	1.69 ± 1.02
J02022+103	0.27 ± 0.1	0.7 ± 0.45	J14173+454	17.66 ± 1.72	16.84 ± 0.92
J02164+135	12.98 ± 0.71	13.39 ± 0.71	J14321+081	8.82 ± 0.55	8.38 ± 0.54
J02465+164	2.51 ± 0.64	2.0 ± 0.1	J14578+566	9.57 ± 0.52	9.13 ± 0.28
J02530+168	0.32 ± 0.02	2.0 ± 0.1	J15305+094	15.89 ± 0.7	15.82 ± 0.65
J02560-006	6.79 ± 0.65	6.33 ± 0.31	J15499+796	26.9 ± 1.32	26.46 ± 0.77
J03090+100	1.26 ± 0.43	0.67 ± 0.44	J16313+408	8.61 ± 0.79	8.07 ± 0.56
J03133+047	0.32 ± 0.03	0.32 ± 0.03	J16555-083	5.43 ± 0.53	5.61 ± 0.19
J03142+286	2.0 ± 0.1	2.0 ± 0.1	J17338+169	37.22 ± 1.29	41.03 ± 2.74
J03230+420	2.09 ± 0.66	1.11 ± 0.48	J18022+642	12.71 ± 0.96	11.98 ± 0.57
J04198+425	3.9 ± 0.95	5.33 ± 0.95	J18027+375	0.48 ± 0.22	2.0 ± 0.1
J04472+206	44.99 ± 1.81	46.89 ± 1.25	J18165+048	0.9 ± 0.36	0.56 ± 0.15
J05394+406	6.35 ± 0.78	30.54 ± 13.22	J18356+329	35.96 ± 3.98	43.66 ± 3.55
J06024+498	0.88 ± 0.31	0.47 ± 0.19	J18482+076	3.53 ± 0.35	3.08 ± 0.14
J06318+414	49.9 ± 1.98	50.98 ± 1.51	J19169+051S	2.43 ± 1.17	3.63 ± 0.77
J06594+193	0.44 ± 0.26	0.65 ± 0.33	J19242+755	0.5 ± 0.23	0.56 ± 0.18
J07051-101	18.5 ± 1.21	17.75 ± 0.52	J19422-207	9.19 ± 1.23	8.12 ± 0.7
J07403-174	0.32 ± 0.04	2.0 ± 0.1	J19573-125	2.0 ± 0.1	3.36 ± 0.75
J08298+267	10.33 ± 0.87	10.96 ± 0.26	J20093-012	6.53 ± 0.95	5.36 ± 0.44
J08413+594	3.68 ± 0.54	0.76 ± 0.36	J20260+585	0.47 ± 0.15	0.32 ± 0.0
J08536-034	38.02 ± 6.84	37.99 ± 5.1	J20556-140S	2.59 ± 0.74	1.04 ± 0.42
J09003+218	13.75 ± 1.1	15.08 ± 0.42	J22114+409	2.36 ± 0.61	1.94 ± 0.65
J09033+056	9.65 ± 1.54	8.64 ± 0.37	J23064-050	1.31 ± 0.67	1.34 ± 0.79
J09449-123	30.02 ± 1.33	30.36 ± 1.12	J23351-023	0.43 ± 0.21	0.57 ± 0.24
J10482-113	2.04 ± 0.74	1.86 ± 0.19	J23419+441	0.34 ± 0.13	0.42 ± 0.11
J10564+070	3.06 ± 0.36	2.21 ± 0.52			

The potential advantages that motivate the use of the NIR over the VIS are not always significant in CARMENES spectra. In particular, the effects of line blending or splitting do not appear to have a measurable impact on the results. The influence of the S/N in the VIS and NIR is also not straightforward to assess through a purely statistical approach, and is better evaluated on a star-by-star basis. Depending on the S/N achieved in each wavelength range, either the VIS or the NIR can provide more precise measurements.

A similar situation arises for the treatment of limb darkening. Individual targets may benefit from the use of NIR data if the adopted limb-darkening approximation is less accurate in the VIS, as its impact is typically reduced at longer wavelengths. Overall, we find that deriving $v \sin i$ from NIR spectra, in addition to the VIS-based catalog, provides a valuable consistency check and increases confidence in the resulting measurements.

4.12 DATA AVAILABILITY

Our pipeline, data, and results are available in a GitHub repository at <https://github.com/rvarasg/vsini-limb-darkening>. Table 4.3 is available in electronic form at the CDS via anonymous ftp to [cdsarc.u-strasbg.fr](ftp://cdsarc.u-strasbg.fr) (130.79.128.5) or via <http://cdsweb.u-strasbg.fr/cgi-bin/qcat?J/A+A/>. The CARMENES DR1 dataset, which includes most of the spectra used in this work, is publicly available at <https://carmenes.cab.inta-csic.es>.

4.13 SUMMARY

We have presented a novel method to determine the projected rotational velocity ($v \sin i$) of stars from CARMENES VIS spectra. This approach upgrades the `serval` pipeline by (i) adopting an order-dependent rotational broadening kernel that accounts for wavelength- and temperature-dependent stellar limb darkening, and (ii) performing spectral oversampling prior to convolution with the template spectrum. The effectiveness of these improvements has been tested using both synthetic and real datasets.

The validation used a set of synthetic spectra with $T_{\text{eff}} = 2500\text{--}4000\text{ K}$ and $v \sin i = 4\text{--}50\text{ km s}^{-1}$, both in the visible and near-infrared range (corresponding to CARMENES VIS and NIR). The oversampling convolution with linear limb darkening proves to be the best approach, over no limb darkening, more sophisticated limb-darkening laws (e.g., power-2 and quadratic), and numerical integration. Moreover, both wavelength ranges yield consistent results, and we further explore the potential advantages of combining them.

Applying this method, we derived a homogeneous catalog of $v \sin i$ measurements for 392 M dwarfs observed with CARMENES VIS. Our results show good overall agreement with previously published values while achieving substantially higher precision. The median relative uncertainty of our measurements is 6.8%, compared to 15.4% for literature values. Additionally, we report 36 new $v \sin i$ measurements that were not previously available.

We expanded this catalog using CARMENES NIR spectra, deriving the $v \sin i$ for 61 stars later than M5.0 V. The results show broad consistency with the VIS estimations, except for a few cases. Three of them match the NIR estimates better, whereas the other four have more reliable estimates based on VIS data. This proves the NIR as a reliable source for projected rotational velocity derivation. We have conducted one of the few studies dedicated to deriving $v \sin i$ for M dwarfs at near-infrared wavelengths, and to date the most detailed one. This includes validation of the method using synthetic spectra and the construction of a homogeneous catalog for CARMENES late M dwarfs.

The near-infrared provides an excellent opportunity for deriving $v \sin i$ measurements, as the limb-darkening effect is significantly smaller than at visible wavelengths. Thus, the possible additional uncertainties coming from the theoretical estimation of the limb-darkening coefficients would be considerably smaller for the NIR than for the VIS. Furthermore, the limb-darkening approximation can be greatly wrong for some specific targets, especially for late M dwarfs, that can be minimized by using NIR spectra. Additionally, for particular targets, the S/N might be higher at near-infrared wavelengths than at the visible, as it is for UCDs. Hence, the NIR will provide a more reliable measurement than the VIS. Anyhow, having estimations from both VIS and NIR is the most reliable approach.

This catalog provides a robust and homogeneous reference for studies of stellar rotation in low-mass stars and will be particularly valuable for characterizing M-dwarf planetary systems, including applications to age estimates, radial-velocity surveys, and spin-orbit investigations.

5.1 SCIENTIFIC CONTEXT

M-dwarf stars are the smallest, coolest, and most abundant stars in our Galaxy. Their masses range from almost half of the Sun to just $0.075M_{\odot}$, and their properties vary significantly among subspectral types, unlike any other star group. M dwarfs are explained in detail in Sect. 1.1 (Chapter 1). UCDs represent the extreme end of the low-mass stars and beyond, including brown dwarfs (BDs; substellar objects). This comprises spectral types later than M6–M7, with masses ~ 0.1 – $0.075 M_{\odot}$ for stars, and down to $13 M_{\text{Jupiter}}$ for BDs, with L, T, and Y spectral types. Their radii are comparable to that of Jupiter, and have effective temperatures (T_{eff}) below 3000K, even a few hundred Kelvin for the coolest BDs. These objects are intrinsically faint, emit most of their radiation in the near-infrared, and are often rapid rotators with strong magnetic activity. At these low T_{eff} , new physical processes become important, such as the formation of condensate clouds in their atmospheres, which strongly affect their spectra and evolution.

Since its launch in December 2013, the European Space Agency astrometric mission *Gaia* (Gaia Collaboration et al., 2016b) has revolutionized our understanding of the Milky Way. Through its successive data releases (Gaia Collaboration et al., 2016a; Gaia Collaboration et al., 2018; Gaia Collaboration et al., 2021), it has provided an unprecedented census of stellar and substellar populations, significantly improving the characterization of low-mass objects in the solar neighborhood. These and new Gaia data releases permit the characterization of the global properties of hundreds of UCDs, including distances, position in the color-absolute magnitude diagram, and the luminosity function, especially at the end of the main sequence (Sarro et al., 2023). Population studies, as well as the detection and characterization of binaries through kinematics, have reached unprecedented precision and statistical significance with Gaia. Additionally, by exploiting the Gaia catalog and the known parameters of UCDs, numerous spectroscopic campaigns aim to achieve a comprehensive characterization of these targets (Ravinet et al., 2024).

The JWST, one of the most important facilities in modern astronomy, has already dedicated, and will continue to dedicate, significant observing time to UCDs. For example, Sanghi et al. (2023) performed multi-filter photometry for several hundred UCDs, deriving absolute magnitude–spectral type relations that enable the estimation of photometric distances in the absence of parallax measurements for JWST UCD targets. Their work is also crucial for distinguishing between high-redshift galaxies and brown dwarfs.

Despite the abundance of UCDs in the solar neighborhood, their planetary populations remain largely unexplored, mainly because of the intrinsic faintness

of these objects. At the same time, UCDs offer particularly favorable conditions for the detection and characterization of small planets. For terrestrial-size planets orbiting in or near the temperate regions of these systems, the very small stellar radii translate into comparatively deep transits, typically of the order of $\sim 1\%$ for Earth-sized planets. Moreover, because the habitable zones of UCDs are located at very short orbital separations, such planets have short orbital periods, enhanced transit probabilities, and frequent transit events. These properties make UCDs especially valuable targets for the study of rocky planets and, in the most favorable cases, for atmospheric characterization, as discussed in Sect. 1.2.7.

The discovery of the TRAPPIST-1 system (Gillon et al., 2017b) marked a major breakthrough in this field. This M8V dwarf hosts seven transiting Earth-sized planets in a compact configuration forming a resonant chain (Luger et al., 2017; Grimm et al., 2018; Agol et al., 2021). The small radius and low mass of the host star enhance the observability of its terrestrial planets, while its low luminosity and effective temperature place the habitable zone at short orbital periods, enabling frequent transits of temperate planets. Together, these properties make the TRAPPIST-1 system a benchmark system for the atmospheric characterization of temperate terrestrial exoplanets with facilities such as JWST (Nutzman and Charbonneau, 2008; Seager, 2013; Morley et al., 2017; Lustig-Yaeger, Meadows, and Lincowski, 2019; Turbet et al., 2022).

The JWST has devoted hundreds of hours to characterizing the atmosphere of UCD-hosted Earth-like exoplanets. In particular, TRAPPIST-1 system has already more than 400 h of observations for the seven planets (Espinoza and Perrin, 2025), making it the system with the largest allocation of observing time on the JWST. However, the JWST observations show significant contamination from stellar surface features that could not be modeled with confidence. Further efforts are being taken, as Allen et al. (2026) have a program for TRAPPIST-1 e that aims to account for stellar contamination using empirical data, using close transits of the airless TRAPPIST-1 b.

Motivated by this discovery, dedicated surveys have been developed to search for planets around ultracool dwarfs. The SPECULOOS (Search for Planets Eclipsing Ultra-cool Stars) project aims to conduct a volume-limited transit survey of nearby very-low-mass stars and brown dwarfs within 40 pc. Using a network of robotic telescopes distributed across both hemispheres, SPECULOOS has already achieved significant results, including the detection of a temperate super-Earth orbiting LP 890-9 (SPECULOOS-2) and an Earth-like planet around SPECULOOS-3, the second-smallest main-sequence star found to host a transiting planet.

To date, only a handful of planetary systems have been confirmed around ultracool dwarfs, including TRAPPIST-1 (Gillon et al., 2017b), SPECULOOS-2 (Delrez et al., 2022), SPECULOOS-3 (Gillon et al., 2024), and Teegarden's star (Zechmeister et al., 2019; Dreizler et al., 2024). While most of these systems have been detected via the transit method, some planets, such as Teegarden b, c, and d, have been identified through radial velocity measurements. Constraining the occurrence rate and properties of planets around ultracool dwarfs remains

challenging, primarily due to observational biases and the intrinsic faintness of their hosts.

RV studies, together with transit observations, are essential for the comprehensive characterization of planetary systems, including the determination of planetary masses, radii, and densities. However, the nature of UCDs poses a significant observational challenge for several reasons, particularly for RV campaigns. Cool stars, in general, are very faint, especially compared with hotter objects at similar distances, leading to low S/N and higher RV uncertainties. Additionally, the RV amplitudes induced by orbiting rocky planets are in general small, in the order of a few m s^{-1} , depending on the orbital period. However, what mostly challenges the observations is the activity of the host stars, which is present in most of UCDs, and easily induces an additional scatter of some m s^{-1} in the RV time series. Consequently, achieving the necessary RV precision, on the order of a few m s^{-1} , or even down to cm s^{-1} level, and obtaining the hundreds of spectra required for a robust detection of a Keplerian signal is extremely demanding.

In this context, ultracool dwarfs provide a crucial laboratory for studying both the low-mass end of star formation and the diversity of planetary systems. Understanding their fundamental properties and planetary companions is essential for placing the Solar System in a broader Galactic context and for assessing the potential habitability of planets around the most common stars.

5.2 ULTRACOOOL DWARFS SURVEYS

5.2.1 *Transit photometry*

The most successful exoplanet detection technique has been transit photometry. This is not different for UCD surveys, as three out of the four known exoplanetary systems hosted by these stars have been discovered via transit. This method, limited by the geometry of the planetary system, benefits from the star-to-planet radius ratio and the close orbits typical of UCD-hosted exoplanetary systems.

The Search for habitable Planets EClipping ULtra-cOOl Stars or just SPECULOOS, is a project devoted to detecting Earth-like exoplanets hosted by ultracool dwarfs¹. SPECULOOS precursor was TRAnsiting Planets and Planetesimals Small Telescopes, or TRAPPIST, with two telescopes, located at ESO's La Silla Observatory (Chile) and Oukaimden Observatory (Morocco). Moreover, these were the telescopes used to discover TRAPPIST-1.

The SPECULOOS Southern Observatory (SSO) facilities are located at ESO's Paranal Observatory in Chile's Atacama desert, whereas the Northern Observatory (SNO) has two facilities, one sited at Teide Observatory in the island of Tenerife (Canarias), and a second one at the National Astronomical Observatory of Mexico, in San Pedro Mártir (i.e., the SAINT-EX Observatory). The SSO has four Ritchey-Chrétien robotic telescopes with a primary mirror of

¹ As mentioned earlier, the hottest UCD is not a clear boundary, and depends on the project. In SPECULOOS, UCD is considered beyond M7.

1 m diameter. The SNO in Tenerife and SAINT-EX have each one of these 1-m robotic telescopes. One of the main goals of SPECULOOS is to find the best rocky-planet candidates for atmospheric characterization with the JWST and the future 39-meter Extremely Large Telescope of ESO.

5.2.2 *Visible and near-infrared radial velocity facilities*

The character of a planet can not be fully understood only using transit observations, as we can only derive some of its properties. The multi-technique approach is crucial because combining RV and transit data allows us to constrain both the planet's mass and radius. Additionally, the transit method can only access systems with very specific geometry, whereas the RV method is more versatile.

Using near-infrared and visible facilities for planetary RV studies allows us to increase the significance of detections and differentiate Keplerian from activity RV signals. This is especially interesting for UCDs, because the RV precision expected from both channels is very similar (Reiners et al., 2018). Chromatic analysis hugely benefits from a big wavelength range. Given the large number of RV measurements required for a robust detection, combining NIR and VIS observations can be highly advantageous.

The first facility to simultaneously operate with VIS and NIR high-resolution spectrographs was CARMENES in 2016 (see Sect. 1.4.1). Although this was a breakthrough in the field, for RV studies the VIS has been used mainly (and solely) (Ribas et al., 2018; Trifonov et al., 2021; Suárez Mascareño et al., 2021; Luque et al., 2023), whereas the NIR has been exploited for atmospheric studies (Nortmann et al., 2018; Allart et al., 2018). Few studies combined data from VIS and NIR, predominantly for atmosphere and stellar characterization (Oshagh et al., 2020; Kossakowski et al., 2022), and some RV studies (Morales et al., 2019). This was a consequence of the poor thermal stability of CARMENES NIR, which led to low-precision or even unreliable RV measurements. Nonetheless, the CARMENES-PLUS project significantly improved the RV precision of the NIR channel, motivating the combination of VIS and NIR observations, particularly for UCD studies, not only for atmospheric science but also for RV detection and characterization. However, the improvement of the joint VIS and NIR RV analysis has yet to be proven.

The first light of NIRPS in 2024 marked the second pair of VIS–NIR high-resolution spectrographs, which can operate simultaneously with HARPS; furthermore, it is the current default operating strategy (Bouchy et al., 2025). Similarly to CARMENES, the front end enables joint operation of both instruments, as there is no significant benefit to observing a target with only one of them. There are only two scenarios where this is not true, the polarimetric mode (HARPS-pol), and observations with the highest signal-to-noise needed between 435 and 455 nm.

The main difference from CARMENES is that NIRPS and HARPS are two separate instruments, not one with two channels. In general, the two instruments integration time should be (roughly) the same in order to minimize

overheads. CARMENES VIS and NIR both have the same integration time, optimized for the target signal-to-noise ratio in the VIS. The work by Suárez Mascareño et al. (2025) is a clear example of NIRPS performance, as well as of the joint operation of NIRPS and HARPS and their performance.

5.3 OPTIMIZING THE RADIAL VELOCITIES OF CARMENES NIR

The RV precision as a function of wavelength is spectral-type-dependent. For early M dwarfs, the highest RV precision is obtained in the blue orders of the visible, but as the T_{eff} decreases, the better precision is obtained in redder orders. For the latest M dwarfs, the NIR provides the best performance. This is a result of RV precision being determined by two main factors: the signal-to-noise ratio and the RV content. Although the RV content is typically higher in the VIS, because there are more spectroscopic features at shorter wavelengths, the signal-to-noise ratio increases, because the spectral energy distribution peaks in the red and infrared wavelengths at lower T_{eff} (Reiners et al., 2018). Thus, using VIS and NIR high-resolution spectrographs becomes crucial for UCD studies. Nowadays, the best performing NIR and VIS spectrograph pairs are CARMENES and HARPS+NIRPS.

Bauer et al. (2020) performed an extensive spectral analysis with CARMENES data, both in the VIS and NIR. Following an iterative approach, they compute the root-mean-square (rms) scatter for individual spectral orders across the entire CARMENES sample, rank them by their median scatter, and progressively remove the orders that contributed least to RV precision. For the VIS channel, nearly all orders (35 out of 41) contributed to optimal RV precision, while the remaining orders had a minimal impact and were kept for final RV computation.

The CARMENES NIR wavelength range covers the Y, J, and H bands, as shown in Fig. 5.1. In total, CARMENES NIR has 28 full orders, split into two half-orders, for a total of 56. 14 of these half-orders are not usable due to telluric contamination. In Bauer et al. (2020) work, only 20 out of the available 42 half-orders were selected for best precision, because the rest increased the scatter significantly.

The conclusions of Bauer et al. (2020) were included in the serval pipeline, which, by default, considers their selected combination of orders. Thus, not all orders are available or used in the NIR RV analysis. Additionally, their work was released in 2020, while the CARMENES NIR thermal stability was greatly improved (Varas et al., 2025) and the correction of telluric absorption in the spectra was implemented afterward (Nagel et al., 2023).

Although the approach used by Bauer et al. (2020) is effective for identifying spectral orders that optimize RV precision across a broad sample of stars, it is not well-suited to our study, which focuses specifically on the coolest stars. Rather than relying on broad statistics derived from all CARMENES targets, we focus exclusively on a smaller subset (see Table 5.1) of stars that belong to the M6–M9² spectral type range, being able to perform a more detailed,

² In this Chapter, we consider as UCDs objects beyond M6.0, in order to work with a broader sample.

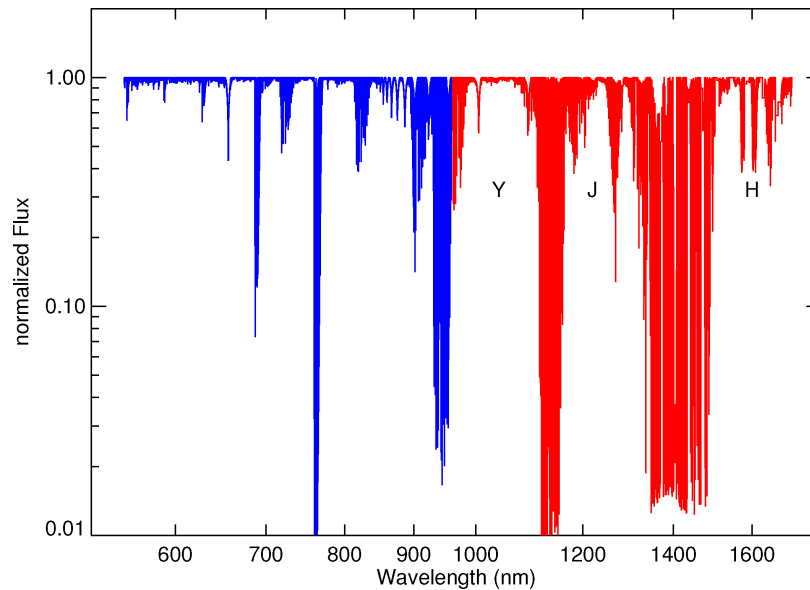


Figure 5.1: Overview of the CARMENES spectral range. The spectrum covered by the VIS channel is shown in blue, and the NIR channel in red. The target shown is the A2V star 50 Cas. The stellar spectrum only exhibits a few hydrogen lines; all strong features are from Earth's atmosphere (Reiners et al., 2018).

star-by-star analysis. Instead of applying a global statistical method, we inspect individual spectral orders for each star to find the best combination of orders that maximizes RV precision. This tailored approach allows us to account for the unique characteristics of these cooler stars, ensuring that the systematics affecting them are identified and handled with greater specificity than a broad-sample analysis would allow.

Table 5.2 shows the correspondence between the CARMENES NIR spectral orders and the échelle ones, with the wavelength range, and the telluric strength in each order. The 14 half-orders not recovered due to the high atmospheric contamination that separates the YJH bands are red-colored.

The radial velocity obtained for a specific target and night is derived from the estimation of the analyzed spectral orders. Using `serval`, the default spectral orders used with NIR data were selected by Bauer et al. (2020). From the 42 half-orders, only 20 were kept for the RV extraction (green in Table 5.2). Their approach was to minimize the observed RV scatter across the CARMENES sample, thus not distinguishing by T_{eff} or any other stellar parameter.

As we are interested in the NIR RV of specific (cool) targets, we followed a different approach. We recovered all NIR half-orders (hereafter, orders) and computed the average RV precision obtained for each and for individual stars. From the CARMENES UCD list, we use J02530+168 (Teegarden's star), J10482-113, and J10564+070 for the following analysis. The RV precision per spectral order of CARMENES NIR for these targets is shown in Fig. 5.2. This value is computed as the trimmed mean of all available observations, excluding a 3% on both ends. At first glance, some specific orders consistently have higher

Table 5.1: List of UCDSs in CARMENES sample.

Star's name	karmin	Spectral type	J (mag)	$v \sin i_*$ (km/s)	Observations (VIS/NIR)	S/N (VIS/NIR)	H_α
LP 411-006	J02465+164	M6.0 V	10.971	2.11	18/18	22.0/35.6	1.0
LP 299-036	J03142+286	M6.0 V	10.993	2.34	13/10	16.2/25.9	1.4
LP 560-035	J14321+081	M6.0 V	10.108	8.09	58/58	32.5/55.4	4.2
Wolf 359	J10564+070	M6.0 V	7.085	3.41	78/63	73.8/187.1	6.4
LP 783-002	J07403-174	M6.0 V	10.155	1.03	53/54	26.9/50.8	1.0
GJ 1111	J08298+267	M6.5 V	8.235	10.67	35/29	76.1/177.8	4.0
LP 731-058	J10482-113	M6.5 V	8.857	2.36	79/72	51.1/122.7	2.8
LP 368-128	J09003+218	M6.5 V	9.436	14.65	25/20	41.1/96.6	5.2
vB 8	J16555-083	M7.0 V	9.776	6.17	128/110	25.3/61.2	4.2
NLTT 20861	J09033+056	M7.0 V	10.766	7.71	31/27	22.5/40.0	3.3
Teegarden's star	J02530+168	M7.0 V	8.394	1.23	298/274	69.6/149.0	1.3
LP 044-162	J17572+707	M7.5 V	11.452	36.83	2/2	15.6/30.2	2.2
LSR J0539+4038	J05394+406	M8.0 V	11.109	5.69	21/29	15.5/41.5	4.3
V1298 Aql	J19169+051S	M8.0 V	9.908	5.48	51/44	22.4/70.0	4.2
LSPM J1925+0938	J19255+096	M8.0 V	11.214	62.84	100/97	9.0/32.1	2.2
TRAPPIST-1	J23064-050	M8.0 V	11.354	3.63	163/130	3.9/13.2	1.5
LSR J0419+4233	J04198+425	M8.5 V	11.094	8.36	35/42	10.4/36.2	8.0
LSR J1835+3259	J18356+329	M8.5 V	10.27	55.88	60/65	13.6/48.5	2.1
LP 666-009	J08536-034	M9.0 V	11.212	9.3	45/43	6.2/29.0	6.0
LSPM J2049+3336	SPECULOOS-3 ^(a)	-	-	-	-	-	-

Notes. ^(a) Does not have a karmin ID. SPECULOOS-3 was observed with CARMENES as part of a campaign, totaling 36 observations.

Table 5.2: Correspondence between échelle orders and CARMENES half-orders, with the corresponding wavelength range, and the strength of the tellurics.

Order	CARM order ^(a)	λ_{\min} [Å]	λ_{\max} [Å]	$\Delta\lambda$ [Å]	Tellurics
63	0 and 1	9618.7	9782.1	163.4	Strong
62	2 and 3	9758.4	9939.9	181.5	Mild
61	4 and 5	9918.3	10102.9	184.6	Weak
60	6 and 7	10083.6	10271.2	187.6	Weak
59	8 and 9	10254.5	10445.3	190.8	Weak
58	10 and 11	10431.3	10625.4	194.1	Weak
57	12 and 13	10614.3	10811.8	197.5	Weak
56	14 and 15	10803.9	11004.9	201.0	Weak
55	16 and 17	11000.3	11205.0	204.7	Weak
54	18 and 19	11204.0	11412.5	208.5	Strong
53	20 and 21	11415.4	11627.8	212.4	Strong
52	22 and 23	11634.9	11851.4	216.5	Mild
51	24 and 25	11863.1	12083.7	220.6	Mild
50	26 and 27	12100.4	12325.4	225.0	Weak
49	28 and 29	12347.3	12576.9	229.6	Weak
48	30 and 31	12604.5	12839.0	234.5	Mild/weak
47	32 and 33	12872.7	13112.1	239.4	Weak
46	34 and 35	13152.6	13397.1	244.5	Weak
45	36 and 37	13444.9	13694.8	249.9	Strong
44	38 and 39	13750.5	14006.1	255.6	Strong
43	40 and 41	14070.3	14331.8	261.5	Strong
42	42 and 43	14405.3	14673.0	267.7	Mild
41	44 and 45	14756.6	15030.8	274.2	Mild
40	46 and 47	15125.6	15406.6	281.0	Weak
39	48 and 49	15513.4	15801.6	288.2	Weak
38	50 and 51	15921.7	16217.4	295.7	Weak
37	52 and 53	16352.1	16655.6	303.5	Weak
36	54 and 55	16806.3	17118.2	311.9	Weak

Notes. ^(a)The red CARMENES half-orders (CARM orders) correspond with the excluded wavelengths due to the strong telluric contamination, separating the YJH bands. The green CARM orders are the serval default.

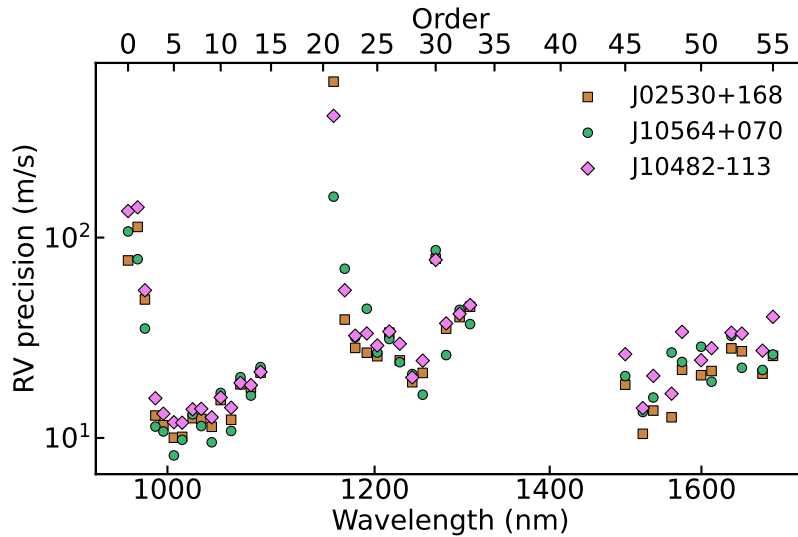


Figure 5.2: Average RV precision per NIR spectral order for three CARMENES UCDs.

average errors across the three targets. For instance, the 0th, 1st, 2nd, 21st, and 30th orders have the highest values.

In order to achieve the most precise RVs, we explore the best combination of orders, with the goal of reducing the average error³ of the resulting time series. Using an iterative approach, we start with the RVs using all orders, compute the average error per order, and for the time series. We then remove the worst-performing order and recompute the RVs. Again, we evaluate the precision of each order and the average error of the time series, and proceed with another iteration, removing the next *worst* order, and this successively. Then, we select the combination of orders with the minimum average error.

This iterative process is illustrated in Fig. 5.3 for the three targets, showing the average RV error of the time series at each iteration. The order excluded in each iteration is plotted inside each marker. Note the minimum error obtained (green) and the `serval`-default average error (yellow). Removing the 21st CARMENES NIR order significantly reduces the derived uncertainties for the three targets, although the most beneficial combination differs. The variation of the mean error has a smaller impact after the first iteration and starts to increase after the minimum. For the three targets there is a clear improvement in the RV error compared with the `serval` default, from 4.31 to 3.81 m s^{-1} for J02530+168, 4.57 to 4.19 m s^{-1} for J10482-113, and 4.49 to 3.84 m s^{-1} for J10564+070; i.e., a 11.6, 8.3 and 14% improvement, respectively.

Correctly selecting the spectral orders used for RV extraction yields better precision. A general analysis, as in Bauer et al. (2020), would not yield the best precision for individual targets, because not all spectral types have the same RV content and precision per order, and not even individual targets do, as already demonstrated. For faint and challenging targets, a dedicated study could be critical for extracting as much information as possible from the available observations.

³ A trimmed average excluding 3% in both ends of the data.

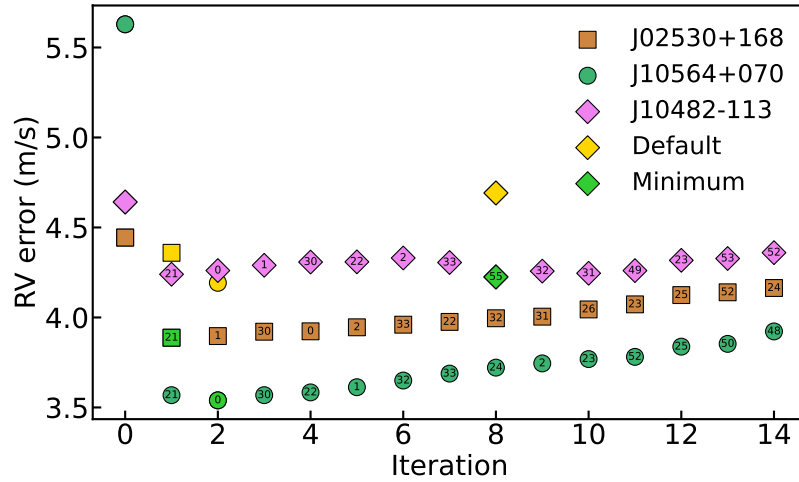


Figure 5.3: Average error obtained for the RV time series for each iteration, for three targets. The number inside each marker corresponds to the order excluded in that iteration. The minimum value is shown in green, and the default serval value in yellow.

5.3.1 Telluric absorption correction

Nagel et al. (2023) developed a template division telluric modeling (TDTM) technique, combining template construction and forward-modeling to correct the CARMENES spectra from telluric absorption lines. First, a telluric mask is applied to the spectra time series, and then a stellar template is built, which is used to remove the stellar contribution from the observations. An atmospheric transmission model from `molecfit`⁴ (Smette et al., 2015) is fitted with the resulting telluric spectrum, free from stellar contribution and built from the observation. The next step is to correct all the CARMENES spectra using the derived telluric model. The method has been proven to work significantly better for a high number of observations and with a good coverage of the barycentric velocity space, which can limit the correction depending on the target's sky position.

The near-infrared wavelengths are more affected by tellurics (see Fig. 5.1), so a proper correction from the atmosphere contribution on the stellar spectra is key for extracting as much RV information as possible. To evaluate the impact of using telluric absorption corrected (tac) instead of the non-corrected spectra (nc), we reanalyzed the RV precision (σ_{rv}) per spectral order, and compare the results in Fig. 5.4. The relative RV precision (i.e., $\sigma_{rv}^{tac} / \sigma_{rv}^{nc}$) improves in almost every order, especially at the edges of the YJH bands. Some orders in the center of the Y band are not improved, or even worsened, in terms of RV precision. Nevertheless, the improvement in JH bands is significant.

If we proceed with the iterative order-wise approach (see Sect. ??), we find a minimum average error of the time series of 3.55 ms^{-1} for J02530+168,

⁴ <https://www.eso.org/sci/software/pipelines/skytools/molecfit>.

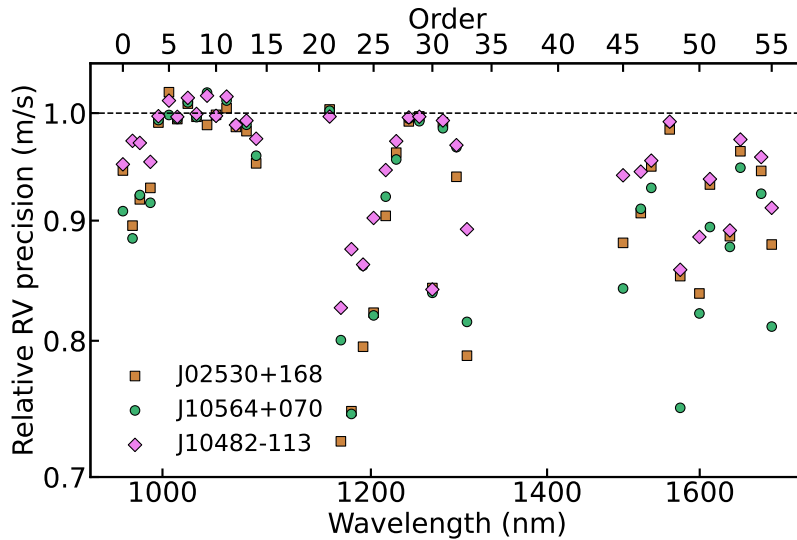


Figure 5.4: Relative RV precision ($\sigma_{rv}^{tac}/\sigma_{rv}^{nc}$) per NIR spectral order for three CARMENES UCDs when including the telluric absorption correction of the spectra.

4.02 m s^{-1} for J10482-113, 3.69 m s^{-1} for J10564+070, a 6.8, 4.1 and 3.9% decrease, respectively, compared with the non-telluric corrected data.

5.4 CARMENES NIR: PROBING TEEGARDEN'S SYSTEM

5.4.1 What we know of Teegarden's star

Among the UCDs, Teegarden's star (discovered by Teegarden et al., 2003) is a benchmark case for several reasons. It is an M7.0 V star (Alonso-Floriano et al., 2015), and the 25th closest (known) star to the Sun, at just 3.831 pc, and with an 8.4 J magnitude. It has a long rotation period of 96.2 days (Lafarga et al., 2021), which translates into a very low $v \sin i$, and is a low magnetic activity star. Consequently, Teegarden's star is an ideal case for RV studies of Earth-like planets around UCD stars.

It has been widely observed, leading to the discovery of Teegarden b and c by Zechmeister et al. (2019), with orbital periods of 4.9 and 11.4 days, respectively. This is the first and (yet) only exoplanetary system detected by an RV campaign hosted by a UCD star. CARMENES VIS was the main instrument used for the discovery, and has not stopped being observed by CARMENES since the beginning of 2016. A total of 409 observations in the VIS and 355 in the NIR⁵ have been collected as of April 2026.

Dreizler et al. (2024) revisited the system (see Table 5.3). They updated the stellar parameters of Teegarden, and made a reanalysis using 346 nightly binned RV data collected from CARMENES⁶, ESPRESSO, MAROON-X, and HPF. They reported a third planet, Teegarden's star d, with an orbital period of

⁵ Excluding observations from January to November 2026.

⁶ In this work, they use CARMENES VIS telluric corrected spectra, and no CARMENES NIR data.

Table 5.3: Stellar and planetary (b, c, and d) parameters of Teegarden's star system.

Stellar parameter	Value	Reference ^(a)
T_{eff} [K]	3034 ± 45	Marf21
$\log g$ [cm s^{-1}]	5.19 ± 0.2	Marf21
[Fe/H]	-0.11 ± 0.28	Marf21
M [M_{\odot}]	0.097 ± 0.010	Dre24
R [R_{\odot}]	0.120 ± 0.012	Dre24
L [$10^{-5} L_{\odot}$]	72.2 ± 0.6	Dre24
P_{rot} [days]	96.2	Laf21
Planet parameter		
P_{b} [days]	4.90634 ± 0.00041	Dre24
K_{b} [m s^{-1}]	2.09 ± 0.15	Dre24
$m_{\text{b}} \sin i$ [M_{\oplus}]	1.16 ± 0.12	Dre24
P_{c} [days]	11.416 ± 0.003	Dre24
K_{c} [m s^{-1}]	1.43 ± 0.16	Dre24
$m_{\text{c}} \sin i$ [M_{\oplus}]	1.05 ± 0.14	Dre24
P_{d} [days]	26.13 ± 0.04	Dre24
K_{d} [m s^{-1}]	0.86 ± 0.17	Dre24
$m_{\text{d}} \sin i$ [M_{\oplus}]	0.82 ± 0.17	Dre24

Notes. ^(a)References are Dre24: Dreizler et al. (2024), Laf21: Lafarga et al. (2021), and Marf21: Marfil et al. (2021).

26.13 ± 0.04 days, and a RV amplitude of $0.86 \pm 0.17 \text{ m s}^{-1}$, which corresponds to a mass minimum of $0.82M_{\oplus}$. Nevertheless, this planet lies outside the host star's habitable zone due to the low T_{eff} . They also discuss other RV signals and their possible nature. Most of these signals require further analysis and measurements to determine whether they are activity- or Keplerian-originated.

Because we are interested in detecting exoplanetary RV signals in UCDs, the Teegarden's star system represents a natural benchmark. It is a relatively bright target for a late M dwarf, hosts multiple confirmed companions, is a slow rotator, and exhibits low levels of magnetic activity. In addition, a large number of spectra are available from both CARMENES VIS and NIR, including more than one hundred observations obtained after the implementation of the C-PLUS upgrades.

However, it is not an ideal target to highlight the advantages of NIR RV measurements over the VIS channel. The primary motivation for using the NIR in UCD studies is that the S/N in the VIS decreases rapidly toward later spectral types, while the NIR S/N becomes dominant (Reiners et al., 2018). In the case of Teegarden's star, its relatively high brightness allows the VIS channel to achieve strong S/N values. Moreover, the intrinsic RV scatter in the NIR remains higher than in the VIS due to photon noise limitations. This effect is particularly pronounced for bright, slowly rotating, and weakly active M dwarfs. Therefore, while Teegarden's star serves as an excellent benchmark within the UCD regime, it is not the optimal target to demonstrate the full potential of the NIR channel.

5.4.2 RV extraction

For the RV extraction, we used the standard CARMENES procedure detailed in Sect. 3.3 and Sect. 4.3. However, we use the tac spectra and the iterative order-wise method to optimize the RV precision obtained, as detailed in Sect. 5.3. For Teegarden's star, the best combination of orders excludes 15 of them (17–21 and 35–44, see Table 5.2), hence, a total of 41 orders are used. The exact command line used for running `serval` to reduce Teegarden's RVs was:

```
serval J02530+168 J02530+168.lis -inst CARM_NIR -safemode 2 -targ Teegardens
-oset 0:56 -o_excl 17,18,19,20,21,35,36,37,38,39,40,41,42,43,44
```

where J02530+168 is Teegarden's karmn name, J02530+168.lis the file with the path of all fits used, `-oset` selects all spectral orders, and `-o_excl` the ones to exclude.

There are several data products after running `serval`, including the RV corrected from drift and secular acceleration, saved in the file with the `.rvc.dat` extension. A final correction is typically applied using the nightly zero points (NZPs; Ribas et al., 2023), as it has been found to significantly improve results. The NZPs imply an RV shift of each point to account for night-to-night variations, and are measured using RV very-stable stars every night (see Sect. 3.3.4 for more details). This process provides a `.avc.dat` file, the fully corrected RVs ready for analysis.

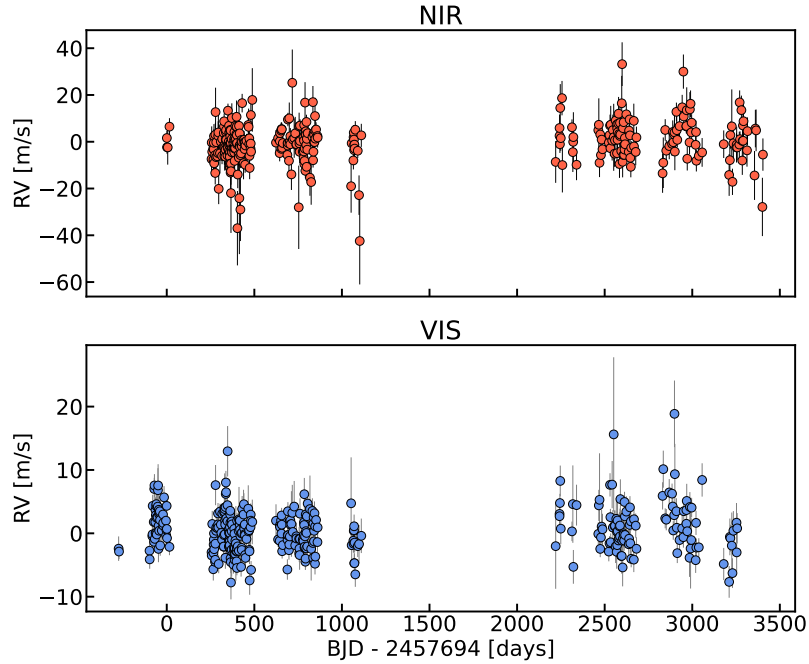


Figure 5.5: RV time series of Teegarden's star for CARMENES NIR (top) and VIS (bottom), fully corrected and optimized to obtain the highest RV precision.

Ideally, the NZP correction should be performed using tac spectra for all stars, particularly for the standard stars employed in the NZP computation. However, the handling and processing of tac spectra are complex and computationally demanding. Consequently, we derived the RVs of Teegarden's using non-tac spectra, and the NZP correction was applied consistently based on the non-tac data.

CARMENES NIR was very unstable from January until November 2016 (see Chapter 3). Thus, we decided to exclude the NIR data before November 2016 to minimize contamination from bad RVs during that period, and computed the time series accordingly. The fully corrected RV time series following all the aforementioned criteria is shown in the top panel of Fig. 5.5. The observed scatter (rms of the RV residuals) of the data is 8.47 m s^{-1} and the average error 5.08 m s^{-1} . For comparison, the VIS time series (see bottom panel of Fig. 5.5) presents a scatter of 3.44 m s^{-1} and an average uncertainty of 1.96 m s^{-1} .

5.4.3 Periodic signals

We computed the generalized Lomb-Scargle periodogram or GLS⁷ (Zechmeister and Kürster, 2009) implemented in *astropy*. The GLS is a statistical tool designed to identify periodic signals in unevenly sampled data. When analyzing a periodogram, it is essential to assess the significance of any detected peak in order to determine whether it reflects a genuine periodic component. This is commonly achieved using the false-alarm probability (FAP), which quantifies

⁷ The GLS is the floating-mean form of the Lomb-Scargle periodogram (Lomb, 1976; Scargle, 1982).

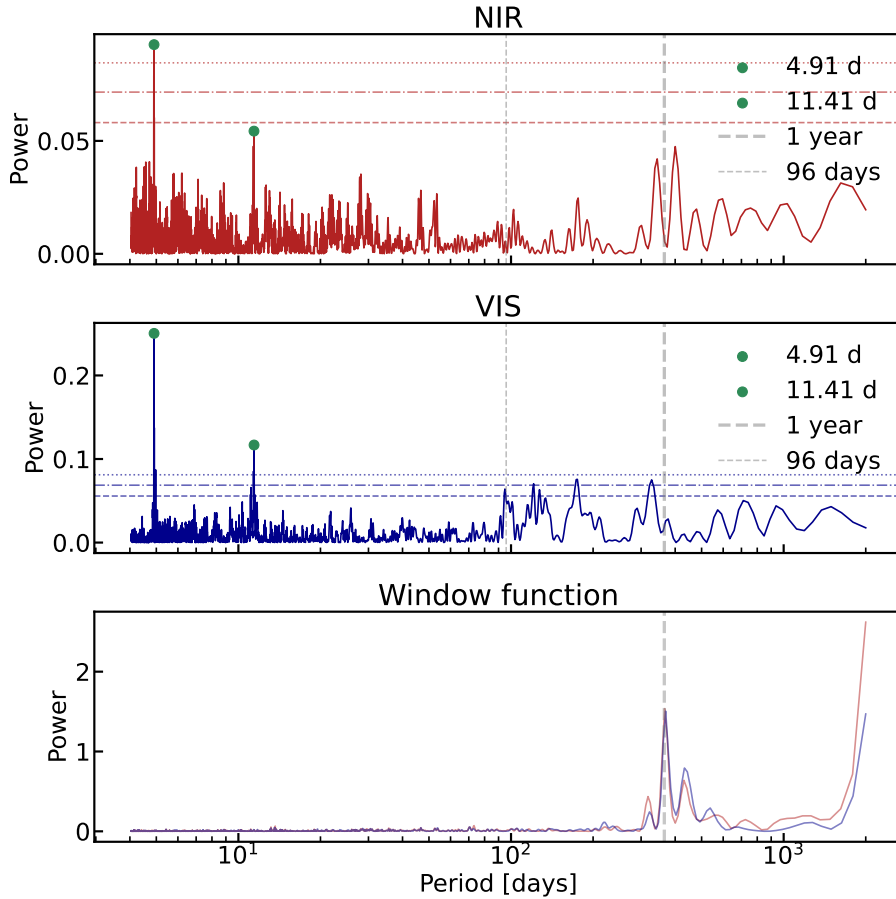


Figure 5.6: Generalized Lomb-Scargle periodogram of Teegarden's star for NIR (top) and VIS (middle) RV time series (see Fig. 5.5). The corresponding window function for both is shown in the bottom panel.

the likelihood of obtaining a peak of a given height under the null hypothesis that the data consist solely of Gaussian noise, with no periodic signal.

Applied to our data, we obtain Fig. 5.6 for the NIR (top panel) and VIS (bottom panel). Given the observational time span of ~ 3400 d, we adopt 2000 d as the longest period that can be reliably probed. We consider three FAP levels of 0.1, 1, and 10% (horizontal lines, from top to bottom).

In the NIR data, the two most prominent peaks occur at 4.905 and 11.406 d, with amplitudes of 1.97 and 1.46 m s^{-1} , corresponding to Teegarden b and c (see Table 5.3). Even without further analysis, these two Keplerian signals can be readily identified in the CARMENES NIR data with high significance; their associated FAPs are 0.003% and $> 15\%$, respectively. Additionally, two significant peaks are found near the one-year alias, while no signal is detected at the stellar rotation period of 96 d.

The VIS periodogram is shown in the middle panel of Fig. 5.6. The two main peaks once again correspond to Teegarden's b and c, with much higher significance than in the NIR. The amplitudes are consistent with the previous results, 2.09 m s^{-1} and 1.31 m s^{-1} , respectively. In the VIS periodogram, a clear

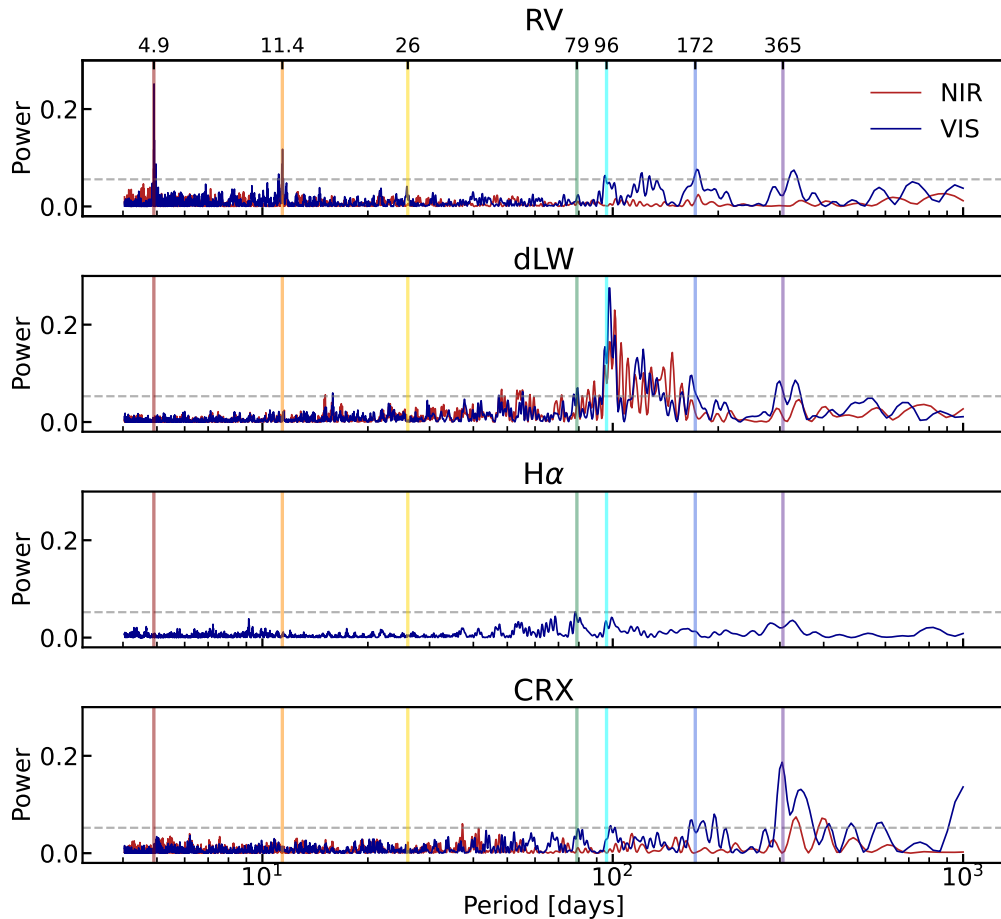


Figure 5.7: GLS periodogram of Teegarden's star of NIR and VIS RV, dLW, H α , and CRX. The vertical lines represent the observed periodic signals, (i) at 4.92, 11.42, and 26.1 days for the Keplerians, (ii) 79 and 96 days for the rotational period, (iii) the 172 days signal, and the 1-year alias.

peak is present at the stellar rotation period of 96 days, whereas in the NIR data no such signal is detected.

The window function, for both VIS and NIR, is shown in the bottom panel of Fig. 5.6. It is built using a constant- or delta-like time series with the same sampling as the RV time series and homogeneous errors. In this case, we replaced all RV and uncertainty values with a 1 m s^{-1} value. There is a significant peak at 1 year, and two aliases around it. These are reflected in both VIS and NIR periodograms. At much lower significance, but still prominent, there are a few peaks; for the VIS at 13.6, 71, and 220 days, and for the NIR at 13.65, 72.5, and a pair at 220 and 244 days. Similar peaks are expected in both time series because the sampling is nearly identical, with a few exceptions (e.g., the data through November 2016 are excluded for the NIR but not for the VIS).

Activity signals

The `serval` pipeline provides spectroscopic indices along the RV measurements (Zechmeister et al., 2018; Schöfer et al., 2019). For this work, we use the differential line width (dLW), the chromatic index (CRX), and the emission strength of the hydrogen α line ($H\alpha$). The dLW is equivalent to the

In Fig. 5.7 we show the GLS periodograms of the activity indices together with the RVs, for both VIS and NIR datasets. The vertical lines correspond to observed periods of (i) the planets at 4.92, 11.42, and 26.1 days; (ii) rotational period of 96 days and its alias at 79 days (Dreizler et al., 2024); (iii) the 172 day signal discussed by Dreizler et al. (2024); and (iv) the 1-year alias.

The Keplerian signals are achromatic, as is the case for the three planets present only in the RV periodogram. The signals at 79 and 96 d, associated with the stellar rotation period, exhibit two clear peaks, particularly the 96 d signal in the dLW. Notably, the highest VIS and NIR peaks in the dLW are at slightly higher periods than the proposed by Dreizler et al. (2024), at 98 and 101 d, respectively. A signal at 172 d is also present in both the VIS RV and dLW. However, the window function had a peak at 244 d, double of this period, and significant peaks are also present in the CRX periodogram. This might suggest that the 172 d signal is not of Keplerian nature, but activity related. Additionally, two peaks appear around the one-year alias, as discussed in the window function (see Fig. 5.6).

5.4.4 GP modeling and planetary signals

The periodogram shows at least two significant peaks, which are potential planetary signals⁸. For a realistic evaluation of these RV signals, we used `kima` (Faria et al., 2018), which allows us to model stellar activity alongside the Keplerian signals. This pipeline uses the diffusive nested sampling algorithm (DNS; Brewer, Pártay, and Csányi, 2011) to sample from the posterior distribution of the model's parameters. This approach allows comparison among models, because it provides an estimate of the marginal likelihood, and the number of planets (N_p) of each model is a free parameter. The goal is to obtain at least 50000 (Figueira et al., 2025) effective samples for the posteriors, which provides high significance for the derived parameters.

The `kima` pipeline models the stellar activity using Gaussian processes (GPs) with a quasi-periodic kernel for the noise. The model is characterized by the hyperparameters η_1 : the amplitude of the GP, η_2 : the evolution timescale, η_3 : the rotational period, and η_4 : the harmonic complexity. They are derived together with the planetary parameters, the star background velocity, and the instrument's noise and offset. This approach comes from photometric activity modeling, with many successful implementations in RV analyses (Haywood et al., 2014; Nicholson and Aigrain, 2022). The priors used for the analysis are summarized in Table 5.4.

⁸ In this particular case, we already know that Teegarden's system has three planetary members, and that the two main peaks of the periodograms correspond to planets b and c.

Table 5.4: Priors in *kima* for the GP models.

Group	Parameter	Prior	units
Planets	K_p	$\mathcal{M}\mathcal{L}\mathcal{U}(0.1, 5)$	m s^{-1}
	P	$\mathcal{L}\mathcal{U}(1, 1000)$	d
	e	$\mathcal{K}(0.867, 3.03)$	–
	ϕ, ω	$\mathcal{U}(0, 2\pi)$	–
Instrument	Jitter	$\mathcal{U}(0.05, 15)$	m s^{-1}
	Offset	$\mathcal{U}(-\Delta RV, \Delta RV)$	m s^{-1}
Stellar GP	η_1	$\mathcal{U}(0.05, 5)$	m s^{-1}
	η_2	$\mathcal{U}(P_{\text{rot}}, 5P_{\text{rot}})$	d
	η_3	$\mathcal{N}(P_{\text{rot}}, \sigma_{P_{\text{rot}}})$	d
	η_4	$\mathcal{U}(0.2, 5)$	–
Star	Linear slope	$\mathcal{N}(0, 10 \frac{\Delta RV}{\Delta t})$	m s^{-1}
	Quadratic slope	$\mathcal{N}(0, 10 \frac{\Delta RV}{\Delta t^2})$	m s^{-1}
	Systematic RV	$\mathcal{U}(RV_{\text{min}}, RV_{\text{max}})$	m s^{-1}

Notes. We used modified log-uniform ($\mathcal{M}\mathcal{L}\mathcal{U}$; Gregory, 2005), log-uniform ($\mathcal{L}\mathcal{U}$), Kumaraswamy (\mathcal{K} ; Kumaraswamy, 1980), uniform (\mathcal{U}), and normal (\mathcal{N}) distributions for the priors.

We use broad, non-informative priors, including only well-defined values, such as the rotational period ($P_{\text{rot}} = 96$ d) for η_2 and η_3 . The former, which represents the evolution or typical life span of spots, is assumed to be larger than the rotational period, and this is implemented in *kima*. This is generally true for Sun-like stars, but not necessarily for slow-rotating M dwarfs. Although there is no clear lifetime for spots in Teegarden, it has been hypothesized to have stable structures over 40 rotations (Dreizler et al., 2024). Thus, we assumed spots to live longer than one rotation period.

We also assume that the RV signals have amplitudes below 5 m s^{-1} , as the time series scatter is smaller, as well as the observed signals in the periodogram. Similarly, periods over 1000 days are not considered, and eccentricity is assumed to be close to zero.

CARMENES VIS

For the CARMENES VIS data, we set the number of planets as a free parameter, ranging from 0 to 4, to capture the three claimed planets and increase it by 1 to account for possible additional signals. The resulting GP posteriors are shown in Table 5.5, and the planetary parameters in Table 5.6. The fitted planets and GP are plotted in Fig. 5.8.

The model with the highest significance includes three planetary signals and consistent orbital parameters for Teegarden's b, c, and d (see Table 5.3). In this case, the full three-planet system is confidently detected only using CARMENES VIS data, with no additional observations from ESPRESSO, MAROON-X, or HPF. The GP posteriors provide robust rotation characterization, with η_3 consistent with the estimated rotational period.

Table 5.5: Posteriors of the GP after running *kima* with the priors in Table 5.4.

Parameter	VIS	NIR	NIR+VIS	Unit
Jitter	$0.6^{+0.2}_{-0.2}$	$2.8^{+0.3}_{-0.3}$	$0.8^{+0.1}_{-0.1}, 2.7^{+0.2}_{-0.2}$	m s^{-1}
η_1	$2.1^{+0.4}_{-0.3}$	$0.9^{+0.7}_{-0.5}$	$2.0^{+0.3}_{-0.3}$	m s^{-1}
η_2	111^{+19}_{-9}	295^{+94}_{-100}	111^{+19}_{-9}	days
η_3	101^{+5}_{-4}	96^{+9}_{-9}	105^{+7}_{-6}	days
η_4	$2.2^{+0.7}_{-0.5}$	$2.2^{+1.1}_{-1.3}$	$2.1^{+0.6}_{-0.5}$	–
RV slope	$0.0002^{+0.0003}_{-0.0003}$	$0.0010^{+0.0003}_{-0.0004}$	$0.0003^{+0.0004}_{-0.0003}$	$\text{m s}^{-1} \text{ yr}^{-1}$
RV quadr	$-3.7^{+5.2}_{-4.5} \cdot 10^{-7}$	$-4.9^{+5.3}_{-5.5} \cdot 10^{-7}$	$-2.4^{+4.1}_{-6.4} \cdot 10^{-7}$	$\text{m s}^{-1} \text{ yr}^{-2}$

Table 5.6: Planetary parameters derived by *kima* for Teegarden's system, for the three CARMENES datasets.

Dataset	Planet	P [days]	K [m/s]	e
VIS	b	$4.9067^{+0.0002}_{-0.0002}$	$2.03^{+0.10}_{-0.10}$	$0.04^{+0.03}_{-0.02}$
	c	$11.418^{+0.002}_{-0.002}$	$1.29^{+0.10}_{-0.10}$	$0.07^{+0.06}_{-0.04}$
	d	$25.88^{+0.02}_{-0.02}$	$0.79^{+0.13}_{-0.11}$	$0.09^{+0.10}_{-0.05}$
NIR	b	$4.903^{+0.001}_{-0.008}$	$2.2^{+0.4}_{-0.5}$	$0.14^{+0.14}_{-0.09}$
	c	$11.407^{+0.004}_{-0.05}$	$1.61^{+0.37}_{-0.47}$	$0.16^{+0.14}_{-0.10}$
NIR+VIS	b	$4.9064^{+0.0002}_{-0.0002}$	$2.03^{+0.10}_{-0.10}$	$0.04^{+0.04}_{-0.02}$
	c	$11.415^{+0.002}_{-0.002}$	$1.32^{+0.10}_{-0.11}$	$0.07^{+0.06}_{-0.04}$
	d	$25.90^{+0.02}_{-0.02}$	$0.69^{+0.13}_{-0.14}$	$0.17^{+0.15}_{-0.11}$

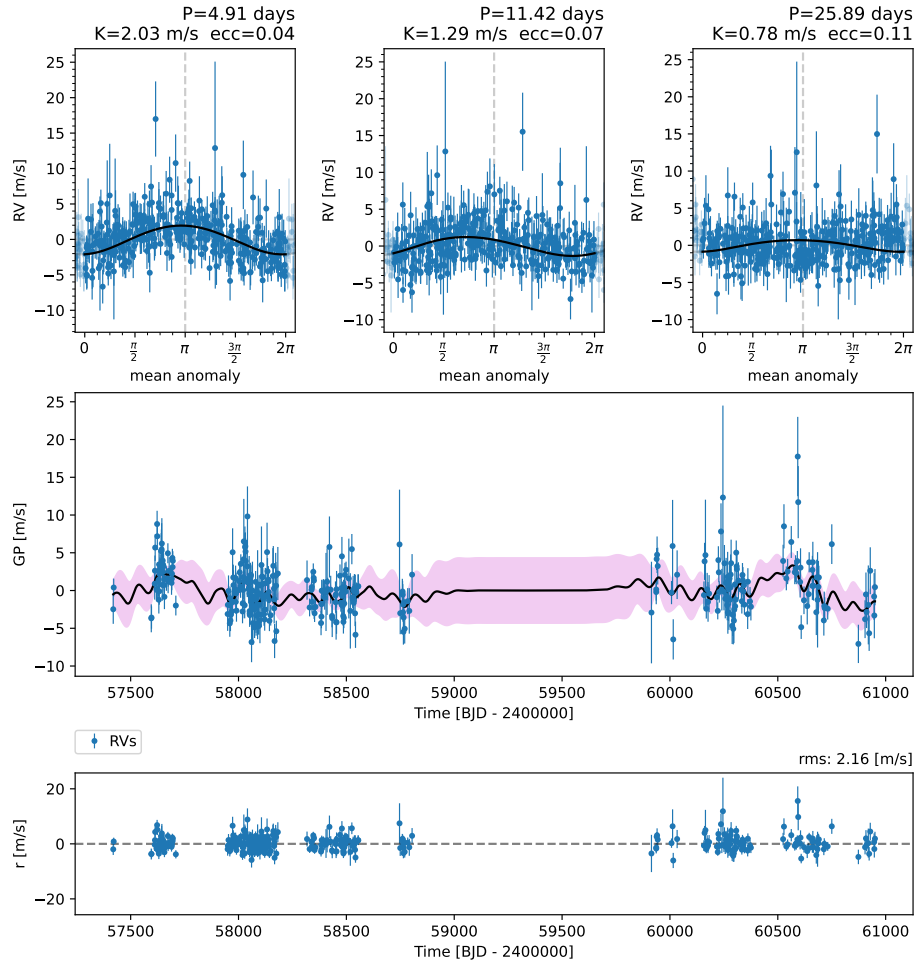


Figure 5.8: Top: fitted planetary signals of Teegarden's b, c, and d for CARMENES VIS time series. Middle: Fitted GP for the stellar component of the RV data. Bottom: residuals after whitening the RV measurements from the stellar and planetary signals.

For the compatibility limits, we run *kima* with the number of previously detected planets fixed at plus one, to explore the range of undetected planets that remain compatible with the data (Standing et al., 2022). The GP posteriors and planetary parameters are consistent with previous results, and no significant signal is observed beyond the 3 detected planets.

CARMENES NIR

Setting the number of planets as free between 0 and 4 for the NIR time series, as in the VIS dataset, the preferred model contains two planetary signals, corresponding to Teegarden b and c. The best-fit posteriors of the model are in Table 5.5, and the planetary parameters in Table 5.6.

Using only CARMENES NIR data, Teegarden's b and c are detected, while planet d is not. Nevertheless, the two inner companions are confidently identified, in agreement with the VIS results. Additionally, the GP posteriors are

consistent, and the stellar rotation period (i.e. η_3) closely matches the previously estimated value of 96 days.

It is worth mentioning that in approximately $\sim 7\%$ of the effective samples from CARMENES NIR data, Teegarden's d is recovered. The significance is too low to claim a robust planetary detection; however, a tentative signal begins to emerge. The inferred planetary parameters are $P = 25.9^{+1.2}_{-0.8}$ d, $K = 0.3^{+4}_{-0.1}$ m s $^{-1}$, and $e = 0.17^{+0.17}_{-0.10}$.

Regarding the compatibility limits, we re-run *kima* with the number of planets fixed, $N_p = 3$. No additional planetary signal (not even Teegarden's d) is compatible with the data, and the GP and planetary parameters recovered match the previous results.

CARMENES VIS and NIR working together

We also used the combined data from CARMENES VIS and NIR, to explore if the significance of the planetary signals increases. We run the GP model with both datasets and the same priors (see Table 5.4), with $0 \geq N_p \geq 4$. For merging both datasets, we sigma-clipped NIR measurements to remove $\cdot 2\sigma$ outliers. A total of 72 of the 344 RVs are excluded.

The complete planetary system is detected with high significance, as the preferred model contains Teegarden's b, c, and d. The results are shown in Fig. 5.9. We reach the same conclusions as using the VIS data, as the GP posteriors and planetary parameters are almost identical. There is no clear advantage in using NIR+VIS in this particular case, although comparing the results from two spectrographs increases the significance and consistency of the analysis, also proving that the signals are achromatic and detected in the three scenarios: VIS, NIR, and NIR+VIS.

5.4.5 Planet detectability

Following the approach of Sabotta et al. (2021), we obtained a detection map, i.e., a function of the projected mass ($m_p \sin i$) and the orbital period (P), using the *ravex* pipeline⁹ (Pozuelos and Varas, 2026). We first remove the Keplerian signals from the RV time series, assuming eccentricity zero and perfectly sinusoidal signals. With the cleaned data, we simulate 50 test planets at each $m_p \sin i - P$ pair, with randomized phase angles, for 50 masses between 0.3 and $5 M_\oplus$, and 50 periods between 1 and 100 days. We injected each of these signals into the cleaned data and attempted to recover it. In order to *recover* a signal, the highest corresponding peak should be above the 1% FAP level. The level at each grid point of the detection map is the ratio of the retrieved to the injected planets.

The detection maps of the CARMENES VIS and VIS+NIR RV residuals are shown in Fig. 5.10, along with three markers, one for each Teegarden's planet. Both planets b and c are clearly detected in both datasets, as the detection prob-

⁹ See Sect. 6.1 in Chapter 6.

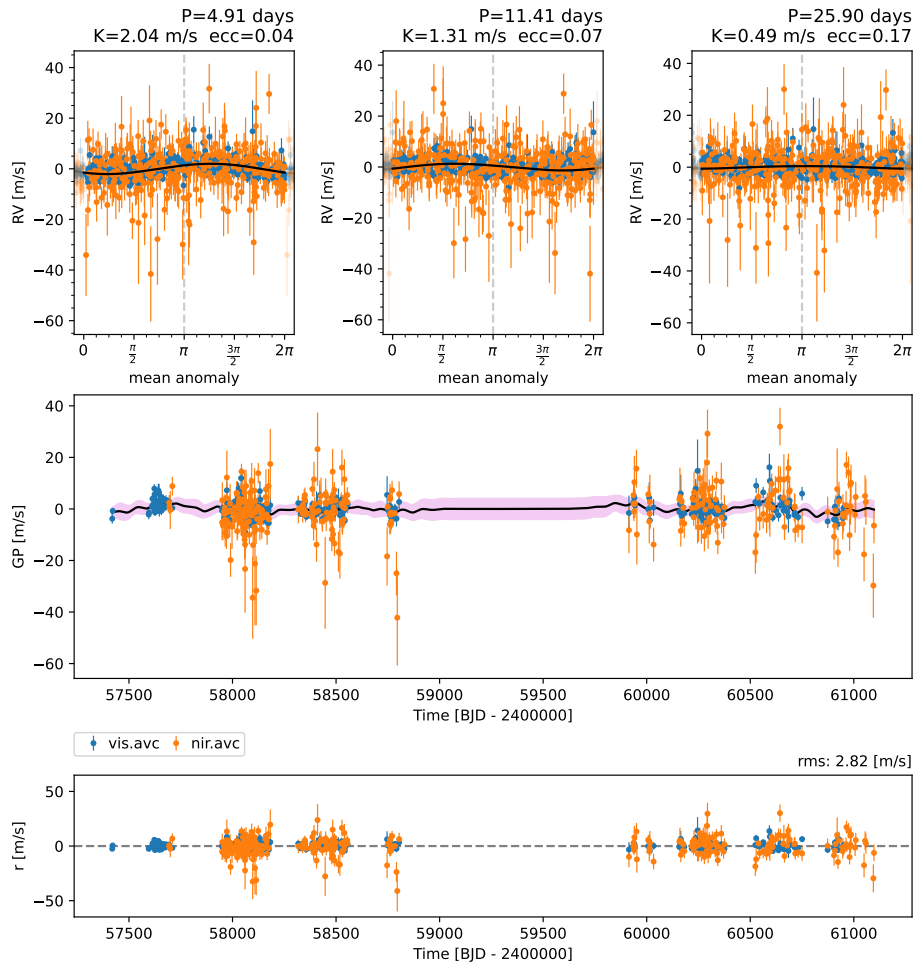


Figure 5.9: Top: fitted planetary signals of Teegarden's b, c, and d for CARMENES VIS+NIR (blue and orange, respectively) time series. Middle: Fitted GP for the stellar component of the RV data. Bottom: residuals after whitening the RV measurements from the stellar and planetary signals.

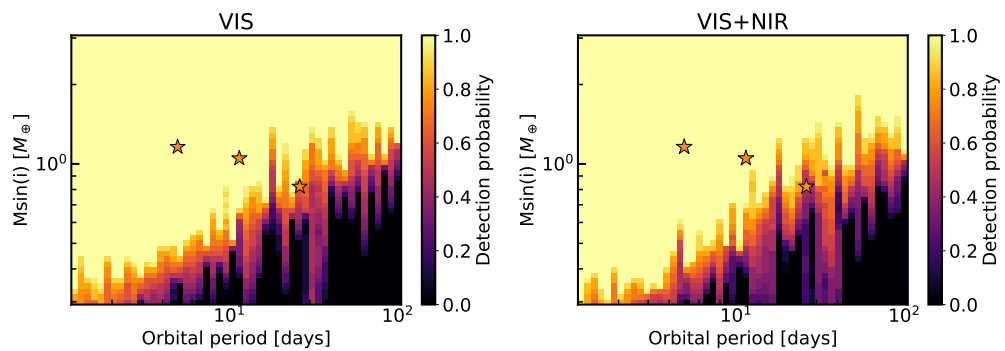


Figure 5.10: Detection maps of Teegarden using whitened VIS and VIS+NIR data. The three detected planets are plotted using star markers, with the corresponding orbital periods and projected masses.

ability is clearly 1, whereas planet d is just above the limit of the detectability. However, this is expected because the lower amplitude of the signal. Thus, using more sophisticated tools than GLS periodograms, such as GP modeling with *kima*, is clearly justified, as not-detected signals with the GLS+FAP method become statistically significant. It is the case of Teegarden's d with VIS data, and planet c for the NIR. Additionally, the rotational period-related signals are consistently characterized by the GPs.

There is not clear advantage of using VIS+NIR instead of VIS for this particular case, as the VIS dominates results. The significant lower scatter and uncertainties of the VIS time series, compare with the NIR, results in a considerable higher weight of the VIS data points during the analysis. Furthermore, as VIS and NIR observations are done simultaneously, there is not higher time-coverage when including NIR RV measurements to the dataset.

Teegarden's b has a significant detection probability in the NIR dataset, whereas planet c is just at the limit, and planet d is considerably below it. Again, as seen in the GLS periodogram, planet b lies above the 1% FAP, while planets c and d lie below. If we increase the FAP to 10% for building the detection map, the three planets are above the zero probability level for the VIS, and similarly are planets b and c with NIR RVs.

5.4.6 CARMENES NIR before and after the upgrades

To evaluate the performance of the current CARMENES NIR configuration, following the upgrades of C-PLUS (see Chapter 3), we performed an analysis on two datasets: pre- and post-C-PLUS. We derived 118 fully corrected RV measurements post-C-PLUS and 219 pre-C-PLUS. To fairly compare the two RV time series, we generated 20 random datasets with 118 RV measurements for pre-C-PLUS. We kept the time span of all datasets similar, between 1100 and 1200 days, as post-C-PLUS is ~ 1100 . Additionally, the pre-C-PLUS spectra are reduced in the *traditional* manner (i.e., with `serval` default), whereas for post-C-PLUS we used the iterative spectral order approach previously described.

We run *kima* for both NIR epochs, using the same priors as in Table 5.4, except we set the maximum number of planets as $N_p = 2$. Due to the limited number of data points and associated uncertainties, we expect, in the most optimistic case, to detect Teegarden's b and c, although this is not necessary for our analysis. Certainly, the preferred model does not include any planetary signal, and the GP posteriors are provided in Table 5.7. Pre-C-PLUS posteriors are computed as the median of the GP obtained for the 20 datasets. In both cases, the rotational period is recovered, and the posteriors are compatible within 1σ , obtaining a similar stellar model.

Subsequently, we whitened the RV time series from the derived stellar GP model, without removing any planetary signal. With the cleaned data, we computed the differential detection map. For pre- and post-C-PLUS, we produced the corresponding detection map and subtracted one from the other (post-C-PLUS – pre-C-PLUS). The resulting differential detection map is in Fig. 5.11.

Table 5.7: Posteriors of the GP after running `kima` for CARMENES NIR pre- and post-C-PLUS.

Parameter	Pre-C-PLUS	Post-C-PLUS	Unit
Jitter	$1.3^{+0.6}_{-0.6}$	$1.45^{+0.5}_{-0.5}$	m s^{-1}
η_1	$2.4^{+1.1}_{-1.0}$	$1.2^{+0.9}_{-0.6}$	m s^{-1}
η_2	580^{+190}_{-210}	534^{+180}_{-195}	days
η_3	101^{+5}_{-7}	97^{+7}_{-7}	days
η_4	$1.75^{+1.5}_{-0.8}$	$1.65^{+1.0}_{-0.9}$	–
RV slope	$-0.001^{+0.002}_{-0.002}$	$-0.003^{+0.001}_{-0.001}$	$\text{m s}^{-1} \text{ yr}^{-1}$
RV quadr	$1.1^{+0.6}_{-0.6} \cdot 10^{-5}$	$0.8^{+0.4}_{-0.5} \cdot 10^{-5}$	$\text{m s}^{-1} \text{ yr}^{-2}$

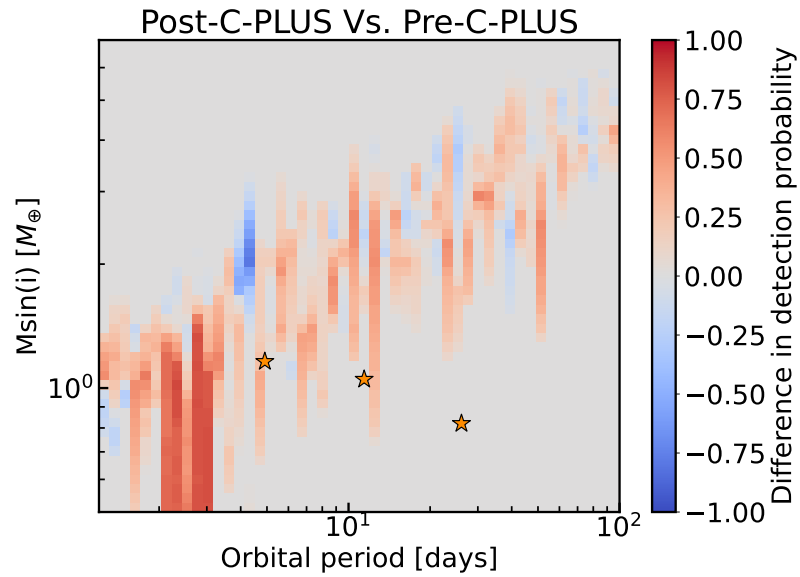


Figure 5.11: Differential detection map between post- and pre-C-PLUS RV time series (i.e. detection map of pre-C-PLUS subtracted from the post-C-PLUS one). Teegarden's b, c, and d are represented by the star markers.

Regions with positive (red) values indicate higher recovery rates (i.e., detection probability) for post-C-PLUS data, whereas negative (blue) values correspond to higher detection probability with pre-C-PLUS data. The gray areas define an equally recovery rate for the $m \sin i - P_{\text{orb}}$ pairs. The gray area on top is the 1 detection probability area, whereas the bottom is the 0 recovery rate region.

The differential detection map shows that the post-C-PLUS dataset generally yields higher detection probabilities than the pre-C-PLUS dataset, as indicated by the predominance of positive (red) regions. This improvement is particularly evident at short orbital periods ($\lesssim 10$ days), where the phase coverage provided by the available 118 measurements is more favorable. At longer periods, the gain appears less pronounced, although this is likely driven, at least in part, by the limited sampling of the dataset rather than by the absence of an instrumental improvement. Overall, these results indicate that the C-PLUS upgrade, together with our iterative spectral-order optimization, enhances the sensitivity of CARMENES NIR to planetary companions. Localized negative (blue) regions are also present in the differential map; these may reflect statistical fluctuations, sampling effects, or local aliasing in the recovery analysis, and therefore should not be over-interpreted in view of the clear global improvement of the post-C-PLUS data.

5.5 SUMMARY

In this chapter, we presented a radial velocity (RV) analysis of Teegarden's star system. we contextualized the importance of RV and transit surveys focused on ultracool dwarfs and the need for near-infrared high-resolution spectrographs. CARMENES, with its visible- and near-infrared arms, is an ideal facility for these studies.

The RV extraction of CARMENES NIR with `serval` can be optimized for specific targets, especially important for the lowest mass stars. Here, we present the optimization of the RV precision using CARMENES NIR data. First, we provide an overview of the default RV extraction with CARMENES NIR and the precision obtained. The selection of spectral orders and their contributions to the RV determine the associated uncertainties. We minimize them through an iterative process and demonstrate an improvement of over 10% for three targets: Teegarden's star, CN Leo, and LP 731-058. Furthermore, we discussed the benefit of using telluric absorption correction in the spectra, which provides an additional improvement of up to $\sim 7\%$.

Teegarden's Star is a benchmark system for ultracool dwarf surveys: it is a slow-rotating, quiet star with three planets already detected (Dreizler et al., 2024) and hundreds of observations with CARMENES. Following the RV optimization approach presented, we obtain the RV time series for Teegarden's Star. As a first step, we compute a generalized Lomb-Scargle periodogram for VIS and NIR data. In both datasets, planets b and c are detected with high significance (particularly for VIS data). Additionally, modulations of the

data due to the rotational period (96 days) of the star are reflected in the VIS periodogram.

A more sophisticated tool is to model the Keplerian signals together with stellar ones using Gaussian processes. The *kima* pipeline is a tool that provides the option to run these models and yields the statistical significance of the different models (with N_p planets). We applied this approach to the CARMENES data, with specific priors for Teegarden's system. For the VIS dataset, *kima* finds the best model with three Keplerian signals, with periods of 4.91, 11.42, and 25.89 days, consistent with those claimed by Dreizler et al. (2024). The NIR only recovers planets b and c, with the same orbital periods and consistent amplitudes as the VIS within the uncertainties. Using NIR and VIS data together is not particularly beneficial, as it yields very similar results as the VIS time series alone. The smaller uncertainties and scatter of the VIS RV measurements, result of the high S/N and RV information, dominates the analysis.

We have also built detection maps using an injection-and-recovery approach, using the residuals of our RV time series after whitening for the Keplerian signals. Using VIS and VIS+NIR data with a FAP level of 1%, Teegarden's b and c are detected with 1 detection probability, whereas planet d is above the detection limit, with a $\gtrsim 0.6$ probability of detection. For the NIR, just planet b is clearly above the zero probability region, whereas Teegarden's c is at the limit, and planet d is evidently below. These results justify the use of tools such as *kima*, as signals not detected by the GLS+FAP method are statistically significant when modeled with GP.

We examined the impact of C-PLUS and the optimized RV extraction with CARMENES NIR spectra. Using the 118 observations of post-C-PLUS, we generated 20 datasets with the same number of RV measurements for pre-C-PLUS. The preferred model using *kima* does not include any planetary signal. We removed the fitted stellar GP model from the RV time series and produced the differential detection map, as the difference between post- and pre-C-PLUS detection maps. The upgraded version of the NIR provides better results, as the detection limit moves towards smaller values of planetary mass and orbital period. Moreover, Teegarden's b starts to have a considerable detection probability at ~ 0.2 , for the post-C-PLUS time series.

5.5.1 *Lessons learned from Teegarden's system*

We have used Teegarden's system as a benchmark to test our methodology. On the one hand, combining the NIR and VIS spectra does not provide a significant advantage over VIS data alone. On the other hand, we have proven the positive impact of the C-PLUS upgrades on the RV precision and the possible detection of Keplerian signals.

Nevertheless, Teegarden's star is not the best target to fully test the advantages of the NIR RV measurements in the search for exoplanets around UCDs. The relatively high brightness (for an M-dwarf star) benefits the VIS over the NIR. One advantage of near-infrared wavelengths is the higher S/N for late M dwarfs, which compensates for the lower RV information available compared to the VIS.

But in Teegarden's case, the VIS has a high S/N, resulting in better performance than the NIR. Additionally, the higher photon noise in redder orders is more pronounced for slowly rotating, low-magnetic-activity stars. Thus, fainter and cooler stars might be better targets than Teegarden's Star to demonstrate the potential of the NIR channel. However, the lessons learned with this object will be invaluable for future NIR RV campaigns with CARMENES.

5.5.2 *Future work*

Further work can increase the significance of the detected signals and improve the derived planetary parameters of Teegarden's system. Some possible refinements include (i) the use of telluric absorption corrected spectra, especially important for CARMENES NIR; (ii) higher number of observations, as Teegarden is regularly observed by CARMENES; (iii) explore in more detail the parameter space for the priors and posteriors of `kima` and a deeper analysis with the GP modeling, e.g., including dLW (equivalent to FWHM) during the process (e.g. Figueira et al., 2025); and (iv) a deeper analysis on the NIR+VIS results in order to understand the possible benefits from combining the data from two different spectrographs.

With the lessons learned from Teegarden's star analysis, we will define a strategy and a sample with the most promising and interesting UCDs observable with CARMENES. Future campaigns and the extension of the CARMENES legacy project will significantly increase the number of observations we have for these targets, especially after C-PLUS. We will also explore the possibility of optimizing the observations (e.g., exposure time) for the NIR channel rather than the VIS channel, as is standard for CARMENES. The new sample will also include faster rotators, more active and fainter stars, making CARMENES NIR a crucial factor in extracting the most RV information possible.

This is the first work to explore in detail the potential of CARMENES NIR and NIR+VIS for radial velocity studies, particularly powerful for ultracool dwarf systems. By means of periodograms and GP modeling (with `kima`), Teegarden's b and c are clearly detected only using CARMENES NIR data. Furthermore, the improvement in the RV precision is a key factor for these challenging objects, which need hundreds of observations for a clear detection, even with CARMENES VIS. This work is a key step in our work on ultracool dwarfs.

ADDITIONAL CONTRIBUTIONS

This chapter presents an overview of participation in additional research projects conducted during the PhD thesis.

6.1 RAVEX: THE RADIAL VELOCITY EXPLORER

ravex¹ (RAdial VELOCITY eXplorer; Pozuelos and Varas, 2026) is an open-source Python package developed to simulate and analyze exoplanetary systems in the context of radial-velocity studies. The package allows the generation of synthetic RV time series for single- and multi-planet systems, including uncertainties associated with instrumental precision and astrophysical noise. In addition, ravex provides a set of tools to inject synthetic planetary signals into observed or simulated RV time series and to analyze their recovery. These tools include Generalized Lomb–Scargle periodogram analyses, detection-growth studies, Monte Carlo predictions of planetary mass precision as a function of the number of observations, and recovery maps in the period–mass parameter space. Several of the most computationally demanding routines are parallelized to improve performance.

ravex is intended to support feasibility studies for RV follow-up observations, instrument-performance evaluations, and the preparation of observing proposals. It has been applied in the context of exoplanet validation and characterization studies (Barkaoui et al., 2025; Morello et al., 2026; Peláez-Torres et al., 2026) as well as in the CARMENES large program dedicated to the accurate characterization of rocky exoplanets, as described in the Sec.6.7.

As part of this thesis, I contributed to the development and validation of ravex. In particular, I actively participated in the implementation of the CARMENES precision module. This module allows the user to generate RV time series with uncertainties representative of the expected CARMENES VIS precision. The generated uncertainties and the corresponding scatter of the simulated measurements are based on the extensive CARMENES RV archive, which contains tens of thousands of observations.

The input parameters of the function are the J -band magnitude, the spectral type, and the projected rotational velocity, $v \sin i$. The CARMENES sample was divided into several spectral-type groups: (i) $\text{SpT} < \text{M1}$, (ii) $\text{M1} \leq \text{SpT} < \text{M3}$, (iii) $\text{M3} \leq \text{SpT} < \text{M4}$, and (iv) $\text{SpT} \geq \text{M4}$. For each spectral-type group, the empirical CARMENES data were fitted to derive two relations: one linking the signal-to-noise ratio with the J -band magnitude, and another linking the RV uncertainty with the signal-to-noise ratio. The $\text{S/N}-J_{\text{mag}}$ relation was modeled as a linear relation,

$$\text{S/N} = a - bJ_{\text{mag}}, \quad (6.1)$$

¹ Source code available at <https://github.com/franpoz/ravex>.

whereas the RV uncertainty was modeled as a power-law relation with an additional noise floor,

$$\sigma_{\text{RV}} = c(\text{S/N})^\alpha + d. \quad (6.2)$$

An additional degradation term was included for targets rotating faster than 2 km s^{-1} , such that

$$\sigma_{\text{RV}}^{v \sin i} = \sigma_{\text{RV}} \cdot [c'(v \sin i)^{\alpha'} + d']. \quad (6.3)$$

Future work will include extending this tool to CARMENES NIR data. The approach will be similar to that adopted for the VIS channel: the empirical relation will first be validated using CARMENES observations, then implemented in `ravex` and made available to the community.

6.2 AN EARTH-LIKE PLANET AROUND SPECULOOS-3

Gillon et al. (2024) presented the discovery of an Earth-like planet around the nearby SPECULOOS-3, an M6.5 V star. It was the fourth planetary system detected hosted by a UCD star, in an orbit of approximately 17 h. The parameters of SPECULOOS-3 b and its host star are detailed in Table 6.1.

Table 6.1: Parameters of the SPECULOOS-3 system from Gillon et al. (2024).

Stellar parameters		
Parameter	Value $\pm 1\text{-}\sigma$ error	Unit
Spectral type	M6.5 \pm 0.5	–
Distance	16.750 \pm 0.012	parsec
Right ascension	20 : 49 : 27.440	HH:MM:SS (J2000)
Declination	+33 : 36 : 50.96	DD:MM:SS (J2000)
Radial velocity	17.816 \pm 0.019	km s^{-1}
R magnitude	16.4 \pm 0.0	mag
J magnitude	11.501 \pm 0.000	mag
Mass	0.1009 \pm 0.0024	M_\odot
[Fe/H]	+0.07 \pm 0.10	dex
Luminosity	0.000835 \pm 0.000019	L_\odot
T_{eff}	2800 \pm 29	K
Radius	0.1230 \pm 0.0022	R_\odot
log g	5.265 \pm 0.014	dex
$v \sin i$	4.2 \pm 0.4	km s^{-1}
Age	6.6 ^{+1.8} _{-2.4}	Gyr
Planetary parameters		
Orbital period	0.71912603 \pm 0.00000057	d
Orbital inclination	89.44 \pm 0.39	deg
Equilibrium temperature T_{eq}	553 \pm 8	K
Radius	0.977 \pm 0.022	R_\oplus

During 2023 and 2024, our team collected 36 observations of SPECULOOS-3 with CARMENES. Two of those nights (22nd of November and 8th of December 2023) are of low S/N and, therefore, not used, neither for the VIS nor the NIR. Additionally, due to a detector malfunction, the first two NIR-channel observations (both on the 28th of September 2023) are unusable as well. Table 6.2 shows the observations and S/N of each observation and each CARMENES channel. The median S/N of the NIR (échelle order 50) is 30.95 whereas the S/N of the VIS (échelle order 82) is 9.42.

Table 6.2: CARMENES observations and the S/N in the VIS (order 82) and NIR (order 50) channels.

Date	S/N (VIS/NIR)	Date	S/N (VIS/NIR)
2023-09-28 19:13:29	10.303/-	2024-09-14 20:34:07	10.03/34.87
2023-09-28 22:41:22	8.84/-	2024-09-14 21:05:11	11.46/37.52
2023-09-29 19:40:04	11.66/36.4	2024-09-14 21:43:04	10.01/34.69
2023-09-29 22:51:15	10.06/31.5	2024-09-14 22:18:22	10.95/37.18
2023-09-30 19:31:53	11.49/37.53	2024-09-14 22:49:21	9.85/33.88
2023-09-30 22:53:47	6.77/24.87	2024-09-14 23:23:45	10.27/32.88
2023-10-01 19:21:35	11.85/38.97	2024-09-16 21:39:12	10.59/35.13
2023-10-01 23:06:04	9.83/28.99	2024-09-16 22:13:03	10.22/34.13
2023-10-18 19:21:21	7.83/28.92	2024-09-16 22:44:01	10.05/33.7
2023-11-24 18:34:09	6.17/24.74	2024-09-16 23:22:53	9.32/30.31
2024-05-28 01:49:14	11.57/40.3	2024-09-16 23:53:51	9.25/28.25
2024-05-30 02:04:46	11.13/39.9	2024-09-17 00:33:41	9.59/24.67
2024-05-31 03:25:16	4.99/31.33	2024-09-17 01:35:38	8.38/17.39
2024-09-12 20:10:50	5.49/21.08	2024-09-18 20:25:30	10.14/32.34
2024-09-13 01:28:53	4.92/14.57	2024-09-18 23:23:47	10.59/32.39
2024-09-13 01:57:29	8.07/17.35	2024-09-18 23:54:45	7.21/21.07
2024-09-14 19:23:09	10.35/36.34	Median value	9.42/30.95
2024-09-14 19:56:45	10.94/37.35		

These observations allowed us to derive the star's projected rotational velocity. We used Teegarden's star as a template for the VIS, using just the 20 reddest orders and all orders (except the telluric-contaminated ones). Taking into account also the estimates from other spectra taken by the SPECULOOS team, which used the CCF method, the proposed $v \sin i$ value in the article was $4.2 \pm 0.4 \text{ km s}^{-1}$. With our more refined method (see Chapter 4), we have revisited the value and estimate $6.0 \pm 0.6 \text{ km s}^{-1}$ for the VIS and $5.59 \pm 0.32 \text{ km s}^{-1}$ for the NIR. This confirms SPECULOOS-3 as a fast-rotating star, challenging the RV determination with high precision.

There are two available TESS sectors, 44 and 51. Using the light curves, the GLS periodogram shows two significant peaks at approximately 0.084 days and 1.13 days. The first is too extreme for this object and must be a contaminating source affecting the light curve. The second peak looks more realistic for SPECULOOS-3, and is selected as the rotational period. With the stellar radius,

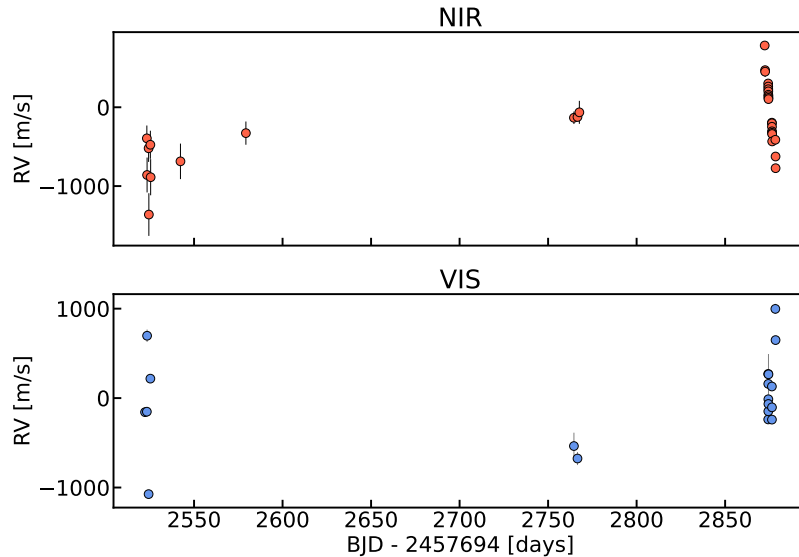


Figure 6.1: SPECULOOS-3 RV time series derived from CARMENES observations.

we can derive the equatorial velocity, $v_{\text{eq}} = 5.51 \text{ km s}^{-1}$. The orbital inclination is close to 90° , and assuming the planet is orbiting at the equatorial plane, $v_{\text{eq}} \approx v \sin i$, that is close to the derived results with the CARMENES data.

The RVs were also derived from the CARMENES spectra; however, the target's faintness and relatively rapid rotation result in large uncertainties, rendering the measurements unreliable. The SPECULOOS-3 RV time series is shown in Fig. 6.1, displaying comparable scatter and uncertainties in both the VIS and NIR channels, of approximately ~ 450 and 65 m s^{-1} , respectively. Notably, the observed scatter significantly exceeds the average error, which may indicate either intrinsically unreliable RV measurements or the presence of an undetected massive companion.

Further work is required to properly exploit these RV data, and additional observations will be necessary to enable a robust attempt to detect SPECULOOS-3 b.

6.3 IMPACT OF ROTATION ON THE RV JITTER IN COOL STARS

In Ruh et al. (2024), we provided a catalog of the jitter of the CARMENES VIS RV time series for 239 M dwarfs, predominantly mid to late spectral type and solar metallicity. Additionally, we analyzed the correlations between stellar rotation and magnetic field and the determined jitter. We found a correlation between jitter and rotation velocity, which can be used to estimate the expected jitter in a star's RV time series. Moreover, we found a jitter floor, and slow rotators ($v_{\text{eq}} < 1 \text{ km s}^{-1}$) have a minimum jitter independent of their rotation, which might be related to granulation, hidden companions, or residual instrument noise. As the magnetic field and rotational velocity are strongly correlated, we derived a relation between the magnetic field and a star's jitter. Notably, some targets exhibited greater jitter than the rest of the sample. We concluded that

Table 6.3: Stellar and planetary parameters of TOI-7166 system (Barkaoui et al., 2025).

<i>Stellar parameter</i>	Value	Unit
Distance	35.2	pc
Spectral-type	M4.0V	–
T_{eff}	3099 ± 50	K
M_{\star}	0.190 ± 0.004	M_{\odot}
R_{\star}	0.222 ± 0.005	R_{\odot}
$\log g_{\star}$	5.02 ± 0.02	dex
[Fe/H]	-0.20 ± 0.12	dex
<i>Planetary parameter</i>	Value	Unit
Orbital period	12.92	d
R_{p}	$2.01^{+0.06}_{-0.05}$	R_{\oplus}
T_{eq}	249 ± 5	K
S_{p}	1.07 ± 0.08	S_{\oplus}

the jitter excess originates from Zeeman-split line profiles, which are affected by the magnetic filling factor. Furthermore, these results suggest that activity-induced signals in RV time series are associated with specific distributions of the magnetic field components.

My main contribution to this work was related to the code validation and analysis of the CARMENES stars RV time series. I further explore the extension of the work to the CARMENES NIR, included in Varas et al. (2025).

6.4 TOI-7166 B: A HZ MINI-NEPTUNE AROUND A LOW-MASS STAR

In Barkaoui et al. (2025), we presented the discovery and planetary validation of a mini-Neptune-size planet orbiting TOI-7166², a M4 star. This target is part of the TESS mission, but multiband photometric observations from SPECULOOS-North, SPECULOOS-South-1mo, TTT-2mo, TRAPPIST-Shouth-0.6m, and LCOGT-1mo telescopes were used for this work. We combined the spectral energy distribution with spectroscopic observations to characterize the host star. Subsequently, we derived the system's physical properties by performing a global fit to the multicolor observations (from both TESS and ground-based facilities).

The stellar and planetary parameters derived for the TOI-7166 system are in Table 6.3. For the equilibrium temperature (T_{eq}), we assumed a null Bond Albedo. With its orbital period of ~ 13 days, TOI-7166 b lies close to the inner edge of the Habitable Zone of its host.

We also explore the system's suitability for an RV campaign follow-up. The predicted amplitude of the RVs is $\approx 4.2^{+2.1}_{-1.1} \text{ m s}^{-1}$ and has a magnitude of $V_{\text{mag}} = 15.8$, making TOI-7166 b an ideal target for MAROON-X observations. Furthermore, its infrared brightness ($J_{\text{mag}} = 11.4$ and $K_{\text{mag}} = 10.6$) and planet-

² TOI: TESS Objects of Interest.

to-radius ratio of ~ 0.08 make the system an exquisite target for transmission spectroscopy with JWST.

We have submitted a proposal to observe this target with MAROON-X for the 2026B semester. We aim to measure TOI-7166 b mass with a 15% precision using ~ 40 RV measurements from MAROON-X. With this precision, we can obtain first-order estimates of the core-mass fraction (CMF) and water-mass fraction (WMF) using physically consistent interior models, as well as a bulk-density estimate with credible intervals (Dorn et al., 2017; Plotnykov and Valencia, 2024). Future atmospheric spectra from facilities such as the JWST will help narrow the permissible envelope composition and mean molecular weight of TOI-7166 b.

My main contribution to this work is regarding the RV suitability of the TOI-7166 system. We used the *ravex* tool to estimate the RV scatter and uncertainties we would obtain for this target using different facilities, such as CARMENES and MAROON-X. The most favorable instrument is MAROON-X, as the faintness of the host star makes CARMENES observations unsuitable.

6.5 FOUR PLANETS FROM THE RADIUS VALLEY TO THE NEPTUNE DESERT

In Morello et al. (2026), we validated the planetary nature of TOI-2133 b, TOI-5734 b, TOI-5938 b, and TOI-7009 b, four candidates orbiting K-dwarf stars from TESS. We used the data from the TESS Follow-up Observing Program (TFOP), including multicolor photometry, spectroscopy, and high-resolution imaging. Multicolor photometry provided the strongest validation for three of the four systems, although it is limited for small planets and by the data quality. Additionally, we conducted statistical validation and used a novel neural-network classifier (*WATSON-Net*) to obtain a consistent picture. TOI-2133 b and TOI-5734 b are close to the upper part of the radius valley. TOI-5938 b and TOI-7009 b are uncommon systems of the sub-Neptune population, as they lie at the boundary of the Neptune desert. We found these transiting systems to be suitable for the precise determination of planetary masses and atmospheric characterization with current facilities. Particularly, we found TOI-5938 b and TOI-7009 b to be high-priority targets for JWST. Ultimately, these four validated systems expand the population of known transiting sub-Neptunes hosted by K-dwarf stars, a regime that remains less accessible to detailed characterization than the more commonly studied M-dwarf systems. As benchmark targets for precise mass measurements and atmospheric characterization, they provide valuable constraints for testing models of planetary formation and evolution around K-dwarf hosts.

My main contribution was to estimate the suitability of the systems for RV follow-up campaigns using our *ravex* code. Additionally, I was involved in this work to further extend my knowledge of multicolor photometry.

6.6 A LAVA WORLD AND A HZ SUB-NEPTUNE ORBITING TOI-1752

In Peláez-Torres et al. (2026), we investigated the planetary nature of the two companions of TOI-1752, an M1 V star, with planet b lying inside the radius valley. Planet b is a short-period companion compatible with a lava-world scenario, whereas planet c is a sub-Neptune candidate located in the optimistic habitable zone of the star. We combined the available TESS photometric data with additional ground-based multi-color photometry from several facilities. We explored the planetary nature of the candidates using the formal statistical validation of the TRICERATOPS framework and the neural-network approach of WATSON-Net. We validate TOI-1752 b as a bona fide planet with a radius of $1.69 \pm 0.07R_{\oplus}$ and an extremely short orbital period of $0.935186^{+0.000001}_{-0.000002}$ d. This makes the planet a promising target for possible atmospheric characterization. TOI-1752 c is inside the optimistic habitable zone and has a radius of $2.29 \pm 0.14R_{\oplus}$, an orbital period of 32.7144 ± 0.0004 d, and an equilibrium temperature of 291 K. This planet can be considered a twin of K2-18 b, one of the most promising candidates for JWST, although its composition and habitability remain controversial.

I participated at various stages of the study, with my main contribution focused on assessing the system's RV suitability using *ravex*. I was also involved in the photometric observations with the OSN. Unfortunately, due to weather conditions, these observations were not included in the final version of the manuscript.

6.7 ROCKY WORLDS IN THE JWST ERA: CARMENES FOLLOW-UP

I am actively involved in an ongoing RV follow-up campaign within the CARMENES collaboration to characterize small transiting planets around M-dwarf stars in the context of the JWST Rocky Worlds DDT program. This is a large program led by Angelica Psaridi (PI) and Francisco J. Pozuelos (co-PI) with ~ 500 h awarded, and focuses on deriving precise planetary masses and bulk densities for a carefully selected sample of short-period ($P_{\text{orb}} \sim 0.9\text{--}13.5$ d), Earth-sized planets ($R_p < 2, R_{\oplus}$) orbiting nearby low-mass stars, which currently lack precise planetary-mass determinations.

The selected targets are drawn from the JWST Targets Under Consideration catalog and were chosen based on several criteria: small planetary radii ($< 2, R_{\oplus}$), bright host stars ($J < 11$), expected RV semi-amplitudes above $\sim 1.5 \text{ m s}^{-1}$, and either missing or poorly constrained masses. The primary scientific goal is to combine high-precision RVs with space-based photometry (TESS and CHEOPS) to determine accurate densities (precise mass measurements, $\lesssim 15\%$) and place these planets in the context of the radius and density valleys, ultimately supporting atmospheric characterization with JWST. Moreover, many of these planets lie near the radius valley, making them particularly valuable for probing the transition between rocky and volatile-rich compositions and for testing planet formation and evolution models.

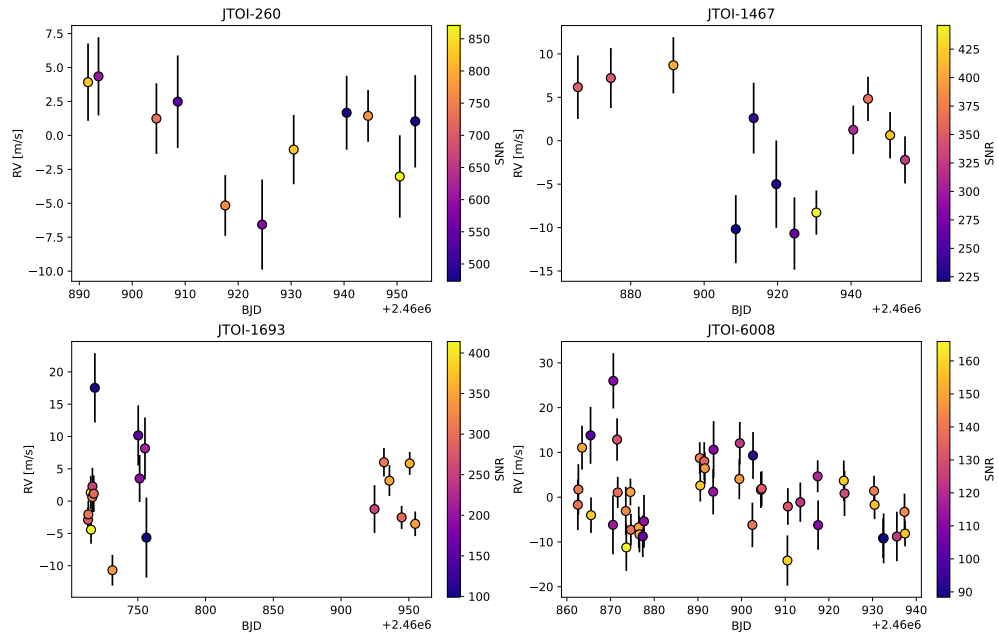


Figure 6.2: Radial velocity time series of the JWST-CARMENES campaign.

A central objective of the program is to place these planets in the context of the Cosmic Shoreline, an empirical relation linking a planet's ability to retain an atmosphere to its escape velocity and the incident high-energy (XUV) irradiation. In this framework, atmospheric survival scales approximately as $I_{\text{XUV}} \propto v_{\text{esc}}^4$, defining a boundary between airless bodies and atmosphere-bearing planets. Precise mass and radius measurements are therefore essential for determining the escape velocity and assessing whether a given planet is expected to retain or lose its atmosphere.

My contribution to this program focuses on reducing and analyzing CARMENES spectroscopic data. I process the raw spectra and extract high-precision RV measurements using the `serval` pipeline, ensuring consistency and quality control across different observing runs. I also participate in modeling the RV time series, including assessing stellar activity signals and their impact on the determination of planetary semi-amplitudes.

The current dataset includes multiple targets such as TOI-260b, TOI-1467b, TOI-1693b, and TOI-6008b (see Table 6.4), for which the available RVs already provide preliminary mass constraints but remain insufficient to reach the desired precision of $\lesssim 15\%$. The RV time series presented in Fig. 6.2 illustrates the current status of this program, which will be extended, at least, up to the 2027A semester.

Table 6.4: Stellar and planetary parameters for the selected targets of the JWST rocky worlds large program of CARMENES.

Target	R_p [R_\oplus]	P_{orb} [d]	SpT	J [mag]	$M_{p,\text{exp}}^a$ [M_\oplus]	K_{exp} [m s^{-1}]	σ_{RV} [m s^{-1}]	Req. ^f RVs	Col. ^g RVs	M_{PC}^h [M_\oplus]
TOI-260 ^b	1.77 ± 0.07^b	13.48	K8V	7.38	5.6–7.4	2.1–2.7	2.25	100	21	$4.44^{+2.31}_{-2.16}$
TOI-1467 ^b	1.83 ± 0.09^b	5.97	Mo.5V	9.38	6.3–8.3	3.6–4.7	2.98	100	22	$6.64^{+2.09}_{-2.10}$
TOI-1693 ^b	1.32 ± 0.04^b	1.77	M2.5V	9.19	2.1–2.6	1.8–2.2	2.3	100	31	$4.72^{+1.53}_{-1.54}$
TOI-2068 ^b	1.98 ± 0.12^b	7.77	M1V	9.87	8.1–10.9	3.9–5.2	–	200	6	–
TOI-6008 ^b	1.03 ± 0.05^d	0.86	M5V	10.42	0.9–1.1	1.7–1.9	3.4	200	47	$1.03^{+0.65}_{-0.56}$
TOI-6086 ^b	1.18 ± 0.07^d	1.39	M4.5V	10.82	1.5–1.7	2.1–2.5	–	200	2	–
HD260655 ^c	1.53 ± 0.05^c	5.71	MoV	6.67	3.5–4.4	2.1–2.8	–	32	88	–

Notes. ^a $M_{p,\text{exp}}$ is estimated from the mass-radius relations from Otegi, Bouchy, and Helled (2020). ^b Our work. ^c From Hobson et al. (2024). ^d From Barakaoui et al. (2024). ^e From Luque et al. (2022). ^f Number of requested CARMENES RVs estimated with our simulations using ravex (Pozuelos and Varas, 2020). ^g Number of existing CARMENES RVs under the 25B-3.5-023 and 26A-3.5-018 programs, the DDT.25A.336 (13 RVs for TOI-1693), and GTO (32 RVs for HD260655c). ^h Masses estimates constrained with the existing CARMENES RVs collected under 25B-3.5-023 and 26A-3.5-018 programs.

CONCLUSIONS AND FUTURE WORK

Throughout this thesis, I have discussed the search for Earth-like exoplanets orbiting ultracool-dwarf stars using the RV technique with high-resolution near-infrared spectrographs. The work covers the context of M-dwarf stars, exoplanet science, and the instrumentation used for their study. Consequently, I have focused on the three working lines of my thesis: instrumentation improvements, stellar rotation characterization, and optimization of radial velocity analysis, and I briefly summarize the chapters and provide the main conclusions:

Enhancement of CARMENES NIR

This work presents improvements to the thermal stability of the CARMENES near-infrared (NIR) spectrograph. These improvements include pressure control optimization, valve replacement to enable continuous flow operation, and enhancements to the liquid nitrogen refilling process. Although the upgrades were implemented individually, they resulted in a fully operational and stable NIR cooling system, enabling improved radial velocity performance.

The thermal improvement was significant, as the thermal variations were reduced from hundreds of millikelvins (mK) over days to a few K over months, and to less than 5 mK over 2 years. We analyze the nightly variation of the RV drift by obtaining the residuals of the Fabry-Pérot measurements after fitting the data. The improved thermal stability led to a considerable improvement in the intrinsic RV precision of the NIR channel. The histogram of the root-mean-square of the RV drift residuals shows a median value below 0.7 m s^{-1} , compared to $\sim 2.6 \text{ m s}^{-1}$ before the upgrades and $\sim 1.0 \text{ m s}^{-1}$ for the VIS channel.

The improvement in thermal stability and calibration variability has also translated into better precision in on-sky measurements. The scatter exhibited by the RV time series of the CARMENES sample has been reduced from over 9.0 m s^{-1} to almost 6.5 m s^{-1} . However, the VIS observations still outperform the NIR, with a median RV scatter of 4.3 m s^{-1} , mainly due to higher photon noise in the NIR and the fact that most targets are early- and mid-M dwarfs, which are brighter at optical wavelengths.

Projected rotational velocity and limb-darkening

In the subsequent chapter, I focused on the method we developed to compute the projected rotational velocity of stars and the catalog we provide for the CARMENES sample. Existing methods for computing the $v \sin i$ of stars do not properly account for limb-darkening, which is especially important for M-dwarf stars. Thus, we proposed a method, validated it with synthetic spectra,

and provided a catalog of $v \sin i$ values for 392 M dwarfs, including updated measurements and 36 new determinations.

Our method was validated with synthetic spectra corresponding to the visible and near-infrared arms of CARMENES. We explore a parameter space including effective temperatures between 2500 and 4000 K and $v \sin i$ values from 4 to 50 km s⁻¹. A linear limb-darkening law was sufficient to model the effect, and the oversampled convolution approach provided the best precision. Our detailed limb-darkening implementation improved the $v \sin i$ measurements by up to 10% and almost halved the uncertainties, compared to standard approaches such as convolution without limb-darkening and numerical integration.

Our detailed limb-darkening implementation improved the results by up to 10% and nearly halved the uncertainties compared to other approaches, such as traditional convolution without limb-darkening and numerical integration.

We implemented our method in the `serval` pipeline and yielded a $v \sin i$ catalog for 392 M-dwarf stars of the CARMENES sample using VIS data. In most cases ($\sim 95\%$), our $v \sin i$ values are consistent with previously published measurements when available. Some targets (21) showed large discrepancies (larger than 1σ); in some cases, our values were unreliable because the targets were multiple systems, where line blending affects the $v \sin i$ determination. Moreover, we proposed updated values from the literature because we found ours to be more consistent with the broadening of the observed spectra. The $v \sin i$ values derived using deep learning approaches tend to be higher, although the broadening of the spectra seems to better match our $v \sin i$ estimates. Furthermore, we provide 36 new $v \sin i$ measurements not previously reported, significantly expanding the available dataset for M-dwarf stars. The final catalog includes the most reliable $v \sin i$ measurements, selected based on data quality and consistency with the spectral analysis.

We extended the method to the CARMENES NIR dataset, following the same approach: first, a validation using synthetic spectra, and later the implementation in `serval`. We performed the analysis on a subsample of 61 stars with spectral types later than M5.0, targeting the ultracool dwarf regime. The results are consistent with those obtained from the VIS channel, showing comparable $v \sin i$ measurements within the uncertainties and supporting the suitability of NIR spectra for such measurements.

Optimizing the radial velocity tools for ultracool dwarfs

The radial velocity extraction implemented in `serval`, the CARMENES RV pipeline, is not optimized for ultracool dwarf studies, and the spectral orders used for the RV computation are also not tailored to these targets, limiting the achievable precision. Thus, we have developed a pipeline that, with an iterative approach, combines the NIR orders that minimize the average uncertainty of the RV time series of a specific target. We observed an improvement of 10–14% for three late M dwarfs observed with CARMENES. We obtain an additional 5% decrease in the uncertainties when using telluric absorption-corrected spectra.

Subsequently, we focus on Teegarden's three-planet system. We derived the RV time series using the method mentioned and obtained periodograms for the VIS and NIR data. In both datasets, the periodogram peaks corresponding to Teegarden b and c at 4.92 and 11.42 days are significantly recovered, whereas their counterparts in the activity indices are absent. We followed a more sophisticated approach and, using *kima*, modeled the planets together with the stellar signal. The preferred model with VIS and VIS+NIR datasets is the three-planet model with periods of 4.92, 11.42, and 25.95 days, yielding minimum masses and RV amplitudes consistent with previously reported values within uncertainties. With the NIR dataset, the highest-significance model includes only planets b and c, although in 7% of the 65000 considered samples, Teegarden's d is also detected. In all cases, the stellar rotation is properly modeled using Gaussian process regression.

We whitened the RV time series across all datasets, using the planetary signals and the stellar GP model, to build the detection maps. Planets b and c are clearly detectable in the VIS and VIS+NIR maps, and we found a high detection probability for Teegarden's d. To our knowledge, this is the first study to identify the three planetary companions of Teegarden's star using only CARMENES data (without additional data from any other instrument), in particular by combining VIS and NIR observations. Additionally, we constructed the differential detection map (i.e., the subtraction of one map from the other) for CARMENES NIR pre- and post-CARMENES-PLUS to evaluate the improvements achieved by this thesis. None of the 100-RVs time series have a significant detection of a planetary signal. Nevertheless, the detection probability limit significantly improves for the improved post-CARMENES-PLUS RV measurements, reaching a detection probability for planet b above 20%.

Ultimately, this thesis presents a comprehensive assessment of the advancements achieved with CARMENES NIR for radial velocity planet searches around ultracool dwarfs, together with the methodological tools required for such studies. The upgrades implemented in CARMENES-PLUS have substantially improved thermal and calibration stability, directly enhancing the instrument's precision. Additionally, the importance of incorporating limb-darkening in spectroscopic analyses of stellar rotation has been clearly demonstrated, yielding more accurate and reliable results. Finally, this work highlights the necessity of developing optimized RV techniques for the coolest and faintest stars, as well as the critical role of CARMENES-PLUS to improve the CARMENES NIR observations, which will ultimately help robustly detect and characterize Earth-like exoplanets orbiting ultracool-dwarf stars.

FUTURE WORK

As with any research line, there is still a lot of work to be done. As the CARMENES NIR was improved back in June 2022 and fully stabilized in February 2024, we still have to fully exploit its capacity. Because CARMENES started operating in 2016 and has been a legacy project since 2020, the post-CARMENES-PLUS configuration has not had many observations, and in some

targets of the CARMENES sample, it has none. Having campaigns focused on ultracool dwarfs can really demonstrate the NIR-enhanced performance and help detect and characterize exoplanets together with the VIS spectrograph.

The $v \sin i$ pipeline we provide can be further validated and tested. For example, a denser, wider grid of T_{eff} , $v \sin i$, and metallicities can help us understand the method's limits. It can also be tested with data from other facilities, in addition to CARMENES, and with F, G, or K stars, for example. We will further explore the advantages of combining VIS and NIR data, as well as weighting the spectral orders with their contribution to the final $v \sin i$ estimation.

We provide an analysis of Teegarden's system, but a deeper study can be carried out to better optimize the parameter space and model the planetary and activity signals using *kima* and similar tools. Moreover, reanalyzing the time series with telluric absorption-corrected spectra can significantly improve the results.

Nevertheless, Teegarden's star was selected first because it has three confirmed planets, hundreds of observations, and, in particular, more than 100 of them after C-PLUS, but it is not the ideal target to highlight the advantages of using NIR data over VIS. One of the main advantages of the NIR is the high S/N obtained for late M dwarfs, which is diluted for such a (relatively) bright star as Teegarden's. Thus, we will define a sample of ultracool dwarfs better suited for RV studies using NIR spectra. It will include fainter stars, possibly faster-rotating and more active stars than Teegarden's.

It will also be important to explore coordinated observing campaigns with complementary facilities. Joint RV campaigns with instruments such as NIRPS would increase the temporal sampling, improve the sensitivity to low-amplitude signals, and provide an independent check of the planetary origin of candidate signals through multi-instrument consistency. In parallel, photometric monitoring with facilities such as SPECULOOS would help identify transiting planets, constrain stellar rotation periods, and characterize activity indicators that are essential for interpreting RV variability in ultracool dwarfs. Such coordinated VIS, NIR, and photometric observations would therefore provide a more complete framework for detecting and characterizing planets around the faintest M dwarfs. This strategy is particularly relevant for targets suitable for atmospheric characterization with JWST, for which precise masses, reliable ephemerides, and a robust assessment of stellar activity are required.

PUBLICATIONS

This is a list of the publications I have contributed to during the thesis.

- Barkaoui, Khalid et al. (Dec. 2025). "TOI-7166 b: a habitable zone mini-Neptune planet around a nearby low-mass star." In: *MNRAS* 544.2, pp. 2637–2652. DOI: [10.1093/mnras/staf1807](https://doi.org/10.1093/mnras/staf1807). arXiv: [2512.06841](https://arxiv.org/abs/2512.06841) [astro-ph.EP].
- Gillon, Michaël et al. (July 2024). "Detection of an Earth-sized exoplanet orbiting the nearby ultracool dwarf star SPECULOOS-3." In: *Nature Astronomy* 8, pp. 865–878. DOI: [10.1038/s41550-024-02271-2](https://doi.org/10.1038/s41550-024-02271-2). arXiv: [2406.00794](https://arxiv.org/abs/2406.00794) [astro-ph.EP].
- Morello, G et al. (Jan. 2026). "The K-dwarfs Survey I. Four Validated Planets from the Radius Valley to the Neptune Desert." In: *Monthly Notices of the Royal Astronomical Society*, stag183. ISSN: 0035-8711. DOI: [10.1093/mnras/stag183](https://doi.org/10.1093/mnras/stag183). eprint: <https://academic.oup.com/mnras/advance-article-pdf/doi/10.1093/mnras/stag183/66590228/stag183.pdf>. URL: <https://doi.org/10.1093/mnras/stag183>.
- Peláez-Torres, A et al. (Apr. 2026). "A gem system with a lava world and a habitable zone sub-Neptune orbiting TOI-1752." In: *Monthly Notices of the Royal Astronomical Society*, stag713. ISSN: 0035-8711. DOI: [10.1093/mnras/stag713](https://doi.org/10.1093/mnras/stag713). eprint: <https://academic.oup.com/mnras/advance-article-pdf/doi/10.1093/mnras/stag713/68088278/stag713.pdf>. URL: <https://doi.org/10.1093/mnras/stag713>.
- Pozuelos, F. J. and R. Varas (Apr. 2026). *ravex: RAdial VELOCITY eXplorer*. DOI: [10.5281/zenodo.19797145](https://doi.org/10.5281/zenodo.19797145). URL: <https://doi.org/10.5281/zenodo.19797145>.
- Ruh, H. L. et al. (Dec. 2024). "The CARMENES search for exoplanets around M dwarfs: The impact of rotation and magnetic fields on the radial velocity jitter in cool stars." In: *A&A* 692, A138, A138. DOI: [10.1051/0004-6361/202450836](https://doi.org/10.1051/0004-6361/202450836). arXiv: [2412.07691](https://arxiv.org/abs/2412.07691) [astro-ph.EP].
- Varas, R. et al. (2025). "Improving radial velocity precision with CARMENES-PLUS." In: *Experimental Astronomy* 60.2, p. 10. ISSN: 1572-9508. DOI: [10.1007/s10686-025-10020-0](https://doi.org/10.1007/s10686-025-10020-0). URL: <https://doi.org/10.1007/s10686-025-10020-0>.
- Varas, R. et al. (2026). *The CARMENES search for exoplanets around M dwarfs. A homogeneous catalogue of projected rotational velocities accounting for limb-darkening*. arXiv: [2604.15428](https://arxiv.org/abs/2604.15428) [astro-ph.SR]. URL: <https://arxiv.org/abs/2604.15428>.

BIBLIOGRAPHY

- Adams, Fred C. and Konstantin Batygin (2022). “Analytic Approach to the Late Stages of Giant Planet Formation.” In: *The Astrophysical Journal* 934.2, p. 111. DOI: [10.3847/1538-4357/ac7a3e](https://doi.org/10.3847/1538-4357/ac7a3e). URL: <https://doi.org/10.3847/1538-4357/ac7a3e>.
- Aerts, C. (2021). “Probing the interior physics of stars through asteroseismology.” In: *Rev. Mod. Phys.* 93 (1), p. 015001. DOI: [10.1103/RevModPhys.93.015001](https://link.aps.org/doi/10.1103/RevModPhys.93.015001). URL: <https://link.aps.org/doi/10.1103/RevModPhys.93.015001>.
- Agol, Eric et al. (Feb. 2021). “Refining the Transit-timing and Photometric Analysis of TRAPPIST-1: Masses, Radii, Densities, Dynamics, and Ephemerides.” In: *PSJ* 2.1, 1, p. 1. DOI: [10.3847/PSJ/abd022](https://doi.org/10.3847/PSJ/abd022). arXiv: [2010.01074](https://arxiv.org/abs/2010.01074).
- Allard, F. (Jan. 2014). “The BT-Settl Model Atmospheres for Stars, Brown Dwarfs and Planets.” In: *Exploring the Formation and Evolution of Planetary Systems*. Ed. by Mark Booth, Brenda C. Matthews, and James R. Graham. Vol. 299. IAU Symposium, pp. 271–272. DOI: [10.1017/S1743921313008545](https://doi.org/10.1017/S1743921313008545).
- Allart, R., V. Bourrier, C. Lovis, D. Ehrenreich, J. J. Spake, A. Wyttenbach, L. Pino, F. Pepe, D. K. Sing, and A. Lecavelier des Etangs (Dec. 2018). “Spectrally resolved helium absorption from the extended atmosphere of a warm Neptune-mass exoplanet.” In: *Science* 362.6421, pp. 1384–1387. DOI: [10.1126/science.aat5879](https://doi.org/10.1126/science.aat5879). arXiv: [1812.02189](https://arxiv.org/abs/1812.02189) [astro-ph.EP].
- Allart, R. et al. (Oct. 2022). “Automatic model-based telluric correction for the ESPRESSO data reduction software. Model description and application to radial velocity computation.” In: *A&A* 666, A196, A196. DOI: [10.1051/0004-6361/202243629](https://doi.org/10.1051/0004-6361/202243629). arXiv: [2209.01296](https://arxiv.org/abs/2209.01296) [astro-ph.EP].
- Allen, Natalie H. et al. (Feb. 2026). “JWST TRAPPIST-1 e/b Program: Motivation and First Observations.” In: *AJ* 171.2, 105, p. 105. DOI: [10.3847/1538-3881/ae28cb](https://doi.org/10.3847/1538-3881/ae28cb). arXiv: [2512.07695](https://arxiv.org/abs/2512.07695) [astro-ph.EP].
- Allende Prieto, C., L. Koesterke, H.-G. Ludwig, B. Freytag, and E. Caffau (Feb. 2013). “Convective line shifts for the Gaia RVS from the CIFIST 3D model atmosphere grid.” In: *A&A* 550, A103, A103. DOI: [10.1051/0004-6361/201220064](https://doi.org/10.1051/0004-6361/201220064). arXiv: [1301.3703](https://arxiv.org/abs/1301.3703) [astro-ph.SR].
- Alonso-Floriano, F. J. et al. (May 2015). “CARMENES input catalogue of M dwarfs. I. Low-resolution spectroscopy with CAFOS.” In: *A&A* 577, A128, A128. DOI: [10.1051/0004-6361/201525803](https://doi.org/10.1051/0004-6361/201525803). arXiv: [1502.07580](https://arxiv.org/abs/1502.07580) [astro-ph.SR].
- An, Jiafu, Difang Huang, Chen Lin, and Mingzhu Tai (Mar. 2025). “Measuring gender and racial biases in large language models: Intersectional evidence from automated resume evaluation.” In: *PNAS Nexus* 4.3, pgafo89. ISSN: 2752-6542. DOI: [10.1093/pnasnexus/pgaf089](https://doi.org/10.1093/pnasnexus/pgaf089). eprint: <https://academic.oup.com/pnasnexus/article-pdf/4/3/pgaf089/62387232/pgaf089.pdf>. URL: <https://doi.org/10.1093/pnasnexus/pgaf089>.

- Anderson, G., A. Bradley, J. Kelley, J. Nelson, and H. Dougherty (1994). "HST: Pre-Servicing Mission Overview and Servicing Mission Results." In: *IFAC Proceedings Volumes* 27.13. IFAC Symposium on Automatic Control in Aerospace 1994, Palo Alto, CA, USA, 12-16 September 1994, pp. 297–302. ISSN: 1474-6670. DOI: [https://doi.org/10.1016/S1474-6670\(17\)45816-2](https://doi.org/10.1016/S1474-6670(17)45816-2). URL: <https://www.sciencedirect.com/science/article/pii/S1474667017458162>.
- Anglada-Escudé, Guillem et al. (Aug. 2016). "A terrestrial planet candidate in a temperate orbit around Proxima Centauri." In: *Nature* 536.7617, pp. 437–440. DOI: [10.1038/nature19106](https://doi.org/10.1038/nature19106). arXiv: [1609.03449](https://arxiv.org/abs/1609.03449) [astro-ph.EP].
- Anglada-Escudé, Guillem and R. Paul Butler (2012). "The HARPS-TERRA Project. I. Description of the Algorithms, Performance, and New Measurements on a Few Remarkable Stars Observed by HARPS." In: *The Astrophysical Journal Supplement Series* 200.2, p. 15. DOI: [10.1088/0067-0049/200/2/15](https://doi.org/10.1088/0067-0049/200/2/15). URL: <https://doi.org/10.1088/0067-0049/200/2/15>.
- Armitage, Philip J. (2020). *Astrophysics of planet formation, Second Edition*.
- Artigau, Étienne et al. (July 2014). "SPIRou: the near-infrared spectropolarimeter high-precision velocimeter for the Canada-France-Hawaii telescope." In: *Ground-based and Airborne Instrumentation for Astronomy V*. Ed. by Suzanne K. Ramsay, Ian S. McLean, and Hideki Takami. Vol. 9147. Society of Photo-Optical Instrumentation Engineers (SPIE) Conference Series, 914715, p. 914715. DOI: [10.1117/12.2055663](https://doi.org/10.1117/12.2055663). arXiv: [1406.6992](https://arxiv.org/abs/1406.6992) [astro-ph.IM].
- Artigau, Étienne et al. (July 2024). "NIRPS first light and early science: breaking the 1 m/s RV precision barrier at infrared wavelengths." In: *Ground-based and Airborne Instrumentation for Astronomy X*. Ed. by Julia J. Bryant, Kentaro Motohara, and Joël. R. D. Vernet. Vol. 13096. Society of Photo-Optical Instrumentation Engineers (SPIE) Conference Series, 130960C, p. 130960C. DOI: [10.1117/12.3018994](https://doi.org/10.1117/12.3018994). arXiv: [2406.08304](https://arxiv.org/abs/2406.08304) [astro-ph.IM].
- Artigau, Étienne et al. (2022). "Line-by-line Velocity Measurements: an Outlier-resistant Method for Precision Velocimetry." In: *The Astronomical Journal* 164.3, p. 84. DOI: [10.3847/1538-3881/ac7ce6](https://doi.org/10.3847/1538-3881/ac7ce6). URL: <https://doi.org/10.3847/1538-3881/ac7ce6>.
- Astudillo-Defru, N., X. Delfosse, X. Bonfils, T. Forveille, C. Lovis, and J. Rameau (Apr. 2017). "Magnetic activity in the HARPS M dwarf sample. The rotation-activity relationship for very low-mass stars through R'_{HK} ." In: *A&A* 600, A13, A13. DOI: [10.1051/0004-6361/201527078](https://doi.org/10.1051/0004-6361/201527078). arXiv: [1610.09007](https://arxiv.org/abs/1610.09007) [astro-ph.SR].
- Astudillo-Defru, N. et al. (Mar. 2015). "The HARPS search for southern extrasolar planets. XXXVI. Planetary systems and stellar activity of the M dwarfs GJ 3293, GJ 3341, and GJ 3543." In: *A&A* 575, A119, A119. DOI: [10.1051/0004-6361/201424253](https://doi.org/10.1051/0004-6361/201424253). arXiv: [1411.7048](https://arxiv.org/abs/1411.7048) [astro-ph.EP].
- Attia, M., V. Bourrier, P. Eggenberger, C. Mordasini, H. Beust, and D. Ehrenreich (Mar. 2021). "The JADE code: Coupling secular exoplanetary dynamics and photo-evaporation." In: *A&A* 647, A40, A40. DOI: [10.1051/0004-6361/202039452](https://doi.org/10.1051/0004-6361/202039452). arXiv: [2103.02627](https://arxiv.org/abs/2103.02627) [astro-ph.EP].

- Baranne, A., D. Queloz, M. Mayor, G. Adrianzyk, G. Knispel, D. Kohler, D. Lacroix, J.-P. Meunier, G. Rimbaud, and A. Vin (Oct. 1996). "ELODIE: A spectrograph for accurate radial velocity measurements." In: *A&As* 119, pp. 373–390.
- Barkaoui, K. et al. (July 2024). "Three short-period Earth-sized planets around M dwarfs discovered by TESS: TOI-5720 b, TOI-6008 b, and TOI-6086 b." In: *A&A* 687, A264, A264. DOI: [10.1051/0004-6361/202349127](https://doi.org/10.1051/0004-6361/202349127). arXiv: [2405.06350](https://arxiv.org/abs/2405.06350) [astro-ph.EP].
- Barkaoui, Khalid et al. (Dec. 2025). "TOI-7166 b: a habitable zone mini-Neptune planet around a nearby low-mass star." In: *MNRAS* 544.2, pp. 2637–2652. DOI: [10.1093/mnras/staf1807](https://doi.org/10.1093/mnras/staf1807). arXiv: [2512.06841](https://arxiv.org/abs/2512.06841) [astro-ph.EP].
- Barnes, J. R. et al. (Feb. 2014). "Precision radial velocities of 15 M5–M9 dwarfs." In: *Monthly Notices of the Royal Astronomical Society* 439.3, pp. 3094–3113. ISSN: 0035-8711. DOI: [10.1093/mnras/stu172](https://doi.org/10.1093/mnras/stu172). eprint: <https://academic.oup.com/mnras/article-pdf/439/3/3094/13764317/stu172.pdf>. URL: <https://doi.org/10.1093/mnras/stu172>.
- Barnes, Sydney A. (Mar. 2003). "On the Rotational Evolution of Solar- and Late-Type Stars, Its Magnetic Origins, and the Possibility of Stellar Gyrochronology." In: *APJ* 586.1, pp. 464–479. DOI: [10.1086/367639](https://doi.org/10.1086/367639). arXiv: [astro-ph/0303631](https://arxiv.org/abs/astro-ph/0303631) [astro-ph].
- Baroch, D. et al. (Sept. 2020). "The CARMENES search for exoplanets around M dwarfs. Convective shift and starspot constraints from chromatic radial velocities." In: *A&A* 641, A69, A69. DOI: [10.1051/0004-6361/202038213](https://doi.org/10.1051/0004-6361/202038213). arXiv: [2006.16608](https://arxiv.org/abs/2006.16608) [astro-ph.SR].
- Basant, Ritvik et al. (Mar. 2025). "Four Sub-Earth Planets Orbiting Barnard's Star from MAROON-X and ESPRESSO." In: *APJL* 982.1, L1, p. L1. DOI: [10.3847/2041-8213/adb8d5](https://doi.org/10.3847/2041-8213/adb8d5). arXiv: [2503.08095](https://arxiv.org/abs/2503.08095) [astro-ph.EP].
- Basri, Gibor (2021). *An Introduction to Stellar Magnetic Activity*. DOI: [10.1088/2514-3433/ac2956](https://doi.org/10.1088/2514-3433/ac2956).
- Bauer, F. F., M. Zechmeister, and A. Reiners (Sept. 2015). "Calibrating echelle spectrographs with Fabry-Pérot etalons." In: *A&A* 581, A117, A117. DOI: [10.1051/0004-6361/201526462](https://doi.org/10.1051/0004-6361/201526462). arXiv: [1506.07887](https://arxiv.org/abs/1506.07887) [astro-ph.IM].
- Bauer, F. F. et al. (2020). "The CARMENES search for exoplanets around M dwarfs - Measuring precise radial velocities in the near infrared: The example of the super-Earth CD Cet b." In: *A&A* 640, A50. DOI: [10.1051/0004-6361/202038031](https://doi.org/10.1051/0004-6361/202038031). URL: <https://doi.org/10.1051/0004-6361/202038031>.
- Becerril, S. et al. (July 2016). "CARMENES-NIR channel spectrograph cooling system AIV: thermo-mechanical performance of the instrument." In: *Advances in Optical and Mechanical Technologies for Telescopes and Instrumentation II*. Ed. by Ramón Navarro and James H. Burge. Vol. 9912. Society of Photo-Optical Instrumentation Engineers (SPIE) Conference Series, 991262, p. 991262. DOI: [10.1117/12.2232322](https://doi.org/10.1117/12.2232322).
- Becerril, S et al. (2017). "Performance and technical commissioning of an ultra-stable cooling system for a mid-range cryogenic astrophysical instrument (CARMENES-NIR)." In: *IOP Conference Series: Materials Science and Engi-*

- neering* 278.1, p. 012191. DOI: 10.1088/1757-899X/278/1/012191. URL: <https://dx.doi.org/10.1088/1757-899X/278/1/012191>.
- Beeck, B., R. H. Cameron, A. Reiners, and M. Schüssler (Oct. 2013a). “Three-dimensional simulations of near-surface convection in main-sequence stars. I. Overall structure.” In: *A&A* 558, A48, A48. DOI: 10.1051/0004-6361/201321343. arXiv: 1308.4874 [astro-ph.SR].
- Beeck, B., R. H. Cameron, A. Reiners, and M. Schüssler (Oct. 2013b). “Three-dimensional simulations of near-surface convection in main-sequence stars. II. Properties of granulation and spectral lines.” In: *A&A* 558, A49, A49. DOI: 10.1051/0004-6361/201321345. arXiv: 1308.4873 [astro-ph.SR].
- Benedict, G. F. et al. (2016). “The Solar Neighborhood. XXXVII. The Mass-Luminosity Relation For Main-Sequence M Dwarfs.” In: *The Astronomical Journal* 152.5, p. 141. DOI: 10.3847/0004-6256/152/5/141. URL: <https://doi.org/10.3847/0004-6256/152/5/141>.
- Benz, Arnold O. and Manuel Güdel (Sept. 2010). “Physical Processes in Magnetically Driven Flares on the Sun, Stars, and Young Stellar Objects.” In: *ARAA* 48, pp. 241–287. DOI: 10.1146/annurev-astro-082708-101757.
- Benz, W. et al. (Feb. 2021). “The CHEOPS mission.” In: *Experimental Astronomy* 51.1, pp. 109–151. DOI: 10.1007/s10686-020-09679-4. arXiv: 2009.11633 [astro-ph.IM].
- Birkby, J. L., R. J. de Kok, M. Brogi, E. J. W. de Mooij, H. Schwarz, S. Albrecht, and I. A. G. Snellen (Nov. 2013). “Detection of water absorption in the day side atmosphere of HD 189733 b using ground-based high-resolution spectroscopy at $3.2\mu\text{m}$.” In: *MNRAS* 436, pp. L35–L39. DOI: 10.1093/mnrasl/slt107. arXiv: 1307.1133 [astro-ph.EP].
- Bischoff, Richard, Markus Mugrauer, Guillermo Torres, Theresa Heyne, Oliver Lux, Vera Munz, Ralph Neuhauser, Susanne Hoffmann, and Anja Trepanovski (Nov. 2020). “Identification of young nearby runaway stars based on Gaia data and the lithium test.” In: *Astronomische Nachrichten* 341.9, pp. 908–942. DOI: 10.1002/asna.202013793. arXiv: 2009.02123 [astro-ph.SR].
- Bitsch, Bertram, Michiel Lambrechts, and Anders Johansen (Oct. 2015). “The growth of planets by pebble accretion in evolving protoplanetary discs.” In: *A&A* 582, A112, A112. DOI: 10.1051/0004-6361/201526463. arXiv: 1507.05209 [astro-ph.EP].
- Blain, Doriann, Alejandro Sánchez-López, and Paul Mollière (Apr. 2024). “A Formally Motivated Retrieval Framework Applied to the High-resolution Transmission Spectrum of HD 189733 b.” In: *AJ* 167.4, 179, p. 179. DOI: 10.3847/1538-3881/ad2c8b. arXiv: 2402.14001 [astro-ph.EP].
- Bochanski, John J., Suzanne L. Hawley, Kevin R. Covey, Andrew A. West, I. Neill Reid, David A. Golimowski, and Željko Ivezić (2010). “THE LUMINOSITY AND MASS FUNCTIONS OF LOW-MASS STARS IN THE GALACTIC DISK. II. THE FIELD.” In: *The Astronomical Journal* 139.6, p. 2679. DOI: 10.1088/0004-6256/139/6/2679. URL: <https://doi.org/10.1088/0004-6256/139/6/2679>.
- Bochanski, John J., Andrew A. West, Suzanne L. Hawley, and Kevin R. Covey (2007). “Low-Mass Dwarf Template Spectra from the Sloan Digital Sky

- Survey." In: *The Astronomical Journal* 133.2, p. 531. DOI: [10.1086/510240](https://doi.org/10.1086/510240). URL: <https://doi.org/10.1086/510240>.
- Bonfils, X. et al. (Oct. 2007). "The HARPS search for southern extra-solar planets. X. A $m \sin i = 11 M_{\oplus}$ planet around the nearby spotted M dwarf GJ 674." In: *A&A* 474.1, pp. 293–299. DOI: [10.1051/0004-6361:20077068](https://doi.org/10.1051/0004-6361/20077068). arXiv: [0704.0270](https://arxiv.org/abs/0704.0270) [astro-ph].
- Bonfils, X. et al. (Jan. 2013). "The HARPS search for southern extra-solar planets. XXXI. The M-dwarf sample." In: *A&A* 549, A109, A109. DOI: [10.1051/0004-6361/201014704](https://doi.org/10.1051/0004-6361/201014704). arXiv: [1111.5019](https://arxiv.org/abs/1111.5019) [astro-ph.EP].
- Borucki, William J. et al. (Feb. 2010). "Kepler Planet-Detection Mission: Introduction and First Results." In: *Science* 327.5968, p. 977. DOI: [10.1126/science.1185402](https://doi.org/10.1126/science.1185402).
- Boucher, Anne et al. (July 2023). "CO or no CO? Narrowing the CO abundance constraint and recovering the H₂O detection in the atmosphere of WASP-127 b using SPIRou." In: *MNRAS* 522.4, pp. 5062–5083. DOI: [10.1093/mnras/stad1247](https://doi.org/10.1093/mnras/stad1247). arXiv: [2303.03232](https://arxiv.org/abs/2303.03232) [astro-ph.EP].
- Bouchy, F., F. Pepe, and D. Queloz (Aug. 2001). "Fundamental photon noise limit to radial velocity measurements." In: *A&A* 374, pp. 733–739. DOI: [10.1051/0004-6361:20010730](https://doi.org/10.1051/0004-6361:20010730).
- Bouchy, Francois, Francois Wildi, and Jonay I. González Hernández (Sept. 2022). "The new Near-Infrared Adaptive-Optics assisted high-resolution NIRPS spectrograph on the ESO 3.6m." In: *European Planetary Science Congress, EPSC2022-937*, EPSC2022-937. DOI: [10.5194/epsc2022-937](https://doi.org/10.5194/epsc2022-937).
- Bouchy, François et al. (Aug. 2025). "NIRPS joining HARPS at ESO 3.6 m: On-sky performance and science objectives." In: *A&A* 700, A10, A10. DOI: [10.1051/0004-6361/202453341](https://doi.org/10.1051/0004-6361/202453341). arXiv: [2507.21767](https://arxiv.org/abs/2507.21767) [astro-ph.IM].
- Boutsikas, Efrosyni (Jan. 2014). "Handbook of Archaeoastronomy and Ethnoastronomy." In: 1573–1581. ISBN: 978-1-4614-6140-1. DOI: [10.1007/978-1-4614-6141-8](https://doi.org/10.1007/978-1-4614-6141-8).
- Boyajian, Tabettha S. et al. (Oct. 2012). "Stellar Diameters and Temperatures. II. Main-sequence K- and M-stars." In: *APJ* 757.2, 112, p. 112. DOI: [10.1088/0004-637X/757/2/112](https://doi.org/10.1088/0004-637X/757/2/112). arXiv: [1208.2431](https://arxiv.org/abs/1208.2431) [astro-ph.SR].
- Brewer, Brendon J., Livia B. Pártay, and Gábor Csányi (2011). "Diffusive nested sampling." In: *Statistics and Computing* 21.4, pp. 649–656. ISSN: 1573-1375. DOI: [10.1007/s11222-010-9198-8](https://doi.org/10.1007/s11222-010-9198-8). URL: <https://doi.org/10.1007/s11222-010-9198-8>.
- Brogi, M., M. Line, J. Bean, J.-M. Désert, and H. Schwarz (2017). "A Framework to Combine Low- and High-resolution Spectroscopy for the Atmospheres of Transiting Exoplanets." In: *The Astrophysical Journal Letters* 839.1, p. L2. DOI: [10.3847/2041-8213/aa6933](https://doi.org/10.3847/2041-8213/aa6933). URL: <https://doi.org/10.3847/2041-8213/aa6933>.
- Brogi, Matteo, Ignas A. G. Snellen, Remco J. de Kok, Simon Albrecht, Jayne Birkby, and Ernst J. W. de Mooij (June 2012). "The signature of orbital motion from the dayside of the planet τ Boötis b." In: *Nature* 486.7404, pp. 502–504. DOI: [10.1038/nature11161](https://doi.org/10.1038/nature11161). arXiv: [1206.6109](https://arxiv.org/abs/1206.6109) [astro-ph.EP].

- Brown, Nadia E, Yusaku Horiuchi, Mala Htun, and David Samuels (2020). "Gender gaps in perceptions of political science journals." In: *PS: Political Science & Politics* 53.1, pp. 114–121.
- Browning, Matthew K., Gibor Basri, Geoffrey W. Marcy, Andrew A. West, and Jiahao Zhang (Feb. 2010). "Rotation and Magnetic Activity in a Sample of M-Dwarfs." In: *AJ* 139.2, pp. 504–518. DOI: [10.1088/0004-6256/139/2/504](https://doi.org/10.1088/0004-6256/139/2/504).
- Bryant, Edward M. et al. (July 2025). "A transiting giant planet in orbit around a 0.2-solar-mass host star." In: *Nature Astronomy* 9, pp. 1031–1044. DOI: [10.1038/s41550-025-02552-4](https://doi.org/10.1038/s41550-025-02552-4). arXiv: [2506.07931](https://arxiv.org/abs/2506.07931) [astro-ph.EP].
- Buccino, Andrea P., Rodrigo F. Díaz, María Luisa Luoni, Ximena C. Abrevaya, and Pablo J. D. Mauas (2010). "Long-Term Chromospheric Activity In Southern M Dwarfs: Gl 229 And Gl 752 A." In: *The Astronomical Journal* 141.2, p. 34. DOI: [10.1088/0004-6256/141/2/34](https://doi.org/10.1088/0004-6256/141/2/34). URL: <https://doi.org/10.1088/0004-6256/141/2/34>.
- Buccino, Andrea P., Guillermo A. Lemarchand, and Pablo J.D. Mauas (2007). "UV habitable zones around M stars." In: *Icarus* 192.2, pp. 582–587. ISSN: 0019-1035. DOI: <https://doi.org/10.1016/j.icarus.2007.08.012>. URL: www.sciencedirect.com/science/article/pii/S0019103507003521.
- Burn, R., M. Schlecker, C. Mordasini, A. Emsenhuber, Y. Alibert, T. Henning, H. Klahr, and W. Benz (Dec. 2021). "The New Generation Planetary Population Synthesis (NGPPS). IV. Planetary systems around low-mass stars." In: *A&A* 656, A72, A72. DOI: [10.1051/0004-6361/202140390](https://doi.org/10.1051/0004-6361/202140390). arXiv: [2105.04596](https://arxiv.org/abs/2105.04596) [astro-ph.EP].
- Burrows, S. M., O. Ogunro, A. A. Frossard, L. M. Russell, P. J. Rasch, and S. M. Elliott (2014). "A physically based framework for modeling the organic fractionation of sea spray aerosol from bubble film Langmuir equilibria." In: *Atmospheric Chemistry and Physics* 14.24, pp. 13601–13629. DOI: [10.5194/acp-14-13601-2014](https://doi.org/10.5194/acp-14-13601-2014). URL: <https://acp.copernicus.org/articles/14/13601/2014/>.
- Burt, Jennifer A., Xavier Dumusque, and Samuel Halverson (Nov. 2025). "Precise Radial Velocities." In: *arXiv e-prints*, arXiv:2511.01954, arXiv:2511.01954. DOI: [10.48550/arXiv.2511.01954](https://doi.org/10.48550/arXiv.2511.01954). arXiv: [2511.01954](https://arxiv.org/abs/2511.01954) [astro-ph.EP].
- Butler, R. P., G. W. Marcy, E. Williams, C. McCarthy, P. Dosanjh, and S. S. Vogt (June 1996). "Attaining Doppler Precision of 3 M s⁻¹." In: *PASP* 108, p. 500. DOI: [10.1086/133755](https://doi.org/10.1086/133755).
- Butler, R. Paul, Geoffrey W. Marcy, Debra A. Fischer, Timothy M. Brown, Adam R. Contos, Sylvain G. Korzennik, Peter Nisenson, and Robert W. Noyes (Dec. 1999). "Evidence for Multiple Companions to *v* Andromedae." In: *APJ* 526.2, pp. 916–927. DOI: [10.1086/308035](https://doi.org/10.1086/308035).
- Butters, O. W. et al. (Sept. 2010). "The first WASP public data release." In: *A&A* 520, L10, p. L10. DOI: [10.1051/0004-6361/201015655](https://doi.org/10.1051/0004-6361/201015655). arXiv: [1009.5306](https://arxiv.org/abs/1009.5306) [astro-ph.EP].
- Caballero, J. A. et al. (July 2016). "CARMENES: data flow." In: *Observatory Operations: Strategies, Processes, and Systems VI*. Ed. by Alison B. Peck, Robert L. Seaman, and Chris R. Benn. Vol. 9910. Society of Photo-Optical In-

- strumentation Engineers (SPIE) Conference Series, 99100E, 99100E. DOI: [10.1117/12.2233574](https://doi.org/10.1117/12.2233574).
- Caballero, J. A. et al. (Mar. 2017). “Carmencita, the CARMENES Cool dwarf Information and daTa Archive.” In: *Highlights on Spanish Astrophysics IX*. Ed. by S. Arribas, A. Alonso-Herrero, F. Figueras, C. Hernández-Monteagudo, A. Sánchez-Lavega, and S. Pérez-Hoyos, pp. 496–496.
- Cannon, Annie J. and Edward C. Pickering (Jan. 1918). “The Henry Draper catalogue oh, 1h, 2h, and 3h.” In: *Annals of Harvard College Observatory* 91, pp. 1–290.
- Canocchi, G., G. Morello, K. Lind, I. Carleo, M. Stangret, and E. Pallé (Dec. 2024). “Probing Na in giant exoplanets with ESPRESSO and 3D NLTE stellar spectra.” In: *A&A* 692, A43, A43. DOI: [10.1051/0004-6361/202451972](https://doi.org/10.1051/0004-6361/202451972). arXiv: [2410.15810](https://arxiv.org/abs/2410.15810) [astro-ph.EP].
- Carvalho, Adolfo and Christopher M. Johns-Krull (May 2023). “A Simple Code for Rotational Broadening of Broad Wavelength Range High-Dispersion Spectra.” In: *Research Notes of the American Astronomical Society* 7.5, 91, p. 91. DOI: [10.3847/2515-5172/acd37e](https://doi.org/10.3847/2515-5172/acd37e). arXiv: [2305.09693](https://arxiv.org/abs/2305.09693) [astro-ph.IM].
- Casasayas-Barris, N. et al. (Mar. 2021). “The atmosphere of HD 209458b seen with ESPRESSO. No detectable planetary absorptions at high resolution.” In: *A&A* 647, A26, A26. DOI: [10.1051/0004-6361/202039539](https://doi.org/10.1051/0004-6361/202039539). arXiv: [2101.04094](https://arxiv.org/abs/2101.04094) [astro-ph.EP].
- Castelli, F. and R. L. Kurucz (Jan. 2003). “New Grids of ATLAS9 Model Atmospheres.” In: *Modelling of Stellar Atmospheres*. Ed. by N. Piskunov, W. W. Weiss, and D. F. Gray. Vol. 210. IAU Symposium, A20. DOI: [10.48550/arXiv.astro-ph/0405087](https://doi.org/10.48550/arXiv.astro-ph/0405087). arXiv: [astro-ph/0405087](https://arxiv.org/abs/astro-ph/0405087) [astro-ph].
- Chachan, Yayaati et al. (2019). “A Hubble PanCET Study of HAT-P-11b: A Cloudy Neptune with a Low Atmospheric Metallicity.” In: *The Astronomical Journal* 158.6, p. 244. DOI: [10.3847/1538-3881/ab4e9a](https://doi.org/10.3847/1538-3881/ab4e9a). URL: <https://doi.org/10.3847/1538-3881/ab4e9a>.
- Chaplin, W. J., H. M. Cegla, C. A. Watson, G. R. Davies, and W. H. Ball (Apr. 2019). “Filtering Solar-Like Oscillations for Exoplanet Detection in Radial Velocity Observations.” In: *AJ* 157.4, 163, p. 163. DOI: [10.3847/1538-3881/ab0c01](https://doi.org/10.3847/1538-3881/ab0c01). arXiv: [1903.00657](https://arxiv.org/abs/1903.00657) [astro-ph.SR].
- Charbonneau, David, Timothy M. Brown, Robert W. Noyes, and Ronald L. Gilliland (Mar. 2002). “Detection of an Extrasolar Planet Atmosphere.” In: *APJ* 568.1, pp. 377–384. DOI: [10.1086/338770](https://doi.org/10.1086/338770). arXiv: [astro-ph/0111544](https://arxiv.org/abs/astro-ph/0111544) [astro-ph].
- Charbonneau, David et al. (June 2005). “Detection of Thermal Emission from an Extrasolar Planet.” In: *APJ* 626.1, pp. 523–529. DOI: [10.1086/429991](https://doi.org/10.1086/429991). arXiv: [astro-ph/0503457](https://arxiv.org/abs/astro-ph/0503457) [astro-ph].
- Chauvin, G., A.-M. Lagrange, C. Dumas, B. Zuckerman, D. Mouillet, I. Song, J.-L. Beuzit, and P. Lowrance (Oct. 2004). “A giant planet candidate near a young brown dwarf. Direct VLT/NACO observations using IR wavefront sensing.” In: *A&A* 425, pp. L29–L32. DOI: [10.1051/0004-6361:200400056](https://doi.org/10.1051/0004-6361:200400056). arXiv: [astro-ph/0409323](https://arxiv.org/abs/astro-ph/0409323) [astro-ph].

- Chubb, Katy L., Michiel Min, Yui Kawashima, Christiane Helling, and Ingo Waldmann (July 2020). "Aluminium oxide in the atmosphere of hot Jupiter WASP-43b." In: *A&A* 639, A3, A3. DOI: [10.1051/0004-6361/201937267](https://doi.org/10.1051/0004-6361/201937267). arXiv: [2004.13679](https://arxiv.org/abs/2004.13679) [astro-ph.EP].
- Cifuentes, C. et al. (Oct. 2020). "CARMENES input catalogue of M dwarfs. V. Luminosities, colours, and spectral energy distributions." In: *A&A* 642, A115, A115. DOI: [10.1051/0004-6361/202038295](https://doi.org/10.1051/0004-6361/202038295). arXiv: [2007.15077](https://arxiv.org/abs/2007.15077) [astro-ph.SR].
- Cifuentes, C. et al. (Jan. 2025). "CARMENES input catalogue of M dwarfs: IX. Multiplicity from close spectroscopic binaries to ultra-wide systems." In: *A&A* 693, A228, A228. DOI: [10.1051/0004-6361/202452527](https://doi.org/10.1051/0004-6361/202452527). arXiv: [2412.12264](https://arxiv.org/abs/2412.12264) [astro-ph.SR].
- Claret, A. (Nov. 2000). "A new non-linear limb-darkening law for LTE stellar atmosphere models. Calculations for $-5.0 \leq \log[M/H] \leq +1$, $2000 \text{ K} \leq T_{\text{eff}} \leq 50000 \text{ K}$ at several surface gravities." In: *A&A* 363, pp. 1081–1190.
- Claret, A., P. H. Hauschildt, and G. Torres (July 2025). "Limb-darkening coefficients for four-term and power-2 laws for the JWST mission adopting spherical PHOENIX models at high resolution: NIRCcam, NIRISS, and NIRSpec passbands." In: *A&A* 699, A97, A97. DOI: [10.1051/0004-6361/202554770](https://doi.org/10.1051/0004-6361/202554770). arXiv: [2506.07265](https://arxiv.org/abs/2506.07265) [astro-ph.SR].
- Claudi, R. et al. (Aug. 2017). "GIARPS@TNG: GIANO-B and HARPS-N together for a wider wavelength range spectroscopy." In: *European Physical Journal Plus* 132.8, 364, p. 364. DOI: [10.1140/epjp/i2017-11647-9](https://doi.org/10.1140/epjp/i2017-11647-9). arXiv: [1707.04553](https://arxiv.org/abs/1707.04553) [astro-ph.IM].
- Collins, Patricia Hill (Dec. 1986). "Learning from the Outsider Within: The Sociological Significance of Black Feminist Thought*." In: *Social Problems* 33.6, s14–s32. ISSN: 0037-7791. DOI: [10.2307/800672](https://doi.org/10.2307/800672). eprint: <https://academic.oup.com/socpro/article-pdf/33/6/s14/4565137/socpro33-0s14.pdf>. URL: <https://doi.org/10.2307/800672>.
- Cont, D. et al. (Dec. 2022). "Atmospheric characterization of the ultra-hot Jupiter WASP-33b. Detection of Ti and V emission lines and retrieval of a broadened line profile." In: *A&A* 668, A53, A53. DOI: [10.1051/0004-6361/202244277](https://doi.org/10.1051/0004-6361/202244277). arXiv: [2209.10618](https://arxiv.org/abs/2209.10618) [astro-ph.EP].
- Cont, D. et al. (Aug. 2024). "Exploring the ultra-hot Jupiter WASP-178b. Constraints on atmospheric chemistry and dynamics from a joint retrieval of VLT/CRIRES+ and space photometric data." In: *A&A* 688, A206, A206. DOI: [10.1051/0004-6361/202450064](https://doi.org/10.1051/0004-6361/202450064). arXiv: [2406.08166](https://arxiv.org/abs/2406.08166) [astro-ph.EP].
- Cont, D. et al. (June 2025). "Retrieving day- and nightside atmospheric properties of the ultra-hot Jupiter TOI-2109b: Detection of Fe and CO emission lines and evidence for inefficient heat transport." In: *A&A* 698, A31, A31. DOI: [10.1051/0004-6361/202554572](https://doi.org/10.1051/0004-6361/202554572). arXiv: [2504.15757](https://arxiv.org/abs/2504.15757) [astro-ph.EP].
- Cook, Neil James et al. (2022). "APER0: A PipelinE to Reduce Observations—Demonstration with SPIRou." In: *Publications of the Astronomical Society of the Pacific* 134.1041, p. 114509. DOI: [10.1088/1538-3873/ac9e74](https://doi.org/10.1088/1538-3873/ac9e74). URL: <https://doi.org/10.1088/1538-3873/ac9e74>.

- Cortés-Contreras, M. et al. (Dec. 2024). “CARMENES input catalogue of M dwarfs: VIII. Kinematics in the solar neighbourhood.” In: *A&A* 692, A206, A206. DOI: [10.1051/0004-6361/202451585](https://doi.org/10.1051/0004-6361/202451585). arXiv: [2411.06825](https://arxiv.org/abs/2411.06825).
- Cortés-Zuleta, P. et al. (May 2023). “Optical and near-infrared stellar activity characterization of the early M dwarf Gl 205 with SOPHIE and SPIRou.” In: *A&A* 673, A14, A14. DOI: [10.1051/0004-6361/202245131](https://doi.org/10.1051/0004-6361/202245131). arXiv: [2301.10614](https://arxiv.org/abs/2301.10614) [[astro-ph.SR](#)].
- Covey, K. R. et al. (Dec. 2007). “Stellar SEDs from 0.3 to 2.5 μm : Tracing the Stellar Locus and Searching for Color Outliers in the SDSS and 2MASS.” In: *AJ* 134.6, pp. 2398–2417. DOI: [10.1086/522052](https://doi.org/10.1086/522052). arXiv: [0707.4473](https://arxiv.org/abs/0707.4473) [[astro-ph](#)].
- Crossfield, Ian J. M. et al. (Sept. 2022). “GJ 1252b: A Hot Terrestrial Super-Earth with No Atmosphere.” In: *APJL* 937.1, L17, p. L17. DOI: [10.3847/2041-8213/ac886b](https://doi.org/10.3847/2041-8213/ac886b). arXiv: [2208.09479](https://arxiv.org/abs/2208.09479) [[astro-ph.EP](#)].
- Czekala, Ian, Kaisey S. Mandel, Sean M. Andrews, Jason A. Dittmann, Sujit K. Ghosh, Benjamin T. Montet, and Elisabeth R. Newton (May 2017). “Disentangling Time-series Spectra with Gaussian Processes: Applications to Radial Velocity Analysis.” In: *APJ* 840.1, 49, p. 49. DOI: [10.3847/1538-4357/aa6aab](https://doi.org/10.3847/1538-4357/aa6aab). arXiv: [1702.05652](https://arxiv.org/abs/1702.05652) [[astro-ph.SR](#)].
- Dai, Ziqi, Dong Ni, Lizhuang Pan, and Yiheng Zhu (2021). “Five Methods of Exoplanet Detection.” In: *Journal of Physics: Conference Series* 2012.1, p. 012135. DOI: [10.1088/1742-6596/2012/1/012135](https://doi.org/10.1088/1742-6596/2012/1/012135). URL: <https://doi.org/10.1088/1742-6596/2012/1/012135>.
- Deibert, Emily K., Ernst J. W. de Mooij, Ray Jayawardhana, Jonathan J. Fortney, Matteo Brogi, Zafar Rustamkulov, and Motohide Tamura (Feb. 2019). “High-resolution Transit Spectroscopy of Warm Saturns.” In: *AJ* 157.2, 58, p. 58. DOI: [10.3847/1538-3881/aaf56b](https://doi.org/10.3847/1538-3881/aaf56b). arXiv: [1812.02748](https://arxiv.org/abs/1812.02748) [[astro-ph.EP](#)].
- Delfosse, X., T. Forveille, C. Perrier, and M. Mayor (Mar. 1998). “Rotation and chromospheric activity in field M dwarfs.” In: *A&A* 331, pp. 581–595.
- Delfosse, X., T. Forveille, D. Ségransan, J.-L. Beuzit, S. Udry, C. Perrier, and M. Mayor (Dec. 2000). “Accurate masses of very low mass stars. IV. Improved mass-luminosity relations.” In: *A&A* 364, pp. 217–224. DOI: [10.48550/arXiv.astro-ph/0010586](https://doi.org/10.48550/arXiv.astro-ph/0010586). arXiv: [astro-ph/0010586](https://arxiv.org/abs/astro-ph/0010586) [[astro-ph](#)].
- Delorme, P., A. Collier Cameron, L. Hebb, J. Rostron, T. A. Lister, A. J. Norton, D. Pollacco, and R. G. West (May 2011). “Stellar rotation in the Hyades and Praesepe: gyrochronology and braking time-scale.” In: *Monthly Notices of the Royal Astronomical Society* 413.3, pp. 2218–2234. ISSN: 0035-8711. DOI: [10.1111/j.1365-2966.2011.18299.x](https://doi.org/10.1111/j.1365-2966.2011.18299.x). eprint: <https://academic.oup.com/mnras/article-pdf/413/3/2218/2907412/mnras0413-2218.pdf>. URL: <https://doi.org/10.1111/j.1365-2966.2011.18299.x>.
- Delrez, L. et al. (Nov. 2022). “Two temperate super-Earths transiting a nearby late-type M dwarf.” In: *A&A* 667, A59, A59. DOI: [10.1051/0004-6361/202244041](https://doi.org/10.1051/0004-6361/202244041). arXiv: [2209.02831](https://arxiv.org/abs/2209.02831) [[astro-ph.EP](#)].
- Deming, Drake and Sara Seager (Jan. 2017). “Illusion and Reality in the Atmospheres of Exoplanets.” In: *arXiv e-prints*, arXiv:1701.00493, arXiv:1701.00493. DOI: [10.48550/arXiv.1701.00493](https://doi.org/10.48550/arXiv.1701.00493). arXiv: [1701.00493](https://arxiv.org/abs/1701.00493) [[astro-ph.EP](#)].

- Deming, Drake, Sara Seager, L. Jeremy Richardson, and Joseph Harrington (Mar. 2005). "Infrared radiation from an extrasolar planet." In: *Nature* 434-7034, pp. 740–743. DOI: [10.1038/nature03507](https://doi.org/10.1038/nature03507). arXiv: [astro-ph/0503554](https://arxiv.org/abs/astro-ph/0503554) [astro-ph].
- Diaz-Cordoves, J. and A. Gimenez (June 1992). "A new nonlinear approximation to the limb-darkening of hot stars." In: *A&A* 259.1, pp. 227–231.
- Dieterich, Sergio B (Sept. 2014). *Understanding the Boundary Between Stars and Substellar Objects in the Solar Neighborhood*. NSF Award Number 1400680. Directorate for Mathematical and Physical Sciences, Division Of Astronomical Sciences. 2014.
- Díez Alonso, E. et al. (Jan. 2019). "CARMENES input catalogue of M dwarfs. IV. New rotation periods from photometric time series." In: *A&A* 621, A126, A126. DOI: [10.1051/0004-6361/201833316](https://doi.org/10.1051/0004-6361/201833316). arXiv: [1810.03338](https://arxiv.org/abs/1810.03338) [astro-ph.SR].
- Dion, Michelle L, Jane Lawrence Sumner, and Sara McLaughlin Mitchell (2018). "Gendered citation patterns across political science and social science methodology fields." In: *Political analysis* 26.3, pp. 312–327.
- Djupe, Paul A, Amy Erica Smith, and Anand Edward Sokhey (2019). "Explaining gender in the journals: How submission practices affect publication patterns in political science." In: *PS: Political Science & Politics* 52.1, pp. 71–77.
- Domagal-Goldman, Shawn D., Julie Crooke, and Courtney Dressing (Dec. 2023). "The Habitable Worlds Observatory: Progress, Future Plans, and Opportunities for Community Participation." In: *AGU Fall Meeting Abstracts*. Vol. 2023. AGU Fall Meeting Abstracts, P23D-3088, P23D-3088.
- Donati, J.-F. et al. (Nov. 2020). "SPIRou: NIR velocimetry and spectropolarimetry at the CFHT." In: *MNRAS* 498.4, pp. 5684–5703. DOI: [10.1093/mnras/staa2569](https://doi.org/10.1093/mnras/staa2569). arXiv: [2008.08949](https://arxiv.org/abs/2008.08949) [astro-ph.IM].
- Dorn, Caroline, Julia Venturini, Amir Khan, Kevin Heng, Yann Alibert, Ravit Helled, Attilio Rivoldini, and Willy Benz (Jan. 2017). "A generalized Bayesian inference method for constraining the interiors of super Earths and sub-Neptunes." In: *A&A* 597, A37, A37. DOI: [10.1051/0004-6361/201628708](https://doi.org/10.1051/0004-6361/201628708). arXiv: [1609.03908](https://arxiv.org/abs/1609.03908) [astro-ph.IM].
- Dorn, R. J. et al. (Mar. 2023). "CRIRES⁺ on sky at the ESO Very Large Telescope. Observing the Universe at infrared wavelengths and high spectral resolution." In: *A&A* 671, A24, A24. DOI: [10.1051/0004-6361/202245217](https://doi.org/10.1051/0004-6361/202245217).
- Dreizler, S. et al. (Apr. 2024). "Teegarden's Star revisited. A nearby planetary system with at least three planets." In: *A&A* 684, A117, A117. DOI: [10.1051/0004-6361/202348033](https://doi.org/10.1051/0004-6361/202348033). arXiv: [2402.00923](https://arxiv.org/abs/2402.00923) [astro-ph.EP].
- Dumusque, X., I. Boisse, and N. C. Santos (Dec. 2014). "SOAP 2.0: A Tool to Estimate the Photometric and Radial Velocity Variations Induced by Stellar Spots and Plages." In: *APJ* 796.2, 132, p. 132. DOI: [10.1088/0004-637X/796/2/132](https://doi.org/10.1088/0004-637X/796/2/132). arXiv: [1409.3594](https://arxiv.org/abs/1409.3594) [astro-ph.SR].
- Dumusque, Xavier, Nuno C. Santos, Stéphane Udry, Christophe Lovis, and Xavier Bonfils (Nov. 2011). "Stellar noise and planet detection. I. Oscillations, granulation and sun-like spots." In: *The Astrophysics of Planetary Systems*:

- Formation, Structure, and Dynamical Evolution*. Ed. by Alessandro Sozzetti, Mario G. Lattanzi, and Alan P. Boss. Vol. 276. IAU Symposium, pp. 527–529. DOI: [10.1017/S1743921311021089](https://doi.org/10.1017/S1743921311021089). arXiv: [1011.5579](https://arxiv.org/abs/1011.5579) [astro-ph.EP].
- Dupuy, Trent J. and Michael C. Liu (2017). “Individual Dynamical Masses of Ultracool Dwarfs.” In: *The Astrophysical Journal Supplement Series* 231.2, p. 15. DOI: [10.3847/1538-4365/aa5e4c](https://doi.org/10.3847/1538-4365/aa5e4c). URL: <https://doi.org/10.3847/1538-4365/aa5e4c>.
- Endl, M., M. Kürster, and S. Els (Oct. 2000). “The planet search program at the ESO Coudé Echelle spectrometer. I. Data modeling technique and radial velocity precision tests.” In: *A&A* 362, pp. 585–594.
- Espinoza, Néstor and Marshall D. Perrin (May 2025). “Highlights from Exoplanet Observations by the James Webb Space Telescope.” In: *arXiv e-prints*, arXiv:2505.20520, arXiv:2505.20520. DOI: [10.48550/arXiv.2505.20520](https://doi.org/10.48550/arXiv.2505.20520). arXiv: [2505.20520](https://arxiv.org/abs/2505.20520) [astro-ph.EP].
- Evans, Thomas M., David K. Sing, Hannah R. Wakeford, Nikolay Nikolov, Gilda E. Ballester, Benjamin Drummond, Tiffany Kataria, Neale P. Gibson, David S. Amundsen, and Jessica Spake (May 2016). “Detection of H₂O and Evidence for TiO/VO in an Ultra-hot Exoplanet Atmosphere.” In: *APJL* 822.1, L4, p. L4. DOI: [10.3847/2041-8205/822/1/L4](https://doi.org/10.3847/2041-8205/822/1/L4). arXiv: [1604.02310](https://arxiv.org/abs/1604.02310) [astro-ph.EP].
- Eyring, V., S. Bony, G. A. Meehl, C. A. Senior, B. Stevens, R. J. Stouffer, and K. E. Taylor (2016). “Overview of the Coupled Model Intercomparison Project Phase 6 (CMIP6) experimental design and organization.” In: *Geoscientific Model Development* 9.5, pp. 1937–1958. DOI: [10.5194/gmd-9-1937-2016](https://doi.org/10.5194/gmd-9-1937-2016). URL: <https://gmd.copernicus.org/articles/9/1937/2016/>.
- Faria, J. P., N. C. Santos, P. Figueira, and B. J. Brewer (June 2018). “kima: Exoplanet detection in radial velocities.” In: *The Journal of Open Source Software* 3.26, p. 487. DOI: [10.21105/joss.00487](https://doi.org/10.21105/joss.00487). arXiv: [1806.08305](https://arxiv.org/abs/1806.08305) [astro-ph.IM].
- Faria, J. P. et al. (Feb. 2022). “A candidate short-period sub-Earth orbiting Proxima Centauri.” In: *A&A* 658, A115, A115. DOI: [10.1051/0004-6361/202142337](https://doi.org/10.1051/0004-6361/202142337). arXiv: [2202.05188](https://arxiv.org/abs/2202.05188) [astro-ph.EP].
- Fernández Izquierdo, Patricia, Jean Louis Lizon, Miguel Á. Núñez Cagigal, Jesús Patrón Recio, Maria Barreto Cabrera, and Francisco Garzón López (July 2014). “Tests and procedures for optimizing EMIR cooling system.” In: *Ground-based and Airborne Instrumentation for Astronomy V*. Ed. by Suzanne K. Ramsay, Ian S. McLean, and Hideki Takami. Vol. 9147. Society of Photo-Optical Instrumentation Engineers (SPIE) Conference Series, 91474H, 91474H. DOI: [10.1117/12.2055811](https://doi.org/10.1117/12.2055811).
- Figueira, P., N. C. Santos, F. Pepe, C. Lovis, and N. Nardetto (Sept. 2013). “Line-profile variations in radial-velocity measurements. Two alternative indicators for planetary searches.” In: *A&A* 557, A93, A93. DOI: [10.1051/0004-6361/201220779](https://doi.org/10.1051/0004-6361/201220779). arXiv: [1307.7279](https://arxiv.org/abs/1307.7279) [astro-ph.EP].
- Figueira, P. et al. (Aug. 2025). “A comprehensive study on radial velocity signals using ESPRESSO: Pushing precision to the 10 cm/s level.” In: *A&A* 700,

- A174, A174. DOI: 10.1051/0004-6361/202553869. arXiv: 2507.07514 [astro-ph.EP].
- Fischer, Debra A. and Jeff Valenti (2005). "The Planet-Metallicity Correlation*." In: *The Astrophysical Journal* 622.2, p. 1102. DOI: 10.1086/428383. URL: <https://doi.org/10.1086/428383>.
- Flowers, Erin, Matteo Brogi, Emily Rauscher, Eliza M.-R. Kempton, and Andrea Chiavassa (May 2019). "The High-resolution Transmission Spectrum of HD 189733b Interpreted with Atmospheric Doppler Shifts from Three-dimensional General Circulation Models." In: *AJ* 157.5, 209, p. 209. DOI: 10.3847/1538-3881/ab164c. arXiv: 1810.06099 [astro-ph.EP].
- Forget, François, Frédéric Hourdin, and Olivier Talagrand (1998). "CO₂Snowfall on Mars: Simulation with a General Circulation Model." In: *Icarus* 131.2, pp. 302–316. ISSN: 0019-1035. DOI: <https://doi.org/10.1006/icar.1997.5874>. URL: <https://www.sciencedirect.com/science/article/pii/S0019103597958747>.
- Fuentes, Agustín (2024). "Scientists as political advocates." In: *Science* 386.6724, eadt7194. DOI: 10.1126/science.adt7194. eprint: <https://www.science.org/doi/pdf/10.1126/science.adt7194>. URL: <https://www.science.org/doi/abs/10.1126/science.adt7194>.
- Fulton, Benjamin J. et al. (Sept. 2017). "The California-Kepler Survey. III. A Gap in the Radius Distribution of Small Planets." In: *The Astronomical Journal* 154.3, 109, p. 109. DOI: 10.3847/1538-3881/aa80eb. arXiv: 1703.10375 [astro-ph.EP].
- Gaia Collaboration et al. (Nov. 2016a). "Gaia Data Release 1. Summary of the astrometric, photometric, and survey properties." In: *A&A* 595, A2, A2. DOI: 10.1051/0004-6361/201629512. arXiv: 1609.04172 [astro-ph.IM].
- Gaia Collaboration et al. (Nov. 2016b). "The Gaia mission." In: *A&A* 595, A1, A1. DOI: 10.1051/0004-6361/201629272. arXiv: 1609.04153 [astro-ph.IM].
- Gaia Collaboration et al. (Aug. 2018). "Gaia Data Release 2. Observational Hertzsprung-Russell diagrams." In: *A&A* 616, A10, A10. DOI: 10.1051/0004-6361/201832843. arXiv: 1804.09378 [astro-ph.SR].
- Gaia Collaboration et al. (May 2021). "Gaia Early Data Release 3. Summary of the contents and survey properties." In: *A&A* 649, A1, A1. DOI: 10.1051/0004-6361/202039657. arXiv: 2012.01533 [astro-ph.GA].
- García Dauder, Dau and Marisa G. Ruiz Trejo (2021). "Un viaje por las emociones en procesos de investigación feminista." In: *Empiria. Revista de metodología de ciencias sociales* 50, 21–41. DOI: 10.5944/empiria.50.2021.30370. URL: <https://revistas.uned.es/index.php/empiria/article/view/30370>.
- Giacobbe, Paolo et al. (Apr. 2021). "Five carbon- and nitrogen-bearing species in a hot giant planet's atmosphere." In: *Nature* 592.7853, pp. 205–208. DOI: 10.1038/s41586-021-03381-x. arXiv: 2104.03352 [astro-ph.EP].
- Gibson, Neale P. et al. (Apr. 2020). "Detection of Fe I in the atmosphere of the ultra-hot Jupiter WASP-121b, and a new likelihood-based approach for Doppler-resolved spectroscopy." In: *MNRAS* 493.2, pp. 2215–2228. DOI: 10.1093/mnras/staa228. arXiv: 2001.06430 [astro-ph.EP].

- Gibson, Steven R. et al. (July 2024). "System design of the Keck Planet Finder." In: *Ground-based and Airborne Instrumentation for Astronomy X*. Ed. by Julia J. Bryant, Kentaro Motohara, and Joël. R. D. Vernet. Vol. 13096. Society of Photo-Optical Instrumentation Engineers (SPIE) Conference Series, 1309609, p. 1309609. DOI: [10.1117/12.3017841](https://doi.org/10.1117/12.3017841).
- Gillon, M., E. Jehin, P. Magain, V. Chantry, D. Hutsemékers, J. Manfroid, D. Queloz, and S. Udry (Feb. 2011). "TRAPPIST: a robotic telescope dedicated to the study of planetary systems." In: *European Physical Journal Web of Conferences*. Vol. 11. European Physical Journal Web of Conferences. EDP, 06002, p. 06002. DOI: [10.1051/epjconf/20101106002](https://doi.org/10.1051/epjconf/20101106002). arXiv: [1101.5807](https://arxiv.org/abs/1101.5807) [astro-ph.EP].
- Gillon, Michaël et al. (Feb. 2017a). "Seven temperate terrestrial planets around the nearby ultracool dwarf star TRAPPIST-1." In: *Nature* 542.7642, pp. 456–460. DOI: [10.1038/nature21360](https://doi.org/10.1038/nature21360). arXiv: [1703.01424](https://arxiv.org/abs/1703.01424) [astro-ph.EP].
- Gillon, Michaël et al. (Feb. 2017b). "Seven temperate terrestrial planets around the nearby ultracool dwarf star TRAPPIST-1." In: *Nature* 542.7642, pp. 456–460. DOI: [10.1038/nature21360](https://doi.org/10.1038/nature21360). arXiv: [1703.01424](https://arxiv.org/abs/1703.01424) [astro-ph.EP].
- Gillon, Michaël et al. (July 2024). "Detection of an Earth-sized exoplanet orbiting the nearby ultracool dwarf star SPECULOOS-3." In: *Nature Astronomy* 8, pp. 865–878. DOI: [10.1038/s41550-024-02271-2](https://doi.org/10.1038/s41550-024-02271-2). arXiv: [2406.00794](https://arxiv.org/abs/2406.00794) [astro-ph.EP].
- Gizis, John E. and I. Neill Reid (1997). "M Subdwarf Secondaries: A Test of the Metallicity Scale." In: *Publications of the Astronomical Society of the Pacific* 109.741, pp. 1233–1236. ISSN: 00046280, 15383873. URL: <http://www.jstor.org/stable/40681026> (visited on 02/18/2026).
- Gomes da Silva, J., N. C. Santos, X. Bonfils, X. Delfosse, T. Forveille, and S. Udry (Oct. 2011). "Long-term magnetic activity of a sample of M-dwarf stars from the HARPS program. I. Comparison of activity indices." In: *A&A* 534, A30, A30. DOI: [10.1051/0004-6361/201116971](https://doi.org/10.1051/0004-6361/201116971). arXiv: [1109.0321](https://arxiv.org/abs/1109.0321) [astro-ph.SR].
- Gomes da Silva, J., N. C. Santos, X. Bonfils, X. Delfosse, T. Forveille, S. Udry, X. Dumusque, and C. Lovis (May 2012). "Long-term magnetic activity of a sample of M-dwarf stars from the HARPS program . II. Activity and radial velocity." In: *A&A* 541, A9, A9. DOI: [10.1051/0004-6361/201118598](https://doi.org/10.1051/0004-6361/201118598). arXiv: [1202.1564](https://arxiv.org/abs/1202.1564) [astro-ph.SR].
- Gray, David F. (2005). *The Observation and Analysis of Stellar Photospheres*. 3rd ed. Cambridge University Press.
- Gregory, P. C. (2005). "A Bayesian Analysis of Extrasolar Planet Data for HD 73526." In: *The Astrophysical Journal* 631.2, p. 1198. DOI: [10.1086/432594](https://doi.org/10.1086/432594). URL: <https://doi.org/10.1086/432594>.
- Grimm, Simon L. et al. (May 2018). "The nature of the TRAPPIST-1 exoplanets." In: *A&A* 613, A68, A68. DOI: [10.1051/0004-6361/201732233](https://doi.org/10.1051/0004-6361/201732233). arXiv: [1802.01377](https://arxiv.org/abs/1802.01377) [astro-ph.EP].
- Grouffal, S., Santerne, A., Hara, N. C., Boisse, I., Coez, S., Heidari, N., and Sulis, S. (2024). "An improved correction of radial velocity systematics

- for the SOPHIE spectrograph." In: *A&A* 687, A148. DOI: [10.1051/0004-6361/202348960](https://doi.org/10.1051/0004-6361/202348960). URL: <https://doi.org/10.1051/0004-6361/202348960>.
- Guest, Olivia et al. (Sept. 2025). "Against the Uncritical Adoption of 'AI' Technologies in Academia." In: DOI: [10.5281/zenodo.17065098](https://doi.org/10.5281/zenodo.17065098).
- Gustafsson, B., B. Edvardsson, K. Eriksson, U. G. Jørgensen, Å. Nordlund, and B. Plez (Aug. 2008). "A grid of MARCS model atmospheres for late-type stars. I. Methods and general properties." In: *A&A* 486.3, pp. 951–970. DOI: [10.1051/0004-6361:200809724](https://doi.org/10.1051/0004-6361:200809724). arXiv: [0805.0554](https://arxiv.org/abs/0805.0554) [astro-ph].
- Hara, Nathan C. and Eric B. Ford (Mar. 2023). "Statistical Methods for Exoplanet Detection with Radial Velocities." In: *Annual Review of Statistics and Its Application* 10.1, pp. 623–649. DOI: [10.1146/annurev-statistics-033021-012225](https://doi.org/10.1146/annurev-statistics-033021-012225). arXiv: [2308.00701](https://arxiv.org/abs/2308.00701) [astro-ph.IM].
- Haraway, Donna Jeanne (1995). *Ciencia, cyborgs y mujeres: la reinvención de la naturaleza*. Vol. 28. Universitat de València.
- Haraway, Donna (2019). *Seguir con el problema: Generar parentesco en el Chthuluceno*. Trans. by Helen Torres. Bilbao: Consonni. ISBN: 9788416205417.
- Hardegree-Ullman, Kevin K., Michael C. Cushing, Philip S. Muirhead, and Jessie L. Christiansen (2019). "Kepler Planet Occurrence Rates for Mid-type M Dwarfs as a Function of Spectral Type." In: *The Astronomical Journal* 158.2, p. 75. DOI: [10.3847/1538-3881/ab21d2](https://doi.org/10.3847/1538-3881/ab21d2). URL: <https://doi.org/10.3847/1538-3881/ab21d2>.
- Harding, Sandra (1996). *Ciencia y feminismo*. Ediciones Morata.
- Hasegawa, M. and K. Nakazawa (Jan. 1990). "Distant encounter between Keplerian particles." In: *A&A* 227.2, pp. 619–627.
- Hauschildt, P. H., T. Barman, E. Baron, J. P. Aufdenberg, and A. Schweitzer (June 2025). "The NewEra model grid." In: *A&A* 698, A47, A47. DOI: [10.1051/0004-6361/202554171](https://doi.org/10.1051/0004-6361/202554171). arXiv: [2504.17597](https://arxiv.org/abs/2504.17597) [astro-ph.SR].
- Hauschildt, Peter H., France Allard, Jason Ferguson, E. Baron, and David R. Alexander (Nov. 1999). "The NEXTGEN Model Atmosphere Grid. II. Spherically Symmetric Model Atmospheres for Giant Stars with Effective Temperatures between 3000 and 6800 K." In: *APJ* 525.2, pp. 871–880. DOI: [10.1086/307954](https://doi.org/10.1086/307954). arXiv: [astro-ph/9907194](https://arxiv.org/abs/astro-ph/9907194) [astro-ph].
- Hawker, George A., Nikku Madhusudhan, Samuel H. C. Cabot, and Siddharth Gandhi (2018). "Evidence for Multiple Molecular Species in the Hot Jupiter HD 209458b." In: *The Astrophysical Journal Letters* 863.1, p. L11. DOI: [10.3847/2041-8213/aac49d](https://doi.org/10.3847/2041-8213/aac49d). URL: <https://doi.org/10.3847/2041-8213/aac49d>.
- Haywood, R. D. et al. (Sept. 2014). "Planets and stellar activity: hide and seek in the CoRoT-7 system." In: *MNRAS* 443.3, pp. 2517–2531. DOI: [10.1093/mnras/stu1320](https://doi.org/10.1093/mnras/stu1320). arXiv: [1407.1044](https://arxiv.org/abs/1407.1044) [astro-ph.EP].
- He, Matthias Y., Amaury Triaud, and Michaël Gillon (2016). "First limits on the occurrence rate of short-period planets orbiting brown dwarfs." In: *Monthly Notices of the Royal Astronomical Society* 464, pp. 2687–2697. URL: <https://api.semanticscholar.org/CorpusID:53692008>.
- Hearty, Fred et al. (July 2014). "Environmental control system for Habitable-zone Planet Finder (HPF)." In: *Ground-based and Airborne Instrumentation*

- for *Astronomy V*. Ed. by Suzanne K. Ramsay, Ian S. McLean, and Hideki Takami. Vol. 9147. Society of Photo-Optical Instrumentation Engineers (SPIE) Conference Series, 914752, p. 914752. DOI: [10.1117/12.2056720](https://doi.org/10.1117/12.2056720).
- Heath, Martin J., Laurance R. Doyle, Manoj M. Joshi, and Robert M. Haberle (Aug. 1999). "Habitability of Planets Around Red Dwarf Stars." In: *Origins of Life and Evolution of the Biosphere* 29.4, pp. 405–424. DOI: [10.1023/A:1006596718708](https://doi.org/10.1023/A:1006596718708).
- Hejazi, Neda, Sébastien Lépine, and Thomas Nordlander (2022). "Chemical Properties of the Local Disk and Halo. II. Abundances of 3745 M Dwarfs and Subdwarfs from Improved Model Fitting of Low-resolution Spectra." In: *The Astrophysical Journal* 927.1, p. 122. DOI: [10.3847/1538-4357/ac4e16](https://doi.org/10.3847/1538-4357/ac4e16). URL: <https://doi.org/10.3847/1538-4357/ac4e16>.
- Henry, Todd J., Otto G. Franz, Lawrence H. Wasserman, G. Fritz Benedict, Peter J. Shelus, Philip A. Ianna, J. Davy Kirkpatrick, and Donald W. McCarthy Jr. (Feb. 1999). "The Optical Mass-Luminosity Relation at the End of the Main Sequence (0.08-0.20 M_{solar})." In: *APJ* 512.2, pp. 864–873. DOI: [10.1086/306793](https://doi.org/10.1086/306793).
- Henry, Todd J. and Wei-Chun Jao (Sept. 2024). "The Character of M Dwarfs." In: *ARA&A* 62.1, pp. 593–633. DOI: [10.1146/annurev-astro-052722-102740](https://doi.org/10.1146/annurev-astro-052722-102740).
- Henry, Todd J., Wei-Chun Jao, John P. Subasavage, Thomas D. Beaulieu, Philip A. Ianna, Edgardo Costa, and René A. Méndez (Dec. 2006). "The Solar Neighborhood. XVII. Parallax Results from the CTIOPI 0.9 m Program: 20 New Members of the RECONS 10 Parsec Sample." In: *AJ* 132.6, pp. 2360–2371. DOI: [10.1086/508233](https://doi.org/10.1086/508233). arXiv: [astro-ph/0608230](https://arxiv.org/abs/astro-ph/0608230) [astro-ph].
- Henry, Todd J., Wei-Chun Jao, Jennifer G. Winters, Sergio B. Dieterich, Charlie T. Finch, Philip A. Ianna, Adric R. Riedel, Michele L. Silverstein, John P. Subasavage, and Eliot Halley Vrijmoet (2018). "The Solar Neighborhood XLIV: RECONS Discoveries within 10 parsecs." In: *The Astronomical Journal* 155.6, p. 265. DOI: [10.3847/1538-3881/aac262](https://doi.org/10.3847/1538-3881/aac262). URL: <https://doi.org/10.3847/1538-3881/aac262>.
- Henry, Todd J. and Donald W. McCarthy Jr. (Aug. 1993). "The Mass-Luminosity Relation for Stars of Mass 1.0 to 0.08 M_{solar} ." In: *AJ* 106, p. 773. DOI: [10.1086/116685](https://doi.org/10.1086/116685).
- Henry, Todd Jackson (Jan. 1991). "A Systematic Search for Low Mass Companions Orbiting Nearby Stars and the Calibration of the End of the Stellar Main Sequence." PhD thesis. University of Arizona.
- Hestroffer, D. (Nov. 1997). "Centre to limb darkening of stars. New model and application to stellar interferometry." In: *A&A* 327, pp. 199–206.
- Hobson, M. J. et al. (Aug. 2024). "Three super-Earths and a possible water world from TESS and ESPRESSO." In: *A&A* 688, A216, A216. DOI: [10.1051/0004-6361/202450505](https://doi.org/10.1051/0004-6361/202450505). arXiv: [2406.06278](https://arxiv.org/abs/2406.06278) [astro-ph.EP].
- Hobson, M. J. and Bouchy, F., Cook, N. J., Artigau, E., Moutou, C., Boisse, I., Lovis, C., Carmona, A., Delfosse, X., Donati, J.-F., and the SPIRou Team (2021). "The SPIRou wavelength calibration for precise radial velocities in the near infrared." In: *A&A* 648, A48. DOI: [10.1051/0004-6361/202038413](https://doi.org/10.1051/0004-6361/202038413). URL: <https://doi.org/10.1051/0004-6361/202038413>.

- Howard, Andrew W. et al. (2012). "Planet Occurrence Within 0.25 AU Of Solar-Type Stars From Kepler." In: *The Astrophysical Journal Supplement Series* 201.2, p. 15. DOI: [10.1088/0067-0049/201/2/15](https://doi.org/10.1088/0067-0049/201/2/15). URL: <https://doi.org/10.1088/0067-0049/201/2/15>.
- Howarth, Ian D. (Dec. 2011). "On stellar limb darkening and exoplanetary transits." In: *MNRAS* 418.2, pp. 1165–1175. DOI: [10.1111/j.1365-2966.2011.19568.x](https://doi.org/10.1111/j.1365-2966.2011.19568.x). arXiv: [1106.4659](https://arxiv.org/abs/1106.4659) [astro-ph.SR].
- Hubbard, Gill, Kathryn Backett-Milburn, and Debbie Kemmer (2001). "Working with emotion: Issues for the researcher in fieldwork and teamwork." In: *International journal of social research methodology* 4.2, pp. 119–137.
- Ida, S. and D. N. C. Lin (2004). "Toward a Deterministic Model of Planetary Formation. I. A Desert in the Mass and Semimajor Axis Distributions of Extrasolar Planets." In: *The Astrophysical Journal* 604.1, p. 388. DOI: [10.1086/381724](https://doi.org/10.1086/381724). URL: <https://doi.org/10.1086/381724>.
- Izidoro, André, Bertram Bitsch, and Rajdeep Dasgupta (2021). "The Effect of a Strong Pressure Bump in the Sun's Natal Disk: Terrestrial Planet Formation via Planetesimal Accretion Rather than Pebble Accretion." In: *The Astrophysical Journal* 915.1, p. 62. DOI: [10.3847/1538-4357/abfe0b](https://doi.org/10.3847/1538-4357/abfe0b). URL: <https://doi.org/10.3847/1538-4357/abfe0b>.
- Jakob, Gerd and Jean-Louis Lizon (July 2010). "Low-vibration high-cooling power 2-stage cryocoolers for ground-based astronomical instrumentation." In: *Ground-based and Airborne Telescopes III*. Ed. by Larry M. Stepp, Roberto Gilmozzi, and Helen J. Hall. Vol. 7733. Society of Photo-Optical Instrumentation Engineers (SPIE) Conference Series, 77333V, p. 77333V. DOI: [10.1117/12.856233](https://doi.org/10.1117/12.856233).
- Jao, Wei-Chun, Todd J. Henry, Douglas R. Gies, and Nigel C. Hambly (July 2018). "A Gap in the Lower Main Sequence Revealed by Gaia Data Release 2." In: *APJL* 861.1, L11, p. L11. DOI: [10.3847/2041-8213/aacdf6](https://doi.org/10.3847/2041-8213/aacdf6). arXiv: [1806.07792](https://arxiv.org/abs/1806.07792) [astro-ph.SR].
- Jeffers, S. V. et al. (June 2018). "CARMENES input catalogue of M dwarfs. III. Rotation and activity from high-resolution spectroscopic observations." In: *A&A* 614, A76, A76. DOI: [10.1051/0004-6361/201629599](https://doi.org/10.1051/0004-6361/201629599). arXiv: [1802.02102](https://arxiv.org/abs/1802.02102) [astro-ph.SR].
- Jeffers, S. V. et al. (July 2022). "The CARMENES search for exoplanets around M dwarfs. Benchmarking the impact of activity in high-precision radial velocity measurements." In: *A&A* 663, A27, A27. DOI: [10.1051/0004-6361/202141880](https://doi.org/10.1051/0004-6361/202141880). arXiv: [2203.00415](https://arxiv.org/abs/2203.00415) [astro-ph.EP].
- Jehin, E. et al. (Dec. 2018). "The SPECULOOS Southern Observatory Begins its Hunt for Rocky Planets." In: *The Messenger* 174, pp. 2–7. DOI: [10.18727/0722-6691/5105](https://doi.org/10.18727/0722-6691/5105).
- Jenkins, J. S., L. W. Ramsey, H. R. A. Jones, Y. Pavlenko, J. Gallardo, J. R. Barnes, and D. J. Pinfield (Oct. 2009). "Rotational Velocities for M Dwarfs." In: *APJ* 704.2, pp. 975–988. DOI: [10.1088/0004-637X/704/2/975](https://doi.org/10.1088/0004-637X/704/2/975). arXiv: [0908.4092](https://arxiv.org/abs/0908.4092) [astro-ph.SR].

- Johansen, Anders and Michiel Lambrechts (Aug. 2017). "Forming Planets via Pebble Accretion." In: *Annual Review of Earth and Planetary Sciences* 45.1, pp. 359–387. DOI: [10.1146/annurev-earth-063016-020226](https://doi.org/10.1146/annurev-earth-063016-020226).
- Johnson, Kelsey E., John E. Hibbard, Sarah C. Gallagher, Jane C. Charlton, Ann E. Hornschemeier, Thomas H. Jarrett, and Amy E. Reines (2007). "The Infrared Properties of Hickson Compact Groups." In: *The Astronomical Journal* 134.4, p. 1522. DOI: [10.1086/520921](https://doi.org/10.1086/520921). URL: <https://doi.org/10.1086/520921>.
- Joy, Alfred H. (Jan. 1947). "Radial Velocities and Spectral Types of 181 Dwarf Stars." In: *APJ* 105, p. 96. DOI: [10.1086/144886](https://doi.org/10.1086/144886).
- Kaminski, A. et al. (Apr. 2025). "The CARMENES search for exoplanets around M dwarfs: Occurrence rates of Earth-like planets around very low-mass stars." In: *A&A* 696, A101, A101. DOI: [10.1051/0004-6361/202453381](https://doi.org/10.1051/0004-6361/202453381). arXiv: [2504.03364](https://arxiv.org/abs/2504.03364) [astro-ph.EP].
- Kasting, J. F. (June 1988). "Runaway and moist greenhouse atmospheres and the evolution of Earth and Venus." In: *Icarus* 74.3, pp. 472–494. DOI: [10.1016/0019-1035\(88\)90116-9](https://doi.org/10.1016/0019-1035(88)90116-9).
- Kasting, James F., Daniel P. Whitmire, and Ray T. Reynolds (Jan. 1993). "Habitable Zones around Main Sequence Stars." In: *Icarus* 101.1, pp. 108–128. DOI: [10.1006/icar.1993.1010](https://doi.org/10.1006/icar.1993.1010).
- Keller, Evelyn Fox (1991). *Reflexiones sobre género y ciencia*. Edicions Alfons el Magnànim. Institució Valenciana d'Estudis i Investigació.
- Kempton, Eliza M.-R. and Heather A. Knutson (July 2024). "Transiting Exoplanet Atmospheres in the Era of JWST." In: *Reviews in Mineralogy and Geochemistry* 90.1, pp. 411–464. ISSN: 1529-6466. DOI: [10.2138/rmg.2024.90.12](https://doi.org/10.2138/rmg.2024.90.12). eprint: <https://pubs.geoscienceworld.org/msa/rimg/article-pdf/90/1/411/6521125/rmg.2024.90.12.pdf>. URL: <https://doi.org/10.2138/rmg.2024.90.12>.
- Key, Ellen M. and Jane Lawrence Sumner (2019). "You Research Like a Girl: Gendered Research Agendas and Their Implications." In: *PS: Political Science & Politics* 52.4, 663–668. DOI: [10.1017/S1049096519000945](https://doi.org/10.1017/S1049096519000945).
- Kirkpatrick, J. D., Todd J. Henry, and Donald W. McCarthy Jr. (Nov. 1991). "A Standard Stellar Spectral Sequence in the Red/Near-Infrared: Classes K5 to M9." In: *APJS* 77, p. 417. DOI: [10.1086/191611](https://doi.org/10.1086/191611).
- Kirkpatrick, J. Davy, I. Neill Reid, James Liebert, Roc M. Cutri, Brant Nelson, Charles A. Beichman, Conard C. Dahn, David G. Monet, John E. Gizis, and Michael F. Skrutskie (July 1999). "Dwarfs Cooler than "M": The Definition of Spectral Type "L" Using Discoveries from the 2 Micron All-Sky Survey (2MASS)." In: *APJ* 519.2, pp. 802–833. DOI: [10.1086/307414](https://doi.org/10.1086/307414).
- Köhler, J. et al. (June 2025). "viper: High-precision radial velocities from the optical to the infrared: Reaching 3 m/s in the K band of CRIRES⁺ with telluric modelling." In: *A&A* 698, A44, A44. DOI: [10.1051/0004-6361/202553919](https://doi.org/10.1051/0004-6361/202553919). arXiv: [2505.08315](https://arxiv.org/abs/2505.08315) [astro-ph.IM].
- Kokubo, Eiichiro and Shigeru Ida (Sept. 1996). "On Runaway Growth of Planetsimals." In: *Icarus* 123.1, pp. 180–191. DOI: [10.1006/icar.1996.0148](https://doi.org/10.1006/icar.1996.0148).

- Kopal, Zdenek (Jan. 1950). "Detailed effects of limb darkening upon light and velocity curves of close binary systems." In: *Harvard College Observatory Circular* 454, pp. 1–12.
- Kopparapu, Ravi Kumar, Ramses Ramirez, James F. Kasting, Vincent Eymet, Tyler D. Robinson, Suvrath Mahadevan, Ryan C. Terrien, Shawn Domagal-Goldman, Victoria Meadows, and Rohit Deshpande (Mar. 2013). "Habitable Zones around Main-sequence Stars: New Estimates." In: *APJ* 765.2, 131, p. 131. DOI: [10.1088/0004-637X/765/2/131](https://doi.org/10.1088/0004-637X/765/2/131). arXiv: [1301.6674](https://arxiv.org/abs/1301.6674) [astro-ph.EP].
- Kossakowski, D. et al. (Oct. 2022). "The CARMENES search for exoplanets around M dwarfs. Stable radial-velocity variations at the rotation period of AD Leonis: A test case study of current limitations to treating stellar activity." In: *A&A* 666, A143, A143. DOI: [10.1051/0004-6361/202243773](https://doi.org/10.1051/0004-6361/202243773). arXiv: [2209.05814](https://arxiv.org/abs/2209.05814) [astro-ph.EP].
- Kotani, Takayuki et al. (July 2018). "The infrared Doppler (IRD) instrument for the Subaru telescope: instrument description and commissioning results." In: *Ground-based and Airborne Instrumentation for Astronomy VII*. Ed. by Christopher J. Evans, Luc Simard, and Hideki Takami. Vol. 10702. Society of Photo-Optical Instrumentation Engineers (SPIE) Conference Series, 1070211, p. 1070211. DOI: [10.1117/12.2311836](https://doi.org/10.1117/12.2311836).
- Kotek, Hadas, Rikker Dockum, and David Sun (2023). "Gender bias and stereotypes in Large Language Models." In: *Proceedings of The ACM Collective Intelligence Conference. CI '23*. Delft, Netherlands: Association for Computing Machinery, 12–24. ISBN: 9798400701139. DOI: [10.1145/3582269.3615599](https://doi.org/10.1145/3582269.3615599). URL: <https://doi.org/10.1145/3582269.3615599>.
- Kozłowski, Diego, Vincent Larivière, Cassidy R. Sugimoto, and Thema Monroe-White (2022). "Intersectional inequalities in science." In: *Proceedings of the National Academy of Sciences* 119.2, e2113067119. DOI: [10.1073/pnas.2113067119](https://doi.org/10.1073/pnas.2113067119). eprint: <https://www.pnas.org/doi/pdf/10.1073/pnas.2113067119>. URL: <https://www.pnas.org/doi/abs/10.1073/pnas.2113067119>.
- Kuiper, G. P. (May 1939). "Two New White Dwarfs; Notes on Proper Motion Stars." In: *APJ* 89, p. 548. DOI: [10.1086/144075](https://doi.org/10.1086/144075).
- Kumaraswamy, P. (1980). "A generalized probability density function for double-bounded random processes." In: *Journal of Hydrology* 46.1, pp. 79–88. ISSN: 0022-1694. DOI: [https://doi.org/10.1016/0022-1694\(80\)90036-0](https://doi.org/10.1016/0022-1694(80)90036-0). URL: <https://www.sciencedirect.com/science/article/pii/0022169480900360>.
- Kuzuhara, Masayuki et al. (June 2024). "Gliese 12 b: A Temperate Earth-sized Planet at 12 pc Ideal for Atmospheric Transmission Spectroscopy." In: *APJL* 967.2, L21, p. L21. DOI: [10.3847/2041-8213/ad3642](https://doi.org/10.3847/2041-8213/ad3642). arXiv: [2405.14708](https://arxiv.org/abs/2405.14708) [astro-ph.EP].
- Lafarga, M. et al. (Aug. 2021). "The CARMENES search for exoplanets around M dwarfs. Mapping stellar activity indicators across the M dwarf domain." In: *A&A* 652, A28, A28. DOI: [10.1051/0004-6361/202140605](https://doi.org/10.1051/0004-6361/202140605). arXiv: [2105.13467](https://arxiv.org/abs/2105.13467) [astro-ph.SR].

- Lagrange, A.-M. et al. (Jan. 2009). "A probable giant planet imaged in the β Pictoris disk. VLT/NaCo deep L'-band imaging." In: *A&A* 493.2, pp. L21–L25. DOI: 10.1051/0004-6361:200811325. arXiv: 0811.3583 [astro-ph].
- Lambrechts, M. and A. Johansen (Aug. 2012). "Rapid growth of gas-giant cores by pebble accretion." In: *A&A* 544, A32, A32. DOI: 10.1051/0004-6361/201219127. arXiv: 1205.3030 [astro-ph.EP].
- Lambrechts, Michiel, Alessandro Morbidelli, Seth A. Jacobson, Anders Johansen, Bertram Bitsch, Andre Izidoro, and Sean N. Raymond (July 2019). "Formation of planetary systems by pebble accretion and migration. How the radial pebble flux determines a terrestrial-planet or super-Earth growth mode." In: *A&A* 627, A83, A83. DOI: 10.1051/0004-6361/201834229. arXiv: 1902.08694 [astro-ph.EP].
- Larregue, Julien and Mathias Nielsen (Apr. 2023). "Knowledge Hierarchies and Gender Disparities in Social Science Funding." In: *Sociology* 58. DOI: 10.1177/00380385231163071.
- Latham, David W. (2011). "Radial-Velocity Planets." In: *Encyclopedia of Astrobiology*. Ed. by Muriel Gargaud, Ricardo Amils, José Cernicharo Quintanilla, Henderson James (Jim) Cleaves, William M. Irvine, Daniele L. Pinti, and Michel Viso. Berlin, Heidelberg: Springer Berlin Heidelberg, pp. 1400–1404. ISBN: 978-3-642-11274-4. DOI: 10.1007/978-3-642-11274-4_1839. URL: https://doi.org/10.1007/978-3-642-11274-4_1839.
- Lebonnois, Sébastien, Frédéric Hourdin, Vincent Eymet, Audrey Cresspin, Richard Fournier, and François Forget (2010). "Superrotation of Venus' atmosphere analyzed with a full general circulation model." In: *Journal of Geophysical Research: Planets* 115.E6. DOI: <https://doi.org/10.1029/2009JE003458>. eprint: <https://agupubs.onlinelibrary.wiley.com/doi/pdf/10.1029/2009JE003458>. URL: <https://agupubs.onlinelibrary.wiley.com/doi/abs/10.1029/2009JE003458>.
- Lesjak, F. et al. (Oct. 2023). "Retrieval of the dayside atmosphere of WASP-43b with CRIRES⁺." In: *A&A* 678, A23, A23. DOI: 10.1051/0004-6361/202347151. arXiv: 2307.11627 [astro-ph.EP].
- Lindgren, Sara and Ulrike Heiter (Aug. 2017). "Metallicity determination of M dwarfs. Expanded parameter range in metallicity and effective temperature." In: *A&A* 604, A97, A97. DOI: 10.1051/0004-6361/201730715. arXiv: 1705.08785 [astro-ph.SR].
- Lingam, Manasvi and Abraham Loeb (Mar. 2017). "Fast Radio Bursts from Extragalactic Light Sails." In: *APJL* 837.2, L23, p. L23. DOI: 10.3847/2041-8213/aa633e. arXiv: 1701.01109 [astro-ph.HE].
- Liu, Jifeng et al. (Nov. 2019). "A wide star-black-hole binary system from radial-velocity measurements." In: *Nature* 575.7784, pp. 618–621. DOI: 10.1038/s41586-019-1766-2. arXiv: 1911.11989 [astro-ph.SR].
- Liu, Yu-Juan and Gang Zhao (Sept. 2005). "The progress of exploring extra-solar planetary systems." In: *Progress in Astronomy* 23.3, pp. 226–238.
- Lizon, J. L. and M. Accardo (July 2010). "LN₂ continuous flow cryostats: a compact vibration free cooling system for single to multiple detector systems." In: *Modern Technologies in Space- and Ground-based Telescopes and Instrumen-*

- tation*. Ed. by Eli Atad-Ettinger and Dietrich Lemke. Vol. 7739. Society of Photo-Optical Instrumentation Engineers (SPIE) Conference Series, 77393E, 77393E. DOI: [10.1117/12.856013](https://doi.org/10.1117/12.856013).
- Lockwood, Alexandra C., John A. Johnson, Chad F. Bender, John S. Carr, Travis Barman, Alexander J. W. Richert, and Geoffrey A. Blake (2014). "Near-IR Direct Detection Of Water Vapor In Tau Boötis b." In: *The Astrophysical Journal Letters* 783.2, p. L29. DOI: [10.1088/2041-8205/783/2/L29](https://doi.org/10.1088/2041-8205/783/2/L29). URL: <https://doi.org/10.1088/2041-8205/783/2/L29>.
- Lomb, N. R. (Feb. 1976). "Least-Squares Frequency Analysis of Unequally Spaced Data." In: *APSS* 39.2, pp. 447–462. DOI: [10.1007/BF00648343](https://doi.org/10.1007/BF00648343).
- Lora, Juan M., Tetsuya Tokano, Jan Vatant d'Ollone, Sébastien Lebonnois, and Ralph D. Lorenz (2019). "A model intercomparison of Titan's climate and low-latitude environment." In: *Icarus* 333, pp. 113–126. ISSN: 0019-1035. DOI: <https://doi.org/10.1016/j.icarus.2019.05.031>. URL: <https://www.sciencedirect.com/science/article/pii/S0019103518307838>.
- Lovis, C. et al. (Apr. 2011). "The HARPS search for southern extra-solar planets. XXVIII. Up to seven planets orbiting HD 10180: probing the architecture of low-mass planetary systems." In: *A&A* 528, A112, A112. DOI: [10.1051/0004-6361/201015577](https://doi.org/10.1051/0004-6361/201015577). arXiv: [1011.4994](https://arxiv.org/abs/1011.4994) [astro-ph.EP].
- Luger, Rodrigo et al. (June 2017). "A seven-planet resonant chain in TRAPPIST-1." In: *Nature Astronomy* 1, 0129, p. 0129. DOI: [10.1038/s41550-017-0129-1](https://doi.org/10.1038/s41550-017-0129-1). arXiv: [1703.04166](https://arxiv.org/abs/1703.04166) [astro-ph.EP].
- Luque, R. et al. (Aug. 2022). "The HD 260655 system: Two rocky worlds transiting a bright M dwarf at 10 pc." In: *A&A* 664, A199, A199. DOI: [10.1051/0004-6361/202243834](https://doi.org/10.1051/0004-6361/202243834). arXiv: [2204.10261](https://arxiv.org/abs/2204.10261) [astro-ph.EP].
- Luque, R. et al. (Nov. 2023). "A resonant sextuplet of sub-Neptunes transiting the bright star HD 110067." In: *Nature* 623.7989, pp. 932–937. DOI: [10.1038/s41586-023-06692-3](https://doi.org/10.1038/s41586-023-06692-3). arXiv: [2311.17775](https://arxiv.org/abs/2311.17775) [astro-ph.EP].
- Lustig-Yaeger, Jacob, Victoria S. Meadows, and Andrew P. Lincowski (July 2019). "The Detectability and Characterization of the TRAPPIST-1 Exoplanet Atmospheres with JWST." In: *AJ* 158.1, 27, p. 27. DOI: [10.3847/1538-3881/ab21e0](https://doi.org/10.3847/1538-3881/ab21e0). arXiv: [1905.07070](https://arxiv.org/abs/1905.07070) [astro-ph.EP].
- Luyten, Willem J. (June 1926). "The Properties of Stars in the Solar Neighborhood." In: *The Scientific Monthly* 22.6, pp. 494–498.
- Lépine, Sébastien, R. Michael Rich, and Michael M. Shara (2007). "Revised Metallicity Classes for Low-Mass Stars: Dwarfs (dM), Subdwarfs (sdM), Extreme Subdwarfs (esdM), and Ultrastardwarfs (usdM)* **." In: *The Astrophysical Journal* 669.2, p. 1235. DOI: [10.1086/521614](https://doi.org/10.1086/521614). URL: <https://doi.org/10.1086/521614>.
- Madhusudhan, N. and S. Seager (Dec. 2009). "A Temperature and Abundance Retrieval Method for Exoplanet Atmospheres." In: *APJ* 707.1, pp. 24–39. DOI: [10.1088/0004-637X/707/1/24](https://doi.org/10.1088/0004-637X/707/1/24). arXiv: [0910.1347](https://arxiv.org/abs/0910.1347) [astro-ph.EP].
- Madhusudhan, Nikku (Aug. 2019). "Exoplanetary Atmospheres: Key Insights, Challenges, and Prospects." In: *ARAA* 57, pp. 617–663. DOI: [10.1146/annurev-astro-081817-051846](https://doi.org/10.1146/annurev-astro-081817-051846). arXiv: [1904.03190](https://arxiv.org/abs/1904.03190) [astro-ph.EP].

- Madhusudhan, Nikku, Marcelino Agúndez, Julianne I. Moses, and Yongyun Hu (Dec. 2016). "Exoplanetary Atmospheres—Chemistry, Formation Conditions, and Habitability." In: *SSR* 205.1-4, pp. 285–348. DOI: [10.1007/s11214-016-0254-3](https://doi.org/10.1007/s11214-016-0254-3). arXiv: 1604.06092 [astro-ph.EP].
- Madhusudhan, Nikku, Nicolas Crouzet, Peter R. McCullough, Drake Deming, and Christina Hedges (2014). "H₂O Abundances In The Atmospheres Of Three Hot Jupiters." In: *The Astrophysical Journal Letters* 791.1, p. L9. DOI: [10.1088/2041-8205/791/1/L9](https://doi.org/10.1088/2041-8205/791/1/L9). URL: <https://doi.org/10.1088/2041-8205/791/1/L9>.
- Makarov, Valeri V. (2010). "Variability of Surface Flows on the Sun and the Implications for Exoplanet Detection." In: *The Astrophysical Journal* 715.1, p. 500. DOI: [10.1088/0004-637X/715/1/500](https://doi.org/10.1088/0004-637X/715/1/500). URL: <https://doi.org/10.1088/0004-637X/715/1/500>.
- Mann, Andrew W. et al. (Jan. 2019). "How to Constrain Your M Dwarf. II. The Mass-Luminosity-Metallicity Relation from 0.075 to 0.70 Solar Masses." In: *APJ* 871.1, 63, p. 63. DOI: [10.3847/1538-4357/aaf3bc](https://doi.org/10.3847/1538-4357/aaf3bc). arXiv: 1811.06938 [astro-ph.SR].
- Marconi, A. et al. (July 2024). "ANDES, the high resolution spectrograph for the ELT: science goals, project overview, and future developments." In: *Ground-based and Airborne Instrumentation for Astronomy X*. Ed. by Julia J. Bryant, Kentaro Motohara, and Joël. R. D. Vernet. Vol. 13096. Society of Photo-Optical Instrumentation Engineers (SPIE) Conference Series, 1309613, p. 1309613. DOI: [10.1117/12.3017966](https://doi.org/10.1117/12.3017966). arXiv: 2407.14601 [astro-ph.IM].
- Marfil, E. et al. (2021). "The CARMENES search for exoplanets around M dwarfs - Stellar atmospheric parameters of target stars with STEPARSYN." In: *A&A* 656, A162. DOI: [10.1051/0004-6361/202141980](https://doi.org/10.1051/0004-6361/202141980). URL: <https://doi.org/10.1051/0004-6361/202141980>.
- Mas-Buitrago, P. et al. (July 2024). "Using autoencoders and deep transfer learning to determine the stellar parameters of 286 CARMENES M dwarfs." In: *A&A* 687, A205, A205. DOI: [10.1051/0004-6361/202449865](https://doi.org/10.1051/0004-6361/202449865). arXiv: 2405.08703 [astro-ph.SR].
- Mayor, M. et al. (Sept. 2011). "The HARPS search for southern extra-solar planets XXXIV. Occurrence, mass distribution and orbital properties of super-Earths and Neptune-mass planets." In: *arXiv e-prints*, arXiv:1109.2497, arXiv:1109.2497. DOI: [10.48550/arXiv.1109.2497](https://doi.org/10.48550/arXiv.1109.2497). arXiv: 1109.2497 [astro-ph.EP].
- Mayor, Michel and Didier Queloz (Nov. 1995). "A Jupiter-mass companion to a solar-type star." In: *Nature* 378.6555, pp. 355–359. DOI: [10.1038/378355a0](https://doi.org/10.1038/378355a0).
- Mazzitelli, I. and F. Dantona (Sept. 1986). "Evolution from the Main Sequence to the White Dwarf Stage for a 3 M_{sun} Star." In: *APJ* 308, p. 706. DOI: [10.1086/164543](https://doi.org/10.1086/164543).
- Medan, Ilija and Sébastien Lépine (Feb. 2023). "Chemodynamical ages of small-scale kinematic structures of the galactic disc in the solar neighbourhood from ~250000 K and M dwarfs." In: *Monthly Notices of the Royal Astronomical Society* 521.1, pp. 208–229. ISSN: 0035-8711. DOI: [10.1093/mnras/stad435](https://doi.org/10.1093/mnras/stad435).

- eprint: <https://academic.oup.com/mnras/article-pdf/521/1/208/49418994/stad435.pdf>. URL: <https://doi.org/10.1093/mnras/stad435>.
- Meunier, N., M. Desort, and A.-M. Lagrange (Mar. 2010). “Using the Sun to estimate Earth-like planets detection capabilities . II. Impact of plagues.” In: *A&A* 512, A39, A39. DOI: [10.1051/0004-6361/200913551](https://doi.org/10.1051/0004-6361/200913551). arXiv: [1001.1638](https://arxiv.org/abs/1001.1638) [astro-ph.EP].
- Meunier, N. and A.-M. Lagrange (Sept. 2019). “Activity time series of old stars from late F to early K. III. Diagnosis from photometry.” In: *A&A* 629, A42, A42. DOI: [10.1051/0004-6361/201935651](https://doi.org/10.1051/0004-6361/201935651). arXiv: [1909.06566](https://arxiv.org/abs/1909.06566) [astro-ph.SR].
- Meunier, N. and A.-M. Lagrange (Oct. 2020). “The effects of granulation and supergranulation on Earth-mass planet detectability in the habitable zone around F6-K4 stars.” In: *A&A* 642, A157, A157. DOI: [10.1051/0004-6361/202038376](https://doi.org/10.1051/0004-6361/202038376). arXiv: [2008.11952](https://arxiv.org/abs/2008.11952) [astro-ph.SR].
- Meunier, N., A.-M. Lagrange, and S. Borgniet (Dec. 2020). “Activity time series of old stars from late F to early K. V. Effect on exoplanet detectability with high-precision astrometry.” In: *A&A* 644, A77, A77. DOI: [10.1051/0004-6361/202038710](https://doi.org/10.1051/0004-6361/202038710). arXiv: [2011.02158](https://arxiv.org/abs/2011.02158) [astro-ph.SR].
- Meunier, N., A.-M. Lagrange, S. Borgniet, and M. Rieutord (Nov. 2015). “Using the Sun to estimate Earth-like planet detection capabilities. VI. Simulation of granulation and supergranulation radial velocity and photometric time series.” In: *A&A* 583, A118, A118. DOI: [10.1051/0004-6361/201525721](https://doi.org/10.1051/0004-6361/201525721).
- Meunier, N., A.-M. Lagrange, L. Mbemba Kabuiku, M. Alex, L. Mignon, and S. Borgniet (Jan. 2017). “Variability of stellar granulation and convective blueshift with spectral type and magnetic activity. I. K and G main sequence stars.” In: *A&A* 597, A52, A52. DOI: [10.1051/0004-6361/201629052](https://doi.org/10.1051/0004-6361/201629052). arXiv: [1610.02168](https://arxiv.org/abs/1610.02168) [astro-ph.SR].
- Meunier, N., L. Mignon, and A.-M. Lagrange (Nov. 2017). “Variability in stellar granulation and convective blueshift with spectral type and magnetic activity . II. From young to old main-sequence K-G-F stars.” In: *A&A* 607, A124, A124. DOI: [10.1051/0004-6361/201731017](https://doi.org/10.1051/0004-6361/201731017). arXiv: [1711.02331](https://arxiv.org/abs/1711.02331) [astro-ph.SR].
- Miao, Lili, Vincent Larivière, Byungkyu Lee, Yong-Yeol Ahn, and Cassidy R. Sugimoto (Oct. 2024). “Persistent Hierarchy in Contemporary International Collaboration.” In: *arXiv e-prints*, arXiv:2410.13020, arXiv:2410.13020. DOI: [10.48550/arXiv.2410.13020](https://doi.org/10.48550/arXiv.2410.13020). arXiv: [2410.13020](https://arxiv.org/abs/2410.13020) [cs.DL].
- Michelson, A. A. and F. G. Pease (May 1921). “Measurement of the Diameter of α Orionis with the Interferometer.” In: *APJ* 53, pp. 249–259. DOI: [10.1086/142603](https://doi.org/10.1086/142603).
- Mignon, L., N. Meunier, X. Delfosse, X. Bonfils, N. C. Santos, T. Forveille, G. Gaisné, N. Astudillo-Defru, C. Lovis, and S. Udry (July 2023). “Characterisation of stellar activity of M dwarfs. I. Long-timescale variability in a large sample and detection of new cycles.” In: *A&A* 675, A168, A168. DOI: [10.1051/0004-6361/202244249](https://doi.org/10.1051/0004-6361/202244249). arXiv: [2303.03998](https://arxiv.org/abs/2303.03998) [astro-ph.SR].
- Miguel, Y., A. Cridland, C. W. Ormel, J. J. Fortney, and S. Ida (Jan. 2020). “Diverse outcomes of planet formation and composition around low-mass

- stars and brown dwarfs." In: *MNRAS* 491.2, pp. 1998–2009. DOI: [10.1093/mnras/stz3007](https://doi.org/10.1093/mnras/stz3007). arXiv: [1909.12320](https://arxiv.org/abs/1909.12320) [astro-ph.EP].
- Miller-Ricci Kempton, Eliza and Emily Rauscher (June 2012). "Constraining High-speed Winds in Exoplanet Atmospheres through Observations of Anomalous Doppler Shifts during Transit." In: *APJ* 751.2, 117, p. 117. DOI: [10.1088/0004-637X/751/2/117](https://doi.org/10.1088/0004-637X/751/2/117). arXiv: [1109.2270](https://arxiv.org/abs/1109.2270) [astro-ph.EP].
- Milne, E. A. (Mar. 1921). "Radiative equilibrium in the outer layers of a star." In: *MNRAS* 81, pp. 361–375. DOI: [10.1093/mnras/81.5.361](https://doi.org/10.1093/mnras/81.5.361).
- Miñoso, Yuderlys Espinosa (2017). "Hacia la construcción de la historia de un (des) encuentro: la razón feminista y la agencia antirracista y decolonial en Abya Yala." In: *Revista Praxis* 76, pp. 1–14.
- Mirabet, E. et al. (July 2014). "CARMENES ultra-stable cooling system: very promising results." In: *Advances in Optical and Mechanical Technologies for Telescopes and Instrumentation*. Ed. by Ramón Navarro, Colin R. Cunningham, and Allison A. Barto. Vol. 9151. Society of Photo-Optical Instrumentation Engineers (SPIE) Conference Series, 91513Y, 91513Y. DOI: [10.1117/12.2055570](https://doi.org/10.1117/12.2055570).
- Mishra, Lokesh, Yann Alibert, Adrien Leleu, Alexandre Emsenhuber, Christoph Mordasini, Remo Burn, Stéphane Udry, and Willy Benz (Dec. 2021). "The New Generation Planetary Population Synthesis (NGPPS) VI. Introducing KOBE: Kepler Observes Bern Exoplanets. Theoretical perspectives on the architecture of planetary systems: Peas in a pod." In: *A&A* 656, A74, A74. DOI: [10.1051/0004-6361/202140761](https://doi.org/10.1051/0004-6361/202140761). arXiv: [2105.12745](https://arxiv.org/abs/2105.12745) [astro-ph.EP].
- Mitchell, Sara McLaughlin, Samantha Lange, and Holly Brus (2013). "Gendered citation patterns in international relations journals." In: *International Studies Perspectives* 14.4, pp. 485–492.
- Mizuno, Hiroshi (Aug. 1980). "Formation of the Giant Planets." In: *Progress of Theoretical Physics* 64.2, pp. 544–557. ISSN: 0033-068X. DOI: [10.1143/PTP.64.544](https://doi.org/10.1143/PTP.64.544). eprint: <https://academic.oup.com/ptp/article-pdf/64/2/544/5289046/64-2-544.pdf>. URL: <https://doi.org/10.1143/PTP.64.544>.
- Morales, J. C. et al. (Sept. 2019). "A giant exoplanet orbiting a very-low-mass star challenges planet formation models." In: *Science* 365.6460, pp. 1441–1445. DOI: [10.1126/science.aax3198](https://doi.org/10.1126/science.aax3198). arXiv: [1909.12174](https://arxiv.org/abs/1909.12174) [astro-ph.EP].
- Morales, Juan Carlos et al. (Feb. 2009). "Absolute Properties of the Low-Mass Eclipsing Binary CM Draconis." In: *APJ* 691.2, pp. 1400–1411. DOI: [10.1088/0004-637X/691/2/1400](https://doi.org/10.1088/0004-637X/691/2/1400). arXiv: [0810.1541](https://arxiv.org/abs/0810.1541) [astro-ph].
- Morello, G., N. Casasayas-Barris, J. Orell-Miquel, E. Pallé, G. Cracchiolo, and G. Micela (Jan. 2022). "The strange case of Na I in the atmosphere of HD 209458 b. Reconciling low- and high-resolution spectroscopic observations." In: *A&A* 657, A97, A97. DOI: [10.1051/0004-6361/202141642](https://doi.org/10.1051/0004-6361/202141642). arXiv: [2110.13548](https://arxiv.org/abs/2110.13548) [astro-ph.EP].
- Morello, G., A. Claret, M. Martin-Lagarde, C. Cossou, A. Tsiaras, and P. O. Lagage (Feb. 2020a). "The ExoTETHyS Package: Tools for Exoplanetary Transits around Host Stars." In: *AJ* 159.2, 75, p. 75. DOI: [10.3847/1538-3881/ab63dc](https://doi.org/10.3847/1538-3881/ab63dc). arXiv: [1908.09599](https://arxiv.org/abs/1908.09599) [astro-ph.EP].

- Morello, G et al. (Jan. 2026). "The K-dwarfs Survey I. Four Validated Planets from the Radius Valley to the Neptune Desert." In: *Monthly Notices of the Royal Astronomical Society*, stag183. ISSN: 0035-8711. DOI: [10.1093/mnras/stag183](https://doi.org/10.1093/mnras/stag183). eprint: <https://academic.oup.com/mnras/advance-article-pdf/doi/10.1093/mnras/stag183/66590228/stag183.pdf>. URL: <https://doi.org/10.1093/mnras/stag183>.
- Morello, Giuseppe, Antonio Claret, Marine Martin-Lagarde, Christophe Cossou, Angelos Tsiara, and Pierre-Olivier Lagage (Feb. 2020b). "ExoTETHyS: Tools for Exoplanetary Transits around host stars." In: *The Journal of Open Source Software* 5.46, 1834, p. 1834. DOI: [10.21105/joss.01834](https://doi.org/10.21105/joss.01834).
- Morley, Caroline V., Heather Knutson, Michael Line, Jonathan J. Fortney, Daniel Thorngren, Mark S. Marley, Dillon Teal, and Roxana Lupu (Feb. 2017). "Forward and Inverse Modeling of the Emission and Transmission Spectrum of GJ 436b: Investigating Metal Enrichment, Tidal Heating, and Clouds." In: *AJ* 153.2, 86, p. 86. DOI: [10.3847/1538-3881/153/2/86](https://doi.org/10.3847/1538-3881/153/2/86). arXiv: [1610.07632](https://arxiv.org/abs/1610.07632) [astro-ph.EP].
- Morrell, Sam and Tim Naylor (Oct. 2019). "Exploring the M-dwarf Luminosity-Temperature-Radius relationships using Gaia DR2." In: *MNRAS* 489.2, pp. 2615–2633. DOI: [10.1093/mnras/stz2242](https://doi.org/10.1093/mnras/stz2242). arXiv: [1908.03025](https://arxiv.org/abs/1908.03025).
- Moutou, C., I. Boisse, G. Hebrard, E. Hebrard, J. F. Donati, X. Delfosse, and D. Kouach (2015). *SPIRou: a spectropolarimeter for the CFHT*. arXiv: [1510.01368](https://arxiv.org/abs/1510.01368) [astro-ph.IM].
- Nagel, E. et al. (Dec. 2023). "The CARMENES search for exoplanets around M dwarfs. Telluric absorption corrected high S/N optical and near-infrared template spectra of 382 M dwarf stars." In: *A&A* 680, A73, A73. DOI: [10.1051/0004-6361/202346524](https://doi.org/10.1051/0004-6361/202346524). arXiv: [2310.14715](https://arxiv.org/abs/2310.14715) [astro-ph.SR].
- Nakagawa, Y., C. Hayashi, and K. Nakazawa (June 1983). "Accumulation of planetesimals in the solar nebula." In: *Icarus* 54.3, pp. 361–376. DOI: [10.1016/0019-1035\(83\)90234-8](https://doi.org/10.1016/0019-1035(83)90234-8).
- Newton, Elisabeth R., Jonathan Irwin, David Charbonneau, Perry Berlind, Michael L. Calkins, and Jessica Mink (Jan. 2017). "The H α Emission of Nearby M Dwarfs and its Relation to Stellar Rotation." In: *APJ* 834.1, 85, p. 85. DOI: [10.3847/1538-4357/834/1/85](https://doi.org/10.3847/1538-4357/834/1/85). arXiv: [1611.03509](https://arxiv.org/abs/1611.03509) [astro-ph.SR].
- Newton, Elisabeth R., Jonathan Irwin, David Charbonneau, Zachory K. Berta-Thompson, Jason A. Dittmann, and Andrew A. West (Apr. 2016). "The Rotation and Galactic Kinematics of Mid M Dwarfs in the Solar Neighborhood." In: *APJ* 821.2, 93, p. 93. DOI: [10.3847/0004-637X/821/2/93](https://doi.org/10.3847/0004-637X/821/2/93). arXiv: [1511.00957](https://arxiv.org/abs/1511.00957) [astro-ph.SR].
- Newton, Elisabeth R. et al. (July 2019). "TESS Hunt for Young and Maturing Exoplanets (THYME): A Planet in the 45 Myr Tucana-Horologium Association." In: *APJL* 880.1, L17, p. L17. DOI: [10.3847/2041-8213/ab2988](https://doi.org/10.3847/2041-8213/ab2988). arXiv: [1906.10703](https://arxiv.org/abs/1906.10703) [astro-ph.EP].
- Nicholson, B. A. and S. Aigrain (Oct. 2022). "Quasi-periodic Gaussian processes for stellar activity: From physical to kernel parameters." In: *MNRAS*

- 515.4, pp. 5251–5266. DOI: [10.1093/mnras/stac2097](https://doi.org/10.1093/mnras/stac2097). arXiv: [2207.12164](https://arxiv.org/abs/2207.12164) [astro-ph.SR].
- Nielsen, Mathias, Jens Peter Andersen, Londa Schiebinger, and Jesper Schneider (Nov. 2017). “One and a half million medical papers reveal a link between author gender and attention to gender and sex analysis.” In: *Nature Human Behaviour* 1. DOI: [10.1038/s41562-017-0235-x](https://doi.org/10.1038/s41562-017-0235-x).
- Nortmann, L. et al. (Jan. 2025). “CRIRES⁺ transmission spectroscopy of WASP-127 b: Detection of the resolved signatures of a supersonic equatorial jet and cool poles in a hot planet.” In: *A&A* 693, A213, A213. DOI: [10.1051/0004-6361/202450438](https://doi.org/10.1051/0004-6361/202450438). arXiv: [2404.12363](https://arxiv.org/abs/2404.12363) [astro-ph.EP].
- Nortmann, Lisa et al. (Dec. 2018). “Ground-based detection of an extended helium atmosphere in the Saturn-mass exoplanet WASP-69b.” In: *Science* 362.6421, pp. 1388–1391. DOI: [10.1126/science.aat5348](https://doi.org/10.1126/science.aat5348). arXiv: [1812.03119](https://arxiv.org/abs/1812.03119) [astro-ph.EP].
- Nutzman, Philip and David Charbonneau (Mar. 2008). “Design Considerations for a Ground-Based Transit Search for Habitable Planets Orbiting M Dwarfs.” In: *PASP* 120.865, p. 317. DOI: [10.1086/533420](https://doi.org/10.1086/533420). arXiv: [0709.2879](https://arxiv.org/abs/0709.2879) [astro-ph].
- Omiya, Masashi, Bun’ei Sato, Hiroki Harakawa, Masayuki Kuzuhara, Teruyuki Hirano, and Norio Narita (Apr. 2014). “Search for Low-Mass Planets Around Late-M Dwarfs Using IRD.” In: *Formation, Detection, and Characterization of Extrasolar Habitable Planets*. Ed. by Nader Haghighipour. Vol. 293. IAU Symposium, pp. 201–203. DOI: [10.1017/S1743921313012830](https://doi.org/10.1017/S1743921313012830).
- Ormel, C. W. and H. H. Klahr (Sept. 2010). “The effect of gas drag on the growth of protoplanets. Analytical expressions for the accretion of small bodies in laminar disks.” In: *A&A* 520, A43, A43. DOI: [10.1051/0004-6361/201014903](https://doi.org/10.1051/0004-6361/201014903). arXiv: [1007.0916](https://arxiv.org/abs/1007.0916) [astro-ph.EP].
- Oshagh, M. et al. (Nov. 2020). “The widest broadband transmission spectrum (0.38–1.71 μm) of HD 189733b from ground-based chromatic Rossiter-McLaughlin observations.” In: *A&A* 643, A64, A64. DOI: [10.1051/0004-6361/202039213](https://doi.org/10.1051/0004-6361/202039213). arXiv: [2009.13823](https://arxiv.org/abs/2009.13823) [astro-ph.EP].
- Oswalt, Terry D. and Martin A. Barstow (2013). *Planets, Stars and Stellar Systems: Volume 4: Stellar Structure and Evolution*. DOI: [10.1007/978-94-007-5615-1](https://doi.org/10.1007/978-94-007-5615-1).
- Otegi, J. F., F. Bouchy, and R. Helled (Feb. 2020). “Revisited mass-radius relations for exoplanets below 120 M_{\oplus} .” In: *A&A* 634, A43, A43. DOI: [10.1051/0004-6361/201936482](https://doi.org/10.1051/0004-6361/201936482). arXiv: [1911.04745](https://arxiv.org/abs/1911.04745) [astro-ph.EP].
- Owen, James E. and Yanqin Wu (2017). “The Evaporation Valley in the Kepler Planets.” In: *The Astrophysical Journal* 847.1, p. 29. DOI: [10.3847/1538-4357/aa890a](https://doi.org/10.3847/1538-4357/aa890a). URL: <https://doi.org/10.3847/1538-4357/aa890a>.
- Padovani, Paolo and Michele Cirasuolo (Jan. 2023). “The Extremely Large Telescope.” In: *Contemporary Physics* 64.1, pp. 47–64. DOI: [10.1080/00107514.2023.2266921](https://doi.org/10.1080/00107514.2023.2266921). arXiv: [2312.04299](https://arxiv.org/abs/2312.04299) [astro-ph.IM].
- Palle, E. et al. (June 2020). “A He I upper atmosphere around the warm Neptune GJ 3470 b.” In: *A&A* 638, A61, A61. DOI: [10.1051/0004-6361/202037719](https://doi.org/10.1051/0004-6361/202037719). arXiv: [2004.12812](https://arxiv.org/abs/2004.12812) [astro-ph.EP].
- Palmer, Christopher (Mar. 2020). *Diffraction Grating Handbook, eighth edition*.

- Pascale, Enzo et al. (July 2018). "The ARIEL space mission." In: *Space Telescopes and Instrumentation 2018: Optical, Infrared, and Millimeter Wave*. Ed. by Makenzie Lystrup, Howard A. MacEwen, Giovanni G. Fazio, Natalie Batalha, Nicholas Siegler, and Edward C. Tong. Vol. 10698. Society of Photo-Optical Instrumentation Engineers (SPIE) Conference Series, 106980H, 106980H. DOI: [10.1117/12.2311838](https://doi.org/10.1117/12.2311838).
- Passegger, V. M. et al. (Oct. 2020). "The CARMENES search for exoplanets around M dwarfs. A deep learning approach to determine fundamental parameters of target stars." In: *A&A* 642, A22, A22. DOI: [10.1051/0004-6361/202038787](https://doi.org/10.1051/0004-6361/202038787). arXiv: [2008.01186](https://arxiv.org/abs/2008.01186) [astro-ph.SR].
- Passegger, V. M. et al. (Feb. 2022). "Metallicities in M dwarfs: Investigating different determination techniques." In: *A&A* 658, A194, A194. DOI: [10.1051/0004-6361/202141920](https://doi.org/10.1051/0004-6361/202141920). arXiv: [2111.14950](https://arxiv.org/abs/2111.14950) [astro-ph.SR].
- Peláez-Torres, A. et al. (Jan. 2026). "Tighter constraints on the atmosphere of GJ 436 b from combined high-resolution CARMENES and CRIRES⁺ observations." In: *A&A* 705, A256, A256. DOI: [10.1051/0004-6361/202557570](https://doi.org/10.1051/0004-6361/202557570). arXiv: [2512.04161](https://arxiv.org/abs/2512.04161) [astro-ph.EP].
- Peláez-Torres, A et al. (Apr. 2026). "A gem system with a lava world and a habitable zone sub-Neptune orbiting TOI-1752." In: *Monthly Notices of the Royal Astronomical Society*, stag713. ISSN: 0035-8711. DOI: [10.1093/mnras/stag713](https://doi.org/10.1093/mnras/stag713). eprint: <https://academic.oup.com/mnras/advance-article-pdf/doi/10.1093/mnras/stag713/68088278/stag713.pdf>. URL: <https://doi.org/10.1093/mnras/stag713>.
- Pepe, F., M. Mayor, F. Galland, D. Naef, D. Queloz, N. C. Santos, S. Udry, and M. Burnet (June 2002). "The CORALIE survey for southern extra-solar planets VII. Two short-period Saturnian companions to HD 108147 and HD 168746." In: *A&A* 388, pp. 632–638. DOI: [10.1051/0004-6361:20020433](https://doi.org/10.1051/0004-6361:20020433). arXiv: [astro-ph/0202457](https://arxiv.org/abs/astro-ph/0202457) [astro-ph].
- Pepe, F. et al. (Jan. 2021). "ESPRESSO at VLT. On-sky performance and first results." In: *A&A* 645, A96, A96. DOI: [10.1051/0004-6361/202038306](https://doi.org/10.1051/0004-6361/202038306). arXiv: [2010.00316](https://arxiv.org/abs/2010.00316) [astro-ph.IM].
- Pepe, Francesco, Michel Mayor, Bernard Delabre, Dominique Kohler, Daniel Lacroix, Didier Queloz, Stephane Udry, Willy Benz, Jean-Loup Bertaux, and Jean-Pierre Sivan (Aug. 2000). "HARPS: a new high-resolution spectrograph for the search of extrasolar planets." In: *Optical and IR Telescope Instrumentation and Detectors*. Ed. by Masanori Iye and Alan F. Moorwood. Vol. 4008. Society of Photo-Optical Instrumentation Engineers (SPIE) Conference Series, pp. 582–592. DOI: [10.1117/12.395516](https://doi.org/10.1117/12.395516).
- Perri, F. and A. G. W. Cameron (Aug. 1974). "Hydrodynamic Instability of the Solar Nebula in the Presence of a Planetary Core." In: *Icarus* 22.4, pp. 416–425. DOI: [10.1016/0019-1035\(74\)90074-8](https://doi.org/10.1016/0019-1035(74)90074-8).
- Pinamonti, M. et al. (Aug. 2022). "HADES RV Programme with HARPS-N at TNG. XV. Planetary occurrence rates around early-M dwarfs." In: *A&A* 664, A65, A65. DOI: [10.1051/0004-6361/202142828](https://doi.org/10.1051/0004-6361/202142828). arXiv: [2203.04648](https://arxiv.org/abs/2203.04648) [astro-ph.EP].

- Pinhas, Arazi, Benjamin V. Rackham, Nikku Madhusudhan, and Dániel Apai (Nov. 2018). "Retrieval of planetary and stellar properties in transmission spectroscopy with AURA." In: *MNRAS* 480.4, pp. 5314–5331. DOI: [10.1093/mnras/sty2209](https://doi.org/10.1093/mnras/sty2209). arXiv: [1808.10017](https://arxiv.org/abs/1808.10017) [astro-ph.EP].
- Pino, Lorenzo, David Ehrenreich, Romain Allart, Christophe Lovis, Matteo Brogi, Matej Malik, Valerio Nascimbeni, Francesco Pepe, and Giampaolo Piotto (Oct. 2018a). "Diagnosing aerosols in extrasolar giant planets with cross-correlation function of water bands." In: *A&A* 619, A3, A3. DOI: [10.1051/0004-6361/201832986](https://doi.org/10.1051/0004-6361/201832986). arXiv: [1807.10769](https://arxiv.org/abs/1807.10769) [astro-ph.EP].
- Pino, Lorenzo et al. (Apr. 2018b). "Combining low- to high-resolution transit spectroscopy of HD 189733b. Linking the troposphere and the thermosphere of a hot gas giant." In: *A&A* 612, A53, A53. DOI: [10.1051/0004-6361/201731244](https://doi.org/10.1051/0004-6361/201731244). arXiv: [1709.09678](https://arxiv.org/abs/1709.09678) [astro-ph.EP].
- Pleteit, Hanna Lina, Michael Debus, Sebastian Schäfer, and Ansgar Reiners (July 2024). "Second-generation Fabry-Pérot unit for CARMENES." In: *Ground-based and Airborne Instrumentation for Astronomy X*. Ed. by Julia J. Bryant, Kentaro Motohara, and Joël. R. D. Vernet. Vol. 13096. Society of Photo-Optical Instrumentation Engineers (SPIE) Conference Series, 130968A, 130968A. DOI: [10.1117/12.3017975](https://doi.org/10.1117/12.3017975).
- Plotnykov, Mykhaylo and Diana Valencia (May 2024). "Observation uncertainty effects on the precision of interior planetary parameters." In: *MNRAS* 530.3, pp. 3488–3499. DOI: [10.1093/mnras/stae993](https://doi.org/10.1093/mnras/stae993). arXiv: [2405.03860](https://arxiv.org/abs/2405.03860) [astro-ph.EP].
- Pollack, James B., Olenka Hubickyj, Peter Bodenheimer, Jack J. Lissauer, Morris Podolak, and Yuval Greenzweig (Nov. 1996). "Formation of the Giant Planets by Concurrent Accretion of Solids and Gas." In: *Icarus* 124.1, pp. 62–85. DOI: [10.1006/icar.1996.0190](https://doi.org/10.1006/icar.1996.0190).
- Pont, Frédéric, Shay Zucker, and Didier Queloz (Nov. 2006). "The effect of red noise on planetary transit detection." In: *MNRAS* 373.1, pp. 231–242. DOI: [10.1111/j.1365-2966.2006.11012.x](https://doi.org/10.1111/j.1365-2966.2006.11012.x). arXiv: [astro-ph/0608597](https://arxiv.org/abs/astro-ph/0608597) [astro-ph].
- Poveda, A., Christine Allen, R. Costero, J. Echevarría, and A. Hernández-Alcántara (Nov. 2009). "G 112-29 (=NLTT 18149): A Very Wide Companion to GJ 282 AB with a Common Proper Motion, Common Parallax, Common Radial Velocity, and Common Age." In: *APJ* 706.1, pp. 343–347. DOI: [10.1088/0004-637X/706/1/343](https://doi.org/10.1088/0004-637X/706/1/343). arXiv: [0910.2956](https://arxiv.org/abs/0910.2956) [astro-ph.GA].
- Pozuelos, F. J. and R. Varas (Apr. 2026). *ravex: RAdial VELOCITY eXplorer*. DOI: [10.5281/zenodo.19797145](https://doi.org/10.5281/zenodo.19797145). URL: <https://doi.org/10.5281/zenodo.19797145>.
- Queloz, D., G. W. Henry, J. P. Sivan, S. L. Baliunas, J. L. Beuzit, R. A. Donahue, M. Mayor, D. Naef, C. Perrier, and S. Udry (Nov. 2001). "No planet for HD 166435." In: *A&A* 379, pp. 279–287. DOI: [10.1051/0004-6361:20011308](https://doi.org/10.1051/0004-6361:20011308). arXiv: [astro-ph/0109491](https://arxiv.org/abs/astro-ph/0109491) [astro-ph].
- Queloz, Didier (1995). "Echelle Spectroscopy by a CCD at Low Signal-to-Noise Ratio." In: *Symposium - International Astronomical Union* 167, 221–229. DOI: [10.1017/S0074180900056473](https://doi.org/10.1017/S0074180900056473).

- Quirrenbach, A. et al. (July 2014). "CARMENES instrument overview." In: *Ground-based and Airborne Instrumentation for Astronomy V*. Ed. by Suzanne K. Ramsay, Ian S. McLean, and Hideki Takami. Vol. 9147. Society of Photo-Optical Instrumentation Engineers (SPIE) Conference Series, 91471F, 91471F. DOI: [10.1117/12.2056453](https://doi.org/10.1117/12.2056453).
- Quirrenbach, A. et al. (July 2018). "CARMENES: high-resolution spectra and precise radial velocities in the red and infrared." In: *Ground-based and Airborne Instrumentation for Astronomy VII*. Ed. by Christopher J. Evans, Luc Simard, and Hideki Takami. Vol. 10702. Society of Photo-Optical Instrumentation Engineers (SPIE) Conference Series, 107020W, 107020W. DOI: [10.1117/12.2313689](https://doi.org/10.1117/12.2313689).
- Ramirez, Ramses M. and Lisa Kaltenegger (2014). "THE HABITABLE ZONES OF PRE-MAIN-SEQUENCE STARS." In: *The Astrophysical Journal Letters* 797.2, p. L25. DOI: [10.1088/2041-8205/797/2/L25](https://doi.org/10.1088/2041-8205/797/2/L25). URL: <https://doi.org/10.1088/2041-8205/797/2/L25>.
- Rauer, Heike et al. (June 2025). "The PLATO mission." In: *Experimental Astronomy* 59.3, 26, p. 26. DOI: [10.1007/s10686-025-09985-9](https://doi.org/10.1007/s10686-025-09985-9). arXiv: [2406.05447](https://arxiv.org/abs/2406.05447) [astro-ph.IM].
- Ravinet, T. et al. (May 2024). "Near-infrared spectroscopic characterisation of Gaia ultra-cool dwarf candidates. Spectral types and peculiarities." In: *A&A* 685, A6, A6. DOI: [10.1051/0004-6361/202347954](https://doi.org/10.1051/0004-6361/202347954). arXiv: [2402.09783](https://arxiv.org/abs/2402.09783) [astro-ph.SR].
- Raymond, Sean N. and Alessandro Morbidelli (Jan. 2022). "Planet Formation: Key Mechanisms and Global Models." In: *Demographics of Exoplanetary Systems, Lecture Notes of the 3rd Advanced School on Exoplanetary Science*. Ed. by Katia Biazzo, Valerio Bozza, Luigi Mancini, and Alessandro Sozzetti. Vol. 466. Astrophysics and Space Science Library, pp. 3–82. DOI: [10.1007/978-3-030-88124-5_1](https://doi.org/10.1007/978-3-030-88124-5_1). arXiv: [2002.05756](https://arxiv.org/abs/2002.05756) [astro-ph.EP].
- Reid, Neill (Apr. 1987). "The stellar mass function at low luminosities." In: *MNRAS* 225, pp. 873–901. DOI: [10.1093/mnras/225.4.873](https://doi.org/10.1093/mnras/225.4.873).
- Reiners, A. and G. Basri (Feb. 2010). "A Volume-Limited Sample of 63 M7-M9.5 Dwarfs. II. Activity, Magnetism, and the Fade of the Rotation-Dominated Dynamo." In: *APJ* 710.2, pp. 924–935. DOI: [10.1088/0004-637X/710/2/924](https://doi.org/10.1088/0004-637X/710/2/924). arXiv: [0912.4259](https://arxiv.org/abs/0912.4259) [astro-ph.SR].
- Reiners, A. et al. (Apr. 2018). "The CARMENES search for exoplanets around M dwarfs. High-resolution optical and near-infrared spectroscopy of 324 survey stars." In: *A&A* 612, A49, A49. DOI: [10.1051/0004-6361/201732054](https://doi.org/10.1051/0004-6361/201732054). arXiv: [1711.06576](https://arxiv.org/abs/1711.06576) [astro-ph.SR].
- Reiners, A. et al. (June 2022). "Magnetism, rotation, and nonthermal emission in cool stars. Average magnetic field measurements in 292 M dwarfs." In: *A&A* 662, A41, A41. DOI: [10.1051/0004-6361/202243251](https://doi.org/10.1051/0004-6361/202243251). arXiv: [2204.00342](https://arxiv.org/abs/2204.00342) [astro-ph.SR].
- Reiners, Ansgar, Nandan Joshi, and Bertrand Goldman (Apr. 2012). "A Catalog of Rotation and Activity in Early-M Stars." In: *AJ* 143.4, 93, p. 93. DOI: [10.1088/0004-6256/143/4/93](https://doi.org/10.1088/0004-6256/143/4/93). arXiv: [1201.5774](https://arxiv.org/abs/1201.5774) [astro-ph.SR].

- Reuyl, Dirk and Erik Holmberg (Jan. 1943). "On the Existence of a Third Component in the System 70 Ophiuchi." In: *APJ* 97, p. 41. DOI: [10.1086/144489](https://doi.org/10.1086/144489).
- Ribas, I. et al. (Nov. 2018). "A candidate super-Earth planet orbiting near the snow line of Barnard's star." In: *Nature* 563.7731, pp. 365–368. DOI: [10.1038/s41586-018-0677-y](https://doi.org/10.1038/s41586-018-0677-y). arXiv: [1811.05955](https://arxiv.org/abs/1811.05955) [astro-ph.EP].
- Ribas, I. et al. (Feb. 2023). "The CARMENES search for exoplanets around M dwarfs. Guaranteed time observations Data Release 1 (2016-2020)." In: *A&A* 670, A139, A139. DOI: [10.1051/0004-6361/202244879](https://doi.org/10.1051/0004-6361/202244879). arXiv: [2302.10528](https://arxiv.org/abs/2302.10528) [astro-ph.EP].
- Ricker, George R. et al. (Jan. 2015). "Transiting Exoplanet Survey Satellite (TESS)." In: *Journal of Astronomical Telescopes, Instruments, and Systems* 1, 014003, p. 014003. DOI: [10.1117/1.JATIS.1.1.014003](https://doi.org/10.1117/1.JATIS.1.1.014003).
- Rivera, Eugenio J., Jack J. Lissauer, R. Paul Butler, Geoffrey W. Marcy, Steven S. Vogt, Debra A. Fischer, Timothy M. Brown, Gregory Laughlin, and Gregory W. Henry (2005). "A $\sim 7.5 M_{\text{Earth}}$ Planet Orbiting the Nearby Star, GJ 876*." In: *The Astrophysical Journal* 634.1, p. 625. DOI: [10.1086/491669](https://doi.org/10.1086/491669). URL: <https://doi.org/10.1086/491669>.
- Robertson, Paul et al. (July 2020). "Persistent Starspot Signals on M Dwarfs: Multiwavelength Doppler Observations with the Habitable-zone Planet Finder and Keck/HIRES." In: *APJ* 897.2, 125, p. 125. DOI: [10.3847/1538-4357/ab989f](https://doi.org/10.3847/1538-4357/ab989f). arXiv: [2005.09657](https://arxiv.org/abs/2005.09657) [astro-ph.SR].
- Rojas-Ayala, Bárbara, Kevin R. Covey, Philip S. Muirhead, and James P. Lloyd (Apr. 2012). "Metallicity and Temperature Indicators in M Dwarf K-band Spectra: Testing New and Updated Calibrations with Observations of 133 Solar Neighborhood M Dwarfs." In: *APJ* 748.2, 93, p. 93. DOI: [10.1088/0004-637X/748/2/93](https://doi.org/10.1088/0004-637X/748/2/93). arXiv: [1112.4567](https://arxiv.org/abs/1112.4567) [astro-ph.SR].
- Roth, Martin M. et al. (June 2005). "PMAS: The Potsdam Multi-Aperture Spectrophotometer. I. Design, Manufacture, and Performance." In: *PASP* 117.832, pp. 620–642. DOI: [10.1086/429877](https://doi.org/10.1086/429877). arXiv: [astro-ph/0502581](https://arxiv.org/abs/astro-ph/0502581) [astro-ph].
- Rubie, D. C., S. A. Jacobson, A. Morbidelli, D. P. O'Brien, E. D. Young, J. de Vries, F. Nimmo, H. Palme, and D. J. Frost (Mar. 2015). "Accretion and differentiation of the terrestrial planets with implications for the compositions of early-formed Solar System bodies and accretion of water." In: *Icarus* 248, pp. 89–108. DOI: [10.1016/j.icarus.2014.10.015](https://doi.org/10.1016/j.icarus.2014.10.015). arXiv: [1410.3509](https://arxiv.org/abs/1410.3509) [astro-ph.EP].
- Rugheimer, S., A. Segura, L. Kaltenegger, and D. Sasselov (2015). "UV Surface Environment of Earth-like Planets Orbiting FGKM Stars Through Geological Evolution." In: *The Astrophysical Journal* 806.1, p. 137. DOI: [10.1088/0004-637X/806/1/137](https://doi.org/10.1088/0004-637X/806/1/137). URL: <https://doi.org/10.1088/0004-637X/806/1/137>.
- Ruh, H. L. et al. (Dec. 2024). "The CARMENES search for exoplanets around M dwarfs: The impact of rotation and magnetic fields on the radial velocity jitter in cool stars." In: *A&A* 692, A138, A138. DOI: [10.1051/0004-6361/202450836](https://doi.org/10.1051/0004-6361/202450836). arXiv: [2412.07691](https://arxiv.org/abs/2412.07691) [astro-ph.EP].

- Saar, Steven H. and Axel Brandenburg (Oct. 1999). "Time Evolution of the Magnetic Activity Cycle Period. II. Results for an Expanded Stellar Sample." In: *APJ* 524.1, pp. 295–310. DOI: [10.1086/307794](https://doi.org/10.1086/307794).
- Saar, Steven H., R. Paul Butler, and Geoffrey W. Marcy (May 1998). "Magnetic Activity-related Radial Velocity Variations in Cool Stars: First Results from the Lick Extrasolar Planet Survey." In: *ApJ* 498.2, pp. L153–L157. DOI: [10.1086/311325](https://doi.org/10.1086/311325).
- Saar, Steven H. and Robert A. Donahue (Aug. 1997). "Activity-Related Radial Velocity Variation in Cool Stars." In: *ApJ* 485.1, pp. 319–327. DOI: [10.1086/304392](https://doi.org/10.1086/304392).
- Sabotta, S. et al. (Sept. 2021). "The CARMENES search for exoplanets around M dwarfs. Planet occurrence rates from a subsample of 71 stars." In: *A&A* 653, A114, A114. DOI: [10.1051/0004-6361/202140968](https://doi.org/10.1051/0004-6361/202140968). arXiv: [2107.03802](https://arxiv.org/abs/2107.03802) [astro-ph.EP].
- Safronov, V. S. (1972). *Evolution of the protoplanetary cloud and formation of the earth and planets*.
- Safronov, V. S. and E. V. Zvjagina (Jan. 1969). "Relative Sizes of the Largest Bodies during the Accumulation of Planets." In: *Icarus* 10.1, pp. 109–115. DOI: [10.1016/0019-1035\(69\)90013-X](https://doi.org/10.1016/0019-1035(69)90013-X).
- Sánchez-López, A., L. Lin, I. A. G. Snellen, N. Casasayas-Barris, A. García Muñoz, M. Lampón, and M. López-Puertas (Oct. 2022). "Detection of Paschen β absorption in the atmosphere of KELT-9 b. A new window into the atmospheres of ultra-hot Jupiters." In: *A&A* 666, L1, p. L1. DOI: [10.1051/0004-6361/202244416](https://doi.org/10.1051/0004-6361/202244416). arXiv: [2209.01854](https://arxiv.org/abs/2209.01854) [astro-ph.EP].
- Sánchez-López, A. et al. (Nov. 2020). "Discriminating between hazy and clear hot-Jupiter atmospheres with CARMENES." In: *A&A* 643, A24, A24. DOI: [10.1051/0004-6361/202038629](https://doi.org/10.1051/0004-6361/202038629). arXiv: [2009.06280](https://arxiv.org/abs/2009.06280) [astro-ph.EP].
- Sanghi, Aniket, Michael C. Liu, William M. Best, Trent J. Dupuy, Robert J. Siverd, and Zhoujian Zhang (Sept. 2023). "Ultracool Dwarf Absolute Magnitude versus Spectral Type Relations for JWST NIRCcam Filters." In: *Research Notes of the American Astronomical Society* 7.9, 194, p. 194. DOI: [10.3847/2515-5172/acf864](https://doi.org/10.3847/2515-5172/acf864).
- Sarro, L. M. et al. (Jan. 2023). "Ultracool dwarfs in Gaia DR3." In: *A&A* 669, A139, A139. DOI: [10.1051/0004-6361/202244507](https://doi.org/10.1051/0004-6361/202244507). arXiv: [2211.03641](https://arxiv.org/abs/2211.03641) [astro-ph.SR].
- Scalo, J. M. (May 1986). "The Stellar Initial Mass Function." In: *FCP* 11, pp. 1–278.
- Scargle, J. D. (Dec. 1982). "Studies in astronomical time series analysis. II. Statistical aspects of spectral analysis of unevenly spaced data." In: *APJ* 263, pp. 835–853. DOI: [10.1086/160554](https://doi.org/10.1086/160554).
- Schäfer, Sebastian, Eike W. Guenther, Ansgar Reiners, Johannes Winkler, Michael Pluto, and Jörg Schiller (July 2018). "Two Fabry-Pérots and two calibration units for CARMENES." In: *Ground-based and Airborne Instrumentation for Astronomy VII*. Ed. by Christopher J. Evans, Luc Simard, and Hideki Takami. Vol. 10702. Society of Photo-Optical Instrumentation Engineers (SPIE) Conference Series, 1070276, p. 1070276. DOI: [10.1117/12.2315241](https://doi.org/10.1117/12.2315241).

- Schlecker, M., C. Mordasini, A. Emsenhuber, H. Klahr, Th. Henning, R. Burn, Y. Alibert, and W. Benz (Dec. 2021a). “The New Generation Planetary Population Synthesis (NGPPS). III. Warm super-Earths and cold Jupiters: a weak occurrence correlation, but with a strong architecture-composition link.” In: *A&A* 656, A71, A71. DOI: [10.1051/0004-6361/202038554](https://doi.org/10.1051/0004-6361/202038554). arXiv: [2007.05563](https://arxiv.org/abs/2007.05563) [astro-ph.EP].
- Schlecker, M., D. Pham, R. Burn, Y. Alibert, C. Mordasini, A. Emsenhuber, H. Klahr, Th. Henning, and L. Mishra (Dec. 2021b). “The New Generation Planetary Population Synthesis (NGPPS). V. Predetermination of planet types in global core accretion models.” In: *A&A* 656, A73, A73. DOI: [10.1051/0004-6361/202140551](https://doi.org/10.1051/0004-6361/202140551). arXiv: [2104.11750](https://arxiv.org/abs/2104.11750) [astro-ph.EP].
- Schöfer, P. et al. (2019). “The CARMENES search for exoplanets around M dwarfs - Activity indicators at visible and near-infrared wavelengths.” In: *A&A* 623, A44. DOI: [10.1051/0004-6361/201834114](https://doi.org/10.1051/0004-6361/201834114). URL: <https://doi.org/10.1051/0004-6361/201834114>.
- Seager, Sara (2013). “Exoplanet Habitability.” In: *Science* 340.6132, pp. 577–581. DOI: [10.1126/science.1232226](https://doi.org/10.1126/science.1232226). eprint: <https://www.science.org/doi/pdf/10.1126/science.1232226>. URL: <https://www.science.org/doi/abs/10.1126/science.1232226>.
- Sebastian, D. et al. (Jan. 2021). “SPECULOOS: Ultracool dwarf transit survey. Target list and strategy.” In: *A&A* 645, A100, A100. DOI: [10.1051/0004-6361/202038827](https://doi.org/10.1051/0004-6361/202038827). arXiv: [2011.02069](https://arxiv.org/abs/2011.02069) [astro-ph.EP].
- Seidel, J. V., D. Ehrenreich, L. Pino, V. Bourrier, B. Lavie, R. Allart, A. Wyttenbach, and C. Lovis (Jan. 2020). “Wind of change: retrieving exoplanet atmospheric winds from high-resolution spectroscopy.” In: *A&A* 633, A86, A86. DOI: [10.1051/0004-6361/201936892](https://doi.org/10.1051/0004-6361/201936892). arXiv: [1912.02787](https://arxiv.org/abs/1912.02787) [astro-ph.EP].
- Seifahrt, Andreas, Julian Stürmer, Jacob L. Bean, and Christian Schwab (July 2018). “MAROON-X: a radial velocity spectrograph for the Gemini Observatory.” In: *Ground-based and Airborne Instrumentation for Astronomy VII*. Ed. by Christopher J. Evans, Luc Simard, and Hideki Takami. Vol. 10702. Society of Photo-Optical Instrumentation Engineers (SPIE) Conference Series, 107026D, p. 107026D. DOI: [10.1117/12.2312936](https://doi.org/10.1117/12.2312936). arXiv: [1805.09276](https://arxiv.org/abs/1805.09276) [astro-ph.IM].
- Selin, Helaine and Xiaochun Sun (Jan. 2000). *Astronomy Across Cultures: The History of Non-Western Astronomy*. Vol. 1. ISBN: 978-94-010-5820-9. DOI: [10.1007/978-94-011-4179-6](https://doi.org/10.1007/978-94-011-4179-6).
- Selsis, F., J. F. Kasting, B. Levrard, J. Paillet, I. Ribas, and X. Delfosse (Dec. 2007). “Habitable planets around the star Gliese 581?” In: *A&A* 476.3, pp. 1373–1387. DOI: [10.1051/0004-6361:20078091](https://doi.org/10.1051/0004-6361:20078091). arXiv: [0710.5294](https://arxiv.org/abs/0710.5294) [astro-ph].
- Serenelli, Aldo et al. (Dec. 2021). “Weighing stars from birth to death: mass determination methods across the HRD.” In: *AAPR* 29.1, 4, p. 4. DOI: [10.1007/s00159-021-00132-9](https://doi.org/10.1007/s00159-021-00132-9). arXiv: [2006.10868](https://arxiv.org/abs/2006.10868) [astro-ph.SR].
- Shan, Y. et al. (Apr. 2024). “CARMENES input catalog of M dwarfs. VII. New rotation periods for the survey stars and their correlations with stellar activity.” In: *A&A* 684, A9, A9. DOI: [10.1051/0004-6361/202346794](https://doi.org/10.1051/0004-6361/202346794). arXiv: [2401.09550](https://arxiv.org/abs/2401.09550) [astro-ph.SR].

- Smette, A. et al. (Apr. 2015). "Molecfit: A general tool for telluric absorption correction. I. Method and application to ESO instruments." In: *A&A* 576, A77, A77. DOI: [10.1051/0004-6361/201423932](https://doi.org/10.1051/0004-6361/201423932). arXiv: [1501.07239](https://arxiv.org/abs/1501.07239) [astro-ph.IM].
- Smith, Peter C. B. et al. (Mar. 2024). "A Combined Ground-based and JWST Atmospheric Retrieval Analysis: Both IGRINS and NIRSpec Agree that the Atmosphere of WASP-77A b Is Metal-poor." In: *AJ* 167.3, 110, p. 110. DOI: [10.3847/1538-3881/ad17bf](https://doi.org/10.3847/1538-3881/ad17bf). arXiv: [2312.13069](https://arxiv.org/abs/2312.13069) [astro-ph.EP].
- Snedden, Christopher Alan (Jan. 1973). "Carbon and Nitrogen Abundances in Metal-Poor Stars." PhD thesis. University of Texas, Austin.
- Snellen, I. A. G., S. Albrecht, E. J. W. de Mooij, and R. S. Le Poole (Aug. 2008). "Ground-based detection of sodium in the transmission spectrum of exoplanet HD 209458b." In: *A&A* 487.1, pp. 357–362. DOI: [10.1051/0004-6361:200809762](https://doi.org/10.1051/0004-6361:200809762). arXiv: [0805.0789](https://arxiv.org/abs/0805.0789) [astro-ph].
- Snellen, Ignas A. G., Remco J. de Kok, Ernst J. W. de Mooij, and Simon Albrecht (June 2010). "The orbital motion, absolute mass and high-altitude winds of exoplanet HD209458b." In: *Nature* 465.7301, pp. 1049–1051. DOI: [10.1038/nature09111](https://doi.org/10.1038/nature09111). arXiv: [1006.4364](https://arxiv.org/abs/1006.4364) [astro-ph.EP].
- Snellen, Ignas A.G. (2025). "Exoplanet Atmospheres at High Spectral Resolution." In: *Annual Review of Astronomy and Astrophysics* 63. Volume 63, 2025, pp. 83–125. ISSN: 1545-4282. DOI: <https://doi.org/10.1146/annurev-astro-052622-031342>. URL: <https://www.annualreviews.org/content/journals/10.1146/annurev-astro-052622-031342>.
- Soto, M. G. et al. (May 2021). "Mass and density of the transiting hot and rocky super-Earth LHS 1478 b (TOI-1640 b)." In: *A&A* 649, A144, A144. DOI: [10.1051/0004-6361/202140618](https://doi.org/10.1051/0004-6361/202140618). arXiv: [2102.11640](https://arxiv.org/abs/2102.11640) [astro-ph.EP].
- Standing, Matthew R. et al. (Apr. 2022). "BEBOP II: sensitivity to sub-Saturn circumbinary planets using radial-velocities." In: *MNRAS* 511.3, pp. 3571–3583. DOI: [10.1093/mnras/stac113](https://doi.org/10.1093/mnras/stac113). arXiv: [2112.05652](https://arxiv.org/abs/2112.05652) [astro-ph.EP].
- Stangret, M., N. Casasayas-Barris, E. Pallé, J. Orell-Miquel, G. Morello, R. Luque, G. Nowak, and F. Yan (June 2022). "High-resolution transmission spectroscopy study of ultra-hot Jupiters HAT-P-57b, KELT-17b, KELT-21b, KELT-7b, MASCARA-1b, and WASP-189b." In: *A&A* 662, A101, A101. DOI: [10.1051/0004-6361/202141799](https://doi.org/10.1051/0004-6361/202141799). arXiv: [2111.13064](https://arxiv.org/abs/2111.13064) [astro-ph.EP].
- Steinrueck, Maria E., Vivien Parmentier, Adam P. Showman, Joshua D. Lothringer, and Roxana E. Lupu (July 2019). "The Effect of 3D Transport-induced Disequilibrium Carbon Chemistry on the Atmospheric Structure, Phase Curves, and Emission Spectra of Hot Jupiter HD 189733b." In: *APJ* 880.1, 14, p. 14. DOI: [10.3847/1538-4357/ab2598](https://doi.org/10.3847/1538-4357/ab2598). arXiv: [1808.02011](https://arxiv.org/abs/1808.02011) [astro-ph.EP].
- Strand, K. Aa. (Feb. 1943). "61 Cygni as a Triple System." In: *PASP* 55.322, pp. 29–32. DOI: [10.1086/125484](https://doi.org/10.1086/125484).
- Strathern, Marilyn (1992). *Reproducing the Future: Essays on Anthropology, Kinship and the New Reproductive Technologies*. Oxford: Manchester University Press.
- Suarez Estrada, Marcela, Müller Barbara, Olivia Guest, and Iris van Rooij (June 2025). *Critical AI Literacy: Beyond hegemonic perspectives on sustainability*. DOI:

- 10.5281/zenodo.15677840. URL: <https://doi.org/10.5281/zenodo.15677840>.
- Suárez Mascareño, A., R. Rebolo, J. I. González Hernández, and M. Esposito (Sept. 2015). "Rotation periods of late-type dwarf stars from time series high-resolution spectroscopy of chromospheric indicators." In: *MNRAS* 452.3, pp. 2745–2756. DOI: 10.1093/mnras/stv1441. arXiv: 1506.08039 [astro-ph.EP].
- Suárez Mascareño, A. et al. (Dec. 2021). "Rapid contraction of giant planets orbiting the 20-million-year-old star V1298 Tau." In: *Nature Astronomy* 6, pp. 232–240. DOI: 10.1038/s41550-021-01533-7. arXiv: 2111.09193 [astro-ph.EP].
- Suárez Mascareño, Alejandro et al. (July 2025). "Diving into the planetary system of Proxima with NIRPS: Breaking the metre per second barrier in the infrared." In: *A&A* 700, A11, A11. DOI: 10.1051/0004-6361/202553728. arXiv: 2507.21751 [astro-ph.EP].
- Sugimoto, CASSIDY R. and VINCENT Larivière (2023). *Equity for Women in Science: Dismantling Systemic Barriers to Advancement*. Harvard University Press. ISBN: 9780674919297. URL: <http://www.jstor.org/stable/j.ctv37qqwrz> (visited on 04/23/2026).
- Takeuchi, Taku and D. N. C. Lin (Dec. 2002). "Radial Flow of Dust Particles in Accretion Disks." In: *APJ* 581.2, pp. 1344–1355. DOI: 10.1086/344437. arXiv: astro-ph/0208552 [astro-ph].
- Tarter, Jill C. et al. (Mar. 2007). "A Reappraisal of The Habitability of Planets around M Dwarf Stars." In: *Astrobiology* 7.1, pp. 30–65. DOI: 10.1089/ast.2006.0124. arXiv: astro-ph/0609799 [astro-ph].
- Teegarden, B. J., S. H. Pravdo, M. Hicks, K. Lawrence, S. B. Shaklan, K. Covey, O. Fraser, S. L. Hawley, T. McGlynn, and I. N. Reid (May 2003). "Discovery of a New Nearby Star." In: *APJL* 589.1, pp. L51–L53. DOI: 10.1086/375803. arXiv: astro-ph/0302206 [astro-ph].
- Teele, Dawn Langan and Kathleen Thelen (2017). "Gender in the journals: Publication patterns in political science." In: *PS: Political Science & Politics* 50.2, pp. 433–447.
- Tozzi, A. et al. (Aug. 2016). "GIANO and HARPS-N together: towards an Earth-mass detection instrument." In: *Ground-based and Airborne Instrumentation for Astronomy VI*. Ed. by Christopher J. Evans, Luc Simard, and Hideki Takami. Vol. 9908. Society of Photo-Optical Instrumentation Engineers (SPIE) Conference Series, 99086C, p. 99086C. DOI: 10.1117/12.2231898.
- Tremblay, P.-E., H.-G. Ludwig, B. Freytag, M. Steffen, and E. Caffau (Sept. 2013). "Granulation properties of giants, dwarfs, and white dwarfs from the CIFIST 3D model atmosphere grid." In: *A&A* 557, A7, A7. DOI: 10.1051/0004-6361/201321878. arXiv: 1307.2810 [astro-ph.SR].
- Trifonov, T. et al. (Feb. 2018). "The CARMENES search for exoplanets around M dwarfs . First visual-channel radial-velocity measurements and orbital parameter updates of seven M-dwarf planetary systems." In: *A&A* 609, A117, A117. DOI: 10.1051/0004-6361/201731442. arXiv: 1710.01595 [astro-ph.EP].

- Trifonov, T. et al. (Mar. 2021). "A nearby transiting rocky exoplanet that is suitable for atmospheric investigation." In: *Science* 371.6533, pp. 1038–1041. DOI: [10.1126/science.abd7645](https://doi.org/10.1126/science.abd7645). arXiv: [2103.04950](https://arxiv.org/abs/2103.04950) [astro-ph.EP].
- Trifonov, Trifon, Tal-Or, Lev, Zechmeister, Mathias, Kaminski, Adrian, Zucker, Shay, and Mazeh, Tsevi (2020). "Public HARPS radial velocity database corrected for systematic errors." In: *A&A* 636, A74. DOI: [10.1051/0004-6361/201936686](https://doi.org/10.1051/0004-6361/201936686). URL: <https://doi.org/10.1051/0004-6361/201936686>.
- Turbet, Martin et al. (Sept. 2022). "The TRAPPIST-1 Habitable Atmosphere Inter-comparison (THAI). I. Dry Cases-The Fellowship of the GCMs." In: *PSJ* 3.9, 211, p. 211. DOI: [10.3847/PSJ/ac6cf0](https://doi.org/10.3847/PSJ/ac6cf0). arXiv: [2109.11457](https://arxiv.org/abs/2109.11457) [astro-ph.EP].
- Valenti, J. A. and N. Piskunov (Sept. 1996). "Spectroscopy made easy: A new tool for fitting observations with synthetic spectra." In: *A&As* 118, pp. 595–603.
- Varas, R. et al. (2025). "Improving radial velocity precision with CARMENES-PLUS." In: *Experimental Astronomy* 60.2, p. 10. ISSN: 1572-9508. DOI: [10.1007/s10686-025-10020-0](https://doi.org/10.1007/s10686-025-10020-0). URL: <https://doi.org/10.1007/s10686-025-10020-0>.
- Varas, R. et al. (2026). *The CARMENES search for exoplanets around M dwarfs. A homogeneous catalogue of projected rotational velocities accounting for limb-darkening*. arXiv: [2604.15428](https://arxiv.org/abs/2604.15428) [astro-ph.SR]. URL: <https://arxiv.org/abs/2604.15428>.
- Vidotto, A. A., R. Fares, M. Jardine, C. Moutou, and J.-F. Donati (June 2015). "On the environment surrounding close-in exoplanets." In: *MNRAS* 449.4, pp. 4117–4130. DOI: [10.1093/mnras/stv618](https://doi.org/10.1093/mnras/stv618). arXiv: [1503.05711](https://arxiv.org/abs/1503.05711).
- Wakeford, H. R. et al. (Jan. 2018). "The Complete Transmission Spectrum of WASP-39b with a Precise Water Constraint." In: *AJ* 155.1, 29, p. 29. DOI: [10.3847/1538-3881/aa9e4e](https://doi.org/10.3847/1538-3881/aa9e4e). arXiv: [1711.10529](https://arxiv.org/abs/1711.10529) [astro-ph.EP].
- Walker, J. C. G., P. B. Hays, and J. F. Kasting (Oct. 1981). "A negative feedback mechanism for the long-term stabilization of the earth's surface temperature." In: *JGR* 86, pp. 9776–9782. DOI: [10.1029/JC086iC10p09776](https://doi.org/10.1029/JC086iC10p09776).
- Ward-Duong, K. et al. (Oct. 2018). *VizieR Online Data Catalog: TBOSS Survey. II. ALMA continuum observations (Ward-Duong+, 2018)*. VizieR On-line Data Catalog: [J/AJ/155/54](https://vizier.cds.cern.ch/vizier/J/AJ/155/54). Originally published in: 2018AJ....155...54W. DOI: [10.26093/cds/vizier.51550054](https://doi.org/10.26093/cds/vizier.51550054).
- Watson, A. J., T. M. Donahue, and J. C. G. Walker (Nov. 1981). "The dynamics of a rapidly escaping atmosphere: Applications to the evolution of Earth and Venus." In: *Icarus* 48.2, pp. 150–166. DOI: [10.1016/0019-1035\(81\)90101-9](https://doi.org/10.1016/0019-1035(81)90101-9).
- Weidenschilling, S. J. (July 1977). "Aerodynamics of solid bodies in the solar nebula." In: *MNRAS* 180, pp. 57–70. DOI: [10.1093/mnras/180.2.57](https://doi.org/10.1093/mnras/180.2.57).
- West, Andrew A., Suzanne L. Hawley, John J. Bochanski, Kevin R. Covey, I. Neill Reid, Saurav Dhital, Eric J. Hilton, and Michael Masuda (Mar. 2008). "Constraining the Age-Activity Relation for Cool Stars: The Sloan Digital Sky Survey Data Release 5 Low-Mass Star Spectroscopic Sample." In: *AJ* 135.3, pp. 785–795. DOI: [10.1088/0004-6256/135/3/785](https://doi.org/10.1088/0004-6256/135/3/785). arXiv: [0712.1590](https://arxiv.org/abs/0712.1590) [astro-ph].

- West, Andrew A. et al. (2011). "The Sloan Digital Sky Survey Data Release 7 Spectroscopic M Dwarf Catalog. I. Data." In: *The Astronomical Journal* 141.3, p. 97. DOI: [10.1088/0004-6256/141/3/97](https://doi.org/10.1088/0004-6256/141/3/97). URL: <https://doi.org/10.1088/0004-6256/141/3/97>.
- Whipple, F. L. (Jan. 1972). "On certain aerodynamic processes for asteroids and comets." In: *From Plasma to Planet*. Ed. by Aina Elvius, p. 211.
- Widder, David Gray, Meredith Whittaker, and Sarah Myers West (Nov. 2024). "Why 'open' AI systems are actually closed, and why this matters." In: *Nature* 635.8040, pp. 827–833. DOI: [10.1038/s41586-024-08141-1](https://doi.org/10.1038/s41586-024-08141-1).
- Winters, Jennifer G., Todd J. Henry, Wei-Chun Jao, John P. Subasavage, Joseph P. Chatelain, Ken Slatten, Adric R. Riedel, Michele L. Silverstein, and Matthew J. Payne (June 2019). "The Solar Neighborhood. XLV. The Stellar Multiplicity Rate of M Dwarfs Within 25 pc." In: *AJ* 157.6, 216, p. 216. DOI: [10.3847/1538-3881/ab05dc](https://doi.org/10.3847/1538-3881/ab05dc). arXiv: [1901.06364](https://arxiv.org/abs/1901.06364) [astro-ph.SR].
- Wolszczan, A. and D. A. Frail (Jan. 1992). "A planetary system around the millisecond pulsar PSR1257 + 12." In: *Nature* 355.6356, pp. 145–147. DOI: [10.1038/355145a0](https://doi.org/10.1038/355145a0).
- Wong, Kekoa and Hannah Rubin (2024). "Social Dynamics and the Evolution of Disciplines." In: *Philosophy of Science* 91.5, 1179–1188. DOI: [10.1017/psa.2023.149](https://doi.org/10.1017/psa.2023.149).
- Woolf, Vincent M. and George Wallerstein (Jan. 2005). "Metallicity measurements using atomic lines in M and K dwarf stars." In: *Monthly Notices of the Royal Astronomical Society* 356.3, pp. 963–968. ISSN: 0035-8711. DOI: [10.1111/j.1365-2966.2004.08515.x](https://doi.org/10.1111/j.1365-2966.2004.08515.x). eprint: <https://academic.oup.com/mnras/article-pdf/356/3/963/3141389/356-3-963.pdf>. URL: <https://doi.org/10.1111/j.1365-2966.2004.08515.x>.
- Wright, Nicholas J., Jeremy J. Drake, Eric E. Mamajek, and Gregory W. Henry (Dec. 2011). "The Stellar-activity-Rotation Relationship and the Evolution of Stellar Dynamos." In: *APJ* 743.1, 48, p. 48. DOI: [10.1088/0004-637X/743/1/48](https://doi.org/10.1088/0004-637X/743/1/48). arXiv: [1109.4634](https://arxiv.org/abs/1109.4634) [astro-ph.SR].
- Wright, Nicholas J., Elisabeth R. Newton, Peter K. G. Williams, Jeremy J. Drake, and Rakesh K. Yadav (Sept. 2018). "The stellar rotation-activity relationship in fully convective M dwarfs." In: *MNRAS* 479.2, pp. 2351–2360. DOI: [10.1093/mnras/sty1670](https://doi.org/10.1093/mnras/sty1670). arXiv: [1807.03304](https://arxiv.org/abs/1807.03304) [astro-ph.SR].
- Wunderlich, Fabian, Mareike Godolt, John Lee Grenfell, Steffen Städt, Alexis M. S. Smith, Stefanie Gebauer, Franz Schreier, Pascal Hedelt, and Heike Rauer (Apr. 2019). "Detectability of atmospheric features of Earth-like planets in the habitable zone around M dwarfs." In: *A&A* 624, A49, A49. DOI: [10.1051/0004-6361/201834504](https://doi.org/10.1051/0004-6361/201834504). arXiv: [1905.02560](https://arxiv.org/abs/1905.02560) [astro-ph.EP].
- Youdin, Andrew N. and Jeremy Goodman (Feb. 2005). "Streaming Instabilities in Protoplanetary Disks." In: *APJ* 620.1, pp. 459–469. DOI: [10.1086/426895](https://doi.org/10.1086/426895). arXiv: [astro-ph/0409263](https://arxiv.org/abs/astro-ph/0409263) [astro-ph].
- Youngblood, Allison et al. (July 2017). "The MUSCLES Treasury Survey. IV. Scaling Relations for Ultraviolet, Ca II K, and Energetic Particle Fluxes from M Dwarfs." In: *APJ* 843.1, 31, p. 31. DOI: [10.3847/1538-4357/aa76dd](https://doi.org/10.3847/1538-4357/aa76dd). arXiv: [1705.04361](https://arxiv.org/abs/1705.04361) [astro-ph.SR].

- Zechmeister, M. and M. Kürster (Mar. 2009). "The generalised Lomb-Scargle periodogram. A new formalism for the floating-mean and Keplerian periodograms." In: *A&A* 496.2, pp. 577–584. DOI: [10.1051/0004-6361:200811296](https://doi.org/10.1051/0004-6361:200811296). arXiv: 0901.2573 [astro-ph.IM].
- Zechmeister, M. et al. (2018). "Spectrum radial velocity analyser (SERVAL) - High-precision radial velocities and two alternative spectral indicators." In: *A&A* 609, A12. DOI: [10.1051/0004-6361/201731483](https://doi.org/10.1051/0004-6361/201731483). URL: <https://doi.org/10.1051/0004-6361/201731483>.
- Zechmeister, M. et al. (July 2019). "The CARMENES search for exoplanets around M dwarfs. Two temperate Earth-mass planet candidates around Teegarden's Star." In: *A&A* 627, A49, A49. DOI: [10.1051/0004-6361/201935460](https://doi.org/10.1051/0004-6361/201935460). arXiv: 1906.07196 [astro-ph.EP].
- de Kok, R. J., M. Brogi, I. A. G. Snellen, J. Birkby, S. Albrecht, and E. J. W. de Mooij (June 2013). "Detection of carbon monoxide in the high-resolution day-side spectrum of the exoplanet HD 189733b." In: *A&A* 554, A82, A82. DOI: [10.1051/0004-6361/201321381](https://doi.org/10.1051/0004-6361/201321381). arXiv: 1304.4014 [astro-ph.EP].
- van de Kamp, P. (Aug. 1969). "Alternate dynamical analysis of Barnard's star." In: *AJ* 74, pp. 757–759. DOI: [10.1086/110852](https://doi.org/10.1086/110852).
- von Bloh, W., C. Bounama, M. Cuntz, and S. Franck (Dec. 2007). "The habitability of super-Earths in Gliese 581." In: *A&A* 476.3, pp. 1365–1371. DOI: [10.1051/0004-6361:20077939](https://doi.org/10.1051/0004-6361:20077939). arXiv: 0705.3758 [astro-ph].